DOCTORAL DISSERTATION
博士論文

Spin Hall Effect in Ferromagnets (強磁性体におけるスピンホール効果)

A Dissertation Submitted for the Degree of Doctor of Philosophy, December 2020
令和2年12月博士(理学)申請

Department of Physics, Graduate School of Science, The University of Tokyo
東京大学大学院理学系研究科 物理学専攻

QU GUANXIONG
曲 冠雄

The unexamined theory is not worth living.

Acknowledgments

Firstly, I would like to thank my supervisor, Prof. Masamitsu Hayashi, for his insightful academic instructions as well as his advice on my life. It is the greatest fortune for me to have an opportunity to study physics as a doctoral student in Hayashi Lab. I would like to thank Prof. Kohji Nakamura for his teaching me the DFT calculation skills as well as his acute comments on my works. I would also like to thank Dr. Junji Fujimoto for sharing his knowledge on the Dirac ferromagnet and the linear response theory.

Additionally, I would like to thank Dr. Lau Yong-Chang for his advices and discussions on the experimental results about spin Hall effect. I would like to thank Chi Zhendong for him sharing his knowledge on the Bi semimetals and Dirac electron system. I am grateful to study with all students and faculties in Hayashi Lab with whom we share our perspective comprehensions on physics as well as talks on daily life during my doctoral program. Besides, I express my gratitude to Mayuko Niwata and staffs in International Liaison Office(ILO) who help me with all the administrative issues on studying and living in Tokyo.

Further, I would like to thank Prof. Kazuhiro Hono who guides me to the field of spintronics and Dr. Yuya Sakuraba for his teaching me experimental skills in my master's program.

Finally, I thank my family, especially my parents, for their unhesitant support and understanding of my pursue.

Abstract

The spin Hall effect (SHE) is the fundamental charge-to-spin conversion mechanism in spintronics, which has been extensively studied in paramagnetic materials. Recent experimental results confirmed the existence of SHE in the ferromagnets but also caused a debate on whether the SHE would be affected by the ferromagnetic ordering. Hence, the crucial issues on SHE in ferromagnets are two-fold: i, its relationship with the anomalous Hall effect (AHE), which is widely considered to share the same mechanisms; ii, whether the SHE depends on the direction of magnetization.

In this dissertation, both numerical and analytical *ab initio* techniques are adapted to study the intrinsic SHE in various types of ferromagnets, in which I primarily focus on the above two issues. Through first principles calculations, relationship between the AHE and SHE are investigated, where I emphasize the unique features of anti-crossings of Bloch states with opposite spin. In such anti-crossings, due to the considerable difference between matrix elements in velocity and spin velocity operators, the Berry curvature and spin Berry curvature behave divergently, which results in the reduction of symmetry of spin Berry curvature comparing with the Berry curvature. The ubiquity of these anti-crossing implies that the intrinsic AHE and SHE may not have strong correlation, as evidenced in experiments. Subsequently, I find the intrinsic SHC in cubic phase ferromagnets (bcc-Fe and fcc-Ni) are highly anisotropic with respect to the direction of magnetization, *i.e.*, the change in the magnitude of intrinsic SHC for bcc-Fe is four-fold. The anisotropy of intrinsic SHC is closely related to the anti-crossings with opposite spin, where the interband matrix elements are enhanced when magnetization is rotated away from the quantization axis. To investigate the anisotropic SHE in the ferromagnets, I choose two types of model Hamiltonian for analytical *ab initio* calculations: 2DEG with exchange interaction and Dirac ferromagnet. The intrinsic SHC is strongly anisotropic in both cases. In the 2DEG model, the anisotropy is attributed to the interplay of

Rashba and Dresselhaus SOC and exchange interaction. In the Dirac ferromagnet, the anisotropy is attributed to the axial anisotropy induced by ferromagnetic ordering. Hence, the anisotropy of SHC does not disappear when the strength of magnetization is asymptotically approaching zero. It suggests that for intrinsic SHC in massive Dirac electron system, a non-trivial transition exists from a ferromagnetic state to paramagnetic state.

Contents

List of Figures

List of Tables

Chapter 1

Introduction

Contents

1.1 The spin Hall effect

Spintronics is the field exploring electron's spin degree of freedom beyond its charge degree of freedom to control various properties of materials and devices [1, 2]. Among the mechanisms of charge-to-spin conversion, the spin Hall effect (SHE) is considered as a promising practice since its first observation in experiments [3–5]. In the SHE, applying an electric current to a material generates a transverse spin current polarized perpendicular to both of the electric current and spin current. Its direct analogy is the anomalous Hall effect (AHE) [6], where an electric current passing through a ferromagnet generates a transverse charge current whose polarization is parallel with the spontaneous magnetization. A more historical tie between SHE and AHE dates back to their very original works [7,8] mutually inspired by the Mott scattering experiment [9, 10]. In the Mott scattering, an unpolarized electron beam is scattered in large angle $\sim 90^\circ$ with asymmetric spin population in left and right directions, due to the strong spin orbit coupling (SOC) of nuclei. It has been, accordingly, acknowledged that both AHE and SHE are caused by the relativistic SOC. Research on SHE remained dormant for nearly three decades after its first proposal and was revived only two decades ago [11,12], owning to enthusiasm on spin current generation. Most of earlier works on SHE relied on process of electron scattered by the impurities, which was categorized as the extrinsic mechanism in modern language. In addition, a strong intrinsic SHE [13, 14] was also purposed in analogy to the intrinsic AHE, which exists even in a perfect crystal without any impurities. The attraction of intrinsic AHE and SHE is their topological nature and close association with the Berry phase of the Bloch bands, for which it draws significant theoretical attentions.

In the experimental perspective, the key issue in detecting the SHE is the lack of direct electrical signal, in contrast to the AHE. The initial proposals on SHE detection mostly relied on the optical means based on the Magneto-optic Kerr effect, with which SHE was evidenced in both extrinsic regime [3] and intrinsic regime [4]. The electric detection [15] of SHE, however, relied on its reciprocal effect, *i.e.*, the inverse spin Hall effect (ISHE) [16], where a spin current passed through a material generates a transverse charge current. Recent experiments on SHE are mostly carried out in ferromagnet-paramagnet heterostructures, where the SHE induced spin current from paramagnet is injected into the ferromagnet and causes its spin dynamics [17, 18].

It should be noted that the the physics and mechanisms of the SHE is constructed

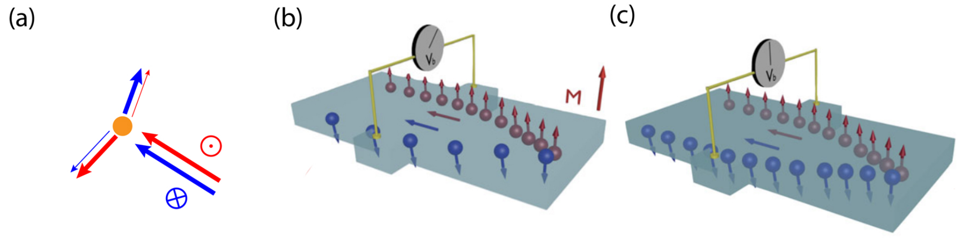

Mott scattering AHE SHE

Figure 1.1: An illustration of Mott scattering, AHE and SHE.
In the Mott scattering (a), unpolarized electron beam is scattered transversely with asymmetric spin population. In the AHE (b), a charge current flow in material generates a transverse voltage in presence of magnetization $\boldsymbol{M}$. In the SHE (c), a charge current flow in material generates a transverse spin accumulation with balanced transverse voltage. Figure (b) and (c) are courtesy of Sinova *et al.* [5].

in analogy to the theoretical frameworks of the AHE. However, an important distinction should be pointed out in the first place. The AHE correlates two charge degrees of freedoms, which are conserved quantities, *via* relativistic SOC. In contrast, the SHE correlates the charge degree of freedom with the spin degree of freedom, which is a non-conserved quantity subject to decay and dephasing [5].

In the following section, we briefly introduce the basic theories on SHE, together with the theories on AHE in analogy.

1.1.1 Theory of the spin Hall effect

The spin Hall effect and anomalous Hall effect are essentially quantum phenomena which originate from the coherent band mixing induced by both the external electric field and the disorder potential. Similar to other coherent interference phenomena, they consequently cannot be fully formulated with semi-classical Boltzmann transport theory. In the modern theory of AHE and SHE, a fully quantum-mechanical approach based on linear response theory has been employed.

The theoretical framework of understanding the AHE and SHE is their phenomenological classification into three main mechanisms: *intrinsic, skew scattering, and side jump* (Fig. 1.2), which depend on the Bloch state transport life time τ [6]. This classification is directly guided by experimental results and by the microscopic theory of AHE in ferromagnetic metals. Within the metallic regime, disorder is treated perturbatively and the scattering processes are expanded in the order of quasiparticle scattering rate τ^{-1}. It is

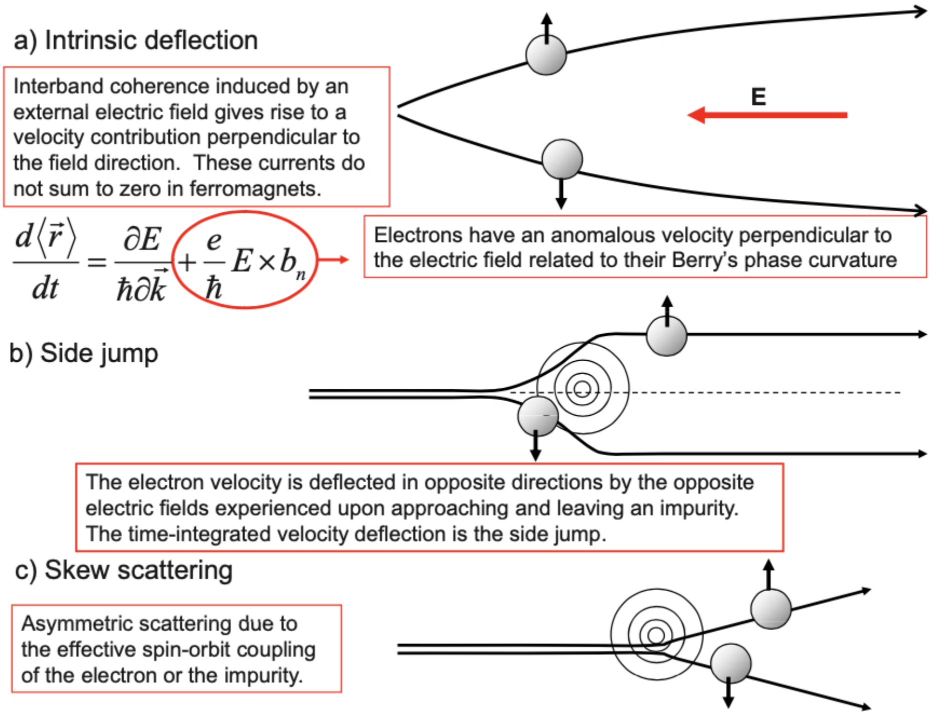

Figure 1.2: Three main mechanisms in AHE.
An illustration of the three main mechanisms that can give rise to AHE: (a) intrinsic contribution; (b) side jump; (c) skew scattering. Courtesy of Nagaosa *et al.* [6].

relatively easy to identify the contributions to the anomalous Hall conductivity (AHC), σ_{xy}, or spin Hall conductivity (SHC), σ^s_{xy}, which vary with lower order, *e.g.*, τ^0 and τ^1. In experiments on the AHE, this separation can sometimes be achieved by plotting σ_{xy} *vs* the longitudinal conductivity σ_{xx}, where τ is varied by altering disorder or varying temperature. For the SHE, the spin current has to be detected as the spin accumulation and can therefore depend on the method of measurement, which complicates the separation of its mechanisms. Experimental attempt on separation of contributions on the SHC has been reported using non-local measurements [19].

It should be noted that several microscopically distinct contributions can share the same τ dependence [20, 21]. The contribution proportional to τ^1 is defined as the skew-scattering contribution, $\sigma^{(s),skew}_{xy}$. The contribution proportional to τ^0 (or independent of σ_{xx}) is further separated into two terms: intrinsic and side jump. Although these two contributions cannot be distinguished experimentally by dc measurements, they can be separated experimentally and theoretically by defining the intrinsic contribution $\sigma^{(s),int}_{xy}$ as the extrapolation of the ac-interband Hall conductivity to zero frequency in the limit $\omega \rightarrow$

0. This leads to a unique definition for the last contribution, termed side jump, as $\sigma_{xy}^{(s),sj} = \sigma_{xy}^{(s)} - \sigma_{xy}^{(s),skew} - \sigma_{xy}^{(s),int}$. Despite the historical terminology, the above definitions have not relied on linking with terms in semiclassical processes such as side-jump scattering [22] or skew scattering from asymmetric contributions to the semiclassical scattering rates [23] but are based on the modern linear response theory of AHE and SHE.

1.1.2 Intrinsic mechanism

The intrinsic contribution is the easiest to evaluate accurately and is also the most attracting one for theoretical studies, due to its topological nature. There is a direct link between the intrinsic mechanism and the semiclassical theory in which the induced interband coherence is captured by an "anomalous velocity" arising from a momentum-space Berry phase.

In the context of the AHE, this contribution was first derived by Karplus [8] termed as the "anomalous velocity" but its topological nature was not fully appreciated until recently [24, 25]. Studies on the intrinsic AHE were motivated by the experimental importance of the AHE in ferromagnetic semiconductors and also by the analysis of the relationship between momentum-space Berry phases and anomalous velocities in semiclassical transport theory [26, 27]. In analogy to intrinsic AHE, the dissipationless intrinsic SHE was proposed by Murakami and Sinova [13, 14].

The intrinsic contribution is defined microscopically as the dc limit of the interband conductivity from the Kubo formula for an ideal lattice [14, 28],

$$\sigma_{ij}^{\alpha,int} = \sum_{n \neq n'} \int \frac{d\boldsymbol{k}}{2\pi^d} (f_{n,\boldsymbol{k}} - f_{n',\boldsymbol{k}}) \mathrm{Im} \frac{\langle n,\boldsymbol{k}| J_i^\alpha |n',\boldsymbol{k}\rangle \langle n',\boldsymbol{k}| J_j |n,\boldsymbol{k}\rangle}{(\varepsilon_{n,\boldsymbol{k}} - \varepsilon_{n',\boldsymbol{k}})^2}, \tag{1.1}$$

where n, n' are band indices, J_i^α represents the charge current operator ($\alpha = 0$) and the spin current operator $\alpha = 1, 2, 3$ for AHE and SHE, respectively. What makes the intrinsic contribution quite unique, particularly in the AHE, is that it is directly linked to the topological properties of the Bloch states. Specifically, the intrinsic AHE is proportional to the integration over the Fermi sea of the Berry curvature of each occupied band [29,30]. Moreover, the intrinsic SHE in Luttinger model can also be described by the curvature tensor of a particular subspace of heavy-hole bands or light-hole bands, which manifests its topological aspect [31].

One of the motivations for identifying the intrinsic contribution $\sigma_{xy}^{(s),int}$ is that it can be evaluated accurately even for materials with relatively complex electronic band structure using microscopic *ab initio* theory techniques. In many materials with strongly spin-orbit-coupled bands, the intrinsic contribution seems to dominate the SHE and AHE. The calculations have given semiquantitative predictions of the expected spin Hall angles, particularly in heavy metals. This is illustrated in the density-functional calculation for Pt [32] and in the microscopic tight-binding calculations for other $4d$ and $5d$ metals [33]. The calculated SHC are predicted to be large in these transition metals, and, in particular, a sign change is predicted between Pt and Ta, which has been observed in experiments.

1.1.3 Skew-scattering mechanism

The skew-scattering contribution to the SHE and the AHE is the mechanism proportional to the Bloch state transport lifetime τ, wherefore it tends to dominate in nearly perfect crystals. It is the only contribution to the SHE and AHE which appears in traditional Boltzmann transport theory where interband coherence effects are usually neglected. Skew scattering is due to chiral features which appear in disorder scattering in the presence of SOC. This mechanism was first identified in ferromagnets by Smit [23] and has its origins in the Mott scattering in relativistic physics [9, 10]. In the semiclassical Boltzmann theory, skew-scattering contribution originates from the chiral features of SOC which break the left-right symmetry of detailed balance in transition probability. In the presence of SOC, either in a Hamiltonian of the perfect crystal or in a disorder Hamiltonian, a transition which is right handed with respect to the magnetization direction has a different probability than the corresponding left-handed transition. When the transition rates are evaluated perturbatively, asymmetric chiral contributions appear at third order. In simple models, the asymmetric chiral contribution to the transition probability of momenta $\boldsymbol{k}, \boldsymbol{k}'$ is often assumed to have the form

$$W_{\boldsymbol{k},\boldsymbol{k}'} \sim (\boldsymbol{k} \times \boldsymbol{k}') \cdot \boldsymbol{M}, \tag{1.2}$$

where $W_{\boldsymbol{k},\boldsymbol{k}'}$ is the transition probability from state $\boldsymbol{k}$ to $\boldsymbol{k}'$ [6]. Inserting this asymmetry into the Boltzmann equation leads to a current proportional to the longitudinal current driven by the electric field $\boldsymbol{E}$ and perpendicular to both $\boldsymbol{E}$ and $\boldsymbol{M}$ or $\boldsymbol{\sigma}$, where $\boldsymbol{M}$ is the magnetization direction in case of the AHE and $\boldsymbol{\sigma}$ is the direction of the polarization of the spin current in case of the SHE. Thus, the corresponding contribution to the Hall conductivity $\sigma_{xy}^{(s),skew}$ and the conductivity σ_{xx} are both proportional to the transport lifetime τ. Studies focused on the skew scattering from an *ab initio* perspective were started by Gradhand *et al.* [34–36]. Further recent studies of skew scattering based on *ab initio* electronic structure and the Boltzmann equation in systems with impurities of Cr, Mn, Fe, Co, and Ni in Pt, Au, and Pd hosts have yielded contributions to the spin Hall angle of a fraction of a percent [37,38].

1.1.4 Side jump mechanism

The definition of side jump contribution is simply the total anomalous (spin) Hall conductivity subtracted by the intrinsic and skew scattering contributions. The semi-classical argument for a side-jump contribution can be stated straightforwardly: when considering the scattering of a Gaussian wave packet from a spherical impurity with SOC ($H_{SOC} = \hbar^2/4m^2c^2(\boldsymbol{\sigma} \times \nabla V) \cdot \boldsymbol{k}$), the center of the wave packet in real space gain a displacement transverse to the wave vector $\boldsymbol{k}$ asymmetrically with respect to the spin ($\Delta \boldsymbol{r} = \hbar^2/4m^2c^2\boldsymbol{\sigma} \times \boldsymbol{k}$). This type of contribution was first noticed, but discarded, by Smit [23] and reintroduced by Berger [22] who argued that it was the key contribution to the AHE. In systems with weak SOC, the side jump contribution can be calculated by only taking the spin orbit interaction in the disorder potential [20,39]. However, when considering materials with strong SOC, there are two sources of side-jump scattering: i. *the extrinsic side jump*, arising from non-spin-orbit coupled wave packet scattered by the disorder potential with SOC; ii. *the intrinsic side jump*, arising from SOC induced part of wave packet scattered by the scalar disorder potential (without SOC). Both of the contributions are independent of τ [40], which means it is difficult to be distinguished them from the intrinsic contribution in experiments. However, side-jump and intrinsic contributions have quite different dependences on more specific system parameters, particularly in systems with complex band structures [41]. It should be noted that studies on simplified models, *e.g.*, semiconductor conduction bands, indicate an exact cancellation between intrinsic mechanism and intrinsic side-jump contributions [42–45]. But it is well understood now that these cancellations are unlikely in more complex models [21,40]. The cancellations can be traced back to the fact that Berry curvature of the Bloch electrons in those systems is a constant independent of momentum, due to these very simple band structures.

1.2 Ferromagnetism

Ferromagnetic materials are characterized by a long-range ordering of the atomic moments on each lattice site. This ferromagnetic ordering exhibits macroscopically a spontaneous magnetization, even in absence of external magnetic field. Above certain temperature, known as the Curie temperature T_c, thermal fluctuation destroys the ferromagnetic ordering with a macroscopic collapse of the spontaneous magnetization, corresponding to a phase transition from a ferromagnetic state to a paramagnetic state. In this section, I briefly introduce the basic theories on ferromagnetism and its quantum mechanical origins.

1.2.1 Mean field theory

a. Molecular field theory

The first modern theory of ferromagnetism was proposed by Pierre Weiss [46], which was an extension of classical description on paramagnetism by Langevin. Weiss assumed an internal "molecular field" proportional to the magnetization of ferromagnet,

$$H_{loc.} = n_W M + H_{ext}, \tag{1.3}$$

where $H_{loc.}$ and H_{ext} are the local magnetic field and the external magnetic field, respectively, M is the magnetization, and n_W is the Weiss coefficient [47]. The magnetic susceptibility $\chi \equiv M/H$ is given by Curie-Weiss law,

$$\chi = \frac{C}{T - T_c}, \tag{1.4}$$

where $C = n_W^{-1} T_c$ is the Curie constant. Apparently, the magnetic susceptibility diverges when the temperature approaches the Curie temperature, charactering a second order phase transitions. Thus, the Weiss' molecular field theory was the first mean field theory describing a phase transition.

b. Stoner criterion

The theory of ferromagnetism in metals is inspired by the idea of Pauli susceptibility. We first consider the band susceptibility in a paramagnetic state (Fig. 1.3 (a)). When an external magnetic field H_{ext} is applied, the spin-up and spin-down bands which are parallel and anti-parallel with H_{ext} are energetically split by a mount of energy,

$$\varepsilon_{para} = 2M_B H_{ext}, \tag{1.5}$$

where M_B is the magnetic moment per state. Thus, the number of electrons states differs in spin-up and spin-down bands by a mount

$$\Delta n = g(\varepsilon_F)\varepsilon_{para}, \tag{1.6}$$

where $g(\varepsilon_F)$ is the density of states at Fermi level.

The induced magnetization is proportional to the asymmetric spin population,

$$\Delta M = 2g(\varepsilon_F)M_B^2 H_{ext}. \tag{1.7}$$

Therefore, the Pauli susceptibility is

$$\chi_p = 2g(\varepsilon_F)M_B^2. \tag{1.8}$$

In the case of a ferromagnetic state (Fig. 1.3 (b)), the external field is replaced by the "molecular field" induced by the magnetization, $H_m = n_W M$. The number of states in spin-up and spin-down channels are

$$N_+ = \int d\varepsilon \; g(\varepsilon)f(\varepsilon_F + M_B H_m), \tag{1.9}$$

$$N_- = \int d\varepsilon \; g(\varepsilon)f(\varepsilon_F - M_B H_m), \tag{1.10}$$

where $f(\varepsilon)$ is the Fermi distribution function. The induced magnetization is

$$M = M_B(N_+ - N_-). \tag{1.11}$$

The ferromagnetic states appear when a non-trivial solution $M \neq 0$ simultaneously satisfies the Eq. 1.9,1.10,1.11. Note that the right hand side of Eq. 1.11 is monotonic with M. The critical condition is

$$\begin{aligned} M_B \frac{d(N_+ - N_-)}{dM} &> 1 \\ 2M_B^2 n_w g(\varepsilon_F) &> 1, \\ n_w \chi_p &> 1, \end{aligned} \tag{1.12}$$

where Eq. 1.12 is the famous Stoner criterion [48]. When the density of states is significantly large at Fermi level, *e.g.*, a narrow or even flat band, the band tends to split energetically, due to the strong electron-electron interaction. Hence, spontaneous ferromagnetic ordering appears.

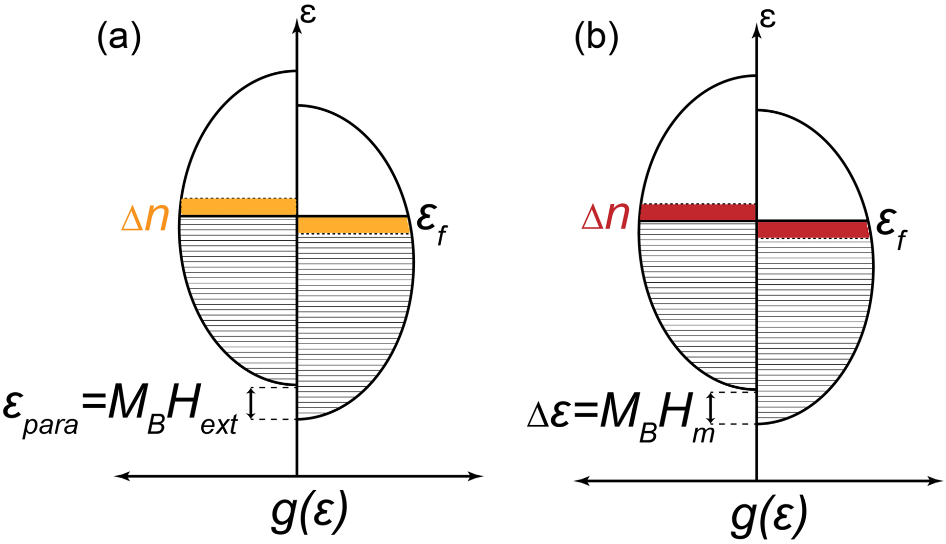

Figure 1.3: Band susceptibility in paramagnetic and ferromagnetic states. (a) band susceptibility in paramagnetic state, Pauli susceptibility. (b) band susceptibility in ferromagnetic state, the Stoner criterion.

1.2.2 Exchange interaction

The microscopic origin of “molecular field” had not been clarified until establishment of quantum mechanics. In fact, all magnetism (ferromagnetism, ferrimagnetism, antiferromagnetism, and *etc.*) share the same microscopic origin, the exchange interaction, which is the consequence of the basic electron-electron interaction, *i.e.*, the Coulomb repulsion, with statistic constraints of fermion imposed by the Pauli exclusion principle.

The Pauli exclusion principle originates from the idea that microscopic particles, such as electrons, are indistinguishable (identical particles). Considering a generic two-particle state $|n_1, n_2\rangle \equiv |n_1\rangle \otimes |n_2\rangle$, the exchange of particle 1 and 2 does not change the probability amplitude of state but can induces an arbitrary phase factor. Thus the two-particle state can be decomposed into

$$|n_1, n_2\rangle \pm |n_2, n_1\rangle \,, \tag{1.13}$$

which are termed as symmetric (+) and antisymmetric (−) exchange. The two distinct states follow different behaviors in quantum statistics, categorized as fermions and bosons. Clearly, if n_1 and n_2 represent the exact same state, the fermionic state vanishes. Hence, Pauli exclusion principle states: *fermion cannot occupy the same quantum state.*

The simplest example of exchange interaction is the Hamiltonian of H_2 molecule with perturbative treatment on the Coulomb interaction of electrons,

$$\begin{aligned} H &= H_0 + H_{ee}, \\ H_0 &= \sum_{i=1,2}\left[-\frac{\hbar^2}{2m}\nabla_i - \frac{e^2}{4\pi\varepsilon_0}\frac{1}{r_i}\right], \quad H_{ee} = \frac{e^2}{4\pi\varepsilon_0 r_{12}}, \end{aligned} \tag{1.14}$$

where H_0 is the Hamiltonian without interaction and H_{ee} is electron-electron interaction (Coulomb repulsion). The H_0 can be decoupled into two separate Schr$\ddot{o}$dinger equations corresponding to each H atom with independent solutions, $\phi_1(\boldsymbol{r}_1)$ and $\phi_2(\boldsymbol{r}_2)$,

Considering the spin state of the electrons ($\chi_1(s_1)$ and $\chi_1(s_2)$), the symmetric and antisymmetric states in the spin space are

$$\chi_s \equiv 1/\sqrt{2}\left(\chi_1(s_1)\chi_2(s_2) + \chi_2(s_1)\chi_1(s_2)\right), \tag{1.15}$$

$$\chi_a \equiv 1/\sqrt{2}\left(\chi_1(s_1)\chi_2(s_2) - \chi_2(s_1)\chi_1(s_2)\right). \tag{1.16}$$

Thus, the total wave functions combining the spatial and spin parts are

$$\Phi_S = 1/\sqrt{2}\left(\phi_1(\boldsymbol{r}_1)\phi_2(\boldsymbol{r}_2) + \phi_2(\boldsymbol{r}_1)\phi_1(\boldsymbol{r}_2)\right)\chi_a, \tag{1.17}$$

$$\Phi_T = 1/\sqrt{2}\left(\phi_1(\boldsymbol{r}_1)\phi_2(\boldsymbol{r}_2) - \phi_2(\boldsymbol{r}_1)\phi_1(\boldsymbol{r}_2)\right)\chi_s. \tag{1.18}$$

where Φ_S is termed as the spin singlet and Φ_T is termed as the spin triplet. The exchange interaction energy (exchange integral) is defined as the energy difference between the singlet and triplet states,

$$\begin{aligned} \mathcal{J} &= \frac{1}{2}(E_T - E_S), \\ &= \int d\boldsymbol{r}_1 d\boldsymbol{r}_2 \phi_1^*(\boldsymbol{r}_2)\phi_2^*(\boldsymbol{r}_1) H_{ee} \phi_1(\boldsymbol{r}_1)\phi_2(\boldsymbol{r}_2). \end{aligned} \tag{1.19}$$

The exchange interaction energy can be also rewritten as,

$$\Delta E = -2\mathcal{J}\boldsymbol{s}_1 \cdot \boldsymbol{s}_2. \tag{1.20}$$

where $\boldsymbol{s}_1 \cdot \boldsymbol{s}_2 = \frac{1}{2}\left[(\boldsymbol{s}_1 + \boldsymbol{s}_2)^2 - \boldsymbol{s}_1^2 - \boldsymbol{s}_2^2\right]$. The total spin quantum number $S = \boldsymbol{s}_1 + \boldsymbol{s}_2$ is 0 or 1, corresponding to the singlet and triplet state, respectively.

Heisenberg generalized Eq. 1.20 to the local spin moment of each lattice site,

$$\mathcal{H}_{Heis.} = -2\sum_{i>j} \mathcal{J}_{ij} \boldsymbol{S}_i \cdot \boldsymbol{S}_j. \tag{1.21}$$

where $\mathcal{J}_{ij}$ represents the exchange interaction of site i and j with spin moment $S_{i,j}$. Apparently, if $\mathcal{J}_{ij} > 0$, spins tend to align parallel, indicating a ferromagnetic state. If $\mathcal{J}_{ij} > 0$, spins tend to align in anti-parallel configuration, indicating an anti-ferromagnetic state. The Heisenberg exchange Hamiltonian can be related to the Weiss' molecular field theory. Suppose the spin of site i only interacts with its nearest neighbors j, Eq. 1.21 can be written as

$$\mathcal{H} = -2\Big[\sum_j \mathcal{J}_{ij} \boldsymbol{S}_j\Big] \cdot \boldsymbol{S}_i. \tag{1.22}$$

where the term inside the parentheses could be seen as the "molecular field" that interacts with the local spin $\boldsymbol{S}_i$.

1.3 Review on previous works

Studies of spin Hall effect has extensively focused on paramagnetic materials and it was only recent that people start to explore the possibility of spin Hall signal in magnetic materials, in which the ferromagnet is the simplest attempt but with most significance. In this section, I review the recent experimental and theoretical works on SHE in ferromagnets chronologically, for which I hope it would elucidate the progress of this developing field and then introduce its unsolved issues that motivate this dissertation.

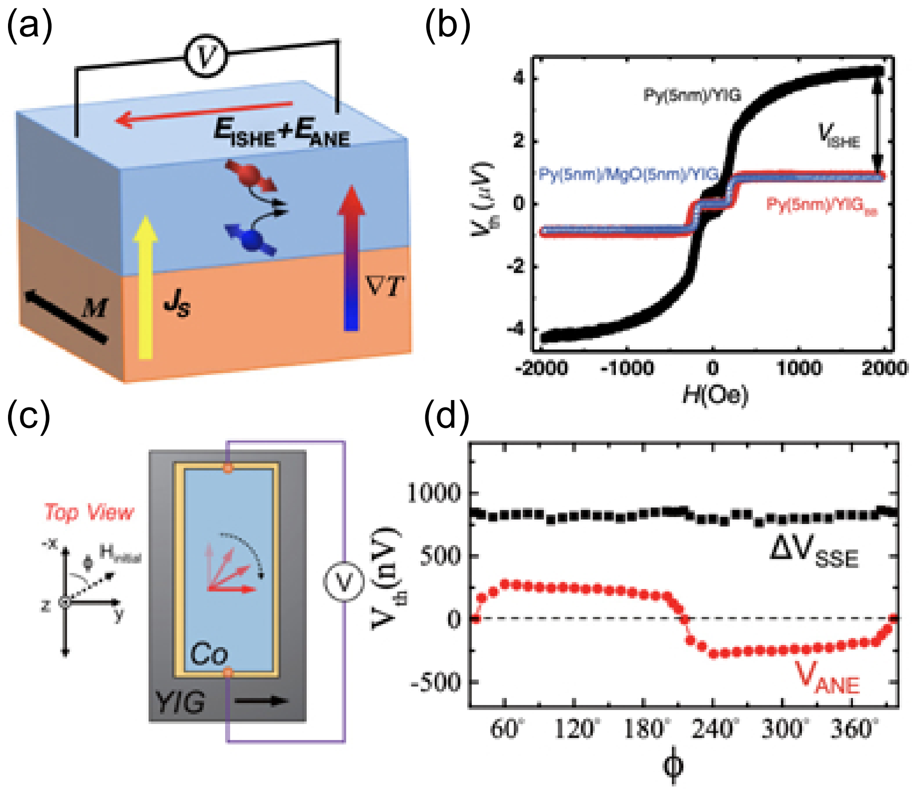

Figure 1.4: Detection of the ISHE in ferromagnets through spin Seebeck effect. Schematic diagrams of experimental setups for (a) Py/YIG under perpendicular temperature gradient and (c) Co/Cu/YIG with rotating the magnetization of Co. (b) Field dependence of thermal voltage V_{th} of Py/YIG. (d) The full angular dependence of thermal voltage ΔV_{SSE} and V_{ANE}. Images adapted from Ref. [49,50].

a. Detection of ISHE through spin Seebeck effect

The first approach to detect of SHE in ferromagnets (FM) is to exploit the ISHE in the Permalloy (Py) [49] through thermally induced spin current. In their experimental setup, Miao *et al.* applied a temperature gradient perpendicular to the Py(Pt)/Yttrium iron garnet (YIG) layered structure, in which a longitudinal spin polarized current was generated through the spin Seebeck effect (SSE) in the ferromagnetic YIG layer [51] and was injected into the adjacent FM layer (Fig. 1.4 (a)). It should be noted that the perpendicular temperature gradient also induces the anomalous Nernst effect (ANE) in the metallic FM layer which shared the same symmetry with the ISHE signal. By inserting an insulating MgO layer between the FM and YIG layers, spin polarized current from SEE was blocked and the thermal voltage only reflected the signal of ANE. The thermal voltage after subtracting the contribution from ANE provides unambiguous evidence of the existence of ISHE in the ferromagnetic Py (Fig. 1.4 (b)).

The same group also implemented a trilayer structure with a Cu insertion layer that decoupled the direct exchange between YIG and FM layer (Fig. 1.4 (c)). The magnetization direction angular dependence of the thermal voltage indicated the SSE signal, corresponding to the ISHE of Co, is independent with magnetization of Co (Fig. 1.4 (d)). They argued that the (inverse) SHE in the ferromagnetic Co was dominated by the intrinsic mechanism which was independent with its magnetization direction [50]. In addition, the experimental results suggested that the transverse spin current which polarization is orthogonal to magnetization ($\boldsymbol{\sigma}_{J_s} \perp \boldsymbol{M}$) did not dephase in the ferromagnets. These arguments are the central issues in the research of SHE in ferromagnets and have been extensively studied.

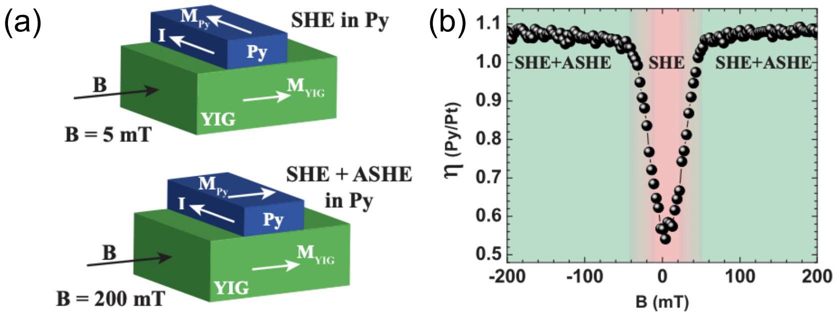

Figure 1.5: Detection of the ISHE in ferromagnets by nonlocal magnon transport. (a) Schematic diagrams of $\boldsymbol{M}_{Py}$ with respect to I for two different magnetic fields ($5mT$ and $200mT$). (b)The relative detection efficiency of Py over Pt [$\eta(Py/Pt)$], as a function of B. Images adapted from Ref. [52].

b. Detection of ISHE through nonlocal magnon transport

A novel approach to detecting ISHE through nonlocal magnon transport [53] was purposed by Das *et al.* [52]. In their experimental setup, a spin polarized current from one FM wire was injected into the insulating YIG layer where spin wave (magnon) was excited and propagated. The magnon was absorbed by another FM layer or heavy metal layer and transformed again back to spin current, which is finally detected *via* the ISHE.

Through delicate control of the shape anisotropy of the ferromagnetic wires, two magnetization configurations of the FM detector ($\boldsymbol{M} \parallel \boldsymbol{I}$ ($\boldsymbol{\sigma}_{J_s} \perp \boldsymbol{M}$) and $\boldsymbol{M} \perp \boldsymbol{I}(\boldsymbol{\sigma}_{J_s} \parallel \boldsymbol{M})$) were achieved (Fig. 1.5 (a)). The ISHE "detection" efficiency η, in comparison with Pt reference sample, showed a strong dependence on the magnetization direction of Py detector (Fig. 1.5 (b)), which contradicted Tian *et al.*'s argument [50]. However, it again confirmed the existence of transverse spin Hall current in ferromagnets.

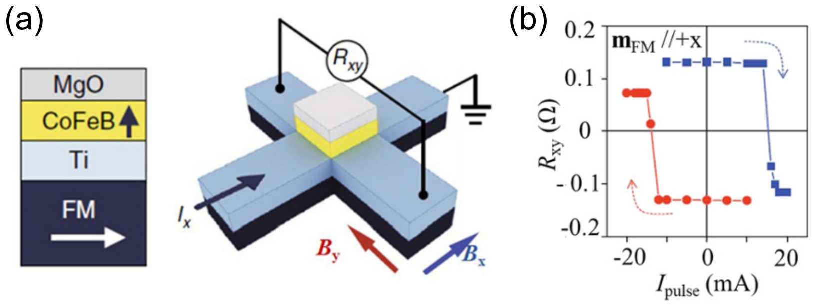

Figure 1.6: Detection of the SHE in ferromagnets by second harmonics measurement. (a) Measurement geometry for field-free switching via out-of-plane polarized spin current. (b) Hall signal to show the reversal of CoFeB magnetization as a function of applied current pulse. Images adapted from Ref. [54].

c. Detection of SHE through second harmonic measurement

The transverse SHE allowed the generation of out-of-plane polarized spin current from an in-plane magnetized film. The out-of-plane polarized spin current could switch a perpendicular magnetization *via* an anti-damping process, which was demonstrated by Baek [54]. The experimental setup is shown in Fig. 1.6 (a). In trilayer structure FM/Ti/CoFeB, the CoFeB is magnetized out of film plane and FM (Py/CoFeB) is in-plane magnetized. They observed that the FM magnetized in the x-direction can generate a transversely polarized spin current with the spin direction in the z-direction, characterized as the transverse SHE. The effective coefficients $\theta_{\perp}^{R}$ for CoFeB and Py are found to be $-1.4 \pm 0.1\%$ and $0.6 \pm 0.06\%$, respectively. In addition, Baek *et al.* demonstrated that the out-of-plane polarized spin current, associated with the transverse SHE, could lead to a field-free magnetization switching (Fig. 1.6 (b)).

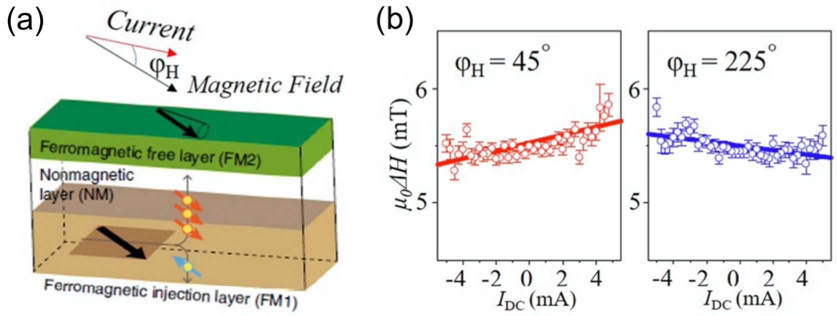

Figure 1.7: Detection of the SHE in ferromagnets by spin torque FMR. (a) SHE-enabled spin-orbit torque studied in a Py/Cu/CoFeB spin valve structure. (b) In this experiment, a dc current generates a spin torque that is either parallel or antiparallel to the magnetization, thus enhancing or reducing the magnetic damping. The magnetic damping change is measured from the linewidth of the ferromagnetic resonance spectrum. Images adapted from Ref. [55].

d. Detection of SHE through spin-torque ferromagnetic resonance

Iihama *et al.* [55] demonstrated the spin-transfer torque induced by the SHE of a ferromagnet by measuring the damping enhancement/suppression [56] in a CoFeB/Cu/Py trilayer. The experimental setup is shown in Fig. 1.7 (a), where an in-plane charge current generates a spin current with spin direction parallel with the CoFeB magnetization via the longitudinal SHE ($\boldsymbol{\sigma}_{J_s} \parallel \boldsymbol{M}$). The spin current generates an anti-damping torque that enhances or reduces the damping of the Py layer depending on the electric current and Py magnetization directions, as shown in Fig. 1.7 (b). The effective damping-like spin-torque efficiency extracted for the CoFeB layer is as large as $14 \pm 5\%$ with the same sign as that of Ta.

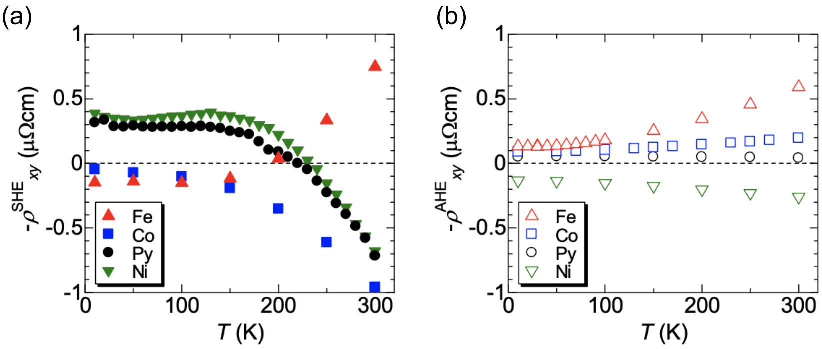

Figure 1.8: Detection of the ISHE in $3d$ ferromagnets through non-local transport. The temperature dependence of (a) longitudinal spin Hall resistivity and (b) anomalous Hall resistivity in Py, Fe, Co and Ni. Images adapted from Ref. [19].

e. Detection of ISHE through non-local spin valves

Omori *et al.* [19] studied the temperature-dependent AHE and SHE simultaneously with a non-local spin valve structure to investigate their quantitative correlations. The extrapolated spin Hall resistivity ($\rho_{xy}^{SHE} = \theta\rho_{xx}$) exhibited much stronger temperature dependence than the anomalous Hall resistivity (ρ_{xy}^{AHE}). It is argued that in the skew scattering mechanism, the longitudinal spin Hall resistivity might scale with the anomalous Hall resistivity and the spin polarization [19]. But such a relation might not hold for other mechanisms such as the intrinsic mechanism and side jump. It should be noted that the SHC measured in this experimental setup was only the $\boldsymbol{M} \parallel \boldsymbol{I}$ case, which was termed as the longitudinal SHE ($\boldsymbol{\sigma}_{j_s} \parallel \boldsymbol{M}$) in some reference [57].

f. Theoretical works in SHE in ferromagnets

Despite the extensive experimental studies on SHE in ferromagnets, theoretical work is limited. Taniguchi *et al.* [58] theoretically predicted that the magnetization can be used as an additional degree of freedom to control the spin direction of the spin current. Due to strong dephasing, Taniguchi *et al.* argued the spin current generated by the AHE should always be polarized parallel to the magnetization, corresponding to the longitudinal SHE.

Amin *et al.* [59] used *ab initio* based tight-binding models to show that single ferromagnetic layer generated spin current flowing perpendicular to the electric field with components of spin direction along $\boldsymbol{m} \times (\boldsymbol{J}_s \times \boldsymbol{E})$ and $\boldsymbol{m}$. This calculation ignored the impurity potentials associated with skew scattering and side jump and the perturbation to electronic wavefunctions, for which the extrinsic and intrinsic mechanisms of spin Hall effect and anomalous Hall effect were not included. Nevertheless, the transport calculations revealed that both bulk and interfacial spin current generation could be significant and proposed the existence of spin current polarized transverse to magnetization.

The intrinsic SHE of $3d$ ferromagnets was calculated by Amin *et al.* through *ab initio* calculations [60]. It was shown that the intrinsic SHE is highly isotropic with respect to the magnetization (Fig. 1.9). They argued that the transverse intrinsic spin current do not dephase, which are protected by perturbed eigenstates that superimpose different spin states with the same Bloch wave vector. As these perturbed eigenstates propagate in space, the two spin components do not accumulate any relative phase, and hence do not precess and subsequently dephase.

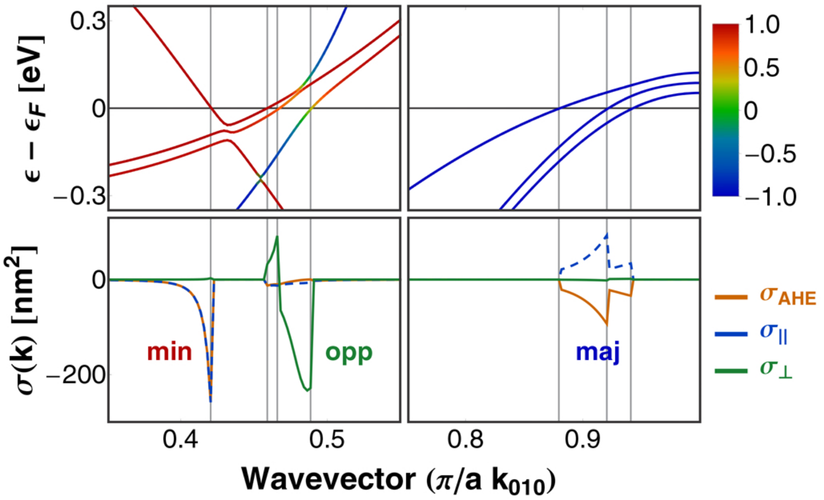

Figure 1.9: First principles calculations on intrinsic SHE in bcc Fe.
Band structure near the Fermi energy (top) and k-dependent intrinsic conductivities (bottom) for bcc Fe, where $\hat{m} = (\hat{y} + \hat{z})/2$. Band color gives value of $\boldsymbol{s} \cdot \hat{m}$, where s is the spin and blue (red) bands corresponding to majority (minority) carriers. Avoided crossings between like (opposite) spin bands contribute strongest to $\sigma_{\parallel}(\sigma_{\perp})$, which describes the spin current with spin direction parallel (perpendicular) to $\hat{m}$. Images adapted from Ref. [60].

Recently, a generalized spin diffusion model was formulated by considering spin-orbit interaction of a ferromagnet [61]. In this model, novel spin transport phenomena: a self-generated spin torque and a self-generated charge pumping in ferromagnet-normal metal bilayers are recognized.

1.4 Purpose of this dissertation

The existence of SHE in ferromagnets has been evidenced without ambiguity through various experimental techniques [19,49,50,52,54,55]. However, there are two key remaining issues of the SHE in ferromagnets:

i. the relationship between the SHE and AHE in both extrinsic and intrinsic regimes.

ii. whether the SHE depends on the magnetization direction and its microscopic origin.

A conventional approach to describe the transport properties in ferromagnets is the two-current model, which treats the majority and minority spin channels as independent carriers that contribute to current conduction [62]. In this context, under the longitudinal external electric field, the transverse charge current (AHE) scales with the transverse spin current (SHE) by the spin polarization of the conduction electron. Therefore, it has been commonly assumed that the AHE is related to the SHE in ferromagnets via the following relation:

$$\sigma^{AHE} = P_{ferro.}\sigma^{SHE}. \tag{1.23}$$

Omori *et al.* experimentally found the above relation between AHE and SHE of Py holds in the skew scattering regime but argues that it is not necessarily the case for the intrinsic regime. Another example of such relation between the AHE and SHE is its quantized Hall counterparts. The quantum spin Hall (QSH) state can be viewed as two copies of the quantum anomalous Hall (QAH) effect where the spin is a good quantum number to describe the surface states [63] ($P = \boldsymbol{s} = \pm 1$). However, the spin of the Bloch states in most materials is not conserved due to the presence of SOC even with strong exchange splitting, *e.g.*, ferromagnets, wherefore the relationship between AHE and SHE (Eq. 1.23) is not exact as in the QSH states. Thus, the relationship, if any, between the AHE and SHE in ferromagnets remains unknown and should be clarified.

Moreover, the spin current emerging from the SHE in ferromagnets should interact with the spontaneous magnetization, since the exchange interaction and SOC both act on the spin degree of freedom. However, experimental results provide contradictory views on the magnetization direction dependence of SHE in ferromagnets [50,52]. In particular, theoretical investigation on this issues is lacking.

These two issues inspire me to work on the dissertation where I investigate the (intrinsic) SHE and AHE in ferromagnets and study the magnetization dependence ofSHC using various models. The outline of this dissertation is as follows:

In Chapter III, the relationship between AHE and SHE is investigated in ferromagnetic CoPt alloy where I emphasize the distinct symmetry of spin Berry curvature and Berry curvature. The symmetry difference of the spin Berry curvature and Berry curvature is investigated by checking the matrix elements of velocity or spin velocity operators at various special symmetry points in the Brillouin zone.

In Chapter IV, the anisotropy of the SHE is investigated in bcc-Fe and fcc-Ni. A non-collinear spin state, where the electron spin direction is allowed to point any direction regardless of the magnetization direction, is employed in the first principles calculation to study the anisotropy. The anisotropy of the SHC is found to originate from the spin Berry curvature at different types of anti-crossing points in the Brillouin zone.

In Chapter V, a simplified model that is based on Rashba and Dresselhaus types SOC is employed to study the anisotropy of SHC. A uniform exchange splitting is introduced to model a ferromagnetic system. The intrinsic SHC is calculated through the Kubo formula and Matsubara Green's function.

In Chapter VI, I study the intrinsic SHC of Dirac electrons system by introducing a ferromagnetic ordering. The anisotropy of the SHC with respect to the direction of magnetization is studied.

Chapter 2

Theoretical background

Contents

2.1 The Green's function method

The Green's function method is useful for solving specific differential equation,*e.g.*, the inhomogeneous Maxwell equations in electrodynamics [64]. In quantum field theory, the Green's function method is used to analyze the dynamics of the system. In this section, we start with the one-particle Green's function for fermion as a pedagogical example and then introduce the analytical properties of retarded and advanced Green's functions. Further, we consider Green's functions at non-zero temperature, the so-called Matsubara Green's function.

2.1.1 Green's function for free electron gas

We shall start with a simple Hamiltonian describing the free electron gas to illustrate the properties of the electron Green's function. The free electron gas Hamiltonian in second quantization (Appendix. 2.A) is

$$\mathcal{H} = \sum_{\lambda} \varepsilon_\lambda a_\lambda a_\lambda^\dagger, \tag{2.1}$$

where ε_λ is the eigenenergy of state λ which labels both the momentum and spin space of electron, $a_\lambda^\dagger$ and a_λ are creation and annihilation operators of fermion.

The electron Green's function is defined as [65]

$$G_\lambda^{(0)}(t,t') = -i \left\langle 0 \right| \mathcal{T} a_\lambda(t) a_\lambda^\dagger(t') \left| 0 \right\rangle , \tag{2.2}$$

where $|0\rangle$ is the vacuum state and $a_\lambda^\dagger(t), a_\lambda(t)$ are creation and annihilation operators in the *Heisenberg picture* (Appendix. 2.B),

$$\begin{aligned} a_\lambda(t) &= e^{i\mathcal{H}t/\hbar} a_\lambda e^{-i\mathcal{H}t/\hbar}, \\ &= e^{-i\varepsilon_\lambda t/\hbar} a_\lambda, \end{aligned} \tag{2.3}$$

where in the last line we apply the commutation relation:

$$\left[a_\lambda, \varepsilon_\lambda a_\lambda a_\lambda^\dagger \right] = \varepsilon_\lambda a_\lambda. \tag{2.4}$$

The time ordering operator, $\mathcal{T}$, in Eq. 2.2 can be expressed explicitly

$$G_\lambda^{(0)}(t,t') = \begin{cases} -i \langle 0| a_\lambda(t) a_\lambda^\dagger(t') |0\rangle, & t > t' \\ i \langle 0| a_\lambda^\dagger(t') a_\lambda(t) |0\rangle, & t \leqslant t' \end{cases} \tag{2.5}$$

where it takes a positive sign associated with the anti-causal case ($t \leqslant t'$), due to the anti-commutation relation of fermion operators. For boson, it should be a negative sign, same with the causal case.

Replacing the creation and annihilation operators with Eq. 2.3, the electron Green's function is

$$G_\lambda^{(0)}(t,t') = \begin{cases} -i \langle 0| a_\lambda a_\lambda^\dagger |0\rangle e^{-i\varepsilon_\lambda(t-t')/\hbar}, & t > t' \\ i \langle 0| a_\lambda^\dagger a_\lambda |0\rangle e^{-i\varepsilon_\lambda(t-t')/\hbar}, & t \leqslant t' \end{cases} \tag{2.6}$$

Note that the $\langle 0| a_\lambda^\dagger a_\lambda |0\rangle$ is just particle number of state λ which reduces to the zero temperature Fermi distribution function, $f(\varepsilon_\lambda)$. The Green's function reduces to

$$G_\lambda^{(0)}(t-t') = \begin{cases} -i(1-f(\varepsilon_\lambda))e^{-i\varepsilon_\lambda(t-t')/\hbar}, & t > t' \\ if(\varepsilon_\lambda)e^{-i\varepsilon_\lambda(t-t')/\hbar}, & t \leqslant t' \end{cases} \tag{2.7}$$

where we rewrite the electron Green's function as $G_\lambda^{(0)}(t-t')$, for it is apparently homogenous in time.

The Fourier transformation of $G_\lambda^{(0)}(t-t')$ gives

$$\begin{aligned} G_\lambda^{(0)}(E) &= -i \int ds\ e^{i(E+i\delta)s/\hbar} G_\lambda^{(0)}(s) \\ &= \frac{1-f(\varepsilon_\lambda)}{E-\varepsilon_\lambda+i\delta} + \frac{f(\varepsilon_\lambda)}{E-\varepsilon_\lambda-i\delta}, \\ &= \frac{1}{E-\varepsilon_\lambda+i\delta_\lambda}, \end{aligned} \tag{2.8}$$

where we introduce an infinitesimal damping term $i\delta$ to converge the Fourier integral and $\delta_\lambda \equiv \text{sgn}(\varepsilon_\lambda - \mu)\delta$ depends on the sign of $(\varepsilon_\lambda - \mu)$.

Another method to obtain $G_\lambda^{(0)}(E)$ is to consider the equation of motion for $G_\lambda^{(0)}(t,t')$. Considering a system homogeneous in time, we define $\tau = t - t'$ and Eq. 2.6 can be rewritten as

$$\begin{aligned} G_\lambda^{(0)}(\tau) &= -i \langle 0| \mathcal{T}_\tau a_\lambda(\tau) a_\lambda^\dagger(0) |0\rangle \\ &= -i \langle 0| a_\lambda(\tau) a_\lambda^\dagger(0) |0\rangle \Theta(\tau) + i \langle 0| a_\lambda^\dagger(0) a_\lambda(\tau) |0\rangle \Theta(-\tau), \end{aligned} \tag{2.9}$$

where the Θ-function is

$$\Theta(\tau) = \begin{cases} 1, \tau > 0 \\ 0, \tau < 0 \end{cases} \tag{2.10}$$

Differentiating Eq. 2.9 with time τ, the equation of motion for Green's function is

$$\begin{aligned} i\hbar\partial_\tau G_\lambda^{(0)}(\tau) &= \hbar \langle 0| \mathcal{T}_\tau \partial_\tau a_\lambda(\tau) a_\lambda^\dagger(0) |0\rangle + \hbar \langle 0| \left\{ a_\lambda, a_\lambda^\dagger \right\} |0\rangle \delta(\tau) \\ &= -i\varepsilon_\lambda \langle 0| a_\lambda a_\lambda^\dagger |0\rangle + \hbar\delta(\tau), \end{aligned} \tag{2.11}$$

where $\delta(\tau)$ comes from the derivative of Θ-function.

It suggests the $G_\lambda^{(0)}(\tau)$ is the solution of differential (Schrödinger) equation,

$$\left(i\partial_\tau - \frac{\varepsilon_\lambda}{\hbar} \right) G_\lambda^{(0)}(\tau) = \delta(\tau). \tag{2.12}$$

which is the exactly the reason that we name it as "Green's function".

By Fourier transforming $G_\lambda^{(0)}(\tau)$ to energy domain, the operator $\left(i\partial_\tau - \frac{\varepsilon_\lambda}{\hbar} \right)$ can be solved,

$$\begin{aligned} \left(i\partial_\tau - \frac{\varepsilon_\lambda}{\hbar} \right) \int dE e^{-iE\tau/\hbar} G_\lambda^{(0)}(E) &= \delta(\tau), \\ (E - \varepsilon_\lambda) G_\lambda^{(0)}(E) \int d\frac{E}{\hbar} e^{-iE\tau/\hbar} &= \delta(\tau), \\ G_\lambda^{(0)}(E) &= \frac{1}{E - \varepsilon_\lambda}. \end{aligned} \tag{2.13}$$

Note that difference between Eq. 2.8 and Eq. 2.13 originates from the boundary condition of differential equation. Clearly, Eq. 2.13 do not resolve the singularity of $E = \varepsilon$ in real axis. By appropriate choice of boundary condition, Eq. 2.13 can agree with Eq. 2.8 without pole on the real axis.

In matrix form, Eq. 2.13 can be generalized as

$$\begin{aligned} (E-\hat{H})\hat{G}^{(0)}(E) &= \hat{I}, \\ \hat{G}^{(0)}(E) &= (E-\hat{H})^{-1}. \end{aligned} \tag{2.14}$$

where $\hat{G}^{(0)}$ is the matrix of Green's function.

2.1.2 Analytical properties of Green's functions

To illustrate the analytical properties of Green's functions, we first introduce the retarded and advanced Green's functions in time domain [65],

$$G^R_\lambda(t,t') = \begin{cases} -i\langle 0| \left\{ a_\lambda(t), a^\dagger_\lambda(t') \right\} |0\rangle, & t \geqslant t' \\ 0, & t < t' \end{cases} \tag{2.15}$$

$$G^A_\lambda(t,t') = \begin{cases} 0, & t \geqslant t' \\ i\langle 0| \left\{ a_\lambda(t), a^\dagger_\lambda(t') \right\} |0\rangle, & t < t' \end{cases} \tag{2.16}$$

Clearly, the retarded Green's function represents propagation forward in time, which is causal. The advanced Green's function, however, represents propagation backward in time, which is anti-causal.

In the equal time limit ($t \to t'$), the anti-commutator of the time-dependent creation and annihilation operator reduces to unity:

$$\lim_{t\to t'} \left\{ a_\lambda(t), a^\dagger_\lambda(t') \right\} = 1. \tag{2.17}$$

which is just the anti-commutator of fermion operators. The retarded and advanced Green's functions in energy (frequency) domain are obtained by Fourier transformation,

$$G^R_\lambda(E) = \frac{1}{E-\varepsilon_\lambda + i\delta}, \tag{2.18}$$

$$G^A_\lambda(E) = \frac{1}{E-\varepsilon_\lambda - i\delta}. \tag{2.19}$$

where δ is positive infinitesimal. Apparently, the retarded and advanced Green's functions have relations:

$$G_\lambda^R(E) = \left[G_\lambda^A(E)\right]^*, \tag{2.20}$$

$$G_\lambda^{R,A}(E) = G_\lambda^{(0)}(E \pm i\delta). \tag{2.21}$$

where we use $G_\lambda^{(0)}(E)$ in Eq. 2.14.

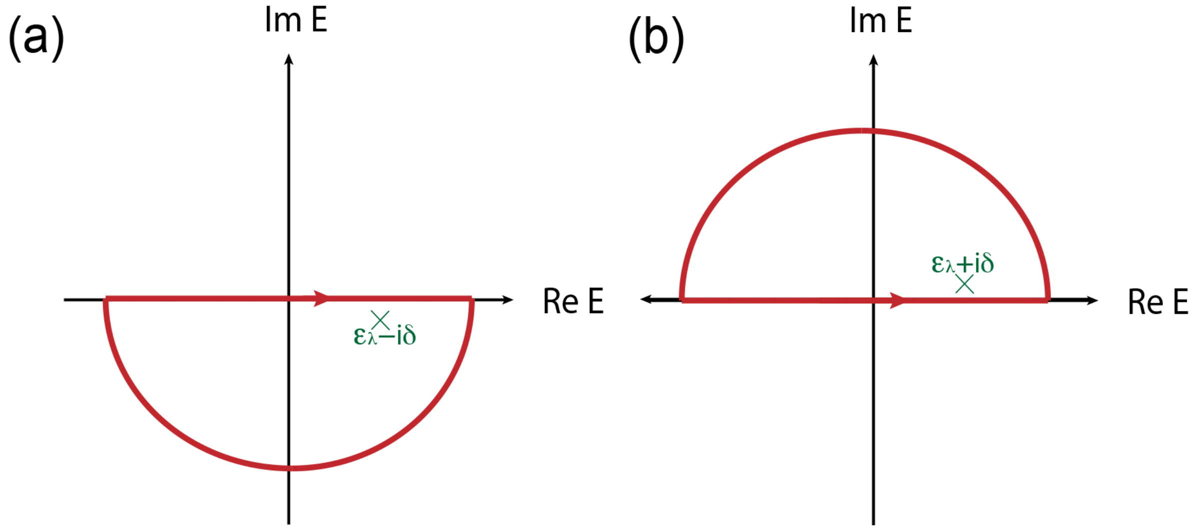

Figure 2.1: The analytical properties of Green's function.
The analytical properties of (a) retarded and (b) advanced Green's functions, in complex plane of energy. The poles are $\varepsilon_\lambda \mp i\delta$ for retarded and advanced Green's functions, respectively.

The retarded Green's function has pole at $\varepsilon_\lambda - i\delta$ and is analytical in the whole upper half of complex plane E, (Fig. 2.1(a)). The inverse Fourier transformation of $G_\lambda^R(E)$ is

$$\begin{aligned} \int \frac{dE}{2\pi}\, e^{-iEt/\hbar} \frac{1}{E-\varepsilon_\lambda + i\delta} &= \int_{C_1} \frac{dz}{2\pi}\, e^{-izt/\hbar} \frac{1}{z-\varepsilon_\lambda+i\delta} \\ &= -ie^{-i\varepsilon_\lambda t/\hbar} e^{-\delta t/\hbar} \\ &= G_\lambda^R(t), \end{aligned} \tag{2.22}$$

where the time is confined to $t > 0$ to converge the integral with $\delta > 0$ and C_1 is the path in Fig. 2.1(a).

The advanced Green's function has pole at $\varepsilon_\lambda + i\delta$ and is analytical in the lower half of complex plane E, (Fig. 2.1(b)). The inverse Fourier transformation of $G^A_\lambda(E)$ is

$$\begin{aligned} \int \frac{dE}{2\pi}\, e^{-iEt/\hbar} \frac{1}{E-\varepsilon_\lambda - i\delta} &= \int_{C_2} \frac{dz}{2\pi}\, e^{-izt/\hbar} \frac{1}{z-\varepsilon_\lambda - i\delta} \\ &= ie^{-i\varepsilon_\lambda t/\hbar} e^{\delta t/\hbar} \\ &= G^A_\lambda(t), \end{aligned} \tag{2.23}$$

where the time is confined to $t < 0$ to converge the integral with $\delta > 0$ and C_2 is the path in Fig. 2.1(b).

2.1.3 Matsubara Green's functions

In above sections, we study the electron Green's function assuming $T = 0$. To extend the Green's function formalism to non-zero temperature, we need to introduce the Matsubara Green's functions [66]. The Matsubara Green's function method is actually easier to use than the zero temperature theory and the zero temperature result can be easily obtained from the Matsubara Green's function method by setting $T = 0$.

We first review some basic of quantum statistical mechanics. At non-zero temperature, the expectation value of any physical observable $\hat{O}$ is given by

$$\langle \hat{O} \rangle = \mathrm{Tr}(\hat{\rho}\hat{O}), \tag{2.24}$$

where $\hat{\rho}$ is the density (statistical) operator,

$$\hat{\rho} = \frac{1}{Z} e^{-\beta \hat{H}}, \tag{2.25}$$

with $Z = \mathrm{Tr}(e^{-\beta\hat{H}})$ is the partition function and $\beta = 1/k_BT$. The $\langle \cdots \rangle$ means to take the thermodynamic average over the ensembles, *e.g.*, *canonical* ensemble in Eq. 2.25.

The Matsubara method is inspired by the close analogy between time evolution (*Heisenberg picture*) and thermal averaging, assuming an imaginary time $\tau = it$. The τ-"evolution" of an arbitrary operator is written as

$$\hat{O}(\tau) = e^{\tau\hat{H}/\hbar} \hat{O} e^{-\tau\hat{H}/\hbar}. \tag{2.26}$$

The electron Green's function in imaginary time [65] is

$$\begin{aligned}\mathcal{G}_\lambda(\tau,\tau') &= -\left\langle \mathcal{T}_\tau a_\lambda(\tau) a_\lambda^\dagger(\tau')\right\rangle,\\ &= -\operatorname{Tr}\left\{e^{-\beta(H-\Omega)}\mathcal{T}_\tau e^{\tau H/\hbar} a_\lambda e^{-(\tau-\tau')H/\hbar} a_\lambda^\dagger e^{-\tau' H/\hbar}\right\}, \end{aligned} \tag{2.27}$$

where the partition function is simplified as $e^{-\beta\Omega} \equiv \operatorname{Tr} e^{-\beta H}$.

Expanding the time-ordering operator, $\mathcal{T}_\tau$, it is easy to show that the Green's function is naturally homogenous in τ,

$$\begin{aligned}\mathcal{G}_\lambda(\tau,\tau') &= -\Theta(\tau-\tau')\operatorname{Tr}\left\{e^{-\beta(H-\Omega)} e^{\tau H/\hbar} a_\lambda e^{-(\tau-\tau')H/\hbar} a_\lambda^\dagger e^{-\tau' H/\hbar}\right\}\\ &+ \Theta(\tau'-\tau)\operatorname{Tr}\left\{e^{-\beta(H-\Omega)} e^{\tau' H/\hbar} a_\tau^\dagger e^{(\tau-\tau')H/\hbar} a_\lambda e^{-\tau H/\hbar}\right\}\\ &= -\Theta(\tau-\tau')\operatorname{Tr}\left\{e^{-\beta(H-\Omega)} e^{-\tau' H/\hbar} e^{\tau H/\hbar} a_\lambda e^{-(\tau-\tau')H/\hbar} a_\lambda^\dagger\right\}\\ &+ \Theta(\tau'-\tau)\operatorname{Tr}\left\{e^{-\beta(H-\Omega)} a_\tau^\dagger e^{(\tau-\tau')H/\hbar} a_\lambda e^{-\tau H/\hbar} e^{\tau' H/\hbar}\right\}\\ &= -\Theta(\tau-\tau')\operatorname{Tr}\left\{e^{-\beta(H-\Omega)} a_\lambda(\tau-\tau') a_\lambda^\dagger\right\}\\ &+ \Theta(\tau'-\tau)\operatorname{Tr}\left\{e^{-\beta(H-\Omega)} a_\tau^\dagger a_\lambda(\tau-\tau')\right\}\\ &= -\left\langle T_{\tau-\tau'} a_\lambda(\tau-\tau') a_\lambda^\dagger\right\rangle, \end{aligned} \tag{2.28}$$

Hence, an equivalent definition of the Green's function is

$$\mathcal{G}_\lambda(\tau) = -\left\langle T_\tau a_\lambda(\tau) a_\lambda^\dagger(0)\right\rangle. \tag{2.29}$$

Now, we examine the periodic property of the Green's function for $0 < \tau < \beta$,

$$\begin{aligned}\mathcal{G}_\lambda(\tau) &= -\operatorname{Tr}\left\{e^{\beta\Omega} e^{-\beta H} e^{\tau H/\hbar} a_\lambda e^{-\tau H/\hbar} a_\lambda^\dagger\right\}\\ &= -\operatorname{Tr}\left\{e^{\beta\Omega} a_\lambda^\dagger e^{-\beta H} e^{\tau H/\hbar} a_\lambda e^{-\tau H/\hbar}\right\}\\ &= -\operatorname{Tr}\left\{e^{\beta\Omega} e^{-\beta H} a_\lambda^\dagger e^{-\beta H} e^{\tau H/\hbar} a_\lambda e^{-\tau H} e^{\beta H/\hbar}\right\}\\ &= -\operatorname{Tr}\left\{e^{\beta\Omega} e^{-\beta H} a_\lambda^\dagger a_\lambda(\tau-\hbar\beta)\right\}\\ &= \left\langle T_\tau a_\lambda(\tau-\hbar\beta) a_\lambda^\dagger\right\rangle,\\ &= -\mathcal{G}_\lambda(\tau-\hbar\beta). \end{aligned} \tag{2.30}$$

The Matsubara Green's function (for fermion) is anti-periodic with period of $\hbar\beta$, where we apply the anti-commutator of fermion operator here. It is easily checked that the Matsubara Green's function for boson is periodic with period of $\hbar\beta$, because of the positive sign in time-ordering operator with anti-causality. In summary, we have

$$\mathcal{G}_\lambda(\tau) = \eta \mathcal{G}_\lambda(\tau - \hbar\beta), \tag{2.31}$$

where $\eta = +1$ for bosons and $\eta = -1$ for fermions with $\tau \in (0, \hbar\beta)$.

In general, the Green's functions (either fermion or boson) are both periodic with period of $2\hbar\beta$. Thus, we can expand the $\mathcal{G}_\lambda(\tau)$ in Fourier series,

$$\mathcal{G}_\lambda(\tau) = \frac{1}{\beta}\sum_n e^{-i\omega_n\tau}\mathcal{G}_\lambda(i\omega_n), \tag{2.32}$$

with $\omega_n = n\pi/(\hbar\beta)$ and the Fourier coefficients are

$$\mathcal{G}_\lambda(i\omega_n) = \frac{1}{2\hbar}\int_{-\hbar\beta}^{\hbar\beta} d\tau \mathcal{G}_\lambda(\tau)e^{i\omega_n\tau}. \tag{2.33}$$

Using the relation Eq. 2.31, the Fourier coefficients can be further reduced. For fermion, we have

$$\begin{aligned}\mathcal{G}_\lambda(i\omega_n) &= \frac{1}{2\hbar}\int_0^{\hbar\beta} d\tau \mathcal{G}_\lambda(\tau)e^{i\omega_n\tau} + \frac{1}{2\hbar}\int_{-\hbar\beta}^{0} d\tau \mathcal{G}_\lambda(\tau)e^{i\omega_n\tau}\\ &= \frac{1}{2\hbar}(1-e^{in\pi})\int_0^{\hbar\beta} d\tau \mathcal{G}_\lambda(\tau)e^{i\omega_n\tau},\end{aligned} \tag{2.34}$$

where Fourier coefficients vanish for all even n.

For boson, we have

$$\begin{aligned}\mathcal{G}_\lambda(i\omega_n) &= \frac{1}{2\hbar}\int_0^{\hbar\beta} d\tau \mathcal{G}_\lambda(\tau)e^{i\omega_n\tau} + \frac{1}{2\hbar}\int_{-\hbar\beta}^{0} d\tau \mathcal{G}_\lambda(\tau)e^{i\omega_n\tau}\\ &= \frac{1}{2\hbar}(1+e^{in\pi})\int_0^{\hbar\beta} d\tau \mathcal{G}_\lambda(\tau)e^{i\omega_n\tau},\end{aligned} \tag{2.35}$$

where Fourier coefficients vanish for all odd n.

In summary, the relation between $\mathcal{G}_\lambda(i\omega_n)$ and $\mathcal{G}_\lambda(\tau)$ are

$$\mathcal{G}_\lambda(i\omega_n) = \frac{1}{\hbar}\int_0^{\hbar\beta} d\tau \mathcal{G}_\lambda(\tau)e^{i\omega_n\tau}, \quad \mathcal{G}_\lambda(\tau) = \frac{1}{\beta}\sum_n e^{-i\omega_n\tau}\mathcal{G}_\lambda(i\omega_n). \tag{2.36}$$

with $\omega_n = (2n+1)\pi/(\hbar\beta)$ for fermion and $\omega_n = 2n\pi/(\hbar\beta)$ for boson.

Now, we consider the free electron gas Hamiltonian in Eq. 2.1, the τ-evolution of fermion operators are

$$a_\lambda(\tau) = e^{\tau\hat{H}/\hbar} a_\lambda e^{-\tau\hat{H}/\hbar} = e^{-\varepsilon_\lambda\tau/\hbar} a_\lambda, \tag{2.37}$$

$$a_\lambda^\dagger(\tau) = e^{\tau\hat{H}/\hbar} a_\lambda e^{-\tau\hat{H}/\hbar} = e^{\varepsilon_\lambda\tau/\hbar} a_\lambda^\dagger. \tag{2.38}$$

Note that $\left[a_\lambda, \hat{H}\right] = -\varepsilon_\lambda a_\lambda$ and $\left[a_\lambda^\dagger, \hat{H}\right] = \varepsilon_\lambda a_\lambda^\dagger$.

The corresponding Matsubara Green's function, $\mathcal{G}_\lambda(\tau)$, is

$$\begin{aligned}
\mathcal{G}_\lambda(\tau) &= -\Theta(\tau) e^{-\varepsilon_\lambda\tau/\hbar} \left\langle a_\lambda a_\lambda^\dagger \right\rangle + \Theta(-\tau) e^{-\varepsilon_\lambda\tau/\hbar} \left\langle a_\lambda^\dagger a_\lambda \right\rangle, \\
&= -e^{-\varepsilon_\lambda\tau/\hbar}\{\Theta(\tau)(1 - n_F(\varepsilon_\lambda)) + \Theta(-\tau) n_F(\varepsilon_\lambda)\}, \\
&= -e^{-\varepsilon_\lambda\tau/\hbar}\{\Theta(\tau) - n_F(\varepsilon_\lambda)\}.
\end{aligned} \tag{2.39}$$

where we note that $n_F(\varepsilon_\lambda) = \langle a_\lambda^\dagger a_\lambda \rangle$ is the Fermi distribution function,

$$n_F(\varepsilon_\lambda) = \frac{1}{e^{\varepsilon_\lambda\beta} + 1}. \tag{2.40}$$

The $\mathcal{G}_\lambda(i\omega_n)$ is obtained by Eq. 2.36,

$$\begin{aligned}
\mathcal{G}_\lambda(i\omega_n) &= -(1 - n_F)\frac{1}{\hbar}\int_0^{\hbar\beta} d\tau \; e^{i\omega_n\tau} e^{-\varepsilon_\lambda\tau/\hbar}, \\
&= -\frac{1}{\hbar}(1 - n_F)\frac{e^{\beta(i\hbar\omega_n - \varepsilon_\lambda)} - 1}{i\omega_n - \varepsilon_\lambda/\hbar}, \\
&= -\frac{1}{\hbar}(1 - n_F)\frac{-e^{-\beta\varepsilon_\lambda} - 1}{i\omega_n - \varepsilon_\lambda/\hbar}, \\
&= \frac{1}{i\hbar\omega_n - \varepsilon_\lambda}.
\end{aligned} \tag{2.41}$$

Note that $e^{i\hbar\omega\beta} = -1$ and $(1 - n_F)(e^{-\beta\varepsilon_\lambda} + 1) = 1$ for fermion.

Comparing Eq. 2.41 with Eq. 2.8, two Green's function are simply connected through *analytic continuation*,

$$i\hbar\omega_n \to E + i\delta. \tag{2.42}$$

2.2 Linear response theory

2.2.1 The Kubo formula

The linear response theory, *i.e.*, the Kubo formula, formulates the linear order response of observables with respect to perturbative external force. For example, the conductivity is the linear response of current to external electric field. The linear response approximation is a tremendous simplification in comparison with general non-equilibrium conditions, since the linear response is uniquely determined by the equilibrium properties of the system.

We shall start with a general Hamiltonian consisting a stationary part and a perturbation,

$$\hat{H}(t) = \hat{H}_0 + \hat{H}'(t), \tag{2.43}$$

where $\hat{H}_0$ represents a system in the absence of the perturbation, $\hat{H}'(t)$, which can vary with time, t is the perturbation.

For a non-equilibrium state, the expectation value of any physical observable $\hat{A}$ is also time-dependent,

$$\langle \hat{A}(t) \rangle = \mathrm{Tr}\left(\hat{\rho}(t)\hat{A}\right), \tag{2.44}$$

where $\hat{\rho}(t)$ is the density operator that evolves with time.

The time evolution of the density operator is governed by the time evolution operator,

$$\hat{\rho}(t) = \hat{U}(t,t')\hat{\rho}(t')\hat{U}^{\dagger}(t,t'), \tag{2.45}$$

where $\hat{\rho}(t') \equiv \hat{\rho}_0$ is defined as density operator at initial time (equilibrium state) and the time evolution operator for a time-dependent Hamiltonian is

$$\hat{U}(t,t') = \mathcal{T}\left[e^{-\frac{i}{\hbar}\int_{t'}^{t} ds \hat{H}(s)}\right], \tag{2.46}$$

where $\mathcal{T}$ is time-ordering operator. Note that the time evolution operator reduces to $e^{-\frac{i}{\hbar}\hat{H}(t-t')}$ when the Hamiltonian is time-independent.

It should be noted that the density matrix operator does not evolve with time in the

Heisenberg picture but it does in the *Schrödinger picture.* It is clear by writing it in the matrix form,

$$\hat{\rho}(t') = \hat{\rho}_0 = \frac{1}{Z}\sum_n e^{-\hat{H}_0\beta}\left|n\right\rangle\left\langle n\right|, \tag{2.47}$$

where $Z = \mathrm{Tr}\, e^{-\hat{H}_0\beta}$ is the partition function. The time-evolution operator acts on the state vectors and gives Eq. 2.45.

The time-ordering operator in the time evolution operator is cumbersome to calculate analytically but we can be expand it in order of $\hat{H}'$ in *Interaction picture*, since the time-dependent part of Hamiltonian is perturbative. To the first order, we have

$$\hat{U}(t,t') = \hat{U}_0(t,t') - \hat{U}_0(t,t_r)\frac{i}{\hbar}\int_{t'}^{t} ds\hat{H}'_I(s)\hat{U}_0^\dagger(t',t_r) + \mathcal{O}(\hat{H}'^2), \tag{2.48}$$

where t_r is the reference time.

Consequently, the time evolved density operator can be expanded to first order of $\hat{H}'$,

$$\begin{aligned}\hat{\rho}(t) &= \Big\{\hat{U}_0(t,t') - \hat{U}_0(t,t_r)\frac{i}{\hbar}\int_{t'}^{t} ds\hat{H}'_I(s)\hat{U}_0^\dagger(t',t_r)\Big\}\hat{\rho}(t') \\ &\quad \Big\{\hat{U}_0^\dagger(t,t') + \hat{U}_0(t',t_r)\frac{i}{\hbar}\int_{t'}^{t} ds\ \hat{H}'_I(s)\hat{U}_0^\dagger(t,t_r)\Big\}, \\ &= \hat{U}_0(t,t')\hat{\rho}(t')\hat{U}_0^\dagger(t,t') + \frac{i}{\hbar}\int_{t'}^{t} ds\ \hat{U}_0(t,t')\hat{\rho}(t')\hat{U}_0(t',t_r)\hat{H}'_I(s)\hat{U}_0^\dagger(t,t_r) \\ &- \hat{U}_0(t,t_r)\hat{H}'_I(s)\hat{U}_0^\dagger(t',t_r)\hat{\rho}(t')\hat{U}_0^\dagger(t,t'). \end{aligned} \tag{2.49}$$

We assume that prior to time $t_r = t' = -\infty$, the external force is absent and the system is in the equilibrium state $\hat{\rho}_0$,

$$\hat{\rho}(t) = \hat{\rho}_0 + \frac{i}{\hbar}\int_{-\infty}^{t} ds\ \hat{U}_0(t,t_r)\hat{\rho}_0\hat{H}'_I(s)\hat{U}_0^\dagger(t,t_r) - \hat{U}_0(t,t_r)\hat{H}'_I(s)\hat{\rho}_0\hat{U}_0^\dagger(t,t'). \tag{2.50}$$

Note that Eq. 2.50 can be treated as the density response to the external force in $\hat{H}'_I$.

Consequently, the expectation value of physical observable $\hat{A}$ under external force is

$$\begin{aligned}
\langle \hat{A}(t) \rangle &= \mathrm{Tr}\left(\hat{\rho}_0 \hat{A}\right) + \frac{i}{\hbar}\int_{-\infty}^{t} ds\, \mathrm{Tr}\left\{\hat{U}_0(t,t_r)\hat{\rho}_0 \hat{H}_I'(s)\hat{U}_0^\dagger(t,t_r)\hat{A} - \hat{U}_0(t,t_r)\hat{H}_I'(s)\hat{\rho}_0\hat{U}_0^\dagger(t,t_r)\hat{A}\right\} \\
&= \mathrm{Tr}\left(\hat{\rho}_0 \hat{A}\right) + \frac{i}{\hbar}\int_{-\infty}^{t} ds\, \mathrm{Tr}\left\{\hat{\rho}_0 \hat{H}_I'(s)\hat{U}_0^\dagger(t,t_r)\hat{A}\hat{U}_0(t,t_r) - \hat{\rho}_0\hat{U}_0^\dagger(t,t_r)\hat{A}\hat{U}_0(t,t_r)\hat{H}_I'(s)\right\} \\
&= \mathrm{Tr}\left(\hat{\rho}_0 \hat{A}\right) + \frac{i}{\hbar}\int_{-\infty}^{t} ds\, \mathrm{Tr}\left\{\hat{\rho}_0\left[\hat{H}_I'(s), \hat{A}_I(t)\right]\right\}. \qquad (2.51)
\end{aligned}$$

In summary, we obtain the Kubo formula,

$$\langle \hat{A}(t) \rangle = \langle \hat{A}(0) \rangle_0 + \frac{i}{\hbar}\int_{-\infty}^{t} ds\, \left\langle \left[\hat{H}_I'(s), \hat{A}_I(t)\right]\right\rangle_0, \qquad (2.52)$$

where $\langle \cdots \rangle_0$ indicates ensemble average over $\hat{\rho}_0$ (equilibrium state). Clearly, the non-equilibrium problem is simplified into the properties of equilibrium state.

2.2.2 Current correlation function

The physical quantity of interest in this dissertation is the Hall conductivity, which can be obtained from the (spin) current-current correlation function. We shall consider the current-current correlation function as an example. The current correlation function represents the linear response of current to the external electric field. We shall employ a Hamiltonian of free electron accompanying a vector potential,

$$\begin{aligned}
\hat{H} &= \frac{1}{2m}(\hat{\mathbf{p}}_{kin})^2 = \frac{1}{2m}(\hat{\mathbf{p}}_{can} - e\boldsymbol{A}(\boldsymbol{r},t))^2 \\
&= \frac{\hat{\mathbf{p}}_{can}^2}{2m} - \frac{e}{2m}(\hat{\mathbf{p}}_{can}\cdot\boldsymbol{A}(\boldsymbol{r},t) + \boldsymbol{A}(\boldsymbol{r},t)\cdot\hat{\mathbf{p}}_{can}) + \frac{e^2}{2m}\boldsymbol{A}^2(\boldsymbol{r},t), \qquad (2.53)
\end{aligned}$$

where e, m are electron charge and electron mass, $\boldsymbol{A}(\boldsymbol{r},t)$ is the vector potential and $\hat{\mathbf{p}}_{can} = i\hbar\nabla$ is the canonical momentum operator. The kinetic momentum operator is simply $\hat{\mathbf{p}}_{can} - e\boldsymbol{A}(\boldsymbol{r},t)$.

The Hamiltonian Eq. 2.53 can be written in second quantization (see Appendix. 2.A),

$$\begin{aligned}
\mathcal{H}_{2nd} &= \int d\boldsymbol{r}\psi^\dagger(\boldsymbol{r})\hat{H}\psi(\boldsymbol{r}) \qquad (2.54)\\
&= \int d\boldsymbol{r}\ \psi^\dagger(\boldsymbol{r})\Big(-\frac{\hbar^2\nabla^2}{2m} - \frac{i\hbar e}{2m}(\nabla\cdot\boldsymbol{A}(\boldsymbol{r},t) + \boldsymbol{A}(\boldsymbol{r},t)\cdot\nabla) + \frac{e^2}{2m}\boldsymbol{A}^2(\boldsymbol{r},t)\Big)\psi(\boldsymbol{r}),
\end{aligned}$$

where $\psi(\boldsymbol{r})$ is the field operator of electron.

The field operator $\psi(\boldsymbol{r})$ and the vector potential $\boldsymbol{A}(\boldsymbol{r},t)$ are written in Fourier series,

$$\begin{aligned}
\psi(\boldsymbol{r}) &= \frac{1}{\sqrt{V}}\sum_{\boldsymbol{k}} a_{\boldsymbol{k}} e^{i\boldsymbol{k}\cdot\boldsymbol{r}}, && (2.55)\\
\boldsymbol{A}(\boldsymbol{r},t) &= \sum_{\boldsymbol{q}}\int\frac{d\omega}{2\pi}\boldsymbol{A}(\boldsymbol{q},\omega)e^{i(\boldsymbol{q}\cdot\boldsymbol{r}-\omega t)}, && (2.56)
\end{aligned}$$

where $a_{\boldsymbol{k}}$ is the annihilation operator of electron.

The $\mathcal{O}(A^0)$ part of Eq. 2.55 is simply the free electron Hamiltonian,

$$\mathcal{H}_0 = \sum_{\boldsymbol{k},\boldsymbol{k}'} a^\dagger_{\boldsymbol{k}} a_{\boldsymbol{k}'}\frac{\hbar^2\boldsymbol{k}\boldsymbol{k}'}{2m}\frac{1}{V}\int d\boldsymbol{r}e^{i(\boldsymbol{k}'-\boldsymbol{k})\cdot\boldsymbol{r}} = \sum_{\boldsymbol{k}} a^\dagger_{\boldsymbol{k}} a_{\boldsymbol{k}}\frac{\hbar^2\boldsymbol{k}^2}{2m}, \tag{2.57}$$

where we define the energy of free electron, $\epsilon_{\boldsymbol{k}} = \frac{\hbar^2\boldsymbol{k}^2}{2m}$.

The $\mathcal{O}(A^1)$ part is

$$\begin{aligned}
\mathcal{H}_1 &= -\int d\boldsymbol{r}\ \frac{1}{\sqrt{V}}\sum_{\boldsymbol{k}} a^\dagger_{\boldsymbol{k}} e^{-i\boldsymbol{k}\cdot\boldsymbol{r}}\frac{i\hbar e}{2m}(\nabla\cdot\boldsymbol{A}(\boldsymbol{r},t)+\boldsymbol{A}(\boldsymbol{r},t)\cdot\nabla)\frac{1}{\sqrt{V}}\sum_{\boldsymbol{k}'} a_{\boldsymbol{k}'}e^{i\boldsymbol{k}'\cdot\boldsymbol{r}}\\
&= -i\frac{\hbar e}{2mV}\int d\boldsymbol{r}\sum_{\boldsymbol{k},\boldsymbol{k}',q} a^\dagger_{\boldsymbol{k}} a_{\boldsymbol{k}'}\int\frac{d\omega}{2\pi}e^{-i\omega t}\ e^{-i\boldsymbol{k}\cdot\boldsymbol{r}}(\nabla\cdot\boldsymbol{A}(\boldsymbol{q},\omega)e^{i\boldsymbol{q}\cdot\boldsymbol{r}}+e^{i\boldsymbol{q}\cdot\boldsymbol{r}}\boldsymbol{A}(\boldsymbol{q},\omega)\cdot\nabla)e^{i\boldsymbol{k}'\cdot\boldsymbol{r}}\\
&= \frac{\hbar e}{2mV}\int d\boldsymbol{r}\sum_{\boldsymbol{k},\boldsymbol{k}',q} a^\dagger_{\boldsymbol{k}} a_{\boldsymbol{k}'}\int\frac{d\omega}{2\pi}e^{-i\omega t}\ e^{-i\boldsymbol{k}\cdot\boldsymbol{r}}(\boldsymbol{k}\cdot\boldsymbol{A}(\boldsymbol{q},\omega)e^{i\boldsymbol{q}\cdot\boldsymbol{r}}+e^{i\boldsymbol{q}\cdot\boldsymbol{r}}\boldsymbol{A}(\boldsymbol{q},\omega)\cdot\boldsymbol{k}')e^{i\boldsymbol{k}'\cdot\boldsymbol{r}}\\
&= \frac{\hbar e}{2m}\sum_{\boldsymbol{k},\boldsymbol{k}',q} a^\dagger_{\boldsymbol{k}} a_{\boldsymbol{k}'}\int\frac{d\omega}{2\pi}(\boldsymbol{k}'+\boldsymbol{k})\cdot\boldsymbol{A}(\boldsymbol{q},\omega)e^{-i\omega t}\ \int d\boldsymbol{r}\frac{1}{V}e^{i(-\boldsymbol{k}+\boldsymbol{q}+\boldsymbol{k}')\cdot\boldsymbol{r}}\\
&= \frac{\hbar e}{2m}\sum_{\boldsymbol{k},q} a^\dagger_{\boldsymbol{k}} a_{\boldsymbol{k}-q}\int\frac{d\omega}{2\pi}(2\boldsymbol{k}-\boldsymbol{q})\cdot\boldsymbol{A}(\boldsymbol{q},\omega)e^{-i\omega t}\\
&= e\sum_{\boldsymbol{k},q} a^\dagger_{\mathbf{k}+\mathbf{q}/\mathbf{2}} a_{\boldsymbol{k}-q/2}\int\frac{d\omega}{2\pi}\frac{\hbar\boldsymbol{k}}{2m}\cdot\boldsymbol{A}(\boldsymbol{q},\omega)e^{-i\omega t},\\
&= -\sum_{q}\int\frac{d\omega}{2\pi}\mathbf{j}_p(-\boldsymbol{q})\cdot\boldsymbol{A}(\boldsymbol{q}\omega)e^{-i\omega t}, && (2.58)
\end{aligned}$$

where the paramagnetic current operator is defined as,

$$\begin{aligned}
\mathbf{j}_p(\boldsymbol{q}) &= -e\sum_{\boldsymbol{k}} a^\dagger_{\mathbf{k}-\mathbf{q}/\mathbf{2}} a_{\boldsymbol{k}+q/2}\frac{\hbar\boldsymbol{k}}{2m},\\
\mathbf{j}^\dagger_p(\boldsymbol{q}) &= -e\sum_{\boldsymbol{k}} a^\dagger_{\mathbf{k}+\mathbf{q}/\mathbf{2}} a_{\boldsymbol{k}-q/2}\frac{\hbar\boldsymbol{k}}{2m} = \mathbf{j}_p(-\boldsymbol{q}). && (2.59)
\end{aligned}$$

The $\mathcal{O}(A^2)$ part of the Hamiltonian is

$$\begin{aligned}\mathcal{H}_2 &= \int d\boldsymbol{r}\ \frac{1}{\sqrt{V}}\sum_{\boldsymbol{k}} a^\dagger_{\boldsymbol{k}} e^{-i\boldsymbol{k}\cdot\boldsymbol{r}}\frac{e^2}{2m}\boldsymbol{A}^2(\boldsymbol{r},t)\frac{1}{\sqrt{V}}\sum_{\boldsymbol{k}'} a_{\boldsymbol{k}'} e^{i\boldsymbol{k}'\cdot\boldsymbol{r}} \\ &= \frac{1}{V}\frac{e^2}{2m}\sum_{\boldsymbol{k},\boldsymbol{k}',\boldsymbol{q},\boldsymbol{q}'} a^\dagger_{\boldsymbol{k}} a_{\boldsymbol{k}'} \int\int \frac{d\omega}{2\pi}\frac{d\omega'}{2\pi}\boldsymbol{A}(\boldsymbol{q},\omega)\cdot\boldsymbol{A}(\boldsymbol{q}',\omega')e^{-i(\omega+\omega')t}\int d\boldsymbol{r}\ e^{i(\boldsymbol{k}'-\boldsymbol{k}+\boldsymbol{q}+\boldsymbol{q}')\cdot r} \\ &= \frac{e^2}{2m}\sum_{\boldsymbol{k},\boldsymbol{q},\boldsymbol{q}'} a^\dagger_{\boldsymbol{k}} a_{\mathbf{k}-\mathbf{q}-\mathbf{q}'}\int\int \frac{d\omega}{2\pi}\frac{d\omega'}{2\pi}\boldsymbol{A}(\boldsymbol{q},\omega)\cdot\boldsymbol{A}(\boldsymbol{q}',\omega')e^{-i(\omega+\omega')t} \\ &= -\frac{1}{2}\sum_{\boldsymbol{q}}\int\frac{d\omega}{2\pi}\mathbf{j}_d(-\boldsymbol{q})\cdot\boldsymbol{A}(\boldsymbol{q},\omega)e^{-i\omega t}, \end{aligned} \tag{2.60}$$

where the diamagnetic current operator is

$$\mathbf{j}_d(\boldsymbol{q}) \ = \ -\frac{e^2}{m}\sum_{\boldsymbol{k},\boldsymbol{q}'} a^\dagger_{\boldsymbol{k}} a_{\mathbf{k}+\mathbf{q}-\mathbf{q}'}\int\frac{d\omega'}{2\pi}e^{-i\omega' t}\boldsymbol{A}(\mathbf{q}',\omega') \tag{2.61}$$

a. Current correlation function

We keep the $\mathcal{O}(A^0)$ part (free electron Hamiltonian) and $\mathcal{O}(A^1)$ part (external electric field) and neglect the higher order part. The perturbation Hamiltonian represents the coupling between paramagnetic current, $\mathbf{j}_p$ and vector potential, $\boldsymbol{A}(\boldsymbol{q},\omega)$ with a specific driving frequency ω,

$$\mathcal{H}'(\boldsymbol{q},\omega,t) = -\mathbf{j}_p(-\boldsymbol{q})\cdot\boldsymbol{A}(\boldsymbol{q},\omega)e^{-i\omega t}. \tag{2.62}$$

The total Hamiltonian in question is

$$\mathcal{H} = \mathcal{H}_0 + \mathcal{H}'(\boldsymbol{q},\omega,t). \tag{2.63}$$

where $\mathcal{H}_0$ is the Hamiltonian without external force (equilibrium state).

Remind the Kubo formula in Eq. 2.53 and the current response function is

$$\begin{aligned} &\langle\hat{j}_i(\boldsymbol{q},t)\rangle - \langle\hat{j}_i(\boldsymbol{q},0)\rangle_0 \\ &= -\frac{i}{\hbar}\int_{-\infty}^{t} ds\,\mathrm{Tr}\left(\hat{\rho}_0\left[\hat{j}_{j,I}(-\boldsymbol{q},s),\hat{j}_{i,I}(\boldsymbol{q},t)\right]\right)\boldsymbol{A}_j(\boldsymbol{q},\omega)e^{-i\omega s} \\ &= -\frac{i}{\hbar}\int_{-\infty}^{+\infty} ds\ \theta(t-s)\,\mathrm{Tr}\left(\hat{\rho}_0\left[\hat{j}_{j,I}(-\boldsymbol{q},0),\hat{j}_{i,I}(\boldsymbol{q},t-s)\right]\right)\boldsymbol{A}_j(\boldsymbol{q},\omega)e^{-i\omega s}. \end{aligned} \tag{2.64}$$

Through Fourier transformation of current correlation function from time domain to frequency domain, we have

$$\begin{aligned}
\langle \hat{j}_i(\boldsymbol{q},\omega)\rangle &= \int_{-\infty}^{+\infty} dt\ \langle \hat{j}_i(\boldsymbol{q},t)\rangle\, e^{i(\omega+i\eta)t} \\
&= -\frac{i}{\hbar}\int_{-\infty}^{+\infty} dt \int_{-\infty}^{+\infty} ds\ \theta(t-s)\,\mathrm{Tr}\left(\hat{\rho}_0\left[\hat{j}_{j,I}(-\boldsymbol{q},0),\hat{j}_{i,I}(\boldsymbol{q},t-s)\right]\right)\boldsymbol{A}_j(\boldsymbol{q},\omega)e^{-i\omega s}e^{i(\omega'+i\eta)t} \\
&= -\frac{i}{\hbar}\int_{-\infty}^{+\infty} ds \int_{-\infty}^{+\infty} dt\ \theta(t-s) \\
&\mathrm{Tr}\left(\hat{\rho}_0\left[\hat{j}_{j,I}(-\boldsymbol{q},0),\hat{j}_{i,I}(\boldsymbol{q},t-s)\right]\right)e^{i(\omega'+i\eta)(t-s)}\boldsymbol{A}_j(\boldsymbol{q},\omega)e^{i(\omega'-\omega+i\eta)s} \\
&= \int_{-\infty}^{+\infty} ds\chi_{ij}(\boldsymbol{q},\omega')\boldsymbol{A}_j(\boldsymbol{q},\omega)e^{i(\omega'-\omega+i\eta)s} \\
&= \chi_{ij}(\boldsymbol{q},\omega)\boldsymbol{A}_j(\boldsymbol{q},\omega), \qquad (2.65)
\end{aligned}$$

where η is infinitesimal to ensure exponential decay at $t \to -\infty$ and the current correlation function χ_{ij} is defined as

$$\chi_{ij}(\boldsymbol{q},\omega) = \frac{i}{\hbar}\int_{0}^{+\infty} dt\ \mathrm{Tr}\left(\hat{\rho}_0\left[\hat{j}_{i,I}(\boldsymbol{q},t),\hat{j}_{j,I}(-\boldsymbol{q},0)\right]\right)e^{i(\omega+i\eta)t}. \qquad (2.66)$$

Note that the external electric field is $\boldsymbol{E} = i\omega\boldsymbol{A}$. Thus, the (optical) conductivity tensor is obtained by

$$\sigma_{ij}^{\alpha}(\boldsymbol{q},\omega) = \frac{\chi_{ij}(\boldsymbol{q},\omega)-\chi_{ij}(\boldsymbol{q},0)}{i\omega}, \qquad (2.67)$$

where $\chi_{ij}(\boldsymbol{q},0)$ cancels the diamagnetic current in diagonal component ($i = j$). The dc (electric) conductivity tensor is simply obtained in the limit $\omega \to 0$

$$\sigma_{ij}^{\alpha}(\boldsymbol{q},0) = \lim_{\omega\to 0}\frac{\chi_{ij}(\boldsymbol{q},\omega)-\chi_{ij}(\boldsymbol{q},0)}{i\omega}. \qquad (2.68)$$

2.2.3 Generalized correlation function

We now generalize the correlation function to arbitrary physical quantities. For a perturbative Hamiltonian in which physical quantity $B_\nu(-\boldsymbol{q})$ couples with field $F_\nu(\boldsymbol{q},\omega)$, the perturbative Hamiltonian of external force with a specific driving frequency ω reads

$$H_{ext} = -B_\nu(-\boldsymbol{q})F_\nu(\boldsymbol{q},\omega)e^{-i\omega t}. \qquad (2.69)$$

Any physical quantity $A_\mu(\boldsymbol{q},\omega)$ responses to perturbation above in linear order is expressed as the "correlation" between A_μ and B_ν,

$$\langle A_\mu(\boldsymbol{q},\omega)\rangle = \chi_{A_\mu,B_\nu}(\boldsymbol{q},\omega)F_\nu(\boldsymbol{q},\omega), \tag{2.70}$$

with the A-B correlation function,

$$\chi_{A_\mu,B_\nu}(\boldsymbol{q},\omega) = \frac{i}{\hbar}\int_0^{+\infty} dt\ \mathrm{Tr}\Big(\hat{\rho}_0\Big[A_\mu(\boldsymbol{q},t),B_\nu(-\boldsymbol{q},0)\Big]\Big)e^{i(\omega+i\eta)t}. \tag{2.71}$$

2.2.4 Energy spectral representation

One method to calculate the correlation function is through its energy spectral representation. We consider the generalized correlation function in Eq. 2.71. In equilibrium state with low particle density, the occupation number for level n is approximated by the Fermi function,

$$\rho_n = e^{-\varepsilon_n\beta}\sum_m e^{-\varepsilon_m\beta} \approx f(\varepsilon_n) = \frac{1}{e^{\varepsilon_n\beta}+1}. \tag{2.72}$$

Thus, the density operator can be simplified as Fermi distribution function with Hamiltonian,

$$\hat{\rho}_0 = f(\hat{H}_0) = \frac{1}{1+e^{\hat{H}_0\beta}}. \tag{2.73}$$

Inserting two identity matrix $I = |n\rangle\langle n|$ and using identity $\hat{H}_0|n\rangle = \varepsilon_n|n\rangle$, the trace part of Eq. 2.71 is

$$\begin{aligned}
& \mathrm{Tr}\Big(\hat{\rho}_0\Big[A_\mu(\boldsymbol{q},t),B_\nu(-\boldsymbol{q},0)\Big]\Big) \\
= & \sum_{n,m}\mathrm{Tr}\Big(f(\hat{H}_0)|n\rangle\langle n|e^{i\hat{H}_0t}A_\mu(\boldsymbol{q},0)e^{-i\hat{H}_0t}|m\rangle\langle m|B_\nu(-\boldsymbol{q},0) \\
& -f(\hat{H}_0)|n\rangle\langle n|B_\nu(-\boldsymbol{q},0)e^{i\hat{H}_0t}|m\rangle\langle m|A_\mu(\boldsymbol{q},0)e^{-i\hat{H}_0t}\Big) \\
= & \sum_{n,m}f(\varepsilon_n)\,\mathrm{Tr}\Big(\langle n|e^{i\hat{H}_0t}A_\mu(\boldsymbol{q},0)e^{-i\hat{H}_0t}|m\rangle\langle m|B_\nu(-\boldsymbol{q},0)|n\rangle \\
& -\langle n|B_\nu(-\boldsymbol{q},0)e^{i\hat{H}_0t}|m\rangle\langle m|A_\mu(\boldsymbol{q},0)e^{-i\hat{H}_0t}|n\rangle\Big)
\end{aligned}$$

$$\begin{aligned}
&= \sum_{n,m} f(\varepsilon_n)\,\mathrm{Tr}\Big(e^{i\varepsilon_n t}e^{-i\varepsilon_m t}\langle n|\,A_\mu(\boldsymbol{q},0)\,|m\rangle\langle m|\,B_\nu(-\boldsymbol{q},0)\,|n\rangle \\
&\quad -e^{i\varepsilon_m t}e^{-i\varepsilon_n t}\langle n|\,B_\nu(-\boldsymbol{q},0)\,|m\rangle\langle m|\,A_\mu(\boldsymbol{q},0)\,|n\rangle\Big) \\
&= \sum_{n,m} f(\varepsilon_n)\Big(e^{\frac{i}{\hbar}(\varepsilon_n-\varepsilon_m)t}A_\mu^{nm}(\boldsymbol{q})B_\nu^{mn}(-\boldsymbol{q}) - e^{\frac{i}{\hbar}(\varepsilon_m-\varepsilon_n)t}B_\nu^{nm}(-\boldsymbol{q})A_\mu^{mn}(\boldsymbol{q})\Big) \\
&= \sum_{n,m}(f(\varepsilon_n)-f(\varepsilon_m))A_\mu^{nm}(\boldsymbol{q})B_\nu^{mn}(-\boldsymbol{q})e^{\frac{i}{\hbar}(\varepsilon_n-\varepsilon_m)t}, \qquad (2.74)
\end{aligned}$$

where A^{nm}, B^{nm} are matrix elements of operator A and B.

The integral in Eq. 2.71 can be calculated with the following identity,

$$\frac{i}{\hbar}\int_0^{+\infty} dt\; e^{\frac{i}{\hbar}(\varepsilon_n-\varepsilon_m)t}e^{i(\omega+i\eta)t} = \frac{i}{\hbar}\int_0^{+\infty} dt\; e^{\frac{i}{\hbar}(\varepsilon_n-\varepsilon_m+\hbar\omega+i\hbar\eta)t} = -\frac{1}{(\varepsilon_n-\varepsilon_m+\hbar\omega+i\eta)} \qquad (2.75)$$

The generalized correlation function in the energy spectral representation is

$$\chi_{A_\mu,B_\nu}(\boldsymbol{q},\omega) = -\sum_{n,m}(f(\varepsilon_n)-f(\varepsilon_m))\frac{A_\mu^{nm}(\boldsymbol{q})B_\nu^{mn}(-\boldsymbol{q})}{(\varepsilon_n-\varepsilon_m+\hbar\omega+i\eta)}. \qquad (2.76)$$

a. Hall conductivity in energy spectral representation

Remind the current correlation function (Eq. 2.66) and its energy spectral representation is

$$\chi_{ij}(\boldsymbol{q},\omega) = -\sum_{n,m}(f(\varepsilon_n)-f(\varepsilon_m))\frac{J_i^{nm}(\boldsymbol{q})J_j^{mn}(-\boldsymbol{q})}{\varepsilon_n-\varepsilon_m+\hbar\omega+i\eta}. \qquad (2.77)$$

The conductivity tensor is obtained by Eq. 2.67,

$$\begin{aligned}
\sigma_{ij}(\boldsymbol{q},\omega) &= -\frac{1}{i\omega}\sum_{n,m}(f(\varepsilon_n)-f(\varepsilon_m))J_i^{nm}(\boldsymbol{q})J_j^{mn}(-\boldsymbol{q})\Big(\frac{1}{\varepsilon_n-\varepsilon_m+\hbar\omega+i\eta}-\frac{1}{\varepsilon_n-\varepsilon_m+i\eta}\Big) \\
&= -\frac{1}{i\omega}\sum_{n,m}(f(\varepsilon_n)-f(\varepsilon_m))J_i^{nm}(\boldsymbol{q})J_j^{mn}(-\boldsymbol{q})\Big(\frac{-\hbar\omega}{(\varepsilon_n-\varepsilon_m+i\eta)(\varepsilon_n-\varepsilon_m+\hbar\omega+i\eta)}\Big) \\
&= \frac{\hbar}{i}\sum_{n,m}(f(\varepsilon_n)-f(\varepsilon_m))\frac{J_i^{nm}(\boldsymbol{q})J_j^{mn}(-\boldsymbol{q})}{(\varepsilon_n-\varepsilon_m+i\eta)(\varepsilon_n-\varepsilon_m+\hbar\omega+i\eta)}. \qquad (2.78)
\end{aligned}$$

In the static limit, the electric conductivity tensor is

$$\sigma_{ij} = \hbar\sum_{n,m}(f(\varepsilon_n)-f(\varepsilon_m))\frac{\mathrm{Im}\left[J_i^{nm}(\boldsymbol{q}=0)J_j^{mn}(-\boldsymbol{q}=0)\right]}{(\varepsilon_n-\varepsilon_m)^2}, \qquad (2.79)$$

where $\boldsymbol{q} = 0$ for zero external magnetic field.

2.2.5 Matsubara substitution

The correlation function can be also calculated through Matsubara substitution. Considering the general correlation function (Eq. 2.71),

$$\begin{aligned}
&\chi_{A_\mu,B_\nu}(\boldsymbol{q},\omega) = \frac{i}{\hbar}\int_0^{+\infty} dt\ \mathrm{Tr}\left(\hat{\rho}_0\Big[A_\mu(\boldsymbol{q},t), B_\nu(-\boldsymbol{q},0)\Big]\right)e^{i(\omega+i\eta)t} \\
&= \frac{i}{\hbar}\int_0^{+\infty} dt\ e^{i(\omega+i\eta)t}\,\mathrm{Tr}\left(\hat{\rho}_0\Big[A_\mu(\boldsymbol{q},t)B_\nu(-\boldsymbol{q},0) - B_\nu(-\boldsymbol{q},0)A_\mu(\boldsymbol{q},t)\Big]\right) \\
&= \frac{i}{Z\hbar}\int_0^{+\infty} dt\ e^{i(\omega+i\eta)t} \\
&\mathrm{Tr}\left(e^{-\beta\hat{H}_0}A_\mu(\boldsymbol{q},t)B_\nu(-\boldsymbol{q},0) - e^{-\beta\hat{H}_0}e^{+\beta\hat{H}_0}A_\mu(\boldsymbol{q},t)e^{-\beta\hat{H}_0}B_\nu(-\boldsymbol{q},0)\right) \\
&= \frac{i}{Z\hbar}\int_0^{+\infty} dt\ e^{i(\omega+i\eta)t}\,\mathrm{Tr}\left(e^{-\beta\hat{H}_0}A_\mu(\boldsymbol{q},t)B_\nu(-\boldsymbol{q},0) - e^{-\beta\hat{H}_0}A_\mu(\boldsymbol{q},t-i\hbar\beta)B_\nu(-\boldsymbol{q},0)\right) \\
&= \frac{i}{\hbar}\int_0^{+\infty} dt\ e^{i(\omega+i\eta)t}\,\mathrm{Tr}\left(\hat{\rho}_0\left(A_\mu(\boldsymbol{q},t)B_\nu(-\boldsymbol{q},0) - A_\mu(\boldsymbol{q},t-i\hbar\beta)B_\nu(-\boldsymbol{q},0)\right)\right).
\end{aligned} \tag{2.80}$$

Replace the frequency, ω, with Matsubara frequency of boson $v = 2m\pi/(\hbar\beta)$ through analytic continuation $iv \to \omega + i\eta$, Eq. 2.80 can be rewritten as

$$\begin{aligned}
&\chi_{A_\mu,B_\nu}(\boldsymbol{q},iv) \\
&= \frac{i}{\hbar}\int_0^{+\infty} dt\ e^{-vt}\,\mathrm{Tr}\left(\hat{\rho}_0A_\mu(\boldsymbol{q},t)B_\nu(-\boldsymbol{q},0)\right) - \frac{i}{\hbar}\int_0^{+\infty} dt\ e^{-vt}\,\mathrm{Tr}\left(\hat{\rho}_0A_\mu(\boldsymbol{q},t-i\hbar\beta)B_\nu(-\boldsymbol{q},0)\right) \\
&= \frac{i}{\hbar}\int_0^{+\infty} d\tau\ e^{-v\tau}\,\mathrm{Tr}\left(\hat{\rho}_0A_\mu(\boldsymbol{q},\tau)B_\nu(-\boldsymbol{q},0)\right) + \frac{i}{\hbar}\int_{+\infty-i\hbar\beta}^{-i\hbar\beta} dt\ e^{-v\tau}\,\mathrm{Tr}\left(\hat{\rho}_0A_\mu(\boldsymbol{q},\tau)B_\nu(-\boldsymbol{q},0)\right) \\
&= \frac{i}{\hbar}\int_0^{-i\hbar\beta} d\tau\ e^{-v\tau}\,\mathrm{Tr}\left(\hat{\rho}_0A_\mu(\boldsymbol{q},\tau)B_\nu(-\boldsymbol{q},0)\right) \\
&= -\frac{1}{\hbar}\int_0^{\hbar\beta} du\ e^{ivu}\left\langle\mathcal{T}_u A_\mu(\boldsymbol{q},u)B_\nu(-\boldsymbol{q},0)\right\rangle_0,
\end{aligned} \tag{2.81}$$

where we add time-ordering operator $\mathcal{T}_u$ to keep the same form with the Matsubara Green's function. Apparently, Eq. 2.81 is time-ordered as $u > 0$.

a. Current correlation function with Matsubara substitution

The current correlation function with Matsubara substitution is

$$\chi_{ij}(\boldsymbol{q}, iv) \quad = \quad -\frac{1}{\hbar}\int_0^{\hbar\beta} du\ e^{ivu} \left\langle \mathcal{T}_u J_i(\boldsymbol{q}, u) J_j(-\boldsymbol{q}) \right\rangle_0, \tag{2.82}$$

with current operator,

$$J_i(\boldsymbol{q}) = -e \sum_{\boldsymbol{k}} a^{\dagger}_{\mathbf{k-q/2}} v_{i,\boldsymbol{k}} a_{\mathbf{k+q/2}}. \tag{2.83}$$

The thermodynamic average term in Eq. 2.82 is

$$\begin{aligned}
\left\langle \mathcal{T}_u J_i(\boldsymbol{q}, u) J_j(-\boldsymbol{q}) \right\rangle_0 \quad &= \quad e^2 \sum_{\boldsymbol{k},\boldsymbol{k}'} \left\langle \mathcal{T}_u a^{\dagger}_{\mathbf{k-q/2}}(u) v_{i,\boldsymbol{k}} a_{\mathbf{k+q/2}}(u) a^{\dagger}_{\mathbf{k'+/2}} v_{j,\boldsymbol{k}'} a_{\mathbf{k'-q/2}} \right\rangle_0 \\
&= \quad e^2 \sum_{\boldsymbol{k},\boldsymbol{k}'} \left\langle a^{\dagger}_{\mathbf{k-q/2}}(u) a_{\mathbf{k+q/2}}(u) \right\rangle_0 v_{i,\boldsymbol{k}} \left\langle a^{\dagger}_{\mathbf{k'+/2}} a_{\mathbf{k'-q/2}} \right\rangle_0 v_{j,\boldsymbol{k}} \\
&\qquad - \left\langle a^{\dagger}_{\mathbf{k-q/2}}(u) a_{\mathbf{k'-q/2}} \right\rangle_0 v_{i,\boldsymbol{k}} \left\langle a_{\mathbf{k+q/2}}(u) a^{\dagger}_{\mathbf{k'+/2}} \right\rangle_0 v_{j,\boldsymbol{k}} \\
&= \quad e^2 \sum_{\boldsymbol{k},\boldsymbol{k}'} \mathcal{G}^{(0)}_{\mathbf{k+q/2,k-q/2}}(0) v_{i,\boldsymbol{k}} \mathcal{G}^{(0)}_{\mathbf{k'-q/2,k'+q/2}}(0) v_{k,\boldsymbol{k}'} \\
&\qquad -e^2 \sum_{\boldsymbol{k},\boldsymbol{k}'} \mathcal{G}^{(0)}_{\mathbf{k'-q/2,k-q/2}}(-u) v_{i,\boldsymbol{k}} \mathcal{G}^{(0)}_{\mathbf{k+q/2,k'+q/2}}(u) v_{j,\boldsymbol{k}},
\end{aligned} \tag{2.84}$$

where the *Wick's theorem* is applied to contract the creation and annihilation operators with Matsubara Green's function, $\mathcal{G}^{(0)}_{\lambda,\lambda'}(\tau - \tau') = -\left\langle T_\tau a_\lambda(\tau) a^{\dagger}_{\lambda'}(\tau') \right\rangle_0$.

Note that the τ-domain Green's function can be written in the frequency domain,

$$\mathcal{G}^{(0)}(\tau) = \frac{1}{\beta} \sum_n \mathcal{G}^{(0)}(i\omega_n) e^{-i\omega_n \tau}. \tag{2.85}$$

The current correlation function is

$$\begin{aligned}
\chi_{ij}(\boldsymbol{q}, iv) \quad &= \quad e^2 \sum_{\boldsymbol{k}} \frac{1}{\hbar} \int_0^{\hbar\beta} du\ e^{ivu} \mathcal{G}^{(0)}_{\mathbf{k-q/2}}(-u) v_{i,\boldsymbol{k}} \mathcal{G}^{(0)}_{\mathbf{k+q/2}}(u) v_{j,\boldsymbol{k}} \\
&= \quad e^2 \sum_{\boldsymbol{k}} \frac{1}{\hbar} \int_0^{\hbar\beta} du\ e^{ivu} \frac{1}{\beta} \sum_n \mathcal{G}_{\mathbf{k-q/2}}(i\omega_n) e^{i\omega_n u} v_{i,\boldsymbol{k}} \frac{1}{\beta} \sum_m \mathcal{G}_{\mathbf{k+q/2}}(i\omega_m) e^{-i\omega_m u} v_{j,\boldsymbol{k}} \\
&= \quad e^2 \sum_{\boldsymbol{k}} \sum_n \sum_m \mathcal{G}^{(0)}_{\mathbf{k-q/2}}(i\omega_n) v_{i,\boldsymbol{k}} \mathcal{G}^{(0)}_{\mathbf{k+q/2}}(i\omega_m) v_{l,\boldsymbol{k}} \frac{1}{\hbar} \frac{1}{\beta^2} \int_0^{\hbar\beta} du\ e^{ivu} e^{i\omega_n u} e^{-i\omega_m u}
\end{aligned}$$

$$
\begin{aligned}
&= e^2 \sum_{\boldsymbol{k}} \sum_{n} \sum_{m} \mathcal{G}^{(0)}_{\mathbf{k-q/2}}(i\omega_n) v_{i,\boldsymbol{k}} \mathcal{G}^{(0)}_{\mathbf{k+q/2}}(i\omega_m) v_{j,\boldsymbol{k}} \frac{1}{\hbar\beta^2} \int_0^{\hbar\beta} du\ e^{i(v+\omega_n-\omega_m)u} \\
&= e^2 \sum_{\boldsymbol{k}} \sum_{n} \sum_{m} \mathcal{G}^{(0)}_{\mathbf{k-q/2}}(i\omega_n) v_{i,\boldsymbol{k}} \mathcal{G}^{(0)}_{\mathbf{k+q/2}}(i\omega_m) v_{j,\boldsymbol{k}} \frac{1}{\beta} \delta(v+\omega_n-\omega_m) \\
&= e^2 \frac{1}{\beta} \sum_{\boldsymbol{k}} \sum_{n} \mathcal{G}^{(0)}_{\mathbf{k-q/2}}(i\omega_n) v_{i,\boldsymbol{k}} \mathcal{G}^{(0)}_{\mathbf{k+q/2}}(i\omega_n + iv) v_{j,\boldsymbol{k}}. \qquad (2.86)
\end{aligned}
$$

b. Evaluation of Matsubara summation

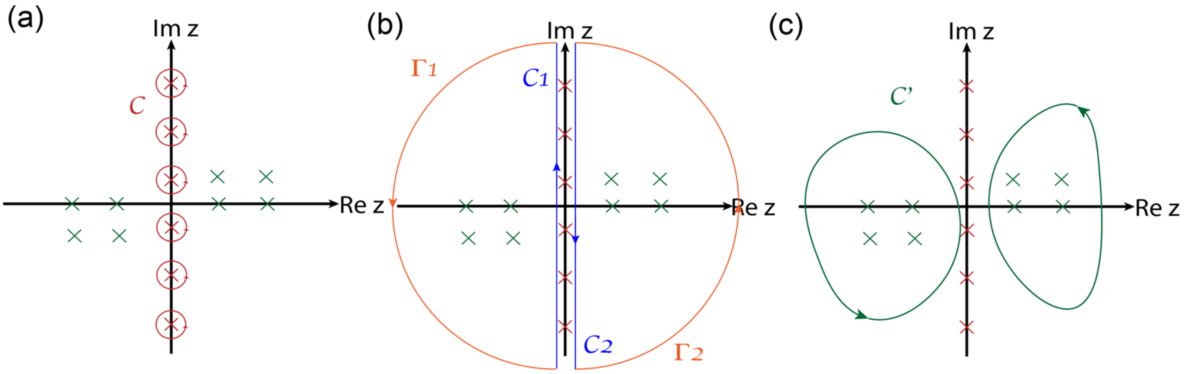

Figure 2.2: Residue theorem on Matsubara summation.
Integration paths of C (a), $C_1, C_2, \Gamma_1, \Gamma_2$ (b), and C' (c) in complex plane of z. The red crosses represent the poles of weighting function $\nu_\beta(z)$ and green crosses represent the poles of $F(z)$.

The Matsubara summation (over ω_n) in Eq. 2.86, can be evaluated through the *residue theorem* [67]. We shall consider Matsubara summation of arbitrary function $F(i\omega_n)$ with fermionic frequency, ($\omega_n = (2n+1)\pi/\beta$), for example,

$$
\frac{1}{\beta} \sum_{n \in \boldsymbol{Z}} F(i\omega_n). \qquad (2.87)
$$

If $F(z)$ does not have any singularity on the imaginary axis, the sum can be considered as summation over multiple poles on the imaginary axis given by fermionic weighting functions, such as $\nu_\beta(z) = \tanh(\beta z/2)$,

$$
\frac{1}{\beta} \sum_{n \in \boldsymbol{Z}} F(i\omega_n) = \frac{1}{2\pi i} \oint_C dz F(z) \nu_\beta(z). \qquad (2.88)
$$

where C is the integration contours surrounding all poles of the fermionic weighting function $\nu_\beta(z)$ (see Fig. 2.2(a)).

It is easily checked that $g(z)\nu_\beta(z)$ converges to zero when $|z| \to \infty$. Thus the integral of left Γ_1 and right Γ_2 hemisphere are asymptotically zero when the radius of the path goes to infinity,

$$\lim_{|z|\to\infty} \frac{1}{2\pi i} \oint_{\Gamma_1} dz F(z)\nu_\beta(z) = \lim_{|z|\to\infty} \frac{1}{2\pi i} \oint_{\Gamma_2} dz F(z)\nu_\beta(z) = 0. \tag{2.89}$$

Thus, the integral over path C can be written as,

$$\begin{aligned} \frac{1}{2\pi i} \oint_C dz F(z)\nu_\beta(z) &= \frac{1}{2\pi i} \oint_{C_1} dz F(z)\nu_\beta(z) \frac{1}{2\pi i} \oint_{C_2} dz F(z)\nu_\beta(z) \\ &= \frac{1}{2\pi i} \oint_{\Gamma_1 + C_1} dz F(z)\nu_\beta(z) + \frac{1}{2\pi i} \oint_{\Gamma_2 + C_2} dz F(z)\nu_\beta(z) \\ &= -\sum_{z=z_a} Res[F(z)\nu_\beta(z)], \end{aligned} \tag{2.90}$$

where z_a are poles of $g(z)$.

The **first identity** of Matsubara summation is to calculate the residue of poles of $F(z)$,

$$\frac{1}{\beta} \sum_{n\in \boldsymbol{Z}} F(i\omega_n) = -\sum_{z=z_a} Res[F(z)\nu_\beta(z)]. \tag{2.91}$$

The **second identity** of Matsubara summation is to calculate the integral with path surrounding all poles of $F(z)$,

$$\frac{1}{\beta} \sum_{n\in \boldsymbol{Z}} F(i\omega_n) = \frac{1}{2\pi i} \int_{C'} dz F(z)\nu_\beta(z). \tag{2.92}$$

where C' surrounds all poles of $F(z)$ (see Fig. 2.2(c)).

It is easily checked that Matsubara summation over bosonic frequency ($\omega_n = 2n\pi/\beta$) can be calculated by choosing other appropriate weighting function, *e.g.*, $\nu_\beta(z) = \coth(\beta z/2)$.

2.3 First principles calculation

2.3.1 Density functional theory

An efficient and accurate scheme for numerically solving many-body problems is the density functional theory (DFT) [68]. To describe a many-particle system such as electrons in a solid, one has to calculate the many-body wave function, which is a formidable task due to the enormous electronic degrees of freedom. However, this complicated many-particle problem can be reduced to an effective single-particle problem by noting that information of the ground-state density is sufficient to calculate all physical quantities of interest. A rigorous foundation of DFT in its modern form was provided by Hohenberg and Kohn [69], and the effective single particle equation for practical application of DFT was derived by Kohn and Sham [70] by introducing the local density approximation.

a. Hohenberg-Kohn theorem

The basic theorems of the density functional formalism were derived by Hohenberg and Kohn. Extending an argument for independent fermions [71], Levy provided a simpler and more general derivation [72], which we present here.

We shall consider a system with N electrons moving in an external potential $V_{ext}(\boldsymbol{r})$. The total Hamiltonian is

$$\hat{H} = \hat{T} + \hat{V}_{ee} + \sum_{i}^{N} V_{ext}(\boldsymbol{r}_i), \tag{2.93}$$

where $\hat{T}$ and $\hat{V}_{ee}$ are the kinetic and electron-electron interaction operators, respectively. We define the following functional $F[\rho]$ of the density $\rho(\boldsymbol{r})$ obtained from an generic antisymmetric (fermion) wave function, $\psi(\boldsymbol{r}_1, \boldsymbol{r}_2, \cdots, \boldsymbol{r}_N)$:

$$F[\rho] = \min_{\psi \to \rho} \langle \psi | \, \hat{T} + \hat{V}_{ee} \, | \psi \rangle \,, \tag{2.94}$$

where the minimum is taken over all possible wave functions, ψ, that give the density ρ.

Assuming the E_{GS}, ψ_{GS} and $\rho_{GS}(\boldsymbol{r})$ to be the energy, wave function, and density of the ground-state, respectively, the *Hohenberg-Kohn theorem* states

$$E[\rho] \;\; \equiv \;\; \int d\boldsymbol{r} V_{ext}(\boldsymbol{r}) \rho(\boldsymbol{r}) + F[\rho] \geqslant E_{GS}, \tag{2.95}$$

for all $\rho(\boldsymbol{r})$ and

$$E_{GS} \;\; = \;\; \int d\boldsymbol{r} V_{ext}(\boldsymbol{r}) \rho_{GS}(\boldsymbol{r}) + F[\rho_{GS}]. \tag{2.96}$$

To prove the variational principle (Eq. 2.95), we introduce the a wave function $\psi_{\rho,min}(\boldsymbol{r})$

that minimizes Eq. 2.94,

$$F[\rho] = \langle \psi_{\rho,min} | \hat{T} + \hat{V}_{ee} | \psi_{\rho,min} \rangle . \tag{2.97}$$

Writing $V = \sum_i V_{ext}(\boldsymbol{r}_i)$, we can prove Eq. 2.95,

$$\int d\boldsymbol{r} V_{ext}(\boldsymbol{r})\rho(\boldsymbol{r}) + F[\rho] = \langle \psi_{\rho,min} | \hat{T} + \hat{V}_{ee} + \hat{V} | \psi_{\rho,min} \rangle \geqslant E_{GS}, \tag{2.98}$$

where we employ the minimum property (Eq. 2.95) of the ground state.

Using the minimum property once more we find

$$E_{GS} = \langle \psi_{GS} | \hat{T} + \hat{V}_{ee} + V | \psi_{GS} \rangle \leqslant \langle \psi_{\rho,min} | \hat{T} + \hat{V}_{ee} + V | \psi_{\rho,min} \rangle , \tag{2.99}$$

$$\langle \psi_{GS} | \hat{T} + \hat{V}_{ee} | \psi_{GS} \rangle \leqslant \langle \psi_{\rho,min} | \hat{T} + \hat{V}_{ee} | \psi_{\rho,min} \rangle , \tag{2.100}$$

where we subtracted the interaction with the external potential in the second inequality.

Comparing with Eq. 2.97, the two inequalities can be simultaneously valid only if

$$\langle \psi_{GS} | \hat{T} + \hat{V}_{ee} | \psi_{GS} \rangle = \langle \psi_{\rho,min} | \hat{T} + \hat{V}_{ee} | \psi_{\rho,min} \rangle . \tag{2.101}$$

Thus, we have

$$\begin{aligned} E_{GS} &= \int d\boldsymbol{r} V_{ext}(\boldsymbol{r})\rho_{GS}(\boldsymbol{r}) + \langle \psi_{GS} | \hat{T} + \hat{V}_{ee} | \psi_{GS} \rangle \\ &= \int d\boldsymbol{r} V_{ext}(\boldsymbol{r})\rho_{GS}(\boldsymbol{r}) + \langle \psi_{\rho,min} | \hat{T} + \hat{V}_{ee} | \psi_{\rho,min} \rangle \\ &= \int d\boldsymbol{r} V_{ext}(\boldsymbol{r})\rho_{GS}(\boldsymbol{r}) + F[\rho_{GS}]. \end{aligned} \tag{2.102}$$

The important result from the Hohenberg-Kohn theorem is that we can obtain the ground-state wave function by minimizing the functional $E[\rho]$ with respect to density ρ. Besides, the theorems provide a general method for calculating other ground state properties. If we also have an approximation to the functional $X[\rho]$ describing other ground-state property X, the same procedure leads to approximations for X.

b. Kohn-Sham single-particle equation

Practical application of Hohenberg-Kohn theorem is still limited by the problematic treatment of the many-particle kinetic energy. Hence, an effective single-particle equation is purposed to deal with the variational principle in many-particle problem [70]. The energy functional is rewritten as

$$\begin{aligned} E[\rho] &= \int d\boldsymbol{r} V_{ext}(\boldsymbol{r})\rho(\boldsymbol{r}) + F[\rho] \\ &= T_0[\rho] + \int d\boldsymbol{r}\rho(\boldsymbol{r})\left(V_{ext}(\boldsymbol{r}) + \frac{1}{2}\Phi(\boldsymbol{r})\right) + E_{ex}[\rho], \end{aligned} \tag{2.103}$$

where $T_0[\rho]$ is the kinetic energy of a system of non-interacting particles with density$\rho(\boldsymbol{r})$, $\Phi(\boldsymbol{r})$ is Coulomb potential for electrons, and $E_{ex}[\rho]$ is the exchange-correlation energy of an interacting system with density $\rho(\boldsymbol{r})$.

The variation principle applied to Eq. 2.103 gives

$$\begin{aligned} \frac{\delta E[\rho]}{\delta\rho} &= \frac{\delta T_0[\rho]}{\delta\rho} + V_{ext}(\boldsymbol{r}) + \frac{1}{2}\Phi(\boldsymbol{r}) + \frac{\delta E_{ex}[\rho]}{\delta\rho} \\ &= \frac{\delta T_0[\rho]}{\delta\rho} + V_{eff}(\boldsymbol{r}), \end{aligned} \tag{2.104}$$

with an effective potential defined as

$$V_{eff}(\boldsymbol{r}) \equiv V_{ext}(\boldsymbol{r}) + \frac{1}{2}\Phi(\boldsymbol{r}) + \frac{\delta E_{ex}[\rho]}{\delta\rho}. \tag{2.105}$$

The solution of Eq. 2.104 is obtained by solving the single-particle Schrӧdinger equation (Kohn-Sham equation) of the non-interacting electrons moving in the effective potential V_{eff},

$$\left(-\frac{1}{2}\nabla^2 + V_{eff}(\boldsymbol{r})\right)\psi_i(\boldsymbol{r}) = \varepsilon_i\psi_i(\boldsymbol{r}), \tag{2.106}$$

with density

$$\rho(\boldsymbol{r}) = \sum_i^N \psi_i^*(\boldsymbol{r})\psi_i(\boldsymbol{r}), \tag{2.107}$$

where we use Hartree units, $\hbar = m = e = 1$.

Apparently, the effective potential depends on the density, $\rho(\boldsymbol{r})$, which is obtained from wave functions, $\psi_i(\boldsymbol{r})$, the solution of Kohn-Sham equation containing the effective potential. Hence, the Kohn-Sham equation can only be solved self-consistently. The Kohn-Sham equation simplifies the interacting many-body problem into a non-interacting single particle problem by introducing an additional exchange-correlation energy, E_{ec}. However, the exchange-correlation energy can not be solved exactly and the approximations for E_{ec} play a central role in the density functional theory.

c. Local spin density approximation

The most used approximation method for exchange correlation energy is the *local spin density* (LSD) approximation, in which the exchange-correlation energy is

$$E_{ex}^{LSD} = \int d\boldsymbol{r}\rho(\boldsymbol{r})\varepsilon_{ex}[\rho_\uparrow(\boldsymbol{r}), \rho_\downarrow(\boldsymbol{r})], \tag{2.108}$$

where $\varepsilon_{ex}[\rho_\uparrow(\boldsymbol{r}), \rho_\downarrow(\boldsymbol{r})]$ is the exchange-correlation energy with spin-up and spin-down densities $\rho_\uparrow(\boldsymbol{r})$ and $\rho_\downarrow(\boldsymbol{r})$, respectively. The approximation is based on the idea that divides the inhomogeneous electron system into small "boxes" of assumptive homogeneous electron gas whose exchange correlation energy depends on the local spin densities, *i.e.*, $\varepsilon_{ex}[\rho_\uparrow(\boldsymbol{r}), \rho_\downarrow(\boldsymbol{r})]$. Therefore, the problem of calculating the exchange-correlation energy in an inhomogeneous electron system has been simplified as the problem of calculating the exchange-correlation energy density, ε_{ex}, of the homogenous electron gases.

However, the LSD approximation has a tendency to underestimate the exchange energy and over-estimate the correlation energy, since the exchange and correlation parts tend to compensate each other to a certain degree [73]. To obtain more accurate approximation on exchange-correlation energy, it is common to expand in terms of the gradient of the density in order to account for the non-homogeneity of the true electron density, which are referred to as generalized gradient approximations (GGA) [74],

$$E_{ex}^{LSD} = \int d\boldsymbol{r}\rho(\boldsymbol{r})\varepsilon_{ex}[\rho_\uparrow(\boldsymbol{r}), \rho_\downarrow(\boldsymbol{r}), \nabla\rho_\uparrow(\boldsymbol{r}), \nabla\rho_\downarrow(\boldsymbol{r})]. \tag{2.109}$$

The exchange-correlation energy density, ε_{ex}, has been calculated successively by many authors [75–82]. In our calculation, we implement a simple but accurate version of GGA purposed by Perdew, Burke and Ernzerhof (PBE 96) [83].

2.3.2 Spin orbit coupling in DFT

The spin orbit coupling is implemented through a second variation method in our first principles calculation [84]. We shall consider the fully relativistic single-particle Kohn-Sham Hamiltonian [85] and its Schrödinger equation,

$$\begin{aligned} H &= -ic\boldsymbol{\alpha}\cdot\nabla + (\beta - I_4)mc^2 - e\phi_{eff} + \mu_B \boldsymbol{B}_{eff}\cdot\boldsymbol{\sigma}\otimes I_2, \\ H\Psi(\boldsymbol{r}) &= \varepsilon\Psi(\boldsymbol{r}). \end{aligned} \tag{2.110}$$

where

$$\boldsymbol{\alpha} = \begin{pmatrix} 0 & \boldsymbol{\sigma} \\ \boldsymbol{\sigma} & 0 \end{pmatrix}, \beta = \begin{pmatrix} I_2 & 0 \\ 0 & -I_2 \end{pmatrix}, \tag{2.111}$$

are the generators of Dirac algebra. The ϕ_{eff} and $\boldsymbol{B}_{eff}$ are effective electric and effective magnetic field, respectively.

The Hamiltonian can be rewritten in matrix form,

$$\begin{pmatrix} V(\boldsymbol{r}) & -ic\boldsymbol{\alpha}\cdot\nabla \\ -ic\boldsymbol{\alpha}\cdot\nabla & V(\boldsymbol{r}) - 2mc^2 I_2 \end{pmatrix} \begin{pmatrix} \Phi \\ \chi \end{pmatrix} = \epsilon \begin{pmatrix} \Phi \\ \chi \end{pmatrix}, \tag{2.112}$$

where Φ and χ are the large and small components of $\Psi(\boldsymbol{r})$, $V(\boldsymbol{r})$ is defined as

$$V(\boldsymbol{r}) = -e\phi_{eff} I_2 + \mu_B \boldsymbol{B}_{eff}\cdot\boldsymbol{\sigma}. \tag{2.113}$$

By defining a factor $f = 2mc^2/(2mc^2 + \varepsilon - V)$, we have two coupled differential equations for Φ and χ,

$$\frac{1}{2m}\boldsymbol{\sigma}\cdot\nabla(f\boldsymbol{\sigma}\cdot\nabla\Phi) + (\varepsilon I_2 - V(\boldsymbol{r})) = 0, \tag{2.114}$$

$$\chi = -\frac{i}{2mc}\boldsymbol{\sigma}\cdot f\nabla\Phi. \tag{2.115}$$

Note that the factor $f \simeq 1$ when $mc^2 \gg \varepsilon - V$.

The relativistic Kohn-Sham Hamiltonian can be separated into a the semi-relativistic

Hamiltonian and a spin-orbit-coupling term,

$$H = H_{semi} + H_{soc}, \tag{2.116}$$

with

$$H_{semi} \begin{pmatrix} \Phi \\ \chi \end{pmatrix} = \begin{pmatrix} V(\boldsymbol{r})\Phi - \frac{1}{2m}\nabla \cdot (f\nabla\Phi) \\ -\frac{i}{2mc}\boldsymbol{\sigma} \cdot (f\nabla\Phi) \end{pmatrix}, \tag{2.117}$$

and

$$H_{soc} \begin{pmatrix} \Phi \\ \chi \end{pmatrix} = \begin{pmatrix} -\frac{i\boldsymbol{\sigma}}{2m} \cdot (\nabla f \times \nabla\Phi) \\ 0 \end{pmatrix}, \tag{2.118}$$

Denote the eigenstates $|n\rangle$ of the semi-relativistic Hamiltonian,

$$H_{semi}\left|n\right\rangle = H_{semi} \begin{pmatrix} \Phi_n \\ \chi_n \end{pmatrix} = \varepsilon_n \begin{pmatrix} \Phi_n \\ \chi_n \end{pmatrix}. \tag{2.119}$$

The matrix elements of the full Hamiltonian can be expressed as,

$$H_{mn} = \delta_{mn}\varepsilon_n + \left\langle m\right| H_{soc} \left|n\right\rangle. \tag{2.120}$$

To incorporate the spin orbit coupling into the semi-relativistic calculation, the second variation procedure is implemented, involving three steps: i. obtain the eigenfunctions of semi-relativistic Hamiltonian H_{semi}; ii.diagonalized the fully relativistic Hamiltonian obtained from Eq. 2.120 with variational method; iii. obtain the eigenfunctions of the diagonalized relativistic Hamiltonian. This approximation is also called *scalar relativistic* approach, in which the SOC effect on the radial part of wave functions is neglected for the valance electron [86, 87].

2.3.3 Full-potential linearized augmented plane wave

In our calculation, the actual implementation of DFT with LSD approximation is achieved by employing the highly precise full-potential linearized augmented plane wave (FLAPW) method [88–90]. The “full-potential” means no shape approximation is made for the density or potential.

In the FLAPW method, the real space is partitioned into spherical regions around each atom (denoted as the α-th atom), the so called "muffin-tin" (MT), and the interstitial region between the atomic spheres (Fig. 2.3). In the spherical region, the basis functions are products of radial functions and spherical harmonics, and in the interstitial region plane waves are used as solutions of the single-particle Kohn-Sham equation.

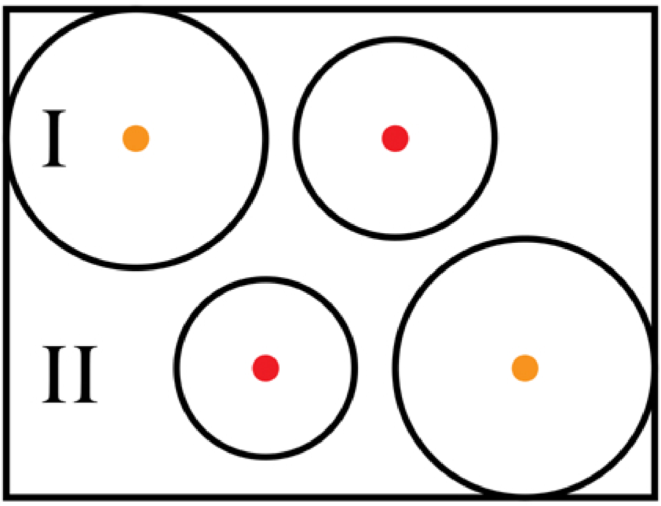

Figure 2.3: Schematic plot of real space partition in FLAPW basis. The real space of the model is partitioned into atomic spheres (MT spheres) (I) and the interstitial region (II). The red and yellow circles represent nucleus of atoms (α) placed at the center of MT spheres.

The FLAPW basis functions are

$$\Psi_{\boldsymbol{K}}(\boldsymbol{r}) = \begin{cases} \Omega^{-1/2} e^{i\boldsymbol{K}\cdot\boldsymbol{r}} & \text{interstitial} \\ \sum_{lm} \left[A^{\alpha}_{lm} u(E_l, r) + B^{\alpha}_{lm} \dot{u}(E_l, r) \right] Y_{lm}(\hat{r}) & \alpha\text{-th MT sphere} \end{cases} \tag{2.121}$$

where Ω is the volume per unit cell, Y_{lm} is spherical harmonics, and the radial function $u(E_l, r)$ is the solution of of the radial Schrödinger equation solved at a fixed energy E_l inside each MT sphere,

$$\frac{1}{2r}\frac{d^2}{dr^2}[ru_l(r)] - \frac{l(l+1)}{2r^2}u_l(r) + [E_l - v_eff r]u_l(r) = 0, \tag{2.122}$$

The its energy derivative $\dot{u}(E_l, \boldsymbol{r})$ satisfies

$$\frac{1}{2r}\frac{d^2}{dr^2}[r\dot{u}_l(r)] - \frac{l(l+1)}{2r^2}\dot{u}_l(r) + [E_l - v_e f f r]\dot{u}_l(r) + u_i(r) = 0, \tag{2.123}$$

where $v_{eff}(r)$ is the spherical component of the effective potential. The coefficients A^{α}_{lm} and B^{α}_{lm} are determined by enforcing continuity of value and the first order radial derivative of the plane waves at the boundary of the α-th MT spheres.

With the FLAPW basis set as given in Eq. 2.122, the single-particle wave functions are determined by solving the secular equation

$$\sum_{\boldsymbol{G}'} \left[H_{\boldsymbol{G},\boldsymbol{G}'} - \varepsilon_i(\boldsymbol{k})O_{\boldsymbol{G},\boldsymbol{G}'}\right] C^i_{\boldsymbol{G}'} = 0, \tag{2.124}$$

where $H_{\boldsymbol{G},\boldsymbol{G}'}$ is the Hamiltonian matrix in the Kohn-Sham equation and $O_{\boldsymbol{G},\boldsymbol{G}'}$ is the overlap matrix,

$$O_{\boldsymbol{G},\boldsymbol{G}'} = \int d\boldsymbol{r}\Psi^*_{\boldsymbol{k},\boldsymbol{G}}(\boldsymbol{r})\Psi_{\boldsymbol{k},\boldsymbol{G}'}.(\boldsymbol{r}). \tag{2.125}$$

The important advantage of the LAPW method over the traditional augmented plane wave (APW) method is that the Hamiltonian and the overlap matrix in Eq. 2.124 are energy independent, which permits the simultaneous determination of the eigenvalues and eigenfuctions within a single diagonalization [91]. The estimated error due to the linearization is of order $(E - E_l)^2$ for the radial function and $\mathcal{O}((E - E_l)^4)$ for the energy [92, 93].

The electron charge density and effective potential are represented by a “natural” representation in both of the spatial regions. Inside the α-th MT-sphere the charge density and effective potential are expressed as the radial expansion of the lattice harmonics, K_ν,

$$\rho_\alpha(\boldsymbol{r}) = \sum_\nu \rho_\nu(\tau_\alpha)K_\nu(\boldsymbol{r}_\alpha) - Z_\alpha\delta(\boldsymbol{r}_\alpha), \tag{2.126}$$

where Z_α is the total charge of the α-th nucleus and the lattice harmonics are defined to satisfy local symmetry of the a α-th atom,

$$K_\nu(\boldsymbol{r}_\alpha) = \sum_m c^\alpha_{\nu,m}Y_{lm}(\boldsymbol{r}_\alpha), \tag{2.127}$$

and satisfy the orthogonality condition for ν,

$$\int d\Omega K_{\nu}(\boldsymbol{r}_{\alpha})K_{\nu'}(\boldsymbol{r}_{\alpha}) = \delta_{\nu'\nu}, \tag{2.128}$$

In the interstitial region the charge density and effective potential are expressed in terms of the star function $\Phi_{\boldsymbol{G}_s}$,

$$\rho(\boldsymbol{r}) = \sum_{\boldsymbol{G}_s} \rho_{\boldsymbol{G}_s}\Phi_{\boldsymbol{G}_s}(\boldsymbol{r}), \tag{2.129}$$

where the star functions are constructed to ensure the symmetry of the lattice space operations,

$$\Phi_{\boldsymbol{G}_s}(\boldsymbol{r}) = \frac{1}{N_{op}}\sum_{R} e^{iR\boldsymbol{G}_s\cdot(r-t_R)}, \tag{2.130}$$

where $\{R|\boldsymbol{t}_R\}$ is the space group operation, N_{op} the number of space group operations, and $\boldsymbol{G}_s$ is the star representative reciprocal vector.

The Coulomb potential $v_{coul}(\boldsymbol{r})$ is obtained by solving Poison's equation in each regions through the pseudo-charge method [94] and the effective single-particle potential is constructed by adding the exchange-correlation potential determined by the charge density. The core electrons are treated fully relativistically using the spherical part of the effective potential, whereas the valence electrons are treated with scalar relativistic approximation.

2.3.4 Intrinsic anomalous and spin Hall conductivity

In first principles calculations, the optical conductivity tensor is commonly calculated through the Kubo formula [95]. The anomalous and spin Hall conductivity is the off-diagonal component of the optical conductivity tensor in the static limit [28, 32]. We remind the result of (spin) optical conductivity tensor in Eq. 2.78,

$$\sigma_{ij}^{\alpha}(\omega) = \frac{\hbar}{i}\sum_{n,m}(f(\varepsilon_n) - f(\varepsilon_m))\frac{J_i^{\alpha,nm}J_j^{0,mn}}{(\varepsilon_n - \varepsilon_m + i\eta)(\varepsilon_n - \varepsilon_m + \hbar\omega + i\eta)}, \tag{2.131}$$

where $J_i^{\alpha,nm}$ is the matrix elements of the generalized velocity operator, $\hat{J}_i^{\alpha}(\alpha = 0, 1, 2, 3)$, consisting of the charge current operator, $\hat{J}_i^0$, and the spin current operator polarized along l-direction, $\hat{J}_i^l (l = 1, 2, 3)$.

The definition of charge current is closely related to the velocity operator,

$$\begin{aligned} \hat{J}_i^0 &= -e\hat{v}_i^0, \\ \hat{v}_i^0 &= \hat{v}_i^{can.} + \frac{\hbar}{4m^2c^2}\boldsymbol{\sigma} \times \nabla V(\boldsymbol{r}), \end{aligned} \tag{2.132}$$

where $v_i^{can.}$ is the canonical velocity operator determined by the Hamiltonian without SOC, *e.g.*, H_{semi} in Eq. 2.117, and the second term is the anomalous velocity [8] induced by spin orbit interaction. However, in actual calculation, the anomalous term is often neglected, due to its relatively small numerical contribution [96, 97].

Although the definition of spin current still involves controversy for its non-conservation property [35, 98–102], a straightforward definition of spin current is frequently used [36, 103],

$$\begin{aligned} \hat{J}_i^l &= \frac{\hbar}{2}\hat{v}_i^l, \\ \hat{v}_i^l &= \frac{1}{2}\left\{\beta\Sigma_l, \hat{v}_i^0\right\}, \end{aligned} \tag{2.133}$$

where $\hat{\beta}\hat{\Sigma}_l = \rho_3 \otimes \sigma_l$ is the relativistic spin operator [104]. In the non-relativistic limit, the 4 × 4 Dirac matrix reduces to the Pauli form,

$$\hat{v}_i^l = \frac{1}{2}\left\{\sigma_l, \hat{v}_i^0\right\}. \tag{2.134}$$

In this definition, the spin current can be treated as $SU(2)$ current which couples to the non-Abelian gauge field [105]. It is a direct analogy of the charge current which couples to the $U(1)$ Abelian gauge field, *i.e*, the vector potential (see Eq. 2.59).

Based on the definition of generalized velocity above, we rewrite Eq. 2.131 in the static limit,

$$\sigma_{ij}^{\alpha} = e^2\hbar \int_{BZ} \frac{d\boldsymbol{k}}{(2\pi)^3} \sum_{n,m} (f(\varepsilon_n) - f(\varepsilon_m)) \frac{\mathrm{Im}\,\langle n, \boldsymbol{k}| \,\hat{v}_i^{\alpha}\, |m, \boldsymbol{k}\rangle \, \langle m, \boldsymbol{k}| \,\hat{v}_j^0\, |n, \boldsymbol{k}\rangle}{(\varepsilon_n - \varepsilon_m)^2}. \tag{2.135}$$

where $|n, \boldsymbol{k}\rangle$ denotes the eigenstates with specific wave vector $\boldsymbol{k}$ and the total conductivity involves an integration over the first Brillouin zone (BZ).

2.3.5 Berry curvature in Hall effect

The Berry phase [106] is a geometric phase accompanying adiabatic changes of the state vector in the parameter space. The physics of Berry phase related effects have gained great interests, due to its direct link with topological properties of the Bloch bands [107,108]. A prominent manifestation of Berry phase and Berry curvature is the intrinsic AHE in a system with breaking time-reversal symmetry [29,30], *e.g.*, the ferromagnets. The intrinsic AHC in Berry language is

$$\sigma_{ij} = -\frac{e^2}{\hbar}\int_{BZ}\frac{d\boldsymbol{k}}{(2\pi)^3}\sum_n f(\varepsilon_n)\epsilon_{ijl}\Omega_{l,n}(\boldsymbol{k}). \tag{2.136}$$

where $\boldsymbol{\Omega}_n(\boldsymbol{k})$ is the Berry curvature of band n in the reciprocal space. The Berry curvature is obtained from the Berry connection of the Bloch band n in $\boldsymbol{k}$ space, $\boldsymbol{A}_n(\boldsymbol{k}) = i\left\langle n,\boldsymbol{k}\right|\nabla_{\boldsymbol{k}}\left|n,\boldsymbol{k}\right\rangle$,

$$\Omega_{l,n}(\boldsymbol{k}) = \epsilon_{ijl}\partial_{k_i}A_{j,n}(\boldsymbol{k}). \tag{2.137}$$

The equivalence between Eq. 2.135 ($\alpha = 0$) and Eq. 2.136 is easily checked [6,36], by noting the definition of velocity operator in the Bloch Hamiltonian,

$$\hat{\boldsymbol{v}}(\boldsymbol{k}) = \frac{1}{i\hbar}\left[\boldsymbol{r}, H(\boldsymbol{k})\right] = \frac{1}{\hbar}\nabla_{\boldsymbol{k}}H(\boldsymbol{k}). \tag{2.138}$$

Thus, we have

$$\frac{\left\langle n,\boldsymbol{k}\right|\hat{v}_i^0\left|m,\boldsymbol{k}\right\rangle}{(\varepsilon_n-\varepsilon_m)} = \frac{1}{\hbar}\frac{\left\langle n,\boldsymbol{k}\right|\partial_{k_i}H(\boldsymbol{k})\left|m,\boldsymbol{k}\right\rangle}{(\varepsilon_n-\varepsilon_m)} = -\frac{1}{\hbar}\left\langle\, n,\boldsymbol{k}\middle|\partial_{k_i}\middle|m,\boldsymbol{k}\right\rangle. \tag{2.139}$$

The Eq. 2.135($\alpha = 0$) can be rewritten as,

$$\sigma_{ij}^0(\omega) = e^2\hbar\int_{BZ}\frac{d\boldsymbol{k}}{(2\pi)^3}\sum_{n,m}f(\varepsilon_n)$$
$$\mathrm{Im}\frac{\left\langle n,\boldsymbol{k}\right|\hat{v}_i^0\left|m,\boldsymbol{k}\right\rangle\left\langle m,\boldsymbol{k}\right|\hat{v}_j^0\left|n,\boldsymbol{k}\right\rangle - \left\langle n,\boldsymbol{k}\right|\hat{v}_j^0\left|m,\boldsymbol{k}\right\rangle\left\langle m,\boldsymbol{k}\right|\hat{v}_i^0\left|n,\boldsymbol{k}\right\rangle}{(\varepsilon_n-\varepsilon_m)^2}$$

$$
\begin{aligned}
&= \frac{e^2}{\hbar}\int_{BZ}\frac{d\boldsymbol{k}}{(2\pi)^3}\sum_{n,m} f(\varepsilon_n) \\
&\mathrm{Im}\left\{\langle n,\boldsymbol{k}|\,\partial_{k_i}\,|m,\boldsymbol{k}\rangle\,\langle m,\boldsymbol{k}|\,\partial_{k_j}\,|n,\boldsymbol{k}\rangle - \langle n,\boldsymbol{k}|\,\partial_{k_j}\,|m,\boldsymbol{k}\rangle\,\langle m,\boldsymbol{k}|\,\partial_{k_i}\,|n,\boldsymbol{k}\rangle\right\} \\
&= \frac{e^2}{\hbar}\int_{BZ}\frac{d\boldsymbol{k}}{(2\pi)^3}\sum_{n,m} f(\varepsilon_n) \\
&\mathrm{Im}\left\{\partial_{k_i}\,\langle n,\boldsymbol{k}|m,\boldsymbol{k}\rangle\,\langle m,\boldsymbol{k}|\,\partial_{k_j}\,|n,\boldsymbol{k}\rangle - \partial_{k_j}\,\langle n,\boldsymbol{k}|m,\boldsymbol{k}\rangle\,\langle m,\boldsymbol{k}|\,\partial_{k_i}\,|n,\boldsymbol{k}\rangle\right\} \\
&= \frac{e^2}{\hbar}\int_{BZ}\frac{d\boldsymbol{k}}{(2\pi)^3}\sum_{n} f(\varepsilon_n)\mathrm{Im}\left\{\partial_{k_i}\,\langle n,\boldsymbol{k}|\,\partial_{k_j}\,|n,\boldsymbol{k}\rangle - \partial_{k_j}\,\langle n,\boldsymbol{k}|\,\partial_{k_i}\,|n,\boldsymbol{k}\rangle\right\} \\
&= -\frac{e^2}{\hbar}\int_{BZ}\frac{d\boldsymbol{k}}{(2\pi)^3}\sum_{n} f(\varepsilon_n)\partial_{k_i}A_{j,n}(\boldsymbol{k}) - \partial_{k_j}A_{i,n}(\boldsymbol{k}) \\
&= -\frac{e^2}{\hbar}\int_{BZ}\frac{d\boldsymbol{k}}{(2\pi)^3}\sum_{n} f(\varepsilon_n)\Omega_{l,n}(\boldsymbol{k}). \qquad (2.140)
\end{aligned}
$$

Therefore, the Berry curvature can be also written in the Kubo formula as,

$$
\epsilon_{ijl}\Omega_{l,n}(\boldsymbol{k}) = -\hbar^2\sum_{n\neq m}\mathrm{Im}\frac{\langle n,\boldsymbol{k}|\,\hat{v}_i^0\,|m,\boldsymbol{k}\rangle\,\langle m,\boldsymbol{k}|\,\hat{v}_j^0\,|n,\boldsymbol{k}\rangle - \langle n,\boldsymbol{k}|\,\hat{v}_j^0\,|m,\boldsymbol{k}\rangle\,\langle m,\boldsymbol{k}|\,\hat{v}_i^0\,|n,\boldsymbol{k}\rangle}{(\varepsilon_n-\varepsilon_m)^2}. \qquad (2.141)
$$

On the contrary, the spin Hall conductivity can be formulated in non-Abelian Berry curvature in semi-classical theory [109], but it is not equivalent with the so-called spin Berry curvature whose form in Kubo formula is

$$
\epsilon_{ijp}\Omega_{p,n}^{l}(\boldsymbol{k}) = -\hbar^2\sum_{n\neq m}\mathrm{Im}\frac{\langle n,\boldsymbol{k}|\,\hat{v}_i^l\,|m,\boldsymbol{k}\rangle\,\langle m,\boldsymbol{k}|\,\hat{v}_j^0\,|n,\boldsymbol{k}\rangle - \langle n,\boldsymbol{k}|\,\hat{v}_j^l\,|m,\boldsymbol{k}\rangle\,\langle m,\boldsymbol{k}|\,\hat{v}_i^0\,|n,\boldsymbol{k}\rangle}{(\varepsilon_n-\varepsilon_m)^2}. \qquad (2.142)
$$

The terminology of spin Berry curvature is widely used in the band analysis of first principle results on intrinsic spin Hall effect [110–112]. It should note that the spin Berry curvature is not a geometric curvature of specific band, since the band summation over $n \neq m$ does not vanish like the case in Berry curvature. Note that the unit of Berry curvature and spin Berry curvature are length^2, where we adapt the $\mathring{A}^2$ in this dissertation.

2.A Appendix: The second quantization

In the second quantization formalism, a quantum mechanical basis is described by an abstract state constructed from a complete set of single-particle states. For a N-particle state, the Fock vector is,

$$\left|n_1, n_2, \cdots, n_\alpha, \cdots\right\rangle, \quad \sum_j n_j = N, \tag{2.A.1}$$

where $n_1, n_2, \cdots, n_\alpha$ represent the occupation number on of the $1, 2, \cdots, \alpha$ single particle states, respectively. For fermions, the occupation number n_j is 0 or 1. For bosons, the occupation number n_j can take any non-negative integer. Note that a vacuum exists where all occupation number are zero, $|0\rangle \equiv |n_1 = 0, n_2 = 0, \cdots, n_\alpha = 0, \cdots\rangle$.

The *creation*, $c_\alpha^\dagger$, and *annihilation*, c_α, operators are introduced to add or remove the particle of the α-state,

$$\begin{aligned} c_\alpha^\dagger \left|n_1, n_2, \cdots, n_\alpha, \cdots\right\rangle &= \sqrt{n_\alpha + 1}\left|n_1, n_2, \cdots, n_\alpha + 1, \cdots\right\rangle, & (2.A.2)\\ c_\alpha \left|n_1, n_2, \cdots, n_\alpha, \cdots\right\rangle &= \sqrt{n_\alpha}\left|n_1, n_2, \cdots, n_\alpha 1, \cdots\right\rangle. & (2.A.3)\end{aligned}$$

The commutation relation between $c_\alpha^\dagger$ and c_α is,

$$\left[c_i, c_j^\dagger\right]_\eta = \delta_{ij}, \quad \left[c_i, c_j\right]_\eta = \left[c_i^\dagger, c_j^\dagger\right]_\eta = 0, \tag{2.A.4}$$

where $\eta = +1$ represents the anti-commutator for fermion and $\eta = -1$ represents the commutator for boson.

The field creation (annihilation) operator can be written as summing over all single particle wave functions,

$$\begin{aligned} \psi^\dagger(\boldsymbol{r}) &= \sum_\alpha c_\alpha^\dagger u_\alpha^*(\boldsymbol{r}), & (2.A.5)\\ c_\alpha^\dagger &= \int d\boldsymbol{r}\psi^\dagger(\boldsymbol{r}) u_\alpha(\boldsymbol{r}), & (2.A.6)\end{aligned}$$

where $u_\alpha(\boldsymbol{r})$ is the single particle wave function.

The one-body operator in the second quantization representation is,

$$\begin{aligned} \mathcal{O} &= \int d\boldsymbol{r}\psi^{\dagger}(\boldsymbol{r})\mathcal{O}(\boldsymbol{r})\psi(\boldsymbol{r}) \\ &= \sum_{i,j} o_{ij}c_i^{\dagger}c_j, \end{aligned} \tag{2.A.7}$$

with matrix elements

$$o_{ij} = \int d\boldsymbol{r}u_i^*(\boldsymbol{r})\mathcal{O}(\boldsymbol{r})u_j(\boldsymbol{r}). \tag{2.A.8}$$

For a two body operator, $\frac{1}{2}\sum_{i\neq j}V(\boldsymbol{r}_i-\boldsymbol{r}_j)$, the second quantization representation is

$$\begin{aligned} V &= \int d\boldsymbol{r}\int d\boldsymbol{r}'\psi^{\dagger}(\boldsymbol{r})\psi^{\dagger}(\boldsymbol{r}')\frac{1}{2}V(\boldsymbol{r}-\boldsymbol{r}')\psi(\boldsymbol{r})\psi(\boldsymbol{r}') \\ &= \frac{1}{2}\sum_{i,j,k,l} v_{ijkl}c_i^{\dagger}c_j^{\dagger}c_kc_l, \end{aligned} \tag{2.A.9}$$

with the matrix elements

$$v_{ijkl} = \int d\boldsymbol{r}\int d\boldsymbol{r}'u_i^*(\boldsymbol{r})u_j^*(\boldsymbol{r}')V(\boldsymbol{r}-\boldsymbol{r}')u_k(\boldsymbol{r})u_l(\boldsymbol{r}'). \tag{2.A.10}$$

Now, we consider a general Hamiltonian,

$$\mathcal{H} = \sum_i H(\boldsymbol{r}_i) + \frac{1}{2}\sum_{i\neq j}V(\boldsymbol{r}_i-\boldsymbol{r}_j). \tag{2.A.11}$$

where $H(\boldsymbol{r}_i)$ is a single particle Hamiltonian of a particle at $\boldsymbol{r}_i$ and $V(\boldsymbol{r}_i-\boldsymbol{r}_j)$ is the interaction term between particles at $\boldsymbol{r}_i$ and $\boldsymbol{r}_j$.

The second quantization Hamiltonian in matrix form is,

$$\mathcal{H}_{2nd} = \sum_{i,j} h_{ij}c_i^{\dagger}c_j + \frac{1}{2}\sum_{i,j,k,l} v_{ijkl}c_i^{\dagger}c_j^{\dagger}c_kc_l, \tag{2.A.12}$$

with the matrix elements h_{ij} and v_{ijkl} defined as,

$$h_{ij} = \int d\boldsymbol{r}u_i^*(\boldsymbol{r})H(\boldsymbol{r})u_j(\boldsymbol{r}), \tag{2.A.13}$$

$$v_{ijkl} = \int d\boldsymbol{r}\int d\boldsymbol{r}'u_i^*(\boldsymbol{r})u_j^*(\boldsymbol{r}')V(\boldsymbol{r}-\boldsymbol{r}')u_k(\boldsymbol{r})u_l(\boldsymbol{r}'). \tag{2.A.14}$$

2.B Appendix: Pictures of time evolution

The time evolution of state vectors and operators in quantum mechanics are always expressed in three different pictures: *Schrödinger picture*; *Heisenberg picture*; *Interaction picture*. To articulate the difference among these representations, we assume a simple Hamiltonian,

$$\hat{H} = \hat{H}_0 + \hat{H}_{int}, \tag{2.B.1}$$

where $\hat{H}_0$ is the stationary Hamiltonian and $\hat{H}_{int}$ represents the interaction.

a. *Schrödinger picture*

The *Schrödinger picture* of time evolution directly originates from the Schrödinger equation, whose solution is the state vector,

$$\begin{aligned} i\hbar\partial_t \left|\Psi_S\right\rangle &= \hat{H}\left|\Psi_S\right\rangle, & (2.B.2)\\ \left|\Psi_S(t)\right\rangle &= e^{-i\hat{H}(t-t_0)/\hbar}\left|\Psi_S(t_0)\right\rangle. & (2.B.3)\end{aligned}$$

where t_0 is an assumptive initial time.

Apparently, the state vector evolves with time. Consequently, the operator is time-independent,

$$\hat{O}_S(t) = \hat{O}_S(t_0) = \hat{O}. \tag{2.B.4}$$

b. *Heisenberg picture*

In the *Heisenberg picture*, the state vector is forced to be time-independent,

$$\left|\Psi_H\right\rangle = e^{i\hat{H}t/\hbar}\left|\Psi_S(t)\right\rangle, \tag{2.B.5}$$

where the Heisenberg state vector is obtained by tracing Schrödinger state vector back to the initial time.

To keep the matrix elements of a given operator invariant, we have,

$$\left\langle\Psi'_S(t)\right|\hat{O}\left|\Psi_S(t)\right\rangle = \left\langle\Psi'_H\right| e^{i\hat{H}t/\hbar}\hat{O}e^{-i\hat{H}t/\hbar}\left|\Psi_H\right\rangle. \tag{2.B.6}$$

The operator in the *Heisenberg picture* evolves with time,

$$\hat{O}_H(t) = e^{i\hat{H}t/\hbar}\hat{O}e^{-i\hat{H}t/\hbar}. \tag{2.B.7}$$

c. *Interaction picture*

In the *interaction picture*, both states and operators evolve with time. The state vector is defined as,

$$|\Psi_I(t)\rangle = e^{i\hat{H}_0 t/\hbar}\,|\Psi_S(t)\rangle\,, \tag{2.B.8}$$

where $\hat{H}_0$ is the stationary Hamiltonian.

The equation of motion of the states in the *interaction picture* is,

$$\begin{aligned} i\hbar\partial_t\,|\Psi_I(t)\rangle &= -\hat{H}_0 e^{i\hat{H}_0 t/\hbar}\,|\Psi_S(t)\rangle + i\hbar e^{i\hat{H}_0 t/\hbar}\partial_t\,|\Psi_S(t)\rangle \\ &= e^{i\hat{H}_0 t/\hbar}\hat{H}_{int}e^{-i\hat{H}_0 t/\hbar}\,|\Psi_I(t)\rangle \\ &= \hat{H}_{int}(t)\,|\Psi_I(t)\rangle\,, \end{aligned} \tag{2.B.9}$$

with $H_{int}(t) \equiv e^{i\hat{H}_0 t/\hbar}H_{int}e^{-i\hat{H}_0 t/\hbar}$.

The state vector in the *interaction picture* evolves with time under the interaction Hamiltonian.

Similar to Eq. 2.B.6, we have,

$$\langle\Psi'_S(t)|\,\hat{O}\,|\Psi_S(t)\rangle = \langle\Psi'_I(t)|\,e^{i\hat{H}_0 t/\hbar}\hat{O}e^{-i\hat{H}_t/\hbar}\,|\Psi_I(t)\rangle\,. \tag{2.B.10}$$

The operator in the *interaction picture* is,

$$\hat{O}_I(t) = e^{i\hat{H}_0 t/\hbar}\hat{O}e^{-i\hat{H}_0 t/\hbar}. \tag{2.B.11}$$

d. Time evolution operator

For a time-independent Hamiltonian, *e.g.*, Eq. 2.B.1, the time evolution operator is simply defined as,

$$\hat{U}(t,t_0) \equiv e^{-i\hat{H}(t-t_0)/\hbar}. \tag{2.B.12}$$

In the *interaction picture*, the operator evolves with time governed by the non-interacting Hamiltonian. Thus the time evolution operator of operators in the *interaction picture* is,

$$\hat{U}_0(t, t_0) \equiv e^{-i\hat{H}_0(t-t_0)/\hbar}. \tag{2.B.13}$$

The time evolution of the state vector in the *interaction picture* is governed by Eq. 2.B.9. The solution is the time evolution operator [113] with interaction Hamiltonian,

$$\hat{U}_I(t, t_0) = \exp\Big(-\frac{i}{\hbar}\mathcal{T}\int_{t_0}^{t} dt'\hat{H}_I(t')\Big), \tag{2.B.14}$$

where $\mathcal{T}$ is the time-ordering operator.

The time evolution of state vector in the *interaction picture* is,

$$|\Psi_I(t)\rangle = U_I(t, t_0)\,|\Psi_I(t_0)\rangle\,. \tag{2.B.15}$$

Chapter 3

Symmetry reduction of spin Berry curvature

Contents

3.1 Introduction

Recent experimental results have shown that a significant spin Hall current emerges from $3d$ transition-metal ferromagnets, despite its relatively small SOC compared to heavy metals [114]. Thus, understanding the mechanism of spin current generation in ferromagnets is of high importance and can provide a new perspective of material search for large spin Hall effect in the absence of heavy elements. In addition, Omori *et al.* argued that the skew scattering contribution to AHE and SHE have strong correlation with the spin populations but they might not be correlated in the intrinsic and side jump contributions, based on their analysis on temperature dependence of SHC [114]. Given the findings of these relationship between AHE and SHE in ferromagnetic materials, we investigate the intrinsic AHE and SHE in ferromagnets simultaneously to provide a direct comparison.

In this chapter, we study the intrinsic AHC and SHC in ferromagnetic L1_0-CoPt *via* first principles calculations. We identify the symmetry of the Berry curvature and the spin Berry curvature to study the relationship between the AHC and SHC. The Berry curvature preserves the C_{4v} crystal rotation symmetry along the c-axis, in accordance with the crystal symmetry, but the symmetry of the spin Berry curvature is reduced to C_{2v}. The symmetry reduction is most notable at anti-crossing points where the Bloch states have opposite spin characters. We show that the symmetry reduction of the spin Berry curvature originates from the difference in the interband matrix elements of velocity and the spin current operators at such crossing points. We also employ a simple model Hamiltonian to show that such symmetry reduction of spin Berry curvature is a common feature in the ferromagnets. The difference in the symmetry of Berry curvature and spin Berry curvature implies the intrinsic AHC and SHE are not correlated, especially at the anti-crossings with opposite spin states, which explains the disrelation between AHE and SHE in the intrinsic regime of ferromagnets [114].

3.2 First principles calculations on ferromagnetic $L1_0$-CoPt

3.2.1 Crystal symmetry and Band structure

The $L1_0$-CoPt compound is a typical ferromagnetic material in tetragonal phase with space group $P4/mmm$ (123). The chemically ordered $L1_0$-phase ferromagnets usually have magnetic easy-axis along the [001] direction, *i.e.* the c-axis (Fig.3.1(b)), with large uniaxial magnetic anisotropy energy [115]. Hence, the crystal structure and electronic structure exhibit four-fold rotation symmetry (C_{4v}) around the c-axis. The irreducible first Brillouin zone is a triangular prism surrounded by Γ-X-M-Z-R-N (Fig.3.1(a)).

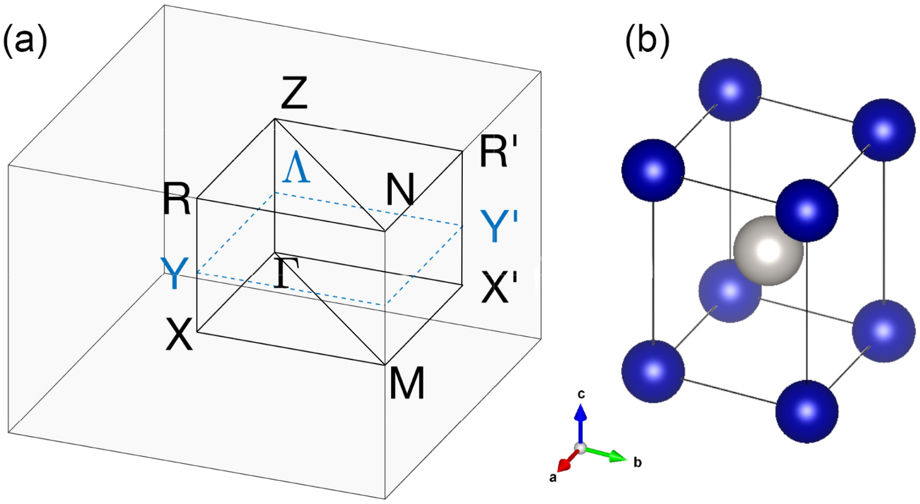

Figure 3.1: Crystal structure and first Brillouin zone of $L1_0$-CoPt. (a)First Brillouin zone and (b) primitive cell of $L1_0$-CoPt compound.

The band structure near the Fermi level is plotted along the high symmetry path of the irreducible first Brillouin zone together with. the Berry curvature (Ω^{00}_{yx}) and the spin Berry curvature (Ω^{30}_{yx}). The peak-valley of Berry curvature and spin Berry curvature in the reciprocal space give the largest contribution to AHC and SHC, which usually coincides with avoided band crossings (anti-crossings) near the Fermi level [32] (Fig.3.2). The small band gaps are opened by the spin orbit interaction at these anti-crossing points. Particularly, we observe a major peak-valley of Ω^{00}_{yx} and Ω^{30}_{yx} in the Γ-X line.

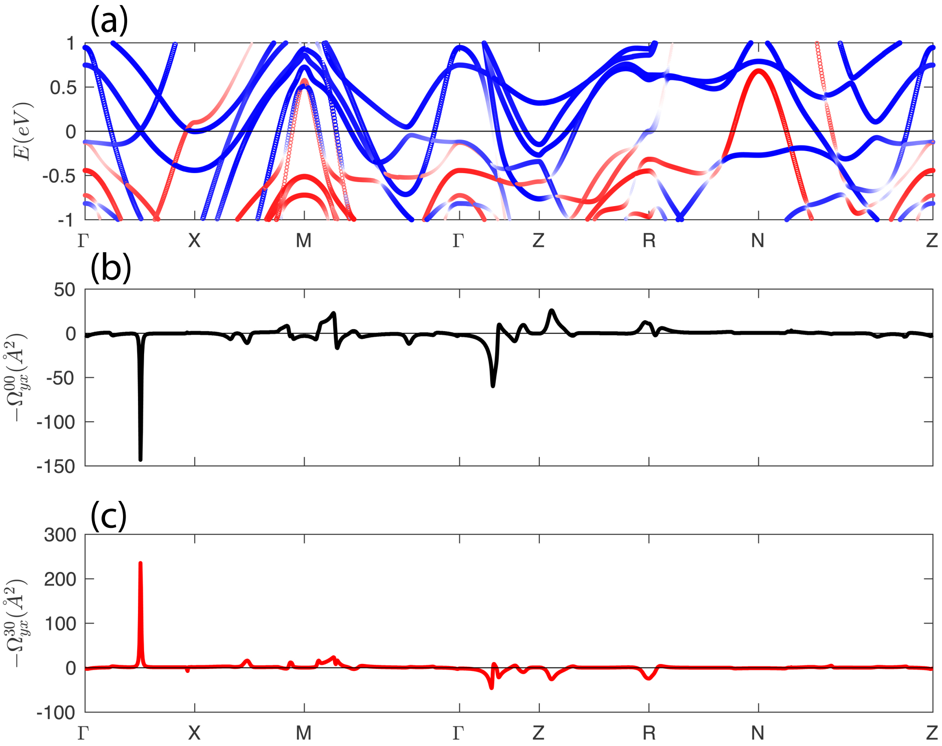

Figure 3.2: Band structure, Berry curvature and spin Berry curvature of CoPt. (a) Band structure, (b) the Berry curvature (Ω^{00}_{yx}) , and (c) the spin Berry curvature (Ω^{30}_{yx}) of L1_0-CoPt along a high symmetry k-path. The bands are colored by its spin characters: majority (red) and minority (blue). The Ω^{00}_{yx} and Ω^{30}_{yx} are in the unit of $\mathring{A}^2$ (length^2).

3.2.2 Symmetry reduction of spin Berry curvature

We first present the stereoscopic projection of the Berry curvature and the spin Berry curvature in the first Brillouin zone (Fig.3.3). Clearly, the Berry curvature follows the symmetry of the crystal structure (band structure) and is symmetric under all symmetry operations of space group $P4/mmm$. On the contrary, the spin Berry curvature has a reduced symmetry group $Pmmm$, only reflecting the spatial inversion symmetry $\Omega^{30}_{yx}(\boldsymbol{k}) = \Omega^{30}_{yx}(-\boldsymbol{k})$. Additionally, we find the symmetry reduction of spin Berry curvature is not homogenous in the reciprocal space. For example in Fig.3.3(d), the inner circle of Ω^{30}_{yx} seems to be C_{4v} symmetric but the outer circle of that is distinctively C_{2v} symmetric. After integrating the whole first Brillouin zone, the σ^{00}_{yx} and σ^{30}_{yx} from the first principles calculations are -3 S/cm and $787(\frac{\hbar}{e})$ S/cm, respectively.

To clearly present the symmetry of the Berry curvature and the spin Berry curvature for comparison, we plot the corresponding quantities in the Γ-X-M plane (Fig.3.4) where large peak/valleys of Ω^{00}_{yx} and Ω^{30}_{yx} are found. A clear distinction of their symmetry is

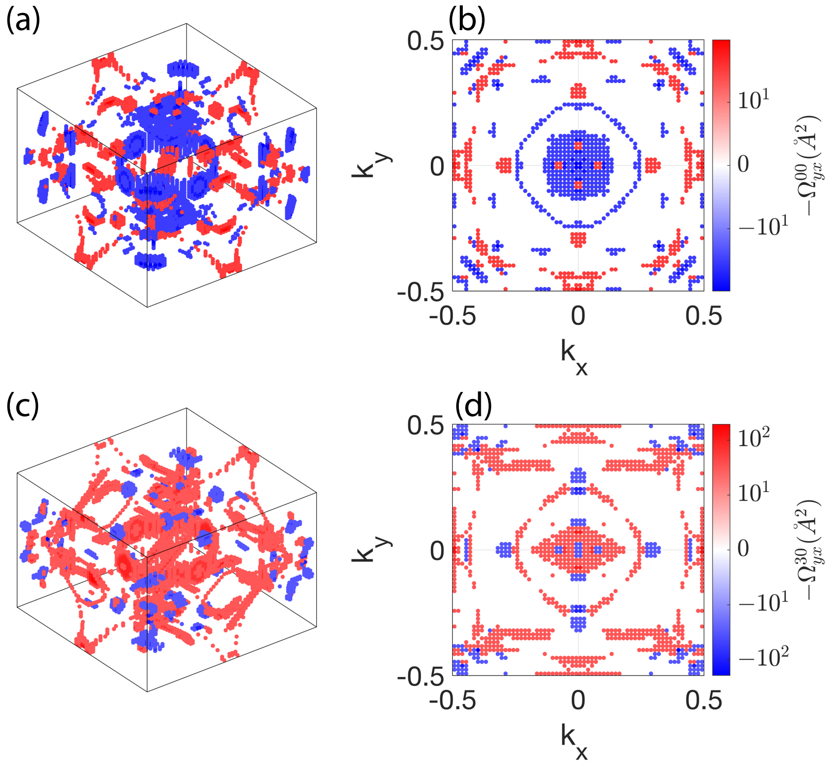

Figure 3.3: Stereoscopic projection of Berry curvature and spin Berry curvature of CoPt. Isometric view (a,c) and top view from the (001) direction (b,d) of Ω_{yx}^{00} (c,d) and Ω_{yx}^{30} (e,f)mapping inside the entire first Brillouin zone. The Ω_{yx}^{00} and Ω_{yx}^{30} are in the unit of $\mathring{A}^2$ (length^2).

observed at the symmetric points in the reciprocal space, *e.g.*, A and A′ and B and B′. The Berry curvature exhibits a C_{4v} rotation symmetry along the c-axis and follows the symmetry of band structure, which can be easily checked by comparing these counterpart points in the reciprocal space. However, the spin Berry curvature exhibits a reduced symmetry, *i.e.*, C_{2v} rotation symmetry along c-axis. For example, the A and A′ points show similar magnitude of Ω_{yx}^{30}, but B and B′ are significantly asymmetric with even opposite sign.

3.2.3 Band analysis on symmetry reduction of Ω_{yx}^{30}

The A and A′ points in Fig. 3.4 correspond the largest peak-valley of $\Omega_{yx}^{00}, \Omega_{yx}^{30}$ in the Γ-X line (Fig. 3.2 (b,c)), characterized by an anti-crossing bands with the same spin (minority spin for A and A′). The B and B′ points correspond a small peak-valley near X point, characterized by an anti-crossing of bands with the opposite spin. We find the

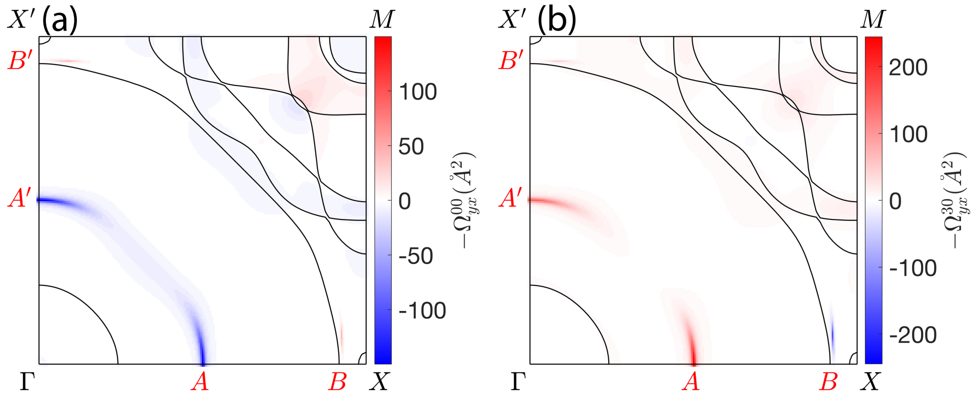

Figure 3.4: Berry curvature and spin Berry curvature in (001) plane. (a) Ω^{00}_{yx} and (b) Ω^{30}_{yx} mapping on the (001) plane in a quarter of the Brillouin zone represented by the colors. The Ω^{00}_{yx} and Ω^{30}_{yx} are in the unit of$\mathring{A}^2$ (length^2).

prominence of the symmetry reduction is closely related to the spin character of anti-crossings. Hence, we categorize the anti-crossings into two classes for further discussion: *Class I* associated with the same spin; and *Class II* associated with the opposite spin.

For *Class I* anti-crossings (A and A′), the spin of the Bloch states are predominantly polarized along the quantization axis (*i.e.*, along the z-direction) near the crossing points. The matrix elements of the generalized velocity $\hat{v}^{0,3}_i$ (see Appendix. 3.A) approximately follow the relation $\hat{v}^3_i \sim s_z \hat{v}^0_i$, where s_z is the expectation value of the z-component of electron spin of the two bands. Hence, Ω^{30}_{yx} is approximately the product of Ω^{00}_{yx} and the average expectation value of s_z. This can also be considered as a two-current model, in which Ω^{00}_{yx} and Ω^{30}_{yx} can be decomposed into majority and minority spin components.

For *Class II* anti-crossings (B and B′ points), the spin character of these Bloch states at the crossing point is a mixture of majority and minority spins. In such cases, a clear symmetry reduction of spin Berry curvature (Ω^{30}_{yx}) is observed: Ω^{30}_{yx} is positive at the B point (0.43,0,0) and negative at the crystallographically identical B′ point (0,0.43,0). The Berry curvature (Ω^{00}_{yx}), in contrast, is exactly the same for both B and B′ points.

To assess the symmetry reduction of spin Berry curvature in a quantitative way, we present plots of Ω^{00}_{yx} and Ω^{30}_{yx} along a selected symmetric path (Fig. 3.5), X-Γ-X′. (X′ is the rotationally symmetric point of X with respect to the [001] axis.) The band structure and spin character are exactly symmetric with respect to the Γ point as expected (Fig. 3.5(a)). For Ω^{00}_{yx} we confirm that all peaks and valleys hold identical values across the Γ point (Fig. 3.5(c)). In contrast, the magnitude, and in some cases, the sign of the peaks of Ω^{30}_{yx}

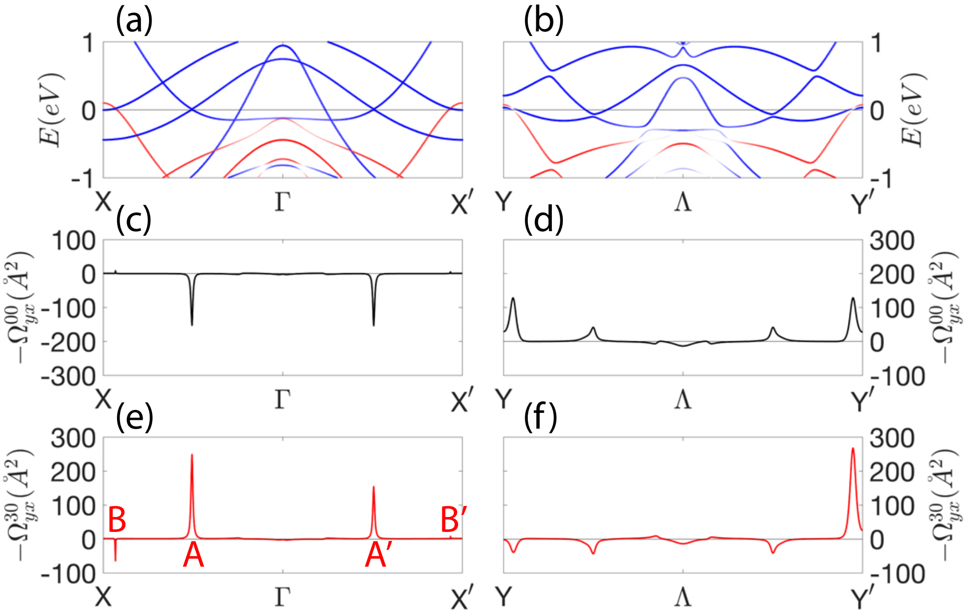

Figure 3.5: Band analysis with spin character of the Bloch states. (a,b) The Band structure along selected symmetric k-paths X(0.5,0,0)-Γ(0,0,0)-X'(0,0.5,0) and Y(0,0.5,0.162)-Λ(0.5,0.5,0.162)-Y'(0.5,0,0.162). The bands are color-coded with its spin character: majority (red), minority (blue). (c-f) Corresponding Berry curvature (c,d) and spin Berry curvature (e,f) along the selected k-paths. The Ω^{00}_{yx} and Ω^{30}_{yx} are in the unit of $\AA^2$ (length^2).

(Fig. 3.5(e)) across the Γ point are different. For example, Ω^{30}_{yx} at the B′ point is nearly zero whereas it is negative at the B point. The reason that Ω^{00}_{yx} and Ω^{30}_{yx} at the B and B′ points are relatively weak in magnitude is due to the fact that the gap opening occurs at an energy level that is far from the Fermi level (comparing with A and A′).

To show the asymmetry of Ω^{30}_{yx} more clearly, we plot another selected symmetric path, Y-Λ-Y′ (Figs. 3.5(b,d,f)), paralleled with the X-Γ-X′ path but with shifted by $k_z = 0.162$. In this path, the Fermi level lies exactly within the gap of bands crossed at B and B′ points. Whereas the band structure (Fig. 3.5(b)) and Ω^{00}_{yx} (Fig. 3.5(d)) are symmetric with respect to the Γ point, Ω^{30}_{yx} exhibits a significant asymmetry: The largest asymmetry is observed near the Y and Y′ points.

In summary, we find that the largest asymmetry of Ω^{30}_{yx} occurs where a pair of bands with opposite spin characters (*Class II*) crosses the Fermi level. Here the spin of the Bloch states are not parallel to the spin quantization axis (z-axis). For pair of bands with the same spin character, the asymmetry of Ω^{30}_{yx} at crystallographically equivalent points is almost negligible.

3.3 Origin of the symmetry reduction of spin Berry curvature

3.3.1 Symmetry analysis on the Kubo formula

In this section, we analyze the symmetry of the Berry curvature and the spin Berry curvature, starting from the Kubo formula,

$$\Omega^{\alpha 0}_{ij,n}(\boldsymbol{k}) = -\hbar^2 \sum_{n' \neq n} \frac{\mathrm{Im}\Big[[v^{\alpha}_{i}]_{n,n'}(\boldsymbol{k})[v^{0}_{j}]_{n',n}(\boldsymbol{k}) - [v^{0}_{j}]_{n,n'}(\boldsymbol{k})[v^{\alpha}_{i}]_{n',n}(\boldsymbol{k})\Big]}{\Big(\epsilon_n(\boldsymbol{k}) - \epsilon_{n'}(\boldsymbol{k})\Big)^2}. \tag{3.1}$$

where $[v^{\alpha}_{i}]_{n',n}(\boldsymbol{k}) = \langle \boldsymbol{k}, n' | \, \hat{v}^{\alpha}_{i} \, | \boldsymbol{k}, n \rangle$ is the matrix element of the generalized velocity operator $\hat{v}^{\alpha}_{i}$ evaluated with a Bloch state with a wave vector $\boldsymbol{k}$. For a Hamiltonian having a C_{4v} symmetry around the z-axis, the global rotation operator on a spinor reads,

$$|\boldsymbol{\Lambda k}, n\rangle = D(\boldsymbol{\Lambda}) \, |\boldsymbol{k}, n\rangle \, , \tag{3.2}$$

where $D(\boldsymbol{\Lambda}) = \exp(i\vec{\theta}\cdot\vec{\sigma}/2)$. The direction and magnitude of $\vec{\theta}$ define the axis and amount of rotation, respectively. The Pauli matrix $\vec{\sigma}$ is the generator of the $SU(2)$ group. We define $\boldsymbol{\Lambda} = \exp(i\vec{\theta} \cdot \vec{J})$, where $\vec{J}$ is the generator of the $SO(3)$ group.

Since the crystal structure of CoPt preserves a C_{4v} rotation symmetry around the z-axis, the Bloch states are both invariant under C_{4v} rotation. However, the generalized velocity matrix element is not invariant. Using the identities $D^{\dagger}(\boldsymbol{\Lambda})\sigma_i D(\boldsymbol{\Lambda}) = \Lambda_{ij}\sigma_j$ and $\partial_{\boldsymbol{\Lambda k}} = \dfrac{\partial_{\boldsymbol{\Lambda k}}}{\partial_{\boldsymbol{k}}}\partial_{\boldsymbol{k}} = \boldsymbol{\Lambda}\partial_{\boldsymbol{k}}$, the matrix elements of the velocity and the spin current operators can be written as:

$$[v^{0}_{i}]_{n',n}(\boldsymbol{\Lambda k}) = \Lambda_{ij}[v^{0}_{j}]_{n',n}(\boldsymbol{k}), \tag{3.3}$$

$$[v^{l}_{i}]_{n',n}(\boldsymbol{\Lambda k}) = \Lambda_{ij}\Lambda_{lp}[v^{p}_{j}]_{n',n}(\boldsymbol{k}). \tag{3.4}$$

Under C_{4v} rotation, the (spin) Berry curvature (Eq. 3.1) obey the following relations:

$$\Omega^{00}_{ij,n}(\boldsymbol{\Lambda k}) = \Lambda_{ir}\Lambda_{js}\Omega^{00}_{rs,n}(\boldsymbol{k}), \tag{3.5}$$

$$\Omega^{l0}_{ij,n}(\boldsymbol{\Lambda k}) = \Lambda_{ir}\Lambda_{js}\Lambda_{lp}\Omega^{p0}_{rs,n}(\boldsymbol{k}). \tag{3.6}$$

Substituting $\theta = (0, 0, \frac{\pi}{2})$ in Eq. 3.5 and Eq. 3.6, *i.e.* $\boldsymbol{\Lambda} = \exp(i\frac{\pi}{2}J_3)$, we find $\Omega^{00}_{yx,n}(\boldsymbol{\Lambda k}) = -\Omega^{00}_{xy,n}(\boldsymbol{k}) = \Omega^{00}_{yx,n}(\boldsymbol{k})$ for the Berry curvature and $\Omega^{30}_{yx,n}(\boldsymbol{\Lambda k}) = -\Omega^{30}_{xy,n}(\boldsymbol{k}) = \Omega^{03}_{yx,n}(\boldsymbol{k})$ for the spin Berry curvature. The last equality of each equation derives from the general relation $\Omega^{\alpha 0}_{ij,n} = -\Omega^{0\alpha}_{ji,n}$. Since $\Omega^{00}_{yx,n}(\boldsymbol{\Lambda k}) = \Omega^{00}_{yx,n}(\boldsymbol{k})$, the Berry curvature preserves the C_{4v} symmetry. For spin Berry curvature, noting that $\Omega^{03}_{yx,n}$ is not necessarily equal to $\Omega^{30}_{yx,n}$ at all k points (see Figs. 3.9(c) and (d)), $\Omega^{30}_{yx,n}(\boldsymbol{\Lambda k}) \neq \Omega^{30}_{yx,n}(\boldsymbol{k})$ and the C_{4v} symmetry is broken. Therefore, the symmetry reduction of the spin Berry curvature originates from the difference between the velocity and the spin velocity operators, while for the Berry curvature the two velocity operators are exchangeable.

3.3.2 Velocity and spin velocity operators

To investigate the difference in matrix elements, we consider a general form of the velocity and the spin velocity operators. Taking into account contribution from the SOC, $\hat{v}^0_i$ and $\hat{v}^l_i$ are expressed as

$$\hat{v}^0_i = \frac{1}{\hbar}\frac{\partial \hat{\mathcal{H}}_0}{\partial k_i}\hat{I} + \frac{\hbar}{4m^2c^2}\epsilon_{ijk}\hat{\sigma}^j\frac{\partial \hat{V}(\boldsymbol{r})}{\partial r_k}, \tag{3.7}$$

$$\hat{v}^3_i = \frac{1}{\hbar}\frac{\partial \hat{\mathcal{H}}_0}{\partial k_i}\hat{\sigma}^3 + \frac{\hbar}{4m^2c^2}\epsilon_{i3k}\frac{\partial \hat{V}(\boldsymbol{r})}{\partial r_k}\hat{I}. \tag{3.8}$$

where $\hat{\mathcal{H}}_0$ is the kinetic energy, $\hat{V}(\boldsymbol{r})$ is the atomic potential energy, ϵ_{ijk} is the *Levi-Civita* symbol, m, $\hbar$ and c are the electron mass, the reduced Planck constant and the speed of light, respectively. The second term of the right hand sides of Eq. 3.7 and Eq. 3.8 are induced by the effect of SOC, which is commonly referred to as the anomalous velocity [8]. This term, however, is often neglected in first principles calculations, including the results presented above, since its contribution is in general negligible compared to that of the first term (*i.e.*, the canonical velocity [96]).

We drop off the anomalous velocity term in evaluating the matrix elements of the velocity and the spin current operators. Using a generic spinor $|\chi\rangle$ ($|\chi'\rangle$) for Bloch state n (n'), the matrix elements reads

$$[v^0_j]_{n,n'}(\boldsymbol{k}) = \langle\chi|\, v_0\hat{I}\,|\chi'\rangle\,, \tag{3.9}$$

$$[v^3_j]_{n,n'}(\boldsymbol{k}) = \langle\chi|\, v_0\hat{\sigma}_3\,|\chi'\rangle\,, \tag{3.10}$$

where $v_0 \equiv \langle \frac{1}{\hbar}\frac{\partial \hat{\mathcal{H}}_0}{\partial k_i} \rangle$ is the spatial part of the interband velocity.

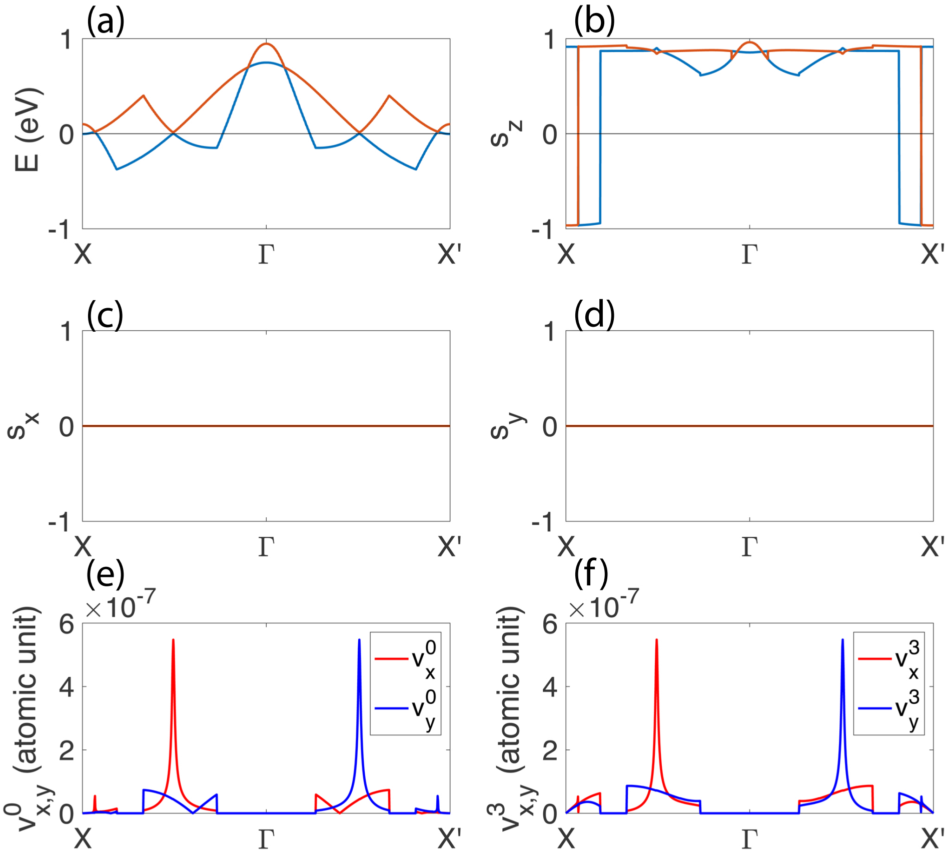

Figure 3.6: Velocity and spin velocity matrix elements of *Class I* anti-crossings. The band dispersion (a) spin components of s_z (b),s_y (c), and s_x (d) of a pair of bands in *Class I* anti-crossing, corresponding to A and A' points. The module of interband velocity (e) and spin velocity (f) matrix elements of the crossings band. The $s_i \equiv \langle n, \boldsymbol{k} | \sigma_i | n, \boldsymbol{k} \rangle$ is the spin component of Bloch states $|n, \boldsymbol{k}\rangle$ along $i = x, y, z$ direction.

For *Class I* anti-crossings, the spinor of the two bands are near parallel, that is, $|\chi\rangle = \begin{bmatrix} \cos\frac{\theta}{2} e^{-i\frac{\varphi}{2}} \\ \sin\frac{\theta}{2} e^{i\frac{\varphi}{2}} \end{bmatrix}$ and $|\chi'\rangle \sim |\chi\rangle$, where θ and φ represent the polar and azimuthal angles of the corresponding spinor. The matrix elements in Eqs. 3.9 and 3.10 are expressed as:

$$[v^0_j]_{n,n'}(\boldsymbol{k}) \sim v_0, \tag{3.11}$$

$$[v^3_j]_{n,n'}(\boldsymbol{k}) \sim v_0 \cos\theta. \tag{3.12}$$

The spin directions of the Bloch states are aligned along the quantization axis (*i.e.* along the z axis) across the crossing point ($\theta = 0$ or π). Consequently, $[v^3_j]_{n,n'}(\boldsymbol{k})$ are identical up to a factor of ±1, depending on the polar angle of the spinors. The magnitude of

$[v_i^0]_{n',n}(\boldsymbol{k})$ and $[v_i^3]_{n',n}(\boldsymbol{k})$ is approximately the same (Fig. 3.6 (e,f)) and the Berry and spin Berry curvatures display nearly the same symmetry for such bands. Thus, we can expect that at *Class I* anti-crossings, the AHC and SHC are highly correlated and are scaled with polarization of Bloch states at the Fermi level, *i.e.*, the spin polarization.

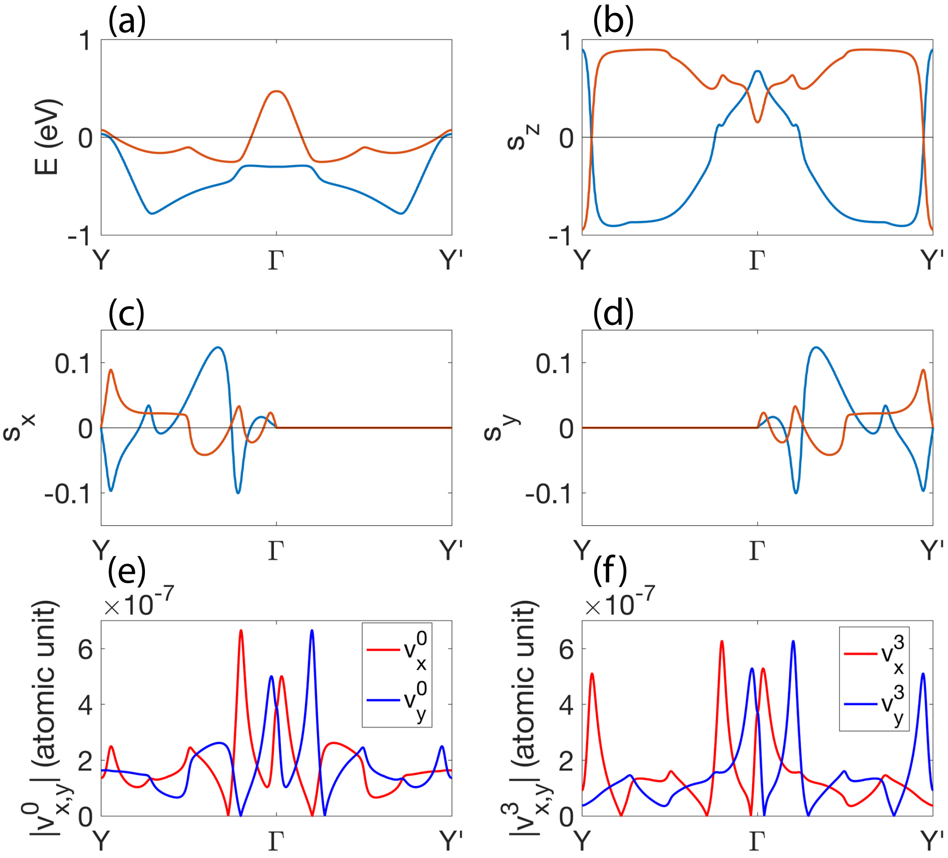

Figure 3.7: Velocity and spin velocity matrix elements of *Class II* anti-crossings. The band dispersion (a) spin components of s_z (b),s_y (c), and s_x (d) of a pair of bands in *Class II* anti-crossing, corresponding to B and B' points. The module of interband velocity (e) and spin velocity (f) matrix elements of the crossings band. The $s_i \equiv \langle n, \boldsymbol{k}| \sigma_i |n, \boldsymbol{k}\rangle$ is the spin component of Bloch states $|n, \boldsymbol{k}\rangle$ along $i = x, y, z$ direction.

In *Class II* anti-crossings, the spinor of the two bands are nearly anti-parallel. Thus $\theta' \sim \pi - \theta, \varphi' \sim \varphi + \pi$ and $|\chi\rangle = \begin{bmatrix} \cos\frac{\theta}{2}e^{-i\frac{\varphi}{2}} \\ \sin\frac{\theta}{2}e^{i\frac{\varphi}{2}} \end{bmatrix}, |\chi'\rangle \sim \begin{bmatrix} -i\sin\frac{\theta}{2}e^{-i\frac{\varphi}{2}} \\ i\cos\frac{\theta}{2}e^{i\frac{\varphi}{2}} \end{bmatrix}$. The matrix elements of the velocity and spin velocity in *Class II* anti-crossings are,

$$[v_j^0]_{n,n'}(\boldsymbol{k}) \sim 0, \tag{3.13}$$

$$[v_j^3]_{n,n'}(\boldsymbol{k}) \sim -2iv_0 \sin\theta. \tag{3.14}$$

It should be noted that the quantity $[v_j^{0,3}]_{n,n'}(\boldsymbol{k})$ is gauge dependent with an arbitrary phase factor $e^{i(\alpha_n-\alpha_{n'})}$. But the product $[v_j^{0,3}]_{n,n'}(\boldsymbol{k})[v_j^{0,3}]_{n',n}(\boldsymbol{k})$ which appears in the Kubo formula is gauge invariant, since the phase factor of the two velocities exactly cancel each other. Here $[v_j^0]_{n,n'}$ is negligible but $[v_j^3]_{n,n'}$ can be significant if the spin direction of the two states are orthogonal to the spin quantization axis, that is, when $\theta \sim \pi/2$. This is exactly the case of *Class II* anti-crossings. As the magnitudes of $[v_i^0]_{n',n}(\boldsymbol{k})$ and $[v_i^3]_{n',n}(\boldsymbol{k})$ are considerably different (the peaks near Y and Y′ in Fig. 3.7 (e,f)), such crossing points can be the source of symmetry difference of the Berry and spin Berry curvatures. Hence, at *Class II* anti-crossings, the AHC and SHC lack correlation. Note that $[v_j^0]_{n,n'} = 0$ only if the spin states of the two bands are exactly antiparallel. In the first principle calculations, we find a slight misalignment between the two states at *Class II* crossing points (i.e. $\varphi' \sim \varphi + \pi + \delta\varphi$ ($\delta\varphi \ll 1$)), seen in Fig. 3.7 (c,d).

3.3.3 Model Hamiltonian

The reduction of the spatial symmetry of the spin Berry curvature with respect to that of the crystal (and the Berry curvature) is a general feature in the ferromagnetic system. To illustrate this, we use the following model Hamiltonian widely used to characterize electron transport in ferromagnets with spin orbit interaction [116]:

$$\hat{\mathcal{H}} = (k_x^2 + k_y^2)\hat{I} + \alpha\Big(\hat{\sigma}_1 k_y - \hat{\sigma}_2 k_x\Big) + \beta\hat{\sigma}_3, \tag{3.15}$$

α, β are parameters controlling the Rashba-type SOC and the exchange splitting, respectively. We use units with $\hbar$ =1.

The eigenenergy ($\epsilon_\pm$) and the corresponding eigenstates $|\Psi_\pm\rangle$ are expressed as:

$$\epsilon_\pm = \boldsymbol{k}^2 \pm \lambda(\boldsymbol{k}), \tag{3.16}$$

$$|\Psi_\pm\rangle = \Big(\pm i e^{-i\theta}\sqrt{\frac{\lambda(\boldsymbol{k})\pm\beta}{2\lambda(\boldsymbol{k})}}, \sqrt{\frac{\lambda(\boldsymbol{k})\mp\beta}{2\lambda(\boldsymbol{k})}}\Big), \tag{3.17}$$

where $\boldsymbol{k}$ is the electron wave vector, $\boldsymbol{k} = \sqrt{k_x^2 + k_y^2}$, $\theta = \arctan(\frac{ky}{kx})$ and $\lambda(\boldsymbol{k}) = \sqrt{\alpha^2\boldsymbol{k}^2 + \beta^2}$.

The energy dispersion relation of the model Hamiltonian is shown in Fig. 3.9(a). Due to the exchange splitting, there are two bands which we refer to as the lower band (blue line) and the upper (red line) band. The spin of the lower and upper bands, represented by the line color, is opposite.

The spin components of each level are,

$$\boldsymbol{s}_{\pm} = \Big(\pm \frac{\alpha k_y}{\lambda(\boldsymbol{k})}, \mp \frac{\alpha k_x}{\lambda(\boldsymbol{k})}, \pm \frac{\beta}{\lambda(\boldsymbol{k})} \Big), \tag{3.18}$$

where the spin components are defined as $s_i \equiv \langle \Psi_{\pm} | \, \sigma_i \, | \Psi_{\pm} \rangle$. Although the z-component of the spin does not change across the crossing point (*i.e.*, the Γ point) in the model system (see Fig. 3.9(a)), which is in contrast to that of *Class II* crossing (see Fig. 3.5(a,b)), the in-plane component of the spin does change as illustrated in Fig. 3.8. Thus the model system defined by the Hamiltonian (Eq. 3.15) can be considered a *Class II* anti-crossing.

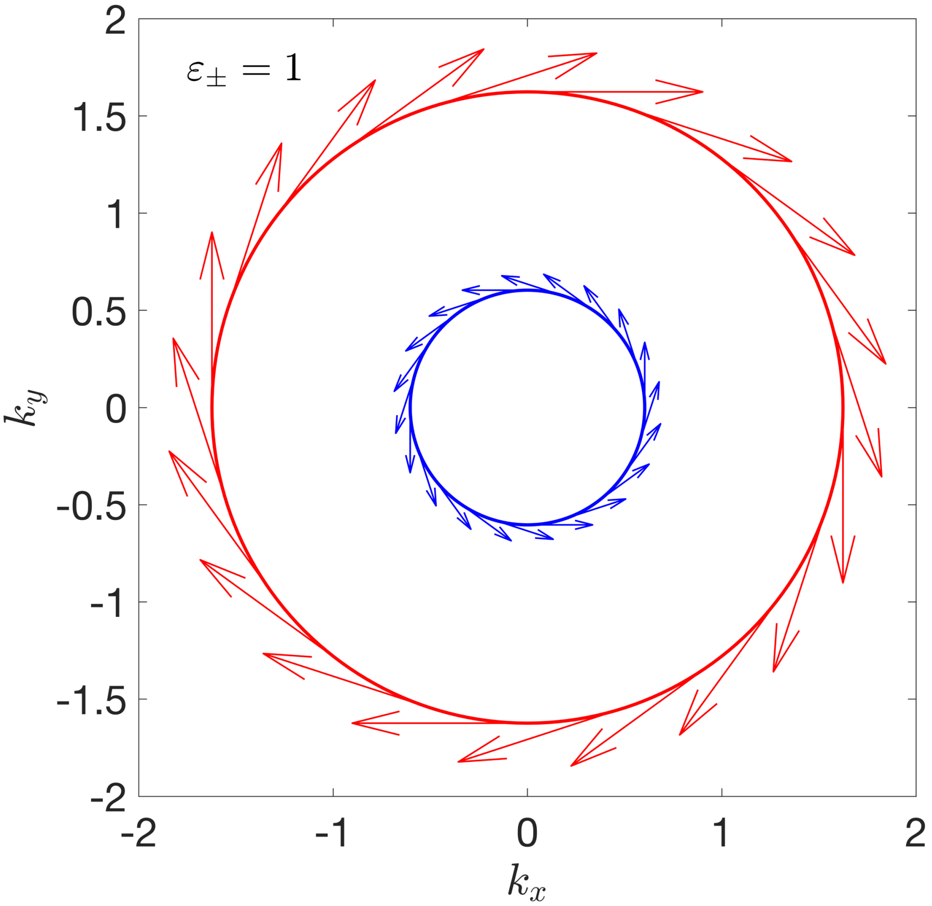

Figure 3.8: Spin components of model Hamiltonian.
The in-plane spin component of two levels whose Fermi contours are in red/blue color, representing ±. The vector shows the spin direction of each level. The parameters used in the calculations are $\alpha = 1$, $\beta = 0.1$.

The velocity and the spin velocity (polarization along z-direction) operators are

$$\hat{v}_i^0 = \frac{\partial \hat{\mathcal{H}}}{\partial k_i} = 2k_i \hat{I} + \alpha \epsilon_{ij} \hat{\sigma}_j, \tag{3.19}$$

$$\hat{v}_i^3 = \frac{1}{2}\Big\{\hat{v}_i^0, \hat{\sigma}_3\Big\} = 2k_i \hat{\sigma}_3, \tag{3.20}$$

where ϵ_{ij} is 2D Levi-Civita symbol with $i, j = x, y$.

The explicit matrix forms of the velocity operator and spin velocity operator of the model Hamiltonian are,

$$\hat{v}_x^0 = \begin{pmatrix} 2k_x & i\alpha \\ -i\alpha & 2k_x \end{pmatrix}, \quad \hat{v}_y^0 = \begin{pmatrix} 2k_y & \alpha \\ \alpha & 2k_y \end{pmatrix},$$

$$\hat{v}_x^3 = \begin{pmatrix} 2k_x & 0 \\ 0 & -2k_x \end{pmatrix}, \quad \hat{v}_y^3 = \begin{pmatrix} 2k_y & 0 \\ 0 & -2k_y \end{pmatrix}.$$

For a two level system, the Berry curvature and spin Berry curvature can be written in the Kubo formula as,

$$\Omega_{ij,\pm}^{\alpha 0}(\boldsymbol{k}) = -\frac{\mathrm{Im}\Big[[v_i^\alpha]_{\pm,\mp}(\boldsymbol{k})[v_j^0]_{\mp,\pm}(\boldsymbol{k}) - [v_j^0]_{\pm,\mp}(\boldsymbol{k})[v_i^\alpha]_{\mp,\pm}(\boldsymbol{k})\Big]}{\Big(\epsilon_-(\boldsymbol{k}) - \epsilon_+(\boldsymbol{k})\Big)^2}, \tag{3.21}$$

with − representing the lower band (1) and + representing the upper band (2).

The off-diagonal velocity and spin velocity matrix elements are,

$$[v_i^0]_{n'n}(\boldsymbol{k}) = \frac{\alpha[\beta k_i - i\epsilon_{n'n}\epsilon_{ij}k_j\lambda(k)]}{\boldsymbol{k}\lambda(k)}, \tag{3.22}$$

$$[v_i^3]_{n'n}(\boldsymbol{k}) = -\frac{2\alpha \boldsymbol{k} k_i}{\lambda(k)}, \tag{3.23}$$

with band index $n', n = \pm$.

After straightforward calculation, we derive the Berry curvature and the spin Berry curvature as the following:

$$\Omega_{xy,\pm}^{00} = \mp\frac{\alpha^2\beta}{2\lambda^3(\boldsymbol{k})}, \ \Omega_{xy,\pm}^{30} = \pm\frac{\alpha^2 k_x^2}{\lambda^3(\boldsymbol{k})}, \ \Omega_{yx,\pm}^{30} = \mp\frac{\alpha^2 k_y^2}{\lambda^3(\boldsymbol{k})}. \tag{3.24}$$

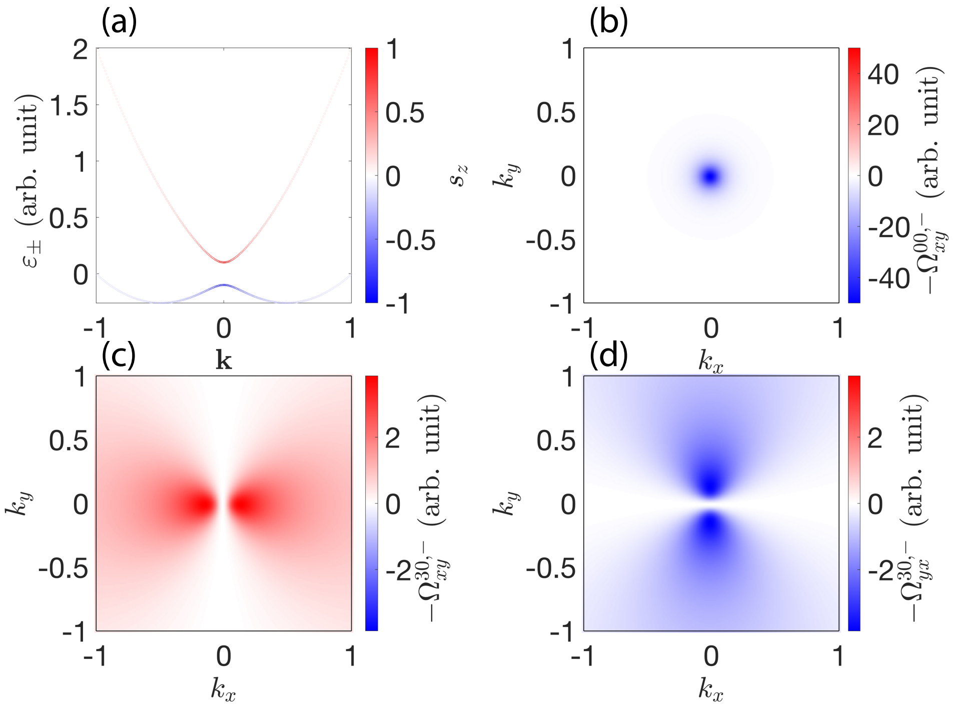

Figure 3.9: Model Hamiltonian calculation.
(a) Band dispersion of the model Hamiltonian. The spin character is represented by the line color. (b) Berry curvature ($\Omega^{0,-}_{xy}$) of the lower band. (c,d) spin Berry curvature of the lower band: (c) $\Omega^{30,-}_{xy}$, (d) $\Omega^{30,-}_{yx}$. The parameters used in the calculations are $\alpha = 1$, $\beta = 0.1$.

The calculated Berry curvature and spin Berry curvature of the $-$ band are presented in Figs. 3.9(b-d). Clearly $\Omega^{00}_{xy,\pm}$ is C_{4v}-symmetric whereas $\Omega^{30}_{xy,\pm}$ reduces to C_{2v}-symmetry. Note that the C_{4v} rotation symmetry is a subgroup of the spherical symmetry group. Figures 3.9(c) and (d) compare $\Omega^{30}_{xy,-}$ and $\Omega^{30}_{yx,-}$. ($\Omega^{30}_{xy,\pm}$ ($\Omega^{30}_{yx,\pm}$) represents the spin Berry curvature when current is passed along the y (x) axis and spin current flows along the x (y) axis.) As evident, $\Omega^{30}_{xy,-}$ and $\Omega^{30}_{yx,-}$ differ in sign and magnitude at each k point. Thus, the symmetry reduction is a general feature of ferromagnets.

3.4 Brief Summary

In this chapter, we investigate the AHE and SHE simultaneously in ferromagnetic CoPt. A large symmetry reduction of the spin Berry curvature is found at the *Class II* anti-crossings, where the crossed Bloch bands have opposite spin. In such anti-crossings, we find the interband matrix elements of spin velocity is essentially different from that of velocity, at which the behavior of the Berry curvature and the spin Berry curvature diverge. Since ferromagnetic systems typically possess large exchange splitting, the Hall current is often modeled using the two current model, *i.e.* the Hall current consists of two independent channels formed by the majority and minority spins. Using a simplified two current model, the AHC and the SHC are related by the spin polarization at the Fermi level P, that is, $\sigma_{AH} = P\sigma_{SH}$. In such context, it is intuitive to think the AHE and SHE in ferromagnets are highly correlated, but this simple scaling does not hold for intrinsic contribution of SHC and AHC in ferromagnets. We find the spin polarization $P = \sigma^{00}_{yx}/\sigma^{30}_{yx}$ is nearly zero from the calculated Hall conductivities ($\sigma_{AH} = -3$ S/cm and $\sigma_{SH} = 787$ S/cm), whereas P estimated from the density of states at the Fermi level (ε_F) using first principles calculations is $P(\varepsilon_F) = -0.69$. Since pairs of bands with opposite spin characters (*Class II*) are ubiquitous inside the Brillouin zone near the Fermi level in ferromagnets, the scaling will not hold in general. Our finding agrees with recent experimental reports showing that indeed the simple scaling does not hold for the intrinsic and extrinsic contributions to the AHC and SHC in $3d$ ferromagnets [114].

3.A Appendix: Calculation method

DFT calculations are performed using FLAPW with GGA for exchange correlation. The lattice constant for CoPt is $a = 2.69$Å and $c = 3.71$Å. LAPW functions have a cutoff, $|k + G| \leqslant 3.9$ a.u.$^{-1}$. MT radius are taken to be 2.2 and 2.4 bohrs for Co and Pt, respectively. The angular momentum expansion inside the MT spheres is truncated at $l = 8$ for the wave functions, charge and spin densities, and potential. The size of k-point mesh is selected as $16 \times 16 \times 16$ for obtaining self-consistent charge and spin densities. Spin orbit coupling (SOC) is treated through a second variational method and zero temperature is assumed. The intrinsic AHC and SHC are calculated using the linear response theory. The Berry curvature (Ω^{00}_{ij}) and the spin Berry curvature (Ω^{l0}_{ij}) are expressed as,

$$\Omega^{\alpha 0}_{ij,n}(\boldsymbol{k}) = -\hbar^2 \sum_{n' \neq n} \frac{\mathrm{Im}\Big[[v^{\alpha}_i]_{n,n'}(\boldsymbol{k})[v^0_j]_{n',n}(\boldsymbol{k}) - [v^0_j]_{n,n'}(\boldsymbol{k})[v^{\alpha}_i]_{n',n}(\boldsymbol{k})\Big]}{\Big(\epsilon_n(\boldsymbol{k}) - \epsilon_{n'}(\boldsymbol{k})\Big)^2}, \tag{3.A.1}$$

$$\Omega^{\alpha 0}_{ij}(\boldsymbol{k}) = \sum_n f(\epsilon_n(\boldsymbol{k}))\Omega^{\alpha 0}_{ij,n}(\boldsymbol{k}), \tag{3.A.2}$$

where $\Omega^{\alpha 0}_{ij,n}(\boldsymbol{k})$ is the Berry curvature and the spin Berry curvature of band n, $|\boldsymbol{k}, n\rangle$ is the Bloch state with energy $\epsilon_n(\boldsymbol{k})$ and wave vector $\boldsymbol{k}$; n describes the band index. $\hat{v}^{\alpha}_i$ is the generalized velocity operator ($i = x, y, z$ and $\alpha = 0, 1, 2, 3$) and $f(\epsilon)$ is the Fermi distribution function. The superscripts α and 0 of $\Omega^{\alpha 0}_{ij}(\boldsymbol{k})$ represent the superscripts of the general velocity v^{α}_i and v^0_j in the right hand side of Eq. (3.A.1). Note that, by definition, $\Omega^{\alpha 0}_{ij} = -\Omega^{0\alpha}_{ji}$. The off-diagonal conductivity tensor ($\sigma^{\alpha 0}_{ij}$) is obtained by integrating the Berry curvature and spin Berry curvature in the first Brillouin zone (BZ):

$$\sigma^{\alpha 0}_{ij} = -\frac{e^2}{\hbar} \int_{BZ} \frac{d^3\boldsymbol{k}}{(2\pi)^3} \Omega^{\alpha 0}_{ij}(\boldsymbol{k}). \tag{3.A.3}$$

Here, e and $\hbar$ are the electric charge and the reduced Planck constant, respectively, σ^{00}_{ij} represents the AHC and σ^{l0}_{ij} represents the SHC with the spin quantization axis along the l-axis in the Cartesian space. The AHC is displayed in units of S/cm and the SHC is multiplied by $-\frac{2e}{\hbar}$ so that it can expressed in units of S/cm. To check the accuracy of the calculations of the AHC and SHC, we extend the size of k-point mesh up to $70 \times 70 \times 70$ with a total 343,000 special k points inside the first BZ.

The convergence of the integrated AHC and SHC calculations are shown in Fig. 3.10. The change in the integrated SHC with increasing the k-mesh size is small (less than 5%), suggesting that the mesh size is sufficiently large. The calculated spin magnetic moment of Co and Pt are 1.76 and 0.40 μ_B respectively, which are in good agreement with previous calculations, confirming the reliability of the calculations.

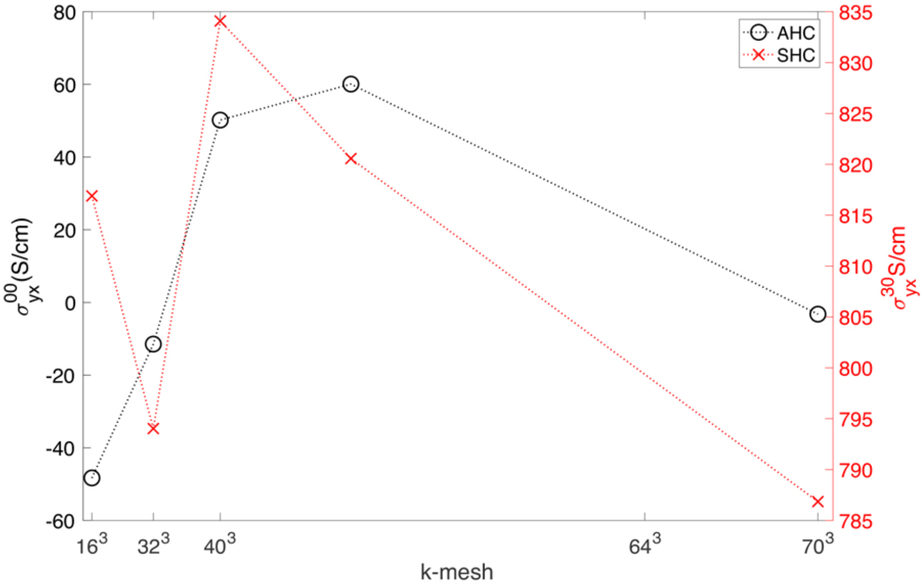

Figure 3.10: Convergence of the integrated AHC and SHC calculations.

3.B Appendix: Symmetry analysis on general Hamiltonian

We start with a generalized periodic Hamiltonian with spin orbit coupling ($\vec{\lambda}$) and exchange splitting in z-direction, which is a model Hamiltonian of a ferromagnet,

$$\begin{aligned} \hat{\mathcal{H}}(\boldsymbol{k}) &= \hat{\mathcal{H}}_0(\boldsymbol{k})I_{2\times2} + \vec{\lambda}\times\vec{k}\cdot\vec{\sigma} + \beta\hat{\sigma}_3, \\ \hat{\mathcal{H}}(\boldsymbol{k}) &= \hat{\mathcal{H}}_0(\boldsymbol{k})I_{2\times2} + \epsilon_{ijk}k_i\hat{\sigma}_j\lambda_k + \beta\hat{\sigma}_3, \end{aligned} \tag{3.B.1}$$

where $\hat{H}_0(k)$ is governed by periodic crystal field, $\vec{\lambda}$ is strength of SOC and β is the exchange interaction. ϵ_{ijk} is Levi-Civita symbol symbol.

The Bloch states are,

$$\hat{\mathcal{H}}(\boldsymbol{k})\left|u_n(\boldsymbol{k})\right\rangle = E_n(\boldsymbol{k})\left|u_n(\boldsymbol{k})\right\rangle, \tag{3.B.2}$$

with band index n and band energy $E_n(\boldsymbol{k})$.

With the exchange splitting breaking the symmetry in z-direction, the system possesses C_4 rotation symmetry in xy-plane. The $\hat{C}_4$ rotation operator for a spinor field consists of two parts,

$$\hat{C}_4 = e^{i\frac{\pi}{4}\hat{\sigma}_3}\hat{R}(\hat{\Lambda}), \tag{3.B.3}$$

where $e^{i\frac{\pi}{4}\hat{\sigma}_3}$ acting on the spinor part of Bloch states and $\hat{R}(\hat{\Lambda})$ acting on the Cartesian coordinates.

The explicit form of the rotation matrix $\hat{\Lambda}$ is,

$$\hat{\Lambda} = e^{i\frac{\pi}{2}\hat{J}_3} = \exp[i\frac{\pi}{2}\begin{pmatrix} 0 & -i & 0 \\ i & 0 & 0 \\ 0 & 0 & 0 \end{pmatrix}] = \begin{pmatrix} 0 & -1 & 0 \\ 1 & 0 & 0 \\ 0 & 0 & 1 \end{pmatrix}, \tag{3.B.4}$$

where $\hat{J}_3$ is the generator of the $SO(3)$ group.

First, we check the invariance of Hamiltonian $\hat{\mathcal{H}}$. Apparently, the crystal Hamiltonian is conserved under C_4 rotation, $[\hat{\mathcal{H}}_0(\boldsymbol{k}), \hat{C}_4] = 0$. The rest of Hamiltonian is,

$$\begin{aligned} [\hat{\mathcal{H}}(\boldsymbol{k}), \hat{C}_4] &= [\epsilon_{ijk}k_i\hat{\sigma}_j\lambda_k + \beta\hat{\sigma}_3, \hat{C}_4] \\ &= [\epsilon_{ijk}k_i\hat{\sigma}_j\lambda_k, \hat{C}_4] + \beta[\hat{\sigma}_3, \hat{C}_4]. \end{aligned} \tag{3.B.5}$$

For the second term (exchange splitting), $\hat{\sigma}_3$ commutes with the matrix exponential of $\hat{\sigma}_3$. Thus, the second term is apparently zero, $[\hat{\sigma}_3, \hat{C}_4] = 0$.

For the first (spin-orbit coupling) term, we have

$$\begin{aligned} [\epsilon_{ijk}k_i\hat{\sigma}_j\lambda_k, \hat{C}_4] &= \epsilon_{ijk}k_i\hat{\sigma}_j\lambda_k\hat{C}_4 - \hat{C}_4\epsilon_{ijk}k_i\hat{\sigma}_j\lambda_k \\ &= \epsilon_{ijk}k_i\hat{\sigma}_j\lambda_k\hat{C}_4 - \hat{C}_4\epsilon_{ijk}k_i\hat{\sigma}_j\lambda_k\hat{C}_4^\dagger\hat{C}_4 \\ &= \epsilon_{ijk}k_i\hat{\sigma}_j\lambda_k\hat{C}_4 - \exp[i\frac{\pi}{4}\sigma_3]\hat{R}(\hat{\Lambda})\epsilon_{ijk}k_i\hat{\sigma}_j\lambda_k\hat{R}(\hat{\Lambda}^{-1})\exp[-i\frac{\pi}{4}\sigma_3]\hat{C}_4 \\ &= \epsilon_{ijk}k_i\sigma_j\lambda_k\hat{C}_4 - \epsilon_{ijk}\Lambda_{im}k_m\Lambda_{jn}\hat{\sigma}_n\Lambda_{kl}\lambda_l\hat{C}_4 \\ &= \epsilon_{ijk}k_i\sigma_j\lambda_k\hat{C}_4 - \epsilon_{mnl}k_m\hat{\sigma}_n\lambda_l\hat{C}_4 \\ &= 0. \end{aligned}$$

Finally, we confirm that the Hamiltonian commutes with C_4 rotation, indicating it is invariant under C_4 rotation, $[\hat{\mathcal{H}}(\boldsymbol{k}), \hat{C}_4] = 0$. Then, we have two identities as the following:

$$\hat{C}_4^\dagger \hat{\mathcal{H}}(\boldsymbol{k}) \hat{C}_4 = \hat{\mathcal{H}}(\hat{\Lambda}\boldsymbol{k}) = \hat{\mathcal{H}}(\boldsymbol{k}), \tag{3.B.6}$$

$$\hat{C}_4 \left| u_n(\boldsymbol{k}) \right\rangle = e^{i\frac{\pi}{4}\sigma_3} \left| u_n(\hat{\Lambda}\boldsymbol{k}) \right\rangle = \left| u_n'(\hat{\Lambda}\boldsymbol{k}) \right\rangle = \left| u_n(\boldsymbol{k}) \right\rangle . \tag{3.B.7}$$

The velocity operator $\hat{v}_i^0$ can be expressed using $\hat{\mathcal{H}}$ as,

$$\hat{v}_i(\boldsymbol{k}) = \dot{\hat{r}}_i(\boldsymbol{k}) = \frac{1}{i\hbar}[\hat{r}_i(\boldsymbol{k}), \hat{\mathcal{H}}(\boldsymbol{k})] = \frac{1}{\hbar}\frac{\partial \hat{\mathcal{H}}(\boldsymbol{k})}{\partial k_i}. \tag{3.B.8}$$

In our generalized Hamiltonian Eq. 3.B.1, the velocity operator is

$$\hat{v}_i^0 \;=\; \frac{1}{\hbar}\frac{\partial \hat{\mathcal{H}}_0(\boldsymbol{k})}{\partial k_i}\hat{I} + \frac{1}{\hbar}\epsilon_{ijk}\hat{\sigma}_j\lambda_k, \tag{3.B.9}$$

where the second term is the anomalous velocity attributed to the SOC.

The spin velocity operator ($\hat{v}_i^\alpha$) is the anti-commutator of the velocity operator and the spin operator,

$$\hat{v}_i^l \;=\; \frac{1}{2}\{\hat{v}_i^3, \hat{\sigma}_l\} = \frac{1}{2\hbar}\{\frac{\partial \hat{\mathcal{H}}(\boldsymbol{k})}{\partial k_i}, \hat{\sigma}_l\} = \frac{1}{\hbar}\frac{\partial \hat{\mathcal{H}}_0(\boldsymbol{k})}{\partial k_i}\hat{\sigma}_\alpha + \frac{1}{\hbar}\epsilon_{ilk}\lambda_k\hat{I}. \tag{3.B.10}$$

Now we check the matrix elements of the velocity and spin velocity under C_4 rotation. The velocity matrix elements are,

$$[v_i^0]_{n'n}(\boldsymbol{k}) = \frac{1}{\hbar}\left\langle u_{n'}(\boldsymbol{k}) \right| \frac{\partial \hat{H}_0(\boldsymbol{k})}{\partial k_i}\hat{I} + \epsilon_{ijk}\hat{\sigma}_j\lambda_k \left| u_n(\boldsymbol{k}) \right\rangle . \tag{3.B.11}$$

Under C_4 rotation, the new wave vector $\boldsymbol{k'}$ under rotation is $\boldsymbol{k'} = \hat{\Lambda}\boldsymbol{k}$,

$$\begin{aligned} [v_i^0]_{n'n}(\boldsymbol{k'}) &= \frac{1}{\hbar}\left\langle u'_{n'}(\boldsymbol{k'}) \right| \frac{\partial \hat{H}_0(\boldsymbol{k'})}{\partial k'_i}\hat{I} + \epsilon_{ijk}\hat{\sigma}_j\lambda_k \left| u'_n(\boldsymbol{k'}) \right\rangle \\ &= \Lambda_{ij}[v_i^0]_{n'n}(\boldsymbol{k}). \end{aligned} \tag{3.B.12}$$

Finally, we have relation between the matrix elements of velocity operator under C_4 rotation, $[v_i^0]_{n'n}(\boldsymbol{k'}) = \Lambda_{ij}[v_i^0]_{n'n}(\boldsymbol{k})$. This is intuitive, since the velocity behaves like a vector field under rotation.

Next, we check the matrix element of the spin velocity operator, $\hat{v}_i^l$ under C_4 rotation. The spin velocity matrix elements are,

$$[v_i^l]_{n'n}(\boldsymbol{k}) \;=\; \frac{1}{\hbar}\langle u_{n'(\boldsymbol{k})}|\,\frac{\partial \hat{\mathcal{H}}_0(\boldsymbol{k})}{\partial k_i}\hat{\sigma}_l + \epsilon_{ilk}\hat{e}_i\lambda_k\hat{I}\,|u_n((\boldsymbol{k})\rangle\,. \tag{3.B.13}$$

Under C_4 rotation, the spin velocity element is,

$$\begin{aligned}
[v_i^l]_{n'n}(\boldsymbol{k}') &= \frac{1}{\hbar}\langle u'_{n'}(\boldsymbol{k}')|\,\frac{\partial \hat{\mathcal{H}}_0(\boldsymbol{k}')}{\partial k'_i}\hat{\sigma}_l + \epsilon_{ilk}\lambda_k\hat{I}\,|u'_n((\boldsymbol{k}')\rangle \\
&= \Lambda_{ij}\Lambda_{lm}[v_j^l]_{n'n}(\boldsymbol{k}).
\end{aligned} \tag{3.B.14}$$

The matrix elements, however, rotate like a rank-2 tensor as, $[v_i^l]_{n'n}(\boldsymbol{k}') = \Lambda_{ij}\Lambda_{lm}[v_j^l]_{n'n}(\boldsymbol{k})$.

Now, we consider the Berry curvature and spin Berry curvature from the Kubo formula,

$$\Omega_{ij,n}^{\alpha 0}(\boldsymbol{k}) \;=\; -\hbar^2\sum_{n\neq m}\mathrm{Im}\Big[\frac{[v_i^\alpha]_{nm}(\boldsymbol{k})[v_j^0]_{mn}(\boldsymbol{k}) - [v_j^0]_{nm}(\boldsymbol{k})[v_i^\alpha]_{mn}(\boldsymbol{k})}{\Big(\epsilon_n(k)-\epsilon_m(k)\Big)^2}\Big]. \tag{3.B.15}$$

By definition, we have identity, $\Omega_{ij}^{\alpha 0} = -\Omega_{ji}^{0\alpha}$.

First, we check the Berry curvature under C_4 rotation,

$$\begin{aligned}
\Omega_{ij,n}^{00}(\boldsymbol{k}') &= -\hbar^2\sum_{n\neq m}\mathrm{Im}\Big[\frac{[v_i^0]_{nm}(\boldsymbol{k}')[v_j^0]_{mn}(\boldsymbol{k}') - [v_j^0]_{nm}(\boldsymbol{k}')[v_i^0]_{mn}(\boldsymbol{k}')}{\Big(\epsilon_n(\boldsymbol{k}')-\epsilon_m(\boldsymbol{k}')\Big)^2}\Big] \\
&= -\hbar^2\sum_{n\neq m}\mathrm{Im}\Big[\frac{\Lambda_{ir}[v_r^0]_{nm}(\boldsymbol{k})\Lambda_{js}[v_s^0]_{mn}(\boldsymbol{k}) - \Lambda_{js}[v_s^0]_{nm}(\boldsymbol{k})\Lambda_{ir}[v_r^0]_{mn}(\boldsymbol{k})}{\Big(\epsilon_n(\boldsymbol{k})-\epsilon_m(\boldsymbol{k})\Big)^2}\Big], \\
&= \Lambda_{ir}\Lambda_{js}\Omega_{rs,n}^{00}(\boldsymbol{k}).
\end{aligned} \tag{3.B.16}$$

Then, the spin Berry curvature under C_4 rotation is,

$$\begin{aligned}
\Omega_{ij,n}^{l0}(\boldsymbol{k}') &= -\hbar^2\sum_{n\neq m}\mathrm{Im}\Big[\frac{[v_i^l]_{nm}(\boldsymbol{k}')[v_j^0]_{mn}(\boldsymbol{k}') - [v_j^0]_{nm}(\boldsymbol{k}')[v_i^l]_{mn}(\boldsymbol{k}')}{\Big(\epsilon_n(\boldsymbol{k}')-\epsilon_m(\boldsymbol{k}')\Big)^2}\Big] \\
&= -\hbar^2\sum_{n\neq m}\mathrm{Im}\Big[\frac{\Lambda_{ir}\Lambda_{lt}[v_r^t]_{nm}(\boldsymbol{k})\Lambda_{js}[v_s^0]_{mn}(\boldsymbol{k}) - \Lambda_{js}[v_s^0]_{nm}(\boldsymbol{k})\Lambda_{lt}\Lambda_{ir}[v_r^t]_{mn}(\boldsymbol{k})}{\Big(\epsilon_n(\boldsymbol{k})-\epsilon_m(\boldsymbol{k})\Big)^2}\Big] \\
&= \Lambda_{ir}\Lambda_{js}\Lambda_{lt}\Omega_{rs,n}^{t0}(\boldsymbol{k}).
\end{aligned} \tag{3.B.17}$$

In summary, the Berry curvature and spin berry curvature have the following relations under C_4 rotation ($\boldsymbol{k}' = \boldsymbol{\Lambda k}$),

$$\begin{aligned}
\Omega^{00}_{ij,n}(\boldsymbol{k}') &= \Lambda_{ir}\Lambda_{js}\Omega^{00}_{rs,n}(\boldsymbol{k}), && (3.B.18)\\
\Omega^{l0}_{ij,n}(\boldsymbol{k}') &= \Lambda_{ir}\Lambda_{js}\Lambda_{lt}\Omega^{t0}_{rs,n}(\boldsymbol{k}). && (3.B.19)
\end{aligned}$$

Note the Berry curvature is an antisymmetric tensor of rank 2 ($\Omega^{00}_{ii,n} = 0, \Omega^{00}_{ij,n} = -\Omega^{00}_{ji,n}$). The Berry curvature tensor has only three independent components. For simplicity, we reduce it to a tensor of rank one with normal permutation relation $\Omega_{(k),n} = \epsilon_{ijk,n}\Omega^{00}_{ij,n}$. Based on Eq. 3.B.18, we can easily check the following identities:

$$\begin{aligned}
\Omega_{(k),n}(\boldsymbol{k}') &= \epsilon_{ijk}\Omega^{00}_{ij,n}(\boldsymbol{k}') = \epsilon_{ijk}\Lambda_{ir}\Lambda_{js}\Omega^{00}_{rs,n}(\boldsymbol{k})\\
&= \Lambda_{kl}\epsilon_{ijk}\Lambda_{kl}\Lambda_{ir}\Lambda_{js}\Omega^{00}_{rs,n}(\boldsymbol{k}) = \Lambda_{kl}\epsilon_{rsl}\Omega^{00}_{rs,n}(\boldsymbol{k})\\
&= \Lambda_{kl}\Omega_{(l),n}(\boldsymbol{k}). && (3.B.20)
\end{aligned}$$

Explicitly, we have:

$$\Omega_{(1),n}(\boldsymbol{k}') = -\Omega_{(2),n}(\boldsymbol{k}), \quad \Omega_{(2),n}(\boldsymbol{k}') = \Omega_{(1),n}(\boldsymbol{k}), \quad \Omega_{(3),n}(\boldsymbol{k}') = \Omega_{(3),n}(\boldsymbol{k}). \quad (3.B.21)$$

The spin Berry curvature is a tensor of rank 3, while the subscripts is not anti-symmetric like the Berry curvature, $\Omega^{l0}_{ij,n} = -\Omega^{0l}_{ji,n} \neq -\Omega^{l0}_{ji,n}$. If we choose the spin quantization axis along z, $l = 3$, we have $\Omega^{30}_{ij,n}(\boldsymbol{k}') = \Lambda_{ir}\Lambda_{js}\Lambda_{33}\Omega^{30}_{rs,n}(\boldsymbol{k}) = \Lambda_{ir}\Lambda_{js}\Omega^{30}_{rs,n}(\boldsymbol{k})$. Thus, $\Omega^{30}_{ij,n}$ is like a tensor of rank 2, following the same tensor rotation as Eq. 3.B.18.

Chapter 4

Magneto anisotropic spin Hall effect in $3d$ ferromagnets

Contents

4.1 Introduction

In experiments, it is difficult to distinguish the source of transversely flowing spin current in ferromagnets, in which the anomalous Hall effect and spin Hall effect exist simultaneously. In addition, it also remains an ambiguity whether the AHE and SHE should have distinct symmetries, since the intrinsic AHE is also governed by the direction of spontaneous magnetization. Recent experiments indicate contradictory pictures on the SHE in ferromagnets, suggesting that it can either be dependent or independent on the magnetization direction [50, 52]. The magnetization dependence of SHE in ferromagnets has, thus, attracted strong theoretical interest. Clarifying the underlying physics of SHE in ferromagnets thus remains as a challenge.

In this chapter, we study the magnetization dependence of SHE in ferromagnets using first principles calculations. We use cubic phase bcc-Fe and fcc-Ni as prototypes of the ferromagnetic systems to study the relation between SHE in ferromagnets and exchange interaction (spontaneous magnetization). We release the constraint of parallel configuration between the spontaneous magnetization and the spin quantization axis of the conduction electrons [117] and find the magnitude of the intrinsic spin Hall conductivity (SHC) in Fe and Ni can be varied *via* changes in the magnetization direction with respect to the spin polarization of the conduction electrons. The origin of the anisotropy of intrinsic spin Hall conductivity is clarified through band analysis with spin character of the Bloch bands. The anisotropy is found to be associated with the competition between the *Class I* and *Class II* anti-crossings.

4.2 Non-collinear magnetic states in DFT

To study the magnetization dependence of SHC in ferromagnets, we first need to avoid the influence of crystalline anisotropy [118]. Hence, we choose cubic phase ferromagnets as targets of our study, *e.g.*, bcc-Fe and fcc-Ni (Fig.4.1). The key technical issue is to separate the magnetization direction from the spin quantization axis. In previous studies, collinear magnetic states are employed in which the magnetic moments are restricted to be parallel or anti-parallel with the spin quantization axis (usually the z-axis). In such case, the SHC of ferromagnets can be only calculated in one magnetic configuration, *i.e.* $\vec{m} \parallel \vec{s}$ (longitudinal SHE). To study the magnetization dependence of the SHC, we employ non-collinear magnetic states which allow the rotation of spin directions (Fig.4.1).

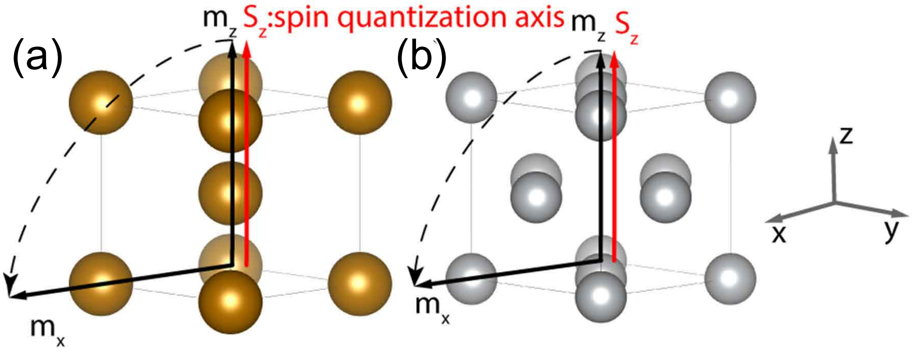

Figure 4.1: Crystal structure and calculation geometry.

In non-collinear magnetic states, the eigenstates are represented by a linear combination of the LAPW basis functions multiplied with a spinor [117]:

$$\Psi_{n,k}(\mathbf{r}) = \sum_{q=k+G}^{G_{\max}} C_{n,q}\psi_{n,q}(\mathbf{r})\chi_{n,q}. \tag{4.1}$$

$\psi_{n,q}(\mathbf{r})$ is the LAPW basis function, $\chi_{n,q}$ is the two component spinor that represents the spin direction of the state (q, n), and $C_{n,q}$ is the expansion coefficient. G is the reciprocal lattice vector. The electron density,

$$\rho_\alpha(\mathbf{r}) = \sum_{k}\sum_{n\in\mathrm{occ}} \Psi^\dagger_{n,k}(\mathbf{r})\sigma_\alpha\Psi_{n,k}(\mathbf{r}), \tag{4.2}$$

contains a $U(1)$ part and a $SU(2)$ part, *i.e.* $\rho_\alpha(\mathbf{r}) = (\rho_0(\mathbf{r}), m_k(\mathbf{r}))$, where $\rho_0(\mathbf{r})$ and $m_k(\mathbf{r})$ correspond to charge density and spin density, respectively. σ_α represents the generalized

Pauli matrix which has four components in our convention, $\sigma_\alpha = (I_2, \sigma_k)$. I_2 is a 2×2 unit matrix, σ_k is the Pauli matrix, the greek indices (*e.g.*, α, β) run from 0 to 3 representing four vectors, and the roman indices (*e.g.*, i, j, k) correspond to space coordinates (*i.e.*, x, y, z). The summation over n in Eq. (4.2) implies summation over all occupied bands.

The Kohn-Sham single-particle Hamiltonian is written as

$$\mathcal{H} = \mathcal{H}_{\text{kin}} I_2 + V_\alpha(\mathbf{r})\sigma_\alpha. \tag{4.3}$$

$\mathcal{H}_{\text{kin}}$ is the kinetic energy term and $V_\alpha = (V_0(\mathbf{r}), V_k(\mathbf{r}))$ is the effective potential with a non-magnetic $U(1)$ part and a magnetic $SU(2)$ part. In our calculation, the spin quantization axis is fixed along the z-axis in the Cartesian coordinate; that is, spin current with polarization along the z-axis is studied. Computations are carried out for two different magnetic configurations, noted as m_z and m_x, by setting the magnetic moment along z and x, respectively (Fig. 4.1).

4.3 Stereoscopic projection of Berry curvature and spin Berry curvature

We first present stereoscopic projection of the non-vanishing components of the Berry curvature ($\Omega^0_{yx}, \Omega^0_{zy}$) and the spin Berry curvature (Ω^3_{yx}) in the first Brillouin zone of bcc-Fe and fcc-Ni (Fig. 4.2). Here, we employ notation $\Omega^0_{yx}, \Omega^0_{zy}, \Omega^3_{yx}$ in abbreviation of $\Omega^{00}_{yx}, \Omega^{00}_{zy}, \Omega^{30}_{yx}$.

For bcc-Fe, upon rotating the magnetization from z to x, the non-vanishing Berry curvature rotates globally following the the axis of spontaneous magnetization (Figs. 4.2(a,b)). The spin Berry curvature, in contrast, changes its profile upon rotation of magnetization (Figs. 4.2(c,d)). The trend is the same for for fcc-Ni: Ω^0_{yx} rotates along with the band structure (Figs. 4.2(e,f)) when the magnetization direction is changed from z to x whereas Ω^3_{yx} changes its profile (Figs. 4.2(g,h)). The region of non-zero Ω^3_{yx} notably increases when the magnetization is rotated, which causes the increase in the SHC.

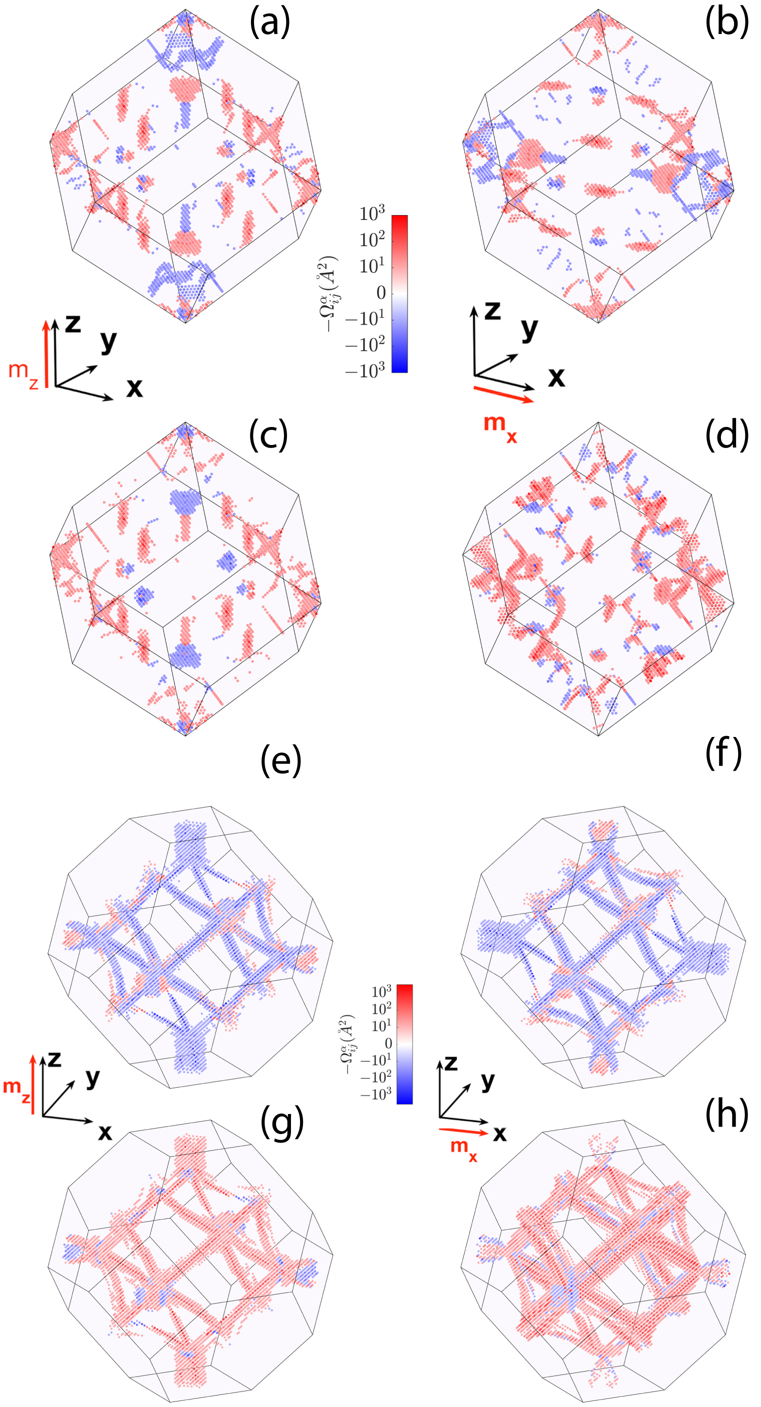

Figure 4.2: Stereoscopic projection of Berry curvature and spin Berry curvature. (a-h) Berry and spin Berry curvatures projected on first Brillouin zone with two different magnetic configurations. The left and right panels present results when the magnetization points along z and x, respectively. (a-d) show calculation results for bcc-Fe, (e-h) display those for fcc-Ni. (a,e) Ω^0_{yx}, (b,f) Ω^0_{zy}, (c,d,g,h) Ω^3_{yx}. The unit of Ω^0_{ij} and Ω^3_{ij} are in $\AA^2$ (length^2).

4.4 Band structure of bcc-Fe and fcc-Ni

The band structure, the Berry curvature and the spin Berry curvature of bcc-Fe are presented in Fig.4.3. Due to the large exchange interaction, the spin expectation (s_z) takes value of ±1 indicating Bloch states are highly polarized along the spin quantization axis (Fig.4.3(a)). Concurrently, spin expectation of Bloch states is near zero after spontaneous magnetization is rotated from z-axis (spin quantization axis) to the x-axis (Fig.4.3(b)).

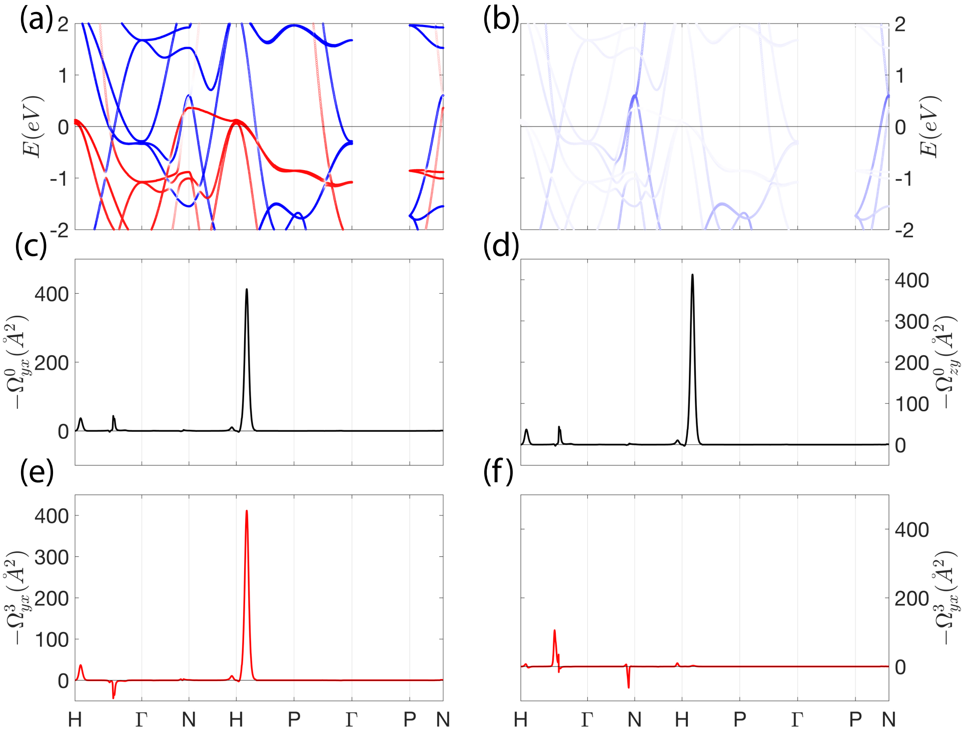

Figure 4.3: Band structure, Berry curvature and spin Berry curvature of bcc-Fe. (a,b) Band structure, (c,d) Berry curvature and (e,f) spin Berry curvature along high symmetry path in first Brillouin zone for bcc-Fe. Two magnetic configurations are plotted: (a,c,e) $\vec{m} \parallel k_z$ and (b,d,f) $\vec{m} \parallel k_x$. The spin expectation value (s_z) of band dispersion is coded with colors: red for majority spin $(s_z \sim +1)$ and blue for minority spin $(s_z \sim -1)$. The unit of Ω^0_{ij} and Ω^3_{ij} are in $\mathring{A}^2$ (length^2).

The non-vanishing component of Berry curvature rotates along with the axis of magnetization: the non-vanishing Berry curvature of the case with $\vec{m} \parallel z$ is Ω^0_{yx} and the non-vanishing Berry curvature of the case $\vec{m} \parallel x$ is Ω^0_{zy}. Further, the magnitude of the Berry curvature show exactly same profile in both cases (Fig.4.3(c,d)). A large peak of Berry curvature is observed near the H-point, corresponding to an anti-crossing point (*Class I*) with bands of the same spin $(s_z \sim 1)$ near the Fermi level. In such anti-crossing point, a large peak of spin Berry curvature is also observed, confirming the correlation of the Berry curvature and the spin Berry curvature in *Class I* anti-crossings. On the contrary, after rotating the direction of spontaneous magnetization from z to x, the geometry of the non-vanishing component of the spin Berry curvature is invariant (Ω^3_{yx} for both cases). But the peak of Ω^3_{yx} near the H point vanishes, while some other peaks or valleys emerges. Specifically, Ω^3_{yx} loses its correlation with the Berry curvature ($\Omega^0_{yx}, \Omega^0_{zy}$), even though the bands at the anti-crossing near the H point possess the same spin but are polarized along the x-axis.

For fcc-Ni, the bands near the Fermi level are mostly with minority spin ($s_z = -1$). Thus, we observe a large valley of Berry curvature ($\Omega^0_{yx}, \Omega^0_{zy}$) and a peak of spin Berry curvature(Ω^3_{yx}) near the X point, corresponding to a *Class I* anti-crossing with the same minority spin. The non-vanishing component of the Berry curvature rotates with respect to the direction of spontaneous magnetization and keeps same profile. However, Ω^3_{yx} near the X point does not vanish and shows even a larger magnitude.

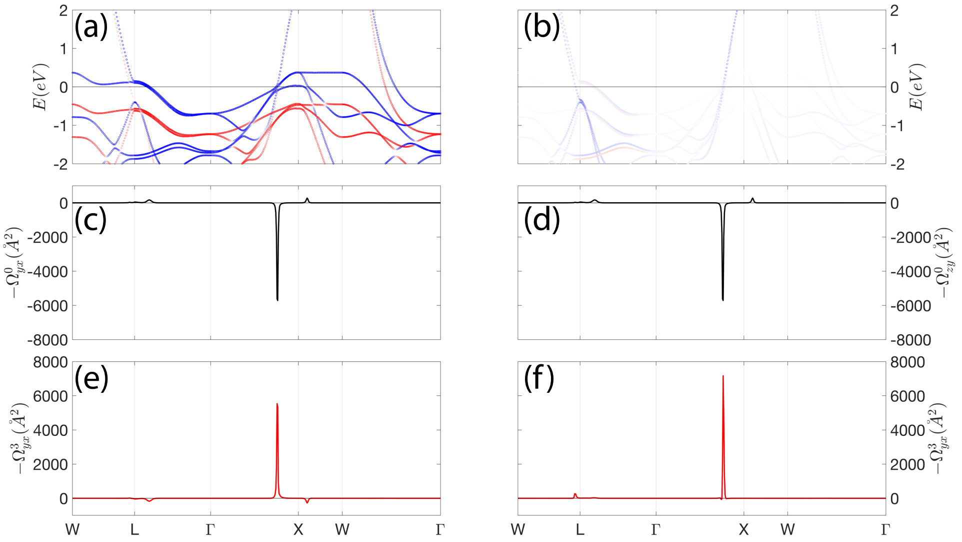

Figure 4.4: Band structure, Berry curvature and spin Berry curvature of fcc-Ni. (a,b) Band structure, (c,d) Berry curvature and (e,f) spin Berry curvature along high symmetry path in first Brillouin zone for fcc-Ni. Two magnetic configurations are plotted: (a,c,e) $\vec{m} \parallel k_z$ and (b,d,f) $\vec{m} \parallel k_x$. The spin expectation value (s_z) of band dispersion is coded with colors: red for majority spin and blue for minority spin. The unit of Ω^0_{ij} and Ω^3_{ij} are in $\mathring{A}^2$ (length^2).

The AHC and SHC for the two magnetization configurations are presented in Table. 4.1. The values of the intrinsic AHC of bcc-Fe and fcc-Ni show good agreement with previous reports [28, 119]. For both bcc-Fe and fcc-Ni, the non-vanishing component of the AHC changes from σ^0_{yx} to σ^0_{zy} when the magnetization direction is changed from being parallel to the z axis to the x axis. The magnitude of the non-vanishing component of the AHC remains the same. In contrast, the non-vanishing component of SHC, σ^3_{yx}, changes with respect to the magnetization direction. Note that here the polarization of the spin current is fixed along the z axis [120] regardless of the magnetization direction. Recent studies have shown that such transverse spin current in ferromagnets, *i.e.*, spin current with polarization orthogonal to the magnetization, does not dephase and persists in typical ferromagnets [60]. Interestingly, the magnitude of SHC considerably varies with changes in the magnetization direction. For example, in bcc-Fe, the SHC changes from 130 $(\frac{e}{\hbar})$ S/cm to 520 $(\frac{\hbar}{e})$ S/cm when the magnetization direction is rotated from the z-axis to the x-axis. Note that the total magnetic moment of the system is exactly the same for both magnetization directions, consistent with the symmetry of cubic systems.

Table 4.1: Table of AHC and SHC of bcc-Fe and fcc-Ni.

Calculated AHC, SHC, and total spin magnetic moment (μ_B) of bcc-Fe and fcc-Ni. The unit of AHC and SHC are S/cm and $(\frac{\hbar}{e})$ S/cm, respectively.

Sample	σ^0_{yx}	σ^0_{zy}	σ^3_{yx}	σ^3_{zy}	m_{tot}
bcc-Fe (m_z)	747	0	130	0	2.18
bcc-Fe (m_x)	0	747	527	0	2.18
fcc-Ni (m_z)	-2414	0	1535	0	0.60
fcc-Ni (m_x)	0	-2414	2358	0	0.60

4.5 Magnetization dependent spin Hall conductivity

4.5.1 Band analysis with spin character

To articulate the change of SHC under rotation of the magnetization, we again categorized the anti-crossings into *Class I* and *Class II*. We find the change in Ω^3_{yx} with magnetization rotation is qualitatively different for the two types of anti-crossings.

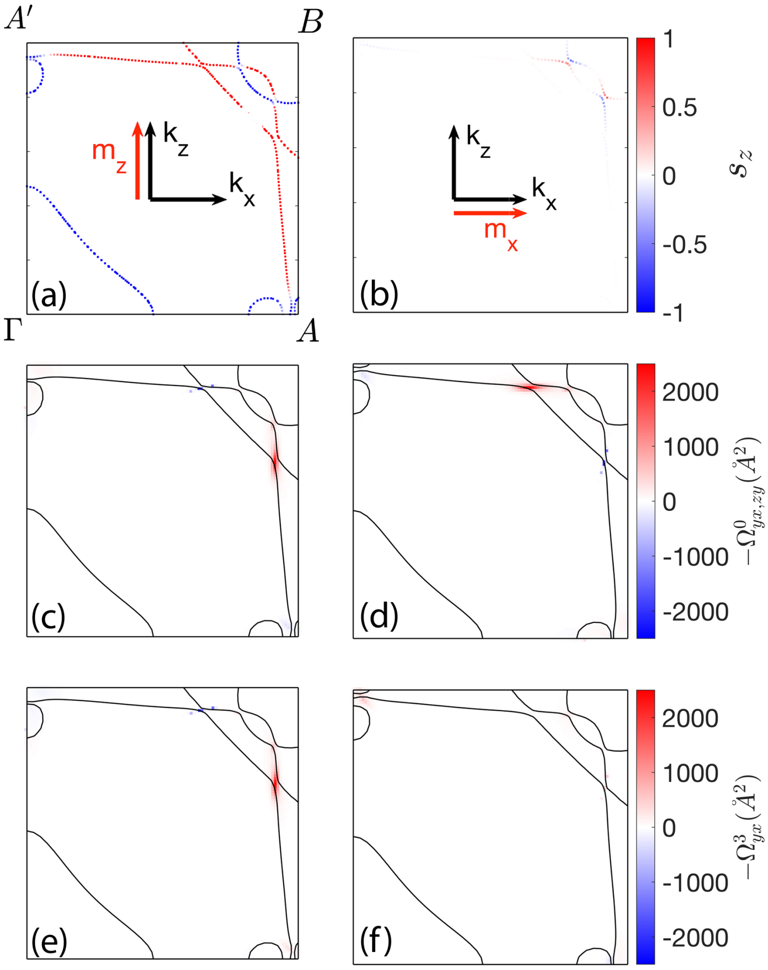

Figure 4.5: Anti-crossing of band with same spin.
Reciprocal plane $\Gamma(0,0,0)$-$A(\frac{1}{2},0,0)$-$A'(0,0,\frac{1}{2})$-$B(\frac{1}{2},0,\frac{1}{2})$ plotted with (a,b) spin expectation value s_z,. (c,d) Berry curvatures Ω^0_{yx} and Ω^0_{zy}. (e,f) spin Berry curvature Ω^3_{yx}. The magnetization points along z (a,c,e,g) and x (b,d,f,h). The Fermi contour of selected plane in Black lines (a-d) and red-blue lines (e-h) coded by spin character. The $s_z \equiv \langle n, \boldsymbol{k}| \sigma_3 |n, \boldsymbol{k}\rangle$ is the spin component of Bloch states along z direction. The unit of Ω^0_{ij} and Ω^3_{ij} are in $\mathring{A}^2$ (length^2).

Characteristics of a representative anti-crossing of *Class I* is shown in Fig. 4.5. Here we show the projection of the spin character, the Berry curvature and the spin Berry curvature on the k_x - k_z plane ($\Gamma(0{,}0{,}0)$- $A(\frac{1}{2}{,}0{,}0)$ -$A'(0{,}0{,}\frac{1}{2})$ plane). The z-component of the spin is plotted in Figs. 4.5(a) and 4.5(b). The color plot shows almost no contrast when the magnetization points along the x-axis (Fig. 4.5(b)) since the polarization for a large number of states tend to be parallel to the magnetization. We focus on the two anti-crossings in the upper right corner of Fig. 4.5(a), where the states involved possess the same (majority) spin character. The Berry curvatures for magnetization along z (Ω^0_{yx}) and x (Ω^0_{zy}) are shown in Fig. 4.5(c) and 4.5(d), respectively. Ω^0_{yx} and Ω^0_{zy} exhibit identical magnitude at the corresponding anti-crossing points, consistent with the symmetry of the AHE [120]. (Note that here we are showing one quadrant of the k_x-k_z plane of the Brillouin zone and the crystal structure has mirror symmetry alone k_y-k_z plane.) The spin Berry curvature, in contrast, shows significant change in its magnitude upon rotation of the magnetization. Whereas a sizable contribution to Ω^3_{yx} is found at one of the anti-crossing point when the magnetization points along z (Fig. 4.5(c)), the corresponding Ω^3_{yx} vanishes when the magnetization is rotated to x (Fig. 4.5(d)). We also note that the Berry and the spin Berry curvatures are nearly identical when the magnetization points along z, however, the relation does not hold when the magnetization is rotated to x. Overall, in *Class I* anti-crossing, we find the magnitude of Ω^3_{yx} changes from a finite value (positive or negative) to near zero upon rotating the magnetization from z to x.

A representative anti-crossing of *Class II* is shown in Fig. 4.6. Here we show projection of the corresponding properties on the same k_x - k_z plane as in Fig. 4.5 but shifted along k_y by $\frac{1}{2}$. In this plane, there are two anti-crossings at the top left and bottom right corners. As evident in Fig. 4.6(a), the anti-crossings are characterized by a pair of bands with opposite spin. For *Class II* anti-crossing, the spin character rapidly changes at the crossing point from majority to minority spins and *vice versa.* Thus s_z of the states involved at the crossing are nearly zero when the magnetization points along z, which is in contrast to the spin states involved in the *Class I* anti-crossing points. For the Berry curvature, again we find it exhibits a two-fold symmetry: upon rotation of the magnetization direction from z to x, Ω^0_{yx} (Fig. 4.6(c)) and Ω^0_{zy} (Fig. 4.6(d)) exhibit the same magnitude at the corresponding anti-crossing points.

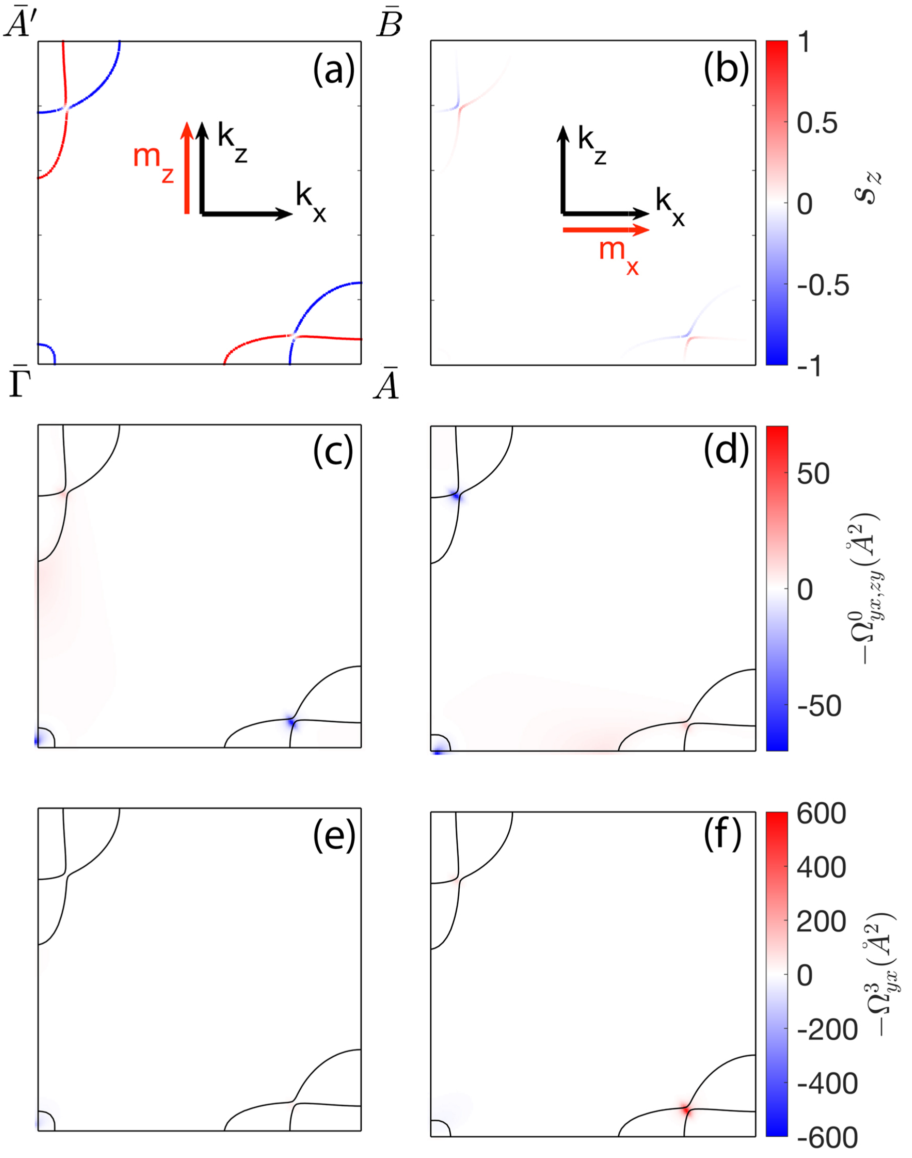

Figure 4.6: Anti-crossing of band with opposite spin.
Reciprocal plane $\bar{\Gamma}(0,\frac{1}{2},0)$-$\bar{A}(\frac{1}{2},\frac{1}{2},0)$-$\bar{A}'(0,\frac{1}{2},\frac{1}{2})$-$\bar{B}(\frac{1}{2},\frac{1}{2},\frac{1}{2})$ plotted with (a,b) spin expectation value s_z,. (c,d) Berry curvatures Ω^0_{yx} and Ω^0_{zy}. (e,f) spin Berry curvature Ω^3_{yx}. The magnetization points along z (a,c,e,g) and x (b,d,f,h). The Fermi contour of selected plane in Black lines (a-d) and red-blue lines (e-h) coded by spin character. The $s_z \equiv \langle n,\boldsymbol{k}|\,\sigma_3\,|n,\boldsymbol{k}\rangle$ is the spin component of Bloch states along z direction. The unit of Ω^0_{ij} and Ω^3_{ij} are in $\AA^2$ (length^2).

The characteristics of the spin Berry curvature, however, is different compared to that of the *Class I* anti-crossing. Interestingly, we find Ω^3_{yx} is nearly zero for magnetization along z (Fig. 4.6(e)) whereas it shows a large positive value when the magnetization is directed along x (Fig. 4.6(f)). It is the large Ω^3_{yx} found at one of the anti-crossings (bottom right of Fig. 4.6(f) and the related points in the Brillouin zone) that contributes to the large SHC when the magnetization points along x. Note that correlation between Ω^0_{yx} and Ω^3_{yx} found in *Class I* anti-crossing (magnetization along z) is lost in *Class II* anti-crossing. In the following, we provide a simple analytical formula that relates the spin character of the states involved in the anti-crossing and the size of Berry and spin Berry curvatures.

4.5.2 Toy model of spin rotation

To describe the characteristics of Berry and spin Berry curvatures in ferromagnets, we model the system using the Bloch wave functions. Let us assume a general spinor for the Bloch state when the magnetization points along $+z$ and $+x$,

$$|n,\boldsymbol{k}\rangle_z = C_n(\boldsymbol{k}) \begin{bmatrix} \cos\frac{\theta_n(\boldsymbol{k})}{2} \\ \sin\frac{\theta_n(\boldsymbol{k})}{2} \end{bmatrix}, \tag{4.4}$$

$$|n,\boldsymbol{k}\rangle_x = C_n(\boldsymbol{k}) \begin{bmatrix} \cos(\frac{\theta_n(\boldsymbol{k})}{2}+\frac{\pi}{4}) \\ \sin(\frac{\theta_n(\boldsymbol{k})}{2}+\frac{\pi}{4}) \end{bmatrix}, \tag{4.5}$$

where $\theta_n(\boldsymbol{k})$ represents the polar angle of the electron spin with respect to the magnetization direction. Note that $\theta_n(\boldsymbol{k})$ depends on the wave vector $\boldsymbol{k}$ and the band index n. For example, when the majority and minority spin bands cross (*i.e.*, *Class II* anti-crossing), the electron spin direction at the crossing point is orthogonal to the magnetization due to the existence of spin orbit interaction. This causes a non-zero Ω^3_{yx} when the magnetization points along x, as will be evident below.

The matrix elements of $\hat{v}^0_i$ and $\hat{v}^3_i$ can be calculated as

$$\langle\hat{v}^0_i\rangle_z \equiv \langle n,\boldsymbol{k}|_z\, \hat{v}^0_i\, |n',\boldsymbol{k}\rangle_z = \langle v_i(\boldsymbol{k})\rangle \cos\frac{\theta'-\theta}{2}, \tag{4.6}$$

$$\langle\hat{v}^0_i\rangle_x \equiv \langle n,\boldsymbol{k}|_x\, \hat{v}^0_i\, |n',\boldsymbol{k}\rangle_x = \langle v_i(\boldsymbol{k})\rangle \cos\frac{\theta'-\theta}{2}, \tag{4.7}$$

$$\langle\hat{v}^3_i\rangle_z \equiv \langle n,\boldsymbol{k}|_z\, \hat{v}^3_i\, |n',\boldsymbol{k}\rangle_z = \langle v_i(\boldsymbol{k})\rangle \cos\frac{\theta'+\theta}{2}, \tag{4.8}$$

$$\langle\hat{v}^3_i\rangle_x \equiv \langle n,\boldsymbol{k}|_x\, \hat{v}^3_i\, |n',\boldsymbol{k}\rangle_x = \langle v_i(\boldsymbol{k})\rangle \sin\frac{\theta'+\theta}{2}, \tag{4.9}$$

where θ and θ' are the average polar angle of the electron spin (averaged over all $\boldsymbol{k}$ states within a band) with respect to the magnetization direction for the two Bloch states $|n, \boldsymbol{k}\rangle_z$ and $|n', \boldsymbol{k}\rangle_z$, respectively. $\langle v_i(\boldsymbol{k})\rangle$ represents the expectation value of the velocity operator with the spatial part of the Bloch state.

According to the Kubo formula, the Berry curvature is represented by the product of two velocity matrix elements, $\langle \hat{v}_i^0 \rangle_{z,x} \langle \hat{v}_j^0 \rangle_{z,x}$, whereas the spin Berry curvature is the product of velocity and spin velocity matrix elements, $\langle \hat{v}_i^3 \rangle_{z,x} \langle \hat{v}_j^0 \rangle_{z,x}$. First, for *Class I* anti-crossing with majority spin states ($\theta = \theta' = 0$), *i.e.* when the magnetization points along z, Eqs. (4.6) and (4.8) indicate that the Berry curvature and the spin Berry curvature take a positive value with the same magnitude. When the magnetization is rotated to x, Eqs. (4.7) and (4.9) suggest that the Berry curvature maintains its magnitude but the spin Berry curvature vanishes. Such characteristics are in agreement with the calculation results shown in Fig. 4.5. Eqs. (4.6) and (4.8) also dictate that the signs of Berry and spin Berry curvature are opposite when the crossing is formed from minority spin states ($\theta = \theta' = \pi$). The effect has been confirmed in the calculations.

For *Class II* anti-crossings with mixed spin states ($\theta + \theta' \sim \pi$ and $\theta = \theta' \sim \frac{\pi}{2}$ at the crossing points), Eqs. (4.6) and (4.7) suggest that the Berry curvature is unchanged under magnetization rotation. In contrast, the spin Berry curvature is expected to be zero when the magnetization points along z and is significantly enhanced when the magnetization is directed along x. These suggestions are consistent with the results shown in Fig. 4.6.

The argument above shows that the SHE in ferromagnetic metals is dependent on the spin character of each band, *i.e.* the spinor part of the Bloch function characterized by θ. Symmetry of Berry curvature does not depend on the absolute spin character of states, θ or θ', but only on the relative angle of polarization between two states, $\theta' - \theta$.

4.6 Fermi energy dependence of AHC and SHC

The Fermi energy dependence of the AHC and SHC for bcc-Fe in two magnetic configurations (m_z and m_x) are presented in Fig. 4.7. The magnitude of AHC for the two magnetic configurations, as expected, are exactly the same, but with different geometries, *i.e.* σ_{yx}^0 for m_z and σ_{zy}^0 for m_x. On the contrary, the SHC shows two distinct profiles for the two magnetic configurations with respect to the shifting of the Fermi energy. The profile of SHC for m_z ($\sigma_{yx}^3(m_z)$) (Black solid line in Fig. 4.7(b)) approximately follows the trend of AHC, indicating significance contributions from the anti-crossing points (*Class I*) with same majority spin, *e.g.* $E_f \sim -0.48$ eV. Consequently, SHC for m_x ($\sigma^3_{yx}(m_x)$) at that Fermi level is relatively small, because of the reduction in spin Berry curvature at *Class I* anti-crossings when magnetization is orthogonal with the spin quantization axis. It indicates at this Fermi level *Class I* anti-crossings are dominant.

When the Fermi level is $E_f \sim -0.8$ eV, we observe a peak of $\sigma^3_{yx}(m_x)$ whose magnitude is over -1400 ($\frac{\hbar}{e}$) S/cm, while the magnitude of both $\sigma^0_{yx}(m_z), \sigma^0_{zy}(m_x)$ and $\sigma^3_{yx}(m_z)$ are less than ±300 ($\frac{\hbar}{e}$) S/cm. The difference between $\sigma^0_{yx}(m_z)$ and $\sigma^0_{yx}(m_x)$ originates from the situation when *Class II* anti-crossings are dominant at Fermi level.

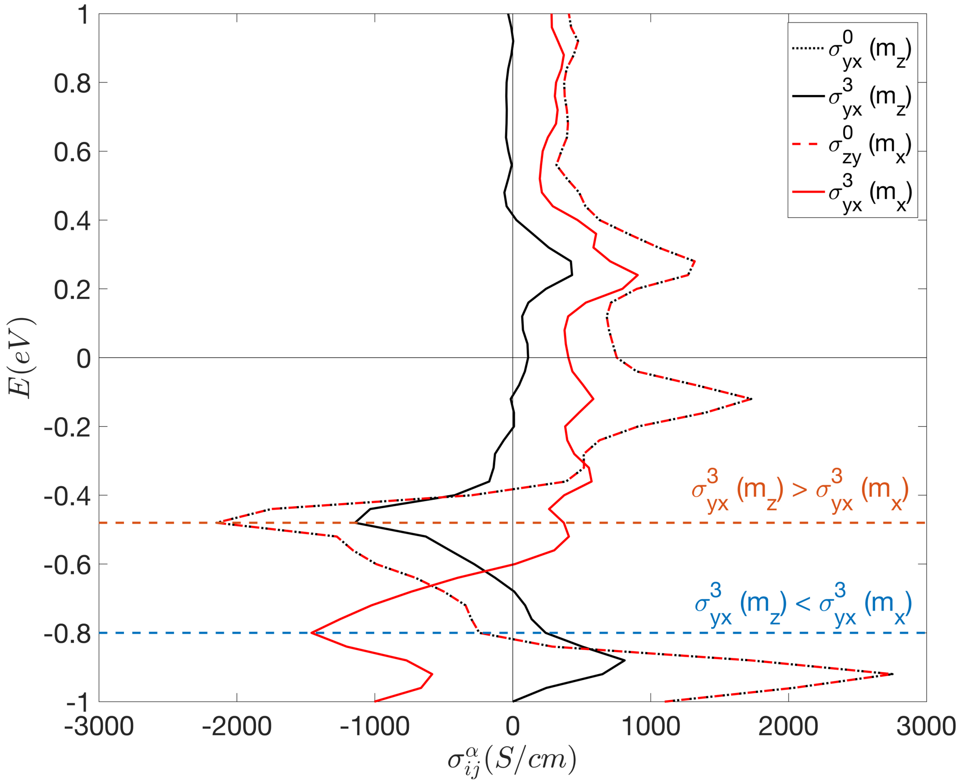

Figure 4.7: Fermi energy dependence of AHC and SHC in bcc-Fe.

For fcc-Ni, the correlation of Fermi energy profiles between $\sigma^3_{yx}(m_z)$ and $\sigma^0_{yx}(m_z), \sigma^0_{zy}(m_x)$ is also clear. The two profiles have opposite signs at Fermi levels $E_f > -0.4$ eV, because of the bands with minority spin (blue lines) in this energy range. The two profiles have the same of sign at Fermi levels $E_f < -0.4$ eV, as bands with majority spin (red lines) appear below -0.4 eV, seen in Fig. 4.8(a). Specifically, AHC and SHC (m_z) both have peaks at $E_f \sim -0.08$ eV (opposite sign) and $E_f \sim -0.72$ eV (same sign), suggesting significant contributions from *Class I* anti-crossings with minority spin and majority spin, respectively.

Peaks of $\sigma^3_{yx}(m_x)$ are observed at around $E_f \sim 0.08$ eV and $E_f \sim -0.52$ eV and magnitude of the AHC and SHC (m_z) are comparably small at these Fermi levels, suggesting the dominance of *Class I* anti-crossings at these Fermi levels.

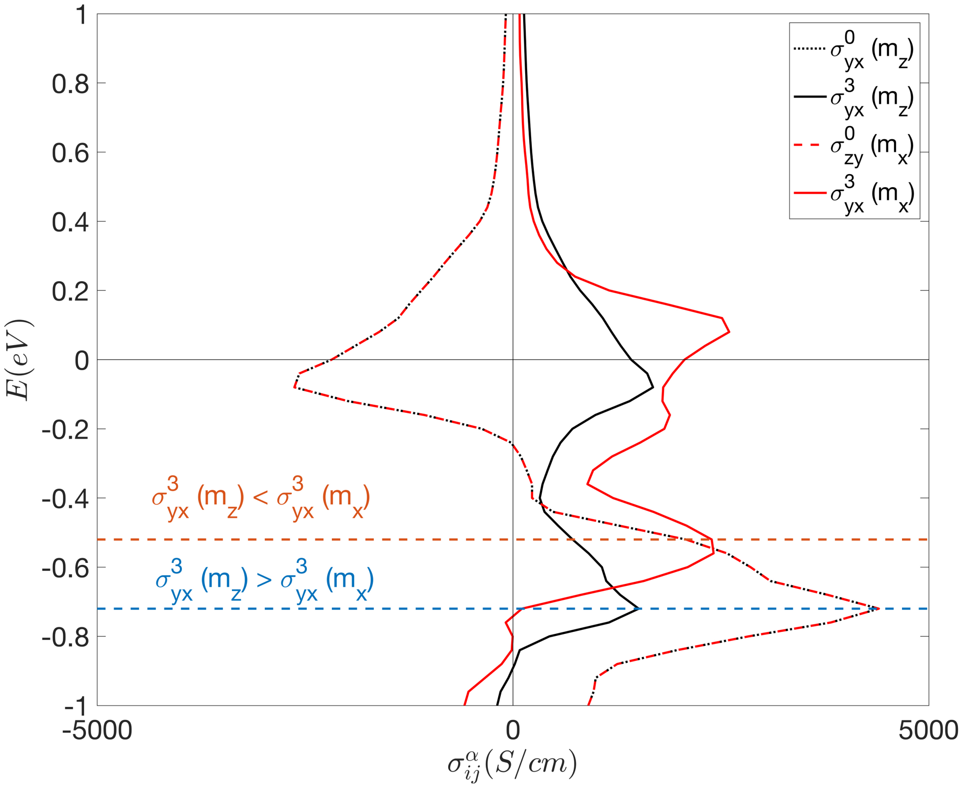

Figure 4.8: Fermi energy dependence of AHC and SHC in fcc-Ni.

It is clear that the relative strength between $\sigma^3_{yx}(m_z)$ and $\sigma^3_{yx}(m_x)$ is highly dependent on the Fermi energy. Specifically, it reflects the competition between *Class I* and *Class II* anti-crossings at the Fermi level. Consequently, the anisotropy of intrinsic spin Hall conductivity, *i.e.*, the magnitude of difference between $\sigma^3_{yx}(m_z)$ and $\sigma^3_{yx}(m_x)$, can be controlled through delicate band engineering. For example, we expect to observe a large longitudinal SHC (m_z case) or a large transverse SHC (m_x case), if shifting the Fermi energy to *Class I* or *Class II* anti-crossings.

4.7 Brief summary

In the Chapter, we have used bcc-Fe and fcc-Ni as a prototype systems to study the intrinsic AHC and SHC in $3d$-ferromagnets, particularly on the magnetization dependence of SHC. Whereas the magnitude of the non-vanishing component of the AHC is independent on the magnetization direction, the non-vanishing component of the SHC is highly dependent on the relative angle between the magnetization and the conduction electron spin orientation. With the conduction electron spin orientation fixed along z, the SHC of bcc-Fe (fcc-Ni) increases by a factor of 4 (1.5) when the magnetization direction is rotated from z to x. Such a magnetization direction dependent SHC originates from the anisotropy of the spin current operator in the spinor space: as the spinor part of the Bloch states changes upon rotating the magnetization direction away from the conduction electron spin orientation, the matrix elements of the spin current operator with the Bloch states vary. The anisotropy of SHE in ferromagnet is found to be associated with the competition between *Class I* and *Class II* anti-crossings at Fermi level. The Fermi energy dependence of SHC indicates the anisotropy of spin Hall conductivity in ferromagnet can be tuned through band engineering. These results show that the SHC in ferromagnets have an extra handle, *i.e.* the magnetization direction, to control its magnitude. It should be noted that spin current with polarization orthogonal to the magnetization does not dephase in ferromagnets, as pointed out by Amin *et al.* [60]. (The origin of the SHC anisotropy in ferromagnets, revealed in this thesis, was not the focus of Amin *et al.*)

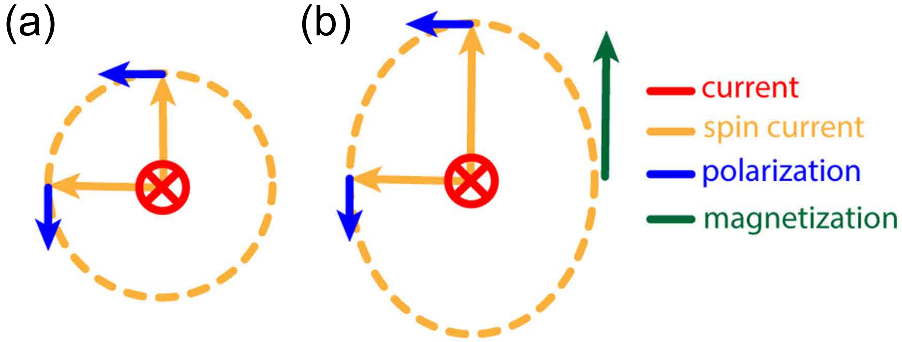

Figure 4.9: Schematic graph of magnetization dependent SHC in ferromagnets.

It is reported that AHE and SHE can be discussed in the same framework of a $U(1) \times SU(2)$ theory [121–124]. For the AHE in ferromagnets, the system has almost always been treated with the spin quantization axis (*i.e.*, the polarization of the electrons) aligned along the magnetization direction. Therefore, the $U(1) \times SU(2)$ theory reduces to a parallel $U(1)$ transport model [123]. For $3d$ transition metals with such parallel configuration, a strong correlation between the Berry curvature and the spin Berry curvature is found, for which one may consider the $U(1) \times U(1)$ theory is a good approximation, specifically for the *Class I* anti-crossings in our studies. This is also possible because the $3d$ transition metals with large exchange splitting do not possess large SOC that will mix the spinor states. However, for a transverse spin current in ferromagnets, *i.e.*, when the spin quantization axis is rotated away from the magnetization direction, the $U(1) \times U(1)$ approximation is no longer valid to discuss the SHE, *e.g.* the *Class II* anti-crossings.

4.A Appendix: Calculation method

The DFT calculations is performed by FLAPW with GGA for the exchange correlation. The primitive cell of bcc-Fe and fcc-Ni are constructed with lattice constant chosen from experimentally determined values, $a_{Fe} = 2.86\text{Å}, a_{Ni} = 3.52\text{Å}$ [125, 126]. MT radius are taken 2.2 bohrs for both Fe and Ni, respectively. The angular momentum expansion inside MT spheres is truncated at $l = 8$ for the wave functions, charge and spin densities, and potential. LAPW functions have a cutoff: $G_{\max}$ is the cutoff vector with $|G_{\max}| = 3.9$ a.u.$^{-1}$. The reciprocal ($\boldsymbol{k}$-) space is divided into $16 \times 16 \times 16$ meshes for calculating charge and spin densities. The spin orbit coupling is treated via the second variational method. The intrinsic AHC and SHC are obtained from the Kubo formula in the static limit,

$$\Omega^{\alpha}_{ij,n}(\boldsymbol{k}) = -\hbar^2 \sum_{n' \neq n} \frac{\mathrm{Im}\Big[[v^{\alpha}_{i}]_{n,n'}(\boldsymbol{k})[v^{0}_{j}]_{n',n}(\boldsymbol{k}) - [v^{0}_{j}]_{n,n'}(\boldsymbol{k})[v^{\alpha}_{i}]_{n',n}(\boldsymbol{k})\Big]}{\Big(\epsilon_n(\boldsymbol{k}) - \epsilon_{n'}(\boldsymbol{k})\Big)^2}, \tag{4.A.1}$$

$$\Omega^{\alpha}_{ij}(\boldsymbol{k}) = \sum_{n} f(\epsilon_n(\boldsymbol{k}))\Omega^{\alpha}_{ij,n}(\boldsymbol{k}), \quad \sigma^{\alpha}_{ij} = -\frac{e^2}{\hbar}\int_{BZ} \frac{d^3\boldsymbol{k}}{(2\pi)^3}\Omega^{\alpha}_{ij}(\boldsymbol{k}). \tag{4.A.2}$$

where σ^{0}_{ij} and σ^{k}_{ij} are the AHC and SHC, respectively, and Ω^{α}_{ij} represents the generalized Berry curvature: Ω^{0}_{ij} and Ω^{k}_{ij} are the Berry and spin Berry curvatures. $v^{\alpha}_{i} = \frac{1}{2}\{\sigma_{\alpha}, v_i\}$ is the general velocity operator with the subscript and superscript denoting the spatial coordinate and the spin quantization axis [122], respectively. v^{0}_{i} and v^{k}_{i} are the charge velocity and spin velocity operators.To reduce numerical error, we extend the size of k-point mesh up to $64 \times 64 \times 64$ with total of 262,144 special k points inside the first BZ to calculate the SHC.

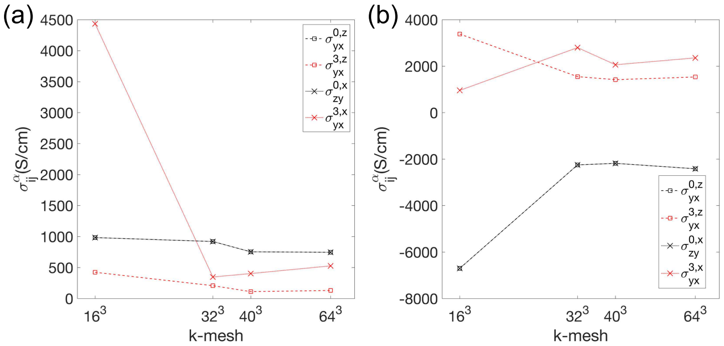

Figure 4.10: Convergence of the integrated AHC and SHC calculations.

Chapter 5

Spin Hall effect in 2DEG with exchange splitting

Contents

5.1 Introduction

The intrinsic spin Hall effect was first predicted to generate a dissipationless spin current in the two-dimensional electron gas (2DEG) with Rashba type spin orbit coupling [14]. In the early theoretical studies, the intrinsic SHE had been extensively focused on 2DEG systems with various type of spin orbit coupling, such as Rashba-type, Dresselhaus-type, Dirac-type, *etc.* [43, 127–130]. It should be noted that the intrinsic SHE in a simple 2DEG Hamiltonian is exactly cancelled by the extrinsic contributions, *e.g.*, the intrinsic side jump, even in the clean limit when considering vertex corrections [43, 44, 128]. However, the cancelation is specifically attributed to the parabolic band dispersion and linearly k-dependent SOC [21, 131], which is rare in realistic material system. Hence, the 2DEG system incorporated with SOC could be treated as the irreducible theoretical model that seizes key features of intrinsic SHE.

In this chapter, we consider a 2DEG system with Rashba-type and Dresselhaus-type SOC and a ferromagnetic ordering. The intrinsic contribution to the SHE is calculated through the Kubo formula in the strong exchange interaction limit and the magnetization direction dependence of SHC is investigated.

5.2 General SU(2) Hamiltonian

5.2.1 intrinsic SHC of general SU(2) Hamiltonian

We shall first consider a free election Hamiltonian with $SU(2)$ gauge field,

$$\mathcal{H}_0(\boldsymbol{k}) \quad = \quad \varepsilon(\boldsymbol{k})\hat{I} + d^a(\boldsymbol{k})\hat{\tau}^a, \tag{5.1}$$

where the first term is the free electron kinetic energy, $\varepsilon(\boldsymbol{k}) = \dfrac{\hbar^2\boldsymbol{k}^2}{2m}$ and $d^a(\boldsymbol{k})$ contains the SOC and exchange interaction.

The band energy of this two level system are,

$$\epsilon_\pm(\boldsymbol{k}) = \epsilon(\boldsymbol{k}) \pm |\boldsymbol{d}|, \tag{5.2}$$

where $|\boldsymbol{d}|$ is the module of vector $\boldsymbol{d} = (d^1, d^2, d^3)$.

Based on the general Hamiltonian, Eq. 5.1, the general velocity operator is defined as,

$$\begin{aligned} v_i^0 &= \frac{1}{\hbar}\frac{\partial \mathcal{H}_0(\boldsymbol{k})}{\partial k_i} = \frac{1}{\hbar}\frac{\partial \varepsilon(\boldsymbol{k})}{\partial k_i} + \frac{1}{\hbar}\frac{\partial d^a(\boldsymbol{k})}{\partial k_i}\hat{\tau}^a, & (5.3)\\ v_i^l &= \frac{1}{2\hbar}\Big\{v_i^0, \hat{\tau}^l\Big\} = \frac{1}{\hbar}\frac{\partial \varepsilon(\boldsymbol{k})}{\partial k_i}\hat{\tau}^l + \frac{1}{\hbar}\frac{\partial d^a(\boldsymbol{k})}{\partial k_i}\delta_{al}, & (5.4) \end{aligned}$$

where v_i^0 represents the charge velocity, while v_i^l represents the spin velocity. The subscript i represents the spatial coordinate for the velocity and the superscripts $0, l$ represent charge and spin velocity polarized along the l-direction, respectively. Note that the charge current operator and spin current operator are simply obtained by multiplying velocity and spin velocity operators with a prefactors $-e$ and $\hbar/2$, respectively.

$$j_i^0 = -ev_i^0, \quad j_i^l = \frac{\hbar}{2}v_i^l. \tag{5.5}$$

The electron Green's function is given as,

$$G_0(\boldsymbol{k}, i\omega_n) = (i\hbar\omega_n + \mu - \mathcal{H}_0(\boldsymbol{k}))^{-1} = f(\boldsymbol{k}, i\omega_n)(g(\boldsymbol{k}, i\omega_n) + d^a(\boldsymbol{k})\hat{\tau}^a), \tag{5.6}$$

where

$$g(\boldsymbol{k}, i\omega_n) = i\hbar\omega_n + \mu - \varepsilon(\boldsymbol{k}), \quad f(\boldsymbol{k}, i\omega_n) = \frac{1}{g^2(\boldsymbol{k}, i\omega_n) - d^a d^a}, \tag{5.7}$$

with μ is the chemical potential, $\omega_n = \frac{(2n+1)\pi}{\hbar\beta}$ is the Matsubara frequency for fermion.

Based on the Kubo formula, the correlation function between the spin velocity v_i^l and the charge velocity v_j^0 reads,

$$\begin{aligned} Q_{ij}^{l0}(iv) &= -\frac{1}{V\hbar}\int_0^{\hbar\beta} du\, e^{ivu}\, \langle \hat{T} v_i^l(u) v_j^0(0)\rangle \\ &= \frac{1}{V\beta}\sum_{\boldsymbol{k},n} tr\Big\{G_0(\boldsymbol{k}, i\omega_n) v_i^\alpha G_0(\boldsymbol{k}, i\omega_n + iv) v_j^0\Big\}, & (5.8) \end{aligned}$$

where $v = \frac{2m\pi}{\hbar\beta}$ and $\beta = 1/k_B T$.

Substituting the unperturbed Green's function and the general velocity operators into Eq. 5.8 and evaluating the Matsubara summation over ω_n, the real and imaginary parts of the correlation function are

$$\begin{aligned}
\mathrm{Re}Q^l_{ij}(iv) &= \frac{4}{V\hbar^2}\sum_k \frac{|\boldsymbol{d}|\Big(n_F(\varepsilon^-(\boldsymbol{k}))-n_F(\varepsilon^+(\boldsymbol{k}))\Big)}{\Big[(\hbar iv)^2-4|\boldsymbol{d}|^2\Big]}\Big\{\frac{d^l}{|\boldsymbol{d}|}\frac{\partial\varepsilon}{\partial k_i}\frac{d^n}{|\boldsymbol{d}|}\frac{\partial d^n}{\partial k_j}-\frac{\partial\varepsilon}{\partial k_i}\frac{\partial d^a}{\partial k_j}\Big\}, \quad (5.9)\\
\mathrm{Im}Q^l_{ij}(iv) &= -\frac{4}{V\hbar^2}\sum_k \frac{\hbar\omega\Big(n_F(\varepsilon^-(\boldsymbol{k}))-n_F(\varepsilon^+(\boldsymbol{k}))\Big)}{2|\boldsymbol{d}|\Big[(\hbar iv)^2-4|\boldsymbol{d}|^2\Big]}\epsilon_{lnm}d^n\frac{\partial\varepsilon}{\partial k_i}\frac{\partial d^m}{\partial k_j}, \quad (5.10)
\end{aligned}$$

where $n_F(\epsilon^{\pm})\equiv n_{F\pm}$ is Fermi distribution function of the lower(-) and upper(+) bands. The calculation details of taking the trace and the Matsubara summation are presented in Appendix. 5.A,5.B.

In the static limit ($iv=\omega\to 0$), we obtain the spin Hall conductivity tensor,

$$\sigma^l_{ij} = -\frac{e\hbar}{2}\lim_{\omega\to 0}\frac{Q^{l0}_{ij}(\omega)-Q^{l0}_{ij}(0)}{i\omega} = \frac{-e}{4V}\sum_k \frac{n_{F-}-n_{F+}}{|\boldsymbol{d}|^3}\epsilon_{lnm}d^n\frac{\partial\varepsilon}{\partial k_i}\frac{\partial d^m}{\partial k_j}. \tag{5.11}$$

Note that the spin Hall conductivity is obtained by multiplying a prefactor $-\frac{e\hbar}{2}$ (see Eq. 5.5).

5.2.2 Strong exchange interaction approximation

The $SU(2)$ gauge field can be further separated into two parts: a $\boldsymbol{k}$-dependent term $A^a(\boldsymbol{k})$, which represents the SOC term; a $\boldsymbol{k}$-independent term $A^a_0(\boldsymbol{M})$, which represents the exchange interaction,

$$d^a = A^a(\boldsymbol{k}) + A^a_0(\boldsymbol{M}), \tag{5.12}$$

where $\boldsymbol{M}$ represents the spontaneous magnetization vector.

Hereafter, we assume that the strength of exchange interaction ($|\boldsymbol{A}_0|$) is much large than the SOC ($|\boldsymbol{A}|$) for a certain range of wave vector $\boldsymbol{k}$, *i.e.*, $|\boldsymbol{A}(\boldsymbol{k})|/|\boldsymbol{A}_0| \ll 1$. In the strong exchange approximation, the band energy can be expanded in orders of $|\boldsymbol{A}_0|$ as

$$\begin{aligned}
\epsilon_{\pm}(\boldsymbol{k}) &= \epsilon_0(\boldsymbol{k}) \pm |\boldsymbol{d}| = \epsilon_0(\boldsymbol{k}) \pm \big(|\boldsymbol{A}|^2+|\boldsymbol{A}_0|^2+2A^aA^a_0\big)^{1/2}\\
&= \epsilon_0(\boldsymbol{k}) \pm \big(|\boldsymbol{A}|^2+|\boldsymbol{A}_0|^2\big)^{1/2} \pm \frac{A^aA^a_0}{\big(|\boldsymbol{A}|^2+|\boldsymbol{A}_0|^2\big)^{1/2}} + \mathcal{O}(|\boldsymbol{A}_0|^0), \quad (5.13)
\end{aligned}$$

Similarly, we rewrite the spin Hall conductivity (Eq. 5.11) in order of exchange interaction $|\boldsymbol{A}_0|$,

$$\begin{aligned}\sigma^l_{ij} &= \frac{-e}{4V}\sum_k \frac{n_{F-}-n_{F+}}{(|\boldsymbol{A}|^2+|\boldsymbol{A}_0|^2+2A^aA^a_0)^{3/2}}\epsilon_{lnm}\left(A^n+A^n_0\right)\frac{\partial\varepsilon}{\partial k_i}\frac{\partial A^m}{\partial k_j}, \\ &= \frac{-e}{4V}\sum_k \frac{n_{F-}-n_{F+}}{(|\boldsymbol{A}|^2+|\boldsymbol{A}_0|^2)^{3/2}}\epsilon_{lnm}\frac{\partial\varepsilon}{\partial k_i}\frac{\partial A^m}{\partial k_j} \\ &\quad \Big\{A^n+A^n_0(\boldsymbol{M})-3A^aA^a_0A^n-3A^aA^a_0A^n_0(\boldsymbol{M})+\mathcal{O}(|\boldsymbol{A}_0|^{-1})\Big\}. \end{aligned} \tag{5.14}$$

The integral in Eq. 5.14 is separated into four parts, $I_0, I_1, I_2,$and I_3,

$$I_0 = \frac{-e}{4V}\sum_k \frac{n_{F-}-n_{F+}}{(|\boldsymbol{A}|^2+|\boldsymbol{A}_0|^2)^{3/2}}\epsilon_{lnm}A^n\frac{\partial\varepsilon}{\partial k_i}\frac{\partial A^m}{\partial k_j}, \tag{5.15a}$$

$$I_1 = \frac{-e}{4V}\sum_k \frac{n_{F-}-n_{F+}}{(|\boldsymbol{A}|^2+|\boldsymbol{A}_0|^2)^{3/2}}\epsilon_{lnm}A^n_0\frac{\partial\varepsilon}{\partial k_i}\frac{\partial A^m}{\partial k_j}, \tag{5.15b}$$

$$I_2 = \frac{3e}{4V}\sum_k \frac{n_{F-}-n_{F+}}{(|\boldsymbol{A}|^2+|\boldsymbol{A}_0|^2)^{5/2}}A^aA^a_0\epsilon_{lnm}A^n\frac{\partial\varepsilon}{\partial k_i}\frac{\partial A^m}{\partial k_j}, \tag{5.15c}$$

$$I_3 = \frac{3e}{4V}\sum_k \frac{n_{F-}-n_{F+}}{(|\boldsymbol{A}|^2+|\boldsymbol{A}_0|^2)^{5/2}}A^aA^a_0\epsilon_{lnm}A^n_0\frac{\partial\varepsilon}{\partial k_i}\frac{\partial A^m}{\partial k_j}. \tag{5.15d}$$

5.3 Rashba and Dresselhaus SOC

5.3.1 Band dispersions and Fermi contours

Now, we consider the explicit form of $A^a(\boldsymbol{k})$ and $A^a_0(\boldsymbol{M})$. $A^a(\boldsymbol{k})$ consists of the Rashba-type and Dresselhaus-type SOC:

$$A^1 = \beta k_x+\alpha k_y, \quad A^2=-\beta k_y-\alpha k_x, \quad A^3=0, \tag{5.16}$$

and $A^a_0(\boldsymbol{M})$ is the exchange interaction as a mean field:

$$A^1_0 = M_1, \quad A^2_0=M_2, \quad A^3_0=M_3, \tag{5.17}$$

where we choose $\hbar=1$, α and β are respectively the strength of Rashba-type and Dresselhaus-type SOC.

The eigenenergies of the above Hamiltonian are,

$$\begin{aligned}\varepsilon_\pm(\boldsymbol{k}) &= \epsilon_0(\boldsymbol{k}) \pm |\boldsymbol{d}| = \epsilon_0(\boldsymbol{k}) \pm \left(|\boldsymbol{A}|^2 + |\boldsymbol{A}_0|^2 + 2A^a A_0^a\right)^{1/2} \\ &= \epsilon_0(\boldsymbol{k}) \pm \left(|\boldsymbol{A}|^2 + |\boldsymbol{A}_0|^2\right)^{1/2} \pm \frac{A^a A_0^a}{\left(|\boldsymbol{A}|^2 + |\boldsymbol{A}_0|^2\right)^{1/2}} + \mathcal{O}(|\boldsymbol{A}_0|^0) \\ &\sim \epsilon_0(\boldsymbol{k}) \pm |\boldsymbol{M}| \pm \frac{A^a A_0^a}{|\boldsymbol{M}|}, \end{aligned} \tag{5.18}$$

where we apply the strong exchange interaction approximation, $|\boldsymbol{A}(\boldsymbol{k})|/|\boldsymbol{A}_0| \ll 1$.

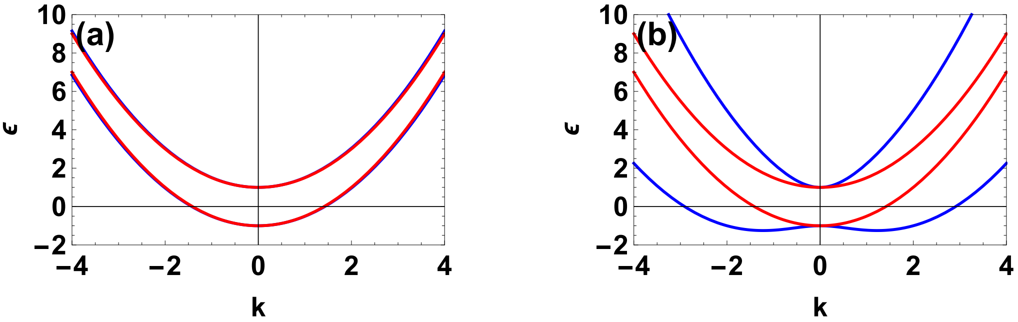

Figure 5.1: Band dispersion under strong exchange interaction approximation. Band energy of model Hamiltonian with exchange splitting along z-direction, $\boldsymbol{A}_0 = (0, 0, M)$. The Red color represents band energy with expansion of $\boldsymbol{M}$. The Blue color represents band energy without expansion. Two sets of parameters are chosen as $m = 1$, $\alpha = \beta = 0.1$, $M = 1$ (a) and $m = 1$, $\alpha = \beta = 1$, $M = 1$ (b).

In Fig. 5.1, we present the band dispersions with and without the strong exchange interaction approximation with the exchange splitting along the z-direction. The band dispersions with the approximation are nearly coincided with those without expansion of $\boldsymbol{A}_0$, indicating the the approximation is robust around Fermi level when strength of SOC is much smaller than exchange interaction, $\alpha, \beta \ll |\boldsymbol{M}|$ (Fig. 5.1(a)). When the strength of SOC is comparable with the exchange splitting (Fig. 5.1(b)), the expansion is no longer valid, as the band dispersions of the two cases diverge significantly.

Under the strong exchange interaction approximation in Eq. 5.18, we investigate the Fermi contours of the two levels when the magnetization is aligned along the following three specific directions: a) M_z case, $\boldsymbol{A}_0 = (0, 0, M)$; b) M_y case, $\boldsymbol{A}_0 = (0, M, 0)$; and c) M_x case, $\boldsymbol{A}_0 = (M, 0, 0)$.

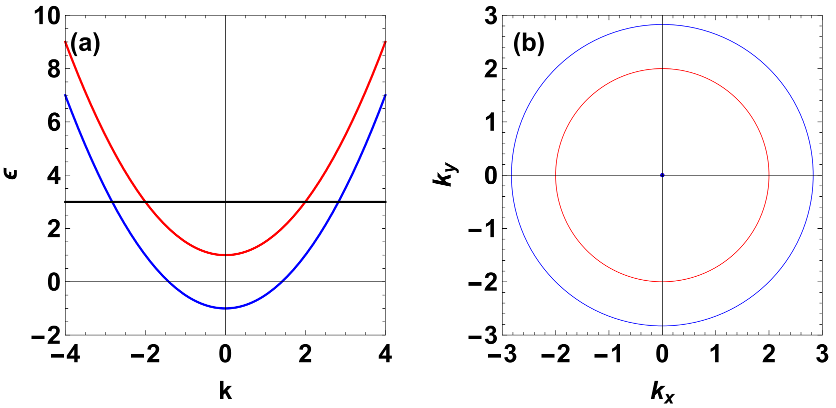

Figure 5.2: Band dispersions and Fermi contours in M_z case.
(a) Band energy of model Hamiltonian with exchange splitting along z-direction ($m = 1$, $\alpha = \beta = 0.1$, $||\boldsymbol{M}|| = 1$). (b) The Fermi contours of bottom(blue) and top(red) bands. The Fermi energy is chosen as $\mu = 3$.

a. Exchange splitting along z direction

When the exchange splitting is along the z direction, the exchange interaction does not entangle with the SOC (A^3=0). Thus, the band energies of two levels are simply parabolic dispersion split by the exchange interaction (Fig. 5.2(a)),

$$\varepsilon_{\pm}(\boldsymbol{k}) \quad = \quad \varepsilon_0(\boldsymbol{k}) \pm |\boldsymbol{M}| = \frac{k_x^2 + k_y^2}{2m} \pm |\boldsymbol{M}|. \tag{5.19}$$

The Fermi contours of the two levels are two concentric circles with the Fermi momentum of the two levels denoted as $k_{\pm} = \sqrt{2m\left(\mu \mp |\boldsymbol{M}|\right)}$ (Fig. 5.2(b)).

b. Exchange splitting along y direction

When the exchange splitting is along the y direction, the exchange interaction entangles with the SOC and the band dispersion of the two levels are shifted toward opposite direction (Fig. 5.3(a)). The band energies of two levels are,

$$\begin{aligned}\varepsilon_{\pm}(\boldsymbol{k}) &= \varepsilon_0(\boldsymbol{k}) \pm |\boldsymbol{M}| \pm \frac{A^2 M}{|\boldsymbol{M}|} = \frac{k_x^2 + k_y^2}{2m} \pm |\boldsymbol{M}| \pm \mathrm{sgn}(M)\left(-\beta k_y - \alpha k_x\right) \\ &= \frac{\left(k_x \mp \mathrm{sgn}(M) m\alpha\right)^2 + \left(k_y \mp \mathrm{sgn}(M) m\beta\right)^2}{2m} - \frac{m}{2}(\beta^2 + \alpha^2) \pm |\boldsymbol{M}|. \end{aligned} \tag{5.20}$$

Concurrently, the Fermi contours of the two levels are two eccentric circles with dis-

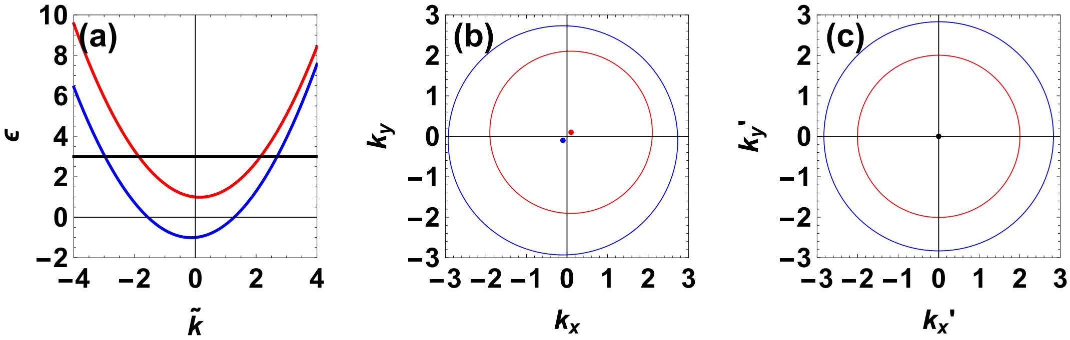

Figure 5.3: Band dispersions and Fermi contours in M_y case.
Band energy of model Hamiltonian with exchange splitting along y-direction ($m = 1$, $\alpha = \beta = 0.1$, $|\boldsymbol{M}| = 1$). (a) The band dispersion along selected wave vector $\tilde{k} = \frac{k}{\sqrt{\alpha^2+\beta^2}}(\alpha, \beta)$. (b) the Fermi contours and (c) the shifted Fermi contours of two level system. The Fermi energy is chosen as $\mu = 3$.

placed center $(\pm m\alpha, \pm m\beta)$ for bottom (blue) and top (red) bands, respectively (Fig. 5.3(b)).

In the following calculations, we shift the Fermi contours of the two levels back to the origin using the following relation,

$$\begin{cases} k'_{x,\pm} = k_x \mp \mathrm{sgn}(M) m\alpha, \\ k'_{y,\pm} = k_y \mp \mathrm{sgn}(M) m\beta. \end{cases} \tag{5.21}$$

The band energies of two levels with shifted wave vector are,

$$\varepsilon_\pm(\boldsymbol{k}) = \frac{k'^2_{x,\pm} + k'^2_{y,\pm}}{2m} - \frac{m}{2}(\beta^2 + \alpha^2) \pm |\boldsymbol{M}|. \tag{5.22}$$

The shifted Fermi contours are concentric circles (Fig. 5.3(c)) with the shifted Fermi momentum, $k'_\pm = \sqrt{2m\left(\mu \mp |\boldsymbol{M}|\right) + m^2(\beta^2 + \alpha^2)}$.

c. Exchange splitting along x direction

The M_x case (exchange splitting along x direction) shares similar features with the M_y case. The exchange splitting again entangles with the SOC while the band dispersions of the two levels are shifted in different direction, *i.e.*, $\tilde{k} = k/\sqrt{\alpha^2 + \beta^2}(\beta, \alpha)$. The band

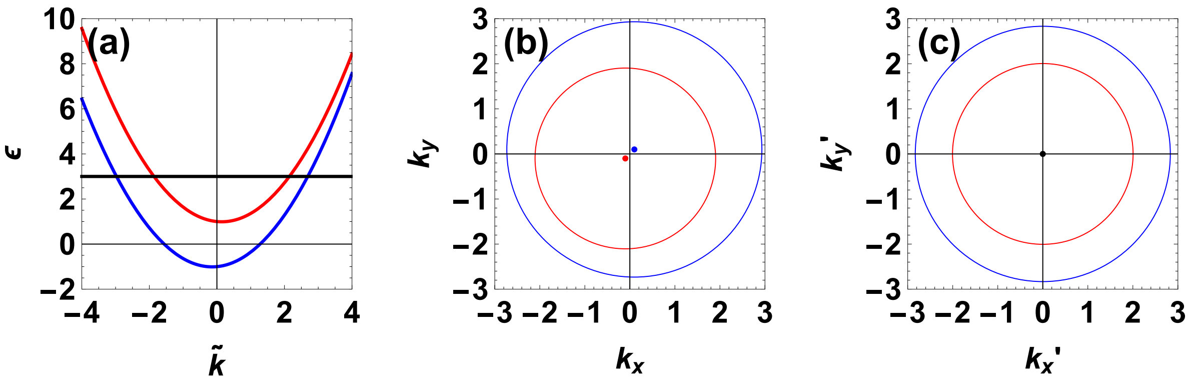

Figure 5.4: Band dispersions and Fermi contours in M_x case. Band energy of model Hamiltonian with magnetic field along y-direction ($m = 1$, $\alpha = \beta = 0.1$, $|\boldsymbol{M}| = 1$). (a) The band dispersion along selected wave vector $\tilde{k} = \frac{k}{\sqrt{\alpha^2+\beta^2}}(\beta, \alpha)$. (b) the Fermi contours and (c) the shifted Fermi contours of two level system. The Fermi energy is chosen as $\mu = 3$.

dispersions for the two levels are,

$$\begin{aligned}\varepsilon_\pm(\boldsymbol{k}) &= \varepsilon_0(\boldsymbol{k}) \pm |\boldsymbol{M}| \pm \frac{A^1 M}{|\boldsymbol{M}|} = \frac{k_x^2 + k_y^2}{2m} \pm |\boldsymbol{M}| \pm \operatorname{sgn}(M)\,(\beta k_x + \alpha k_y) \\ &= \frac{(k_x \pm \operatorname{sgn}(M) m\beta)^2 + (k_y \pm \operatorname{sgn}(M) m\alpha)^2}{2m} - \frac{m}{2}(\beta^2 + \alpha^2) \pm |\boldsymbol{M}|. \quad (5.23)\end{aligned}$$

Here, the Fermi contours of two level are two eccentric circles with different centers $(\mp m\beta, \mp m\alpha)$ (Fig. 5.4(b)).

Similarly, we can shift the Fermi contours back to the origin using the relation,

$$\begin{cases} k'_{x,\pm} = k_x \pm \operatorname{sgn}(M) m\beta, \\ k'_{y,\pm} = k_y \pm \operatorname{sgn}(M) m\alpha. \end{cases} \tag{5.24}$$

The shifted band energy of the two levels are,

$$\varepsilon_\pm(\boldsymbol{k}) = \frac{k'^2_{x,\pm} + k'^2_{y,\pm}}{2m} - \frac{m}{2}(\beta^2 + \alpha^2) \pm |\boldsymbol{M}|, \tag{5.25}$$

with the shifted Fermi momentum, $k'_\pm = \sqrt{2m\,(\mu \mp |\boldsymbol{M}|) + m^2(\beta^2 + \alpha^2)}$.

5.3.2 Intrinsic SHC of 2DEGs with SOC and exchange interaction

The spin Hall conductivity is calculated separately for the above three cases: a) M_z case, $\boldsymbol{A}_0 = (0, 0, M)$; b) M_y case, $\boldsymbol{A}_0 = (0, M, 0)$; and c) M_x case, $\boldsymbol{A}_0 = (M, 0, 0)$.

a. Exchange splitting along z direction, $\boldsymbol{A}_0 = (0, 0, M)$

When the exchange splitting is not entangled with the SOC, the last three terms in Eq. 5.15 all vanish. The spin Hall conductivity, σ^3_{yx}, is reduced to the following integrals,

$$
\begin{aligned}
I_0(M_3) &= e\frac{\alpha^2 - \beta^2}{4mV|\boldsymbol{M}|^3}\sum_k \left(n_{F-} - n_{F+}\right) k_y^2, \\
I_1(M_3) &= I_2(M_3) = I_3(M_3) = 0. \qquad (5.26)
\end{aligned}
$$

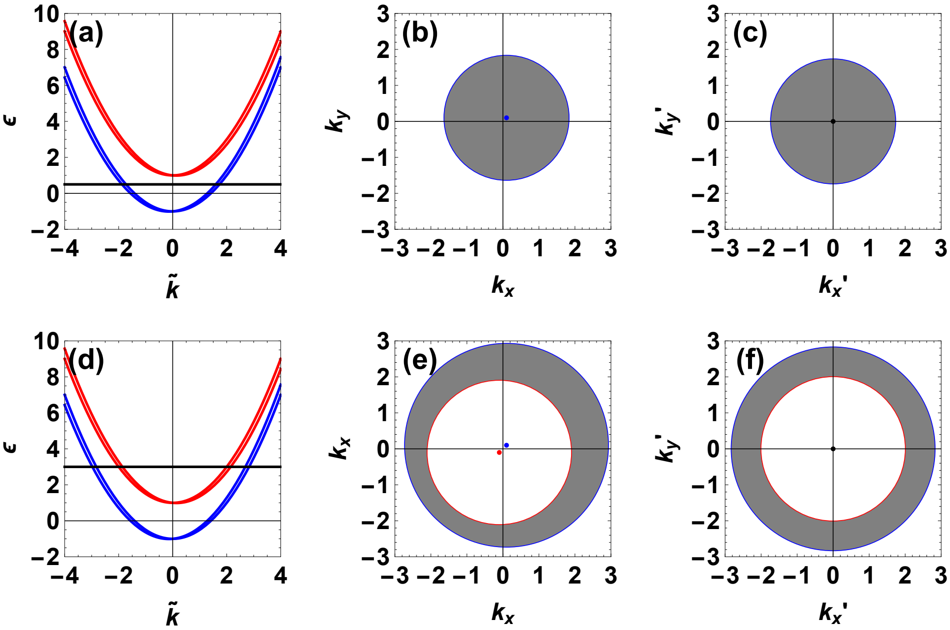

Figure 5.5: Two types of integration area.
Two types of integration area: i)a circle of bottom band (a,b,c); ii) ring between bottom band and top band (d,e,f). (a,d) the band dispersion of bottom and top bands. (b,e) Fermi contours of two levels with integration area colored in gray. (c,f) shifted Fermi contours of two levels with integration area colored in gray.

Assuming zero temperature, the Fermi distribution function is reduced to a step function. We categorize the integration area into two groups: i) a circle of the bottom band

($-|\boldsymbol{M}| < \mu < |\boldsymbol{M}|$); ii) a ring between the bottom band and the top band $\mu > |\boldsymbol{M}|$ (Fig. 5.5). The integration areas over the bottom and the top bands are defined as $\Omega_{\pm}$. The calculation detail are described in Appendix 5.C.

The spin Hall conductivity in the M_z case, $\boldsymbol{A}_0 = (0, 0, M)$, is

$$\sigma^3_{yx}(\mu) = \begin{cases} \dfrac{em\left(\alpha^2 - \beta^2\right)}{16\pi|\boldsymbol{M}|^3}\left(|\boldsymbol{M}| + \mu\right)^2 & -|\boldsymbol{M}| < \mu < |\boldsymbol{M}| \\ \dfrac{em(\alpha^2 - \beta^2)}{4\pi|\boldsymbol{M}|^2}\mu & |\boldsymbol{M}| < \mu \end{cases} \tag{5.27}$$

b. Exchange splitting along y direction, $\boldsymbol{A}_0 = (0, M, 0)$

In the M_y case ($\boldsymbol{A}_0 = (0, M, 0)$), the spin Hall conductivity in Eq. 5.15 is calculated explicitly,

$$I_0(M_2) = e\frac{\alpha^2 - \beta^2}{4mV|\boldsymbol{M}|^3}\sum_k \left(n_{F-} - n_{F+}\right) k_y^2 \tag{5.28a}$$

$$I_1(M_2) = e\frac{M\beta}{4mV|\boldsymbol{M}|^3}\sum_k \left(n_{F-} - n_{F+}\right) k_y \tag{5.28b}$$

$$I_2(M_2) = -e\frac{3M}{4mV|\boldsymbol{M}|^5}\sum_k \left(n_{F-} - n_{F+}\right)(\alpha^2 - \beta^2)(\beta k_y^3 + \alpha k_y^2 k_x) \tag{5.28c}$$

$$I_3(M_2) = -e\frac{3}{4mV|\boldsymbol{M}|^3}\sum_k \left(n_{F-} - n_{F+}\right)(-\beta^2 k_y^2 - \beta\alpha k_y k_x) \tag{5.28d}$$

To simplify the calculation, we change variables using the relation denoted in Eq. 5.21 and shift the integration area back to the origin (Fig. 5.5(c,f)), as described in Appendix 5.C. The spin Hall conductivity in the M_y case, $\boldsymbol{A}_0 = (0, 0, M)$, is

$$\sigma^3_{yx}(\mu) \approx \begin{cases} \dfrac{em}{16\pi M^3}(\mu + M)\left[M\left(\alpha^2 + \beta^2\right) + \mu\left(\alpha^2 + 2\beta^2\right)\right] & -|\boldsymbol{M}| < \mu < |\boldsymbol{M}| \\ \dfrac{em}{8\pi M^4}\left[\mu M^2\left(2\alpha^2 + 3\beta^2\right) + 3m\mu^2\left(\alpha^2 - \beta^2\right)\left(\alpha^2 + 3\beta^3\right)\right] & |\boldsymbol{M}| < \mu \end{cases} \tag{5.29}$$

c. Exchange splitting along x direction, $\boldsymbol{A}_0 = (M, 0, 0)$

In the M_x case, the spin Hall conductivity in Eq. 5.15 is shown by the following integrals,

$$I_0(M_1) = e\frac{\alpha^2 - \beta^2}{4mV|\boldsymbol{M}|^3}\sum_{\boldsymbol{k}} (n_{F-} - n_{F+})\, k_y^2 \tag{5.30a}$$

$$I_1(M_1) = e\frac{M\alpha}{4mV|\boldsymbol{M}|^3}\sum_{\boldsymbol{k}} (n_{F-} - n_{F+})\, k_y \tag{5.30b}$$

$$I_2(M_1) = -e\frac{3M}{4mV|\boldsymbol{M}|^5}\sum_{\boldsymbol{k}} (n_{F-} - n_{F+})\, (\alpha^2 - \beta^2)(\alpha k_y^3 + \beta k_y^2 k_x) \tag{5.30c}$$

$$I_3(M_{)} = -e\frac{3}{4mV|\boldsymbol{M}|^3}\sum_{\boldsymbol{k}} (n_{F-} - n_{F+})\, (\alpha^2 k_y^2 + \alpha\beta k_y k_x) \tag{5.30d}$$

Shifting the wave vector $\boldsymbol{k}$ along different direction (Eq. 5.23), the spin Hall conductivity in the M_x case, $\boldsymbol{A}_0 = (M, 0, 0)$, is

$$\sigma_{yx}^3(\mu) \approx \begin{cases} -\dfrac{em}{16\pi M^3}(\mu + M)\left[M\left(\alpha^2 + \beta^2\right) + \mu\left(2\alpha^2 + \beta^2\right)\right] & -|\boldsymbol{M}| < \mu < |\boldsymbol{M}| \\ -e\dfrac{m}{8\pi M^4}\left[\mu M^2\left(3\alpha^2 + 2\beta^2\right) + 3m\mu^2\left(\alpha^2 - \beta^2\right)\left(3\alpha^2 + \beta^3\right)\right] & |\boldsymbol{M}| < \mu \end{cases} \tag{5.31}$$

The σ_{yx}^3 of the M_x case (Eq. 5.31) is related to that of M_y (Eq. 5.29) by exchanging the strength of Rashba-type (α) and Dresselhaus-type (β) SOC and multiplying a minus sign.

5.4 Numerical calculation

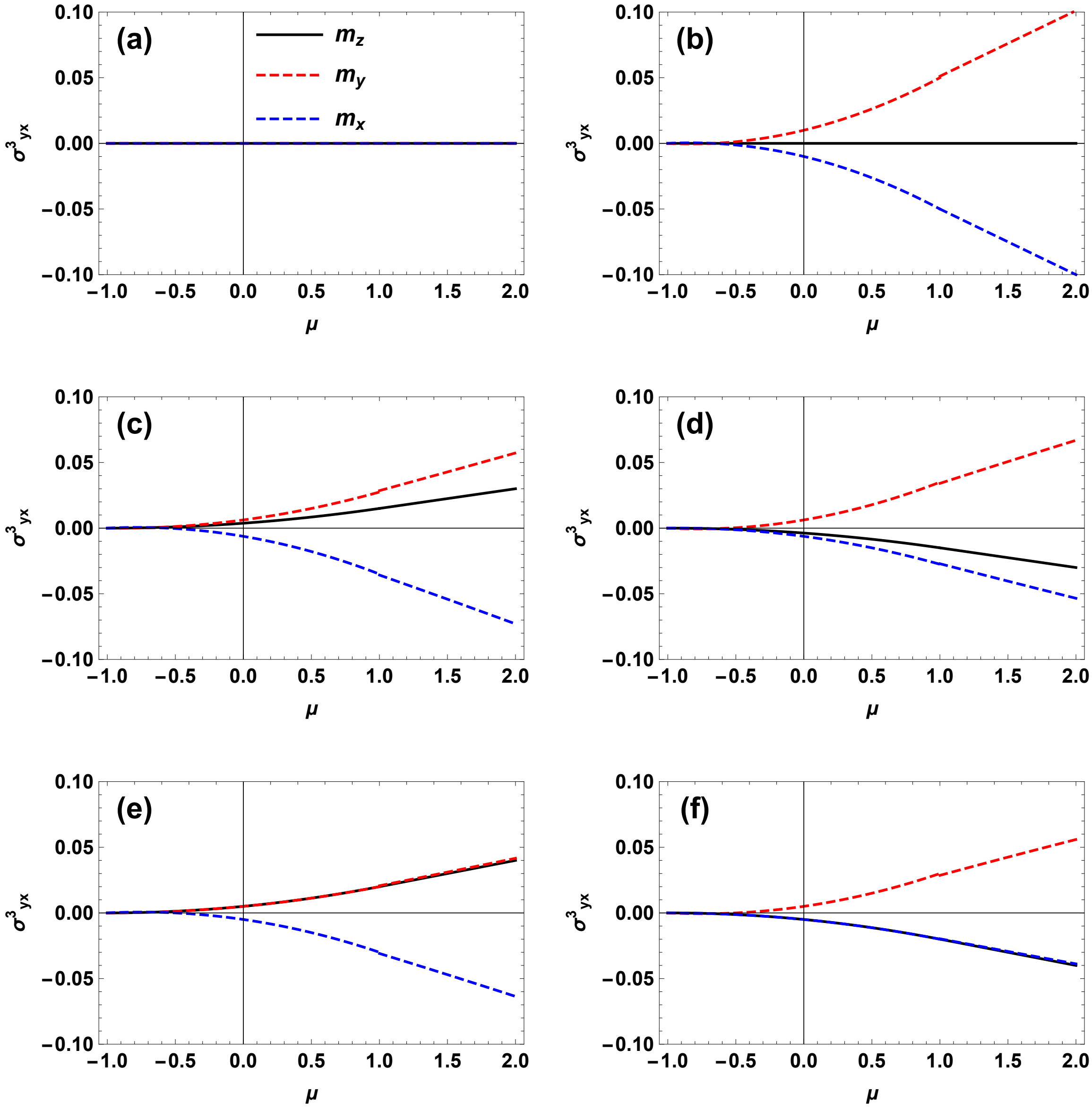

Figure 5.6: Numerical results of spin Hall conductivity σ^3_{yx}.

Numerical calculation results of σ^3_{yx} in three cases: a) $\boldsymbol{A}_0 = (0, 0, M)$ (black); b) $\boldsymbol{A}_0 = (0, M, 0)$ (red); and c) $\boldsymbol{A}_0 = (M, 0, 0)$ (blue). The parameters are $|\boldsymbol{M}| = m = 1$. (a) $\alpha = \beta = 0$,(b) $\alpha = \beta = 0.1$,(c) $\alpha = 0.1, \beta = 0.05$,(d) $\alpha = 0.05, \beta = 0.1$, (e) $\alpha = 0.1, \beta = 0$, and (f) $\alpha = 0, \beta = 0.1$. The σ^3_{yx} is in unit of $\frac{e}{8\pi}$.

The intrinsic SHC σ^3_{yx}, of the three specific exchange splitting directions (M_z, M_y, M_x) are calculated numerically with changing the relative strength of Rashba-type (α) and

Dresselhaus-type (β) SOC (Fig. 5.6). The maximum strength of SOC is limited to be much smaller than the exchange splitting, $|\boldsymbol{M}|$.

In Fig. 5.6(a), σ_{yx}^{3} vanishes for all cases when the two types of SOC are set to zero. This confirms that the intrinsic SHC universally originates from the SOC [14]. If the strength of Rashba and Dresselhaus SOC are equal ($|\alpha| = |\beta|$), σ_{yx}^{3} in the M_z case also vanishes and σ_{yx}^{3} in the M_y, M_x cases have same magnitude but with opposite sign (Fig. 5.6(b)). The exact cancelation of σ_{yx}^{3} in the M_z case is attributed to a delicate interplay between the Dresselhaus and the Rashba SOC, which leads to momentum-independent eigenspinors [132–134]. However, when the exchange interaction is in-plane, *i.e.*, the M_y and M_x cases, the exchange interaction entangles with the SOC and breaks the cancellation, leading to a non-vanishing σ_{yx}^{3}.

When the relative strength of Rashba and Dresselhaus SOC differs (Fig. 5.6(c,d)), σ_{yx}^{3} is non-zero in the M_z case and its sign depends on the relative magnitude of $|\alpha|$ and $|\beta|$: positive for $|\alpha| > |\beta|$; negative for $|\alpha| < |\beta|$. σ_{yx}^{3} in the M_y and M_x cases have opposite sign and unequal magnitude due to the difference of $|\alpha|$ and $|\beta|$. The magnitude reduces with decreasing strength of SOC (either $|\alpha|$ or $|\beta|$).

In Fig. 5.6(e), we turn off the Dresselhaus-type SOC ($\beta = 0$). In such case, σ_{yx}^{3} in the M_z and M_y are exactly the same, while σ_{yx}^{3} in the M_x case differs in magnitude with opposite sign. In the absence of Dresselhaus-type SOC, the Fermi contours of the two levels are shifted only along the x direction in the M_y case and along the y direction in the M_x case. It is the Fermi contours shifted along the y direction that contributes to σ_{yx}^{3} nontrivially, which can be seen from Eqs. 5.28,5.30. On the contrary, when the Rashba-type SOC is turned off ($\beta = 0$), σ_{yx}^{3} for the M_z and M_x cases are the same (Fig. 5.6(f)). Note that in such case, the Fermi contours of the two levels is shifted only along the y direction in the M_y case and along the x direction in the M_x case. Thus, σ_{yx}^{3} in the M_y case has a distinct magnitude and sign.

5.5 Brief summary

In this chapter, we have presented a theory of anisotropic SHC for 2DEG with SOC and large exchange interaction in its intrinsic regime. Both Rashba-type and Dresselhaus spin orbit coupling are investigated by choosing the exchange interaction along three specific directions,*i.e.*, M_z, M_y, and M_x axes. The intrinsic SHC is found to be highly anisotropic due to the entanglement between exchange interaction and SOC. When exchange splitting is in plane (M_y and M_x cases), the exchange interaction entangles with both Rashba and Dresselhaus SOC, shifting the Fermi contours of the two levels away from origin. I

In the case of equal strength of Rashba and Dresselhaus SOC ($|\alpha| = |\beta|$), σ^3_{yx} disappears in the M_z case, indicating a strong cancelation when the Fermi contours of the two levels are concentric. However, σ^3_{yx} for the M_y and M_x cases are finite, due to the Fermi contours shifted by the SOC and exchange interaction. σ^3_{yx} for the M_y and M_x cases are always kept opposite sign, for which the Fermi contours in the two cases are shifted towards different directions. Thus, in the case for $|\alpha| = |\beta|$, σ^3_{yx} vanishes when spontaneous magnetization is out-of plane and is highly anisotropic with in-plane magnetization.

For the case of different relative strength of Rashba and Dresselhaus SOC ($|\alpha| \neq |\beta|$), the σ^3_{yx} is always finite, even for the M_z case where the exchange splitting is not entangled with SOC. The appearance of σ^3_{yx} originates from partial cancelation between Rashba and Dresselhaus SOC. Consequently, σ^3_{yx} is fully anisotropic along z, y, and x axes. Two special cases are studied when we turn off one type of SOCs. For example, if we consider the Rashba-SOC only, σ^3_{yx} is isotropic when the spontaneous magnetization is in zy-plane. If we consider the Dresselhaus SOC only, σ^3_{yx} is isotropic when the spontaneous magnetization is in z-x plane. This distinct behavior originates from the shifted Fermi contours.

In summary, we study the intrinsic SHE in 2DEG with ferromagnetic ordering. In 2DEG, the coexistence of Rashba-type and Dresselhaus SOC strongly cancels the intrinsic SHC even with out-of-plane magnetization. However, the exact cancellation is broken if an in-plane magnetization is induced due to the entanglement between the exchange splitting and SOCs. σ^3_{yx} is highly anisotropic with respect to the direction of exchange splitting, $\vec{M}$, depending on the relative strength of $|\alpha|$ and $|\beta|$. The entanglement between the exchange splitting and SOCs modifies the Fermi contours (shifted away from origin), where the shifted area of Fermi contours contributes to the intrinsic SHC nontrivially.

5.A Appendix: Trace calculation

Here, we present the explicit calculation of trace in Eq. 5.8. Substituting the unperturbed Green's function and velocity operators, the velocity-spin velocity correlation function reads

$$
\begin{aligned}
Q^{l0}_{ij}(iv) &= -\frac{1}{V}\int_0^\beta du\; e^{ivu}\,\langle \hat{T} v^l_i(u) v^0_j(0)\rangle \\
&= \frac{1}{2\hbar^2 V\beta}\sum_{k,n} tr\Big\{G(k,i\omega_n)\Big\{\frac{\partial\varepsilon(\boldsymbol{k})}{\partial k_i}+\frac{\partial d^b(\boldsymbol{k})}{\partial k_i}\tau^b,\tau^l\Big\}G(k,i\omega_n+iv)\Big(\frac{\partial\varepsilon(\boldsymbol{k})}{\partial k_j}+\frac{\partial d^c(\boldsymbol{k})}{\partial k_j}\tau^c\Big) \\
&= \frac{1}{\hbar^2 V\beta}\sum_{k,n} f(\boldsymbol{k},i\omega_n+iv) f(\boldsymbol{k},i\omega_n) \\
&\times tr\Big\{\Big(g(\boldsymbol{k},i\omega_n)+d^d(\boldsymbol{k})\tau^d\Big)\Big(\frac{\partial\varepsilon(\boldsymbol{k})}{\partial k_i}\tau^l+\frac{\partial d^l(\boldsymbol{k})}{\partial k_i}\Big) \\
&\times \Big(g(\boldsymbol{k},i\omega_n+iv)+d^e(\boldsymbol{k})\tau^e\Big)\Big(\frac{\partial\varepsilon(\boldsymbol{k})}{\partial k_j}+\frac{\partial d^c(\boldsymbol{k})}{\partial k_j}\tau^c\Big)\Big\}.
\end{aligned}
\tag{5.A.1}
$$

Considering the trace part in Eq. 5.A.1, we employ the following identities of trace calculation on Pauli matrices.

$$tr\{\tau^a\} = 0, \tag{5.A.2a}$$

$$tr\{\tau^a\tau^b\} = 2\delta_{ab}, \tag{5.A.2b}$$

$$tr\{\tau^a\tau^b\tau^c\} = 2i\epsilon_{abc}, \tag{5.A.2c}$$

$$tr\{\tau^a\tau^b\tau^c\tau^d\} = 2(\delta_{ab}\delta_{cd}-\delta_{ac}\delta_{bd}+\delta_{ad}\delta_{bc}). \tag{5.A.2d}$$

Thus, we only need to consider the $0, 2, 3, 4$ times of τ^a matrix multiplication inside the trace calculation. The trace is calculated separately: i.) $0-\tau$ term ; ii.) $2-\tau$ term; iii.) $3-\tau$ term; iv.) $4-\tau$ term.

i.) The $0-\tau$ term is the purely $U(1)$ part in the trace calculation. It reads

$$tr\Big\{g(\boldsymbol{k},i\omega_n)\frac{\partial d^l(\boldsymbol{k})}{\partial k_i}g(\boldsymbol{k},i\omega_n+iv)\frac{\partial\varepsilon(\boldsymbol{k})}{\partial k_j}\Big\} \;= 2g(\boldsymbol{k},i\omega_n+iv)g(\boldsymbol{k},i\omega_n)\frac{\partial d^l(\boldsymbol{k})}{\partial k_i}\frac{\partial\varepsilon(\boldsymbol{k})}{\partial k_j}. \tag{5.A.3}$$

ii.) The $2-\tau$ term consists of the following six parts:

$$\begin{aligned}
tr\Big\{d^d(\boldsymbol{k})\tau^d\frac{\partial\varepsilon(\boldsymbol{k})}{\partial k_i}\tau^l g(\boldsymbol{k},i\omega_n+iv)\frac{\partial\varepsilon(\boldsymbol{k})}{\partial k_j}\Big\} &= 2g(\boldsymbol{k},i\omega_n+iv)d^l(\boldsymbol{k})\frac{\partial\varepsilon(\boldsymbol{k})}{\partial k_i}\frac{\partial\varepsilon(\boldsymbol{k})}{\partial k_j},\\
tr\Big\{d^d(\boldsymbol{k})\tau^d\frac{\partial d^l(\boldsymbol{k})}{\partial k_i}d^e(\boldsymbol{k})\tau^e\frac{\partial\varepsilon(\boldsymbol{k})}{\partial k_j}\Big\} &= 2d^e d^e\frac{\partial d^l(\boldsymbol{k})}{\partial k_i}\frac{\partial\varepsilon(\boldsymbol{k})}{\partial k_j},\\
tr\Big\{d^d(\boldsymbol{k})\tau^d\frac{\partial d^l(\boldsymbol{k})}{\partial k_i}g(\boldsymbol{k},i\omega_n+iv)\frac{\partial d^c(\boldsymbol{k})}{\partial k_j}\tau^c\Big\} &= 2g(\boldsymbol{k},i\omega_n+iv)\frac{\partial d^l(\boldsymbol{k})}{\partial k_i}d^c\frac{\partial d^c(\boldsymbol{k})}{\partial k_j},\\
tr\Big\{g(\boldsymbol{k},i\omega_n)\frac{\partial\varepsilon(\boldsymbol{k})}{\partial k_i}\tau^l d^e(\boldsymbol{k})\tau^e\frac{\partial\varepsilon(\boldsymbol{k})}{\partial k_j}\Big\} &= 2g(\boldsymbol{k},i\omega_n)d^l\frac{\partial\varepsilon(\boldsymbol{k})}{\partial k_i}\frac{\partial\varepsilon(\boldsymbol{k})}{\partial k_j},\\
tr\Big\{g(\boldsymbol{k},i\omega_n)\frac{\partial\varepsilon(\boldsymbol{k})}{\partial k_i}\tau^l g(\boldsymbol{k},i\omega_n+iv)\frac{\partial d^c(\boldsymbol{k})}{\partial k_j}\tau^c\Big\} &= 2g(\boldsymbol{k},i\omega_n+iv)g(\boldsymbol{k},i\omega_n)\frac{\partial\varepsilon(\boldsymbol{k})}{\partial k_i}\frac{\partial d^l(\boldsymbol{k})}{\partial k_j},\\
tr\Big\{g(\boldsymbol{k},i\omega_n)\frac{\partial d^l(\boldsymbol{k})}{\partial k_i}d^e(\boldsymbol{k})\tau^e\frac{\partial d^c(\boldsymbol{k})}{\partial k_j}\tau^c\Big\} &= 2g(\boldsymbol{k},i\omega_n)\frac{\partial d^l(\boldsymbol{k})}{\partial k_i}d^c\frac{\partial d^c(\boldsymbol{k})}{\partial k_j}. \qquad (5.A.4)
\end{aligned}$$

iii.) The $3-\tau$ term consists of following four parts:

$$\begin{aligned}
tr\Big\{g(\boldsymbol{k},i\omega_n)\frac{\partial\varepsilon(\boldsymbol{k})}{\partial k_i}\tau^l d^e(\boldsymbol{k})\tau^e\frac{\partial d^c(\boldsymbol{k})}{\partial k_j}\tau^c\Big\} &= 2i\epsilon_{lmn}g(\boldsymbol{k},i\omega_n)d^m(\boldsymbol{k})\frac{\partial\varepsilon(\boldsymbol{k})}{\partial k_i}\frac{\partial d^n(\boldsymbol{k})}{\partial k_j},\\
tr\Big\{d^d(\boldsymbol{k})\tau^d\frac{\partial d^l(\boldsymbol{k})}{\partial k_i}d^e(\boldsymbol{k})\tau^e\frac{\partial d^c(\boldsymbol{k})}{\partial k_j}\tau^c\Big\} &= 2i\epsilon_{amn}d^a(\boldsymbol{k})d^m(\boldsymbol{k})\frac{\partial d^a(\boldsymbol{k})}{\partial k_i}\frac{\partial d^n(\boldsymbol{k})}{\partial k_j},\\
tr\Big\{d^d(\boldsymbol{k})\tau^d\frac{\partial\varepsilon(\boldsymbol{k})}{\partial k_i}\tau^l g(\boldsymbol{k},i\omega_n+iv)\frac{d^c(\boldsymbol{k})}{\partial k_j}\tau^c\Big\} &= -2i\epsilon_{lmn}g(\boldsymbol{k},i\omega_n+iv)d^m(\boldsymbol{k})\frac{\partial\varepsilon(\boldsymbol{k})}{\partial k_i}\frac{d^n(\boldsymbol{k})}{\partial k_j},\\
tr\Big\{d^d(\boldsymbol{k})\tau^d\frac{\partial\varepsilon(\boldsymbol{k})}{\partial k_i}\tau^l d^e(\boldsymbol{k})\tau^e\frac{\partial\varepsilon(\boldsymbol{k})}{\partial k_j}\Big\} &= -2i\epsilon_{lmn}d^m(\boldsymbol{k})d^n(\boldsymbol{k})\frac{\partial\varepsilon(\boldsymbol{k})}{\partial k_i}\frac{\partial\varepsilon(\boldsymbol{k})}{\partial k_j}. \qquad (5.A.5)
\end{aligned}$$

iv.) The $4-\tau$ term is

$$\begin{aligned}
& tr\Big\{d^d(\boldsymbol{k})\tau^d\frac{\partial\varepsilon(\boldsymbol{k})}{\partial k_i}\tau^a d^e(\boldsymbol{k})\tau^e\frac{\partial d^c(\boldsymbol{k})}{\partial k_j}\tau^c\Big\}\\
= \;& 2\Big(d^a(\boldsymbol{k})\frac{\partial\varepsilon(\boldsymbol{k})}{\partial k_i}d^l\frac{\partial d^l(\boldsymbol{k})}{\partial k_j} - d^m d^m\frac{\partial\varepsilon(\boldsymbol{k})}{\partial k_i}\frac{\partial d^a(\boldsymbol{k})}{\partial k_j} + d^n\frac{\partial d^n(\boldsymbol{k})}{\partial k_j}\frac{\partial\varepsilon(\boldsymbol{k})}{\partial k_i}d^a(\boldsymbol{k})\Big) \qquad (5.A.6)
\end{aligned}$$

Summing over all contributions (Eq.5.A.3-5.A.6), the total trace term is

$$\begin{aligned}
tr\Big\{\cdots\Big\} &= 2g(\boldsymbol{k},i\omega_n+iv)g(\boldsymbol{k},i\omega_n)\Big(\frac{\partial d^l(\boldsymbol{k})}{\partial k_i}\frac{\partial\varepsilon(\boldsymbol{k})}{\partial k_j} + \frac{\partial\varepsilon(\boldsymbol{k})}{\partial k_i}\frac{\partial d^l(\boldsymbol{k})}{\partial k_j}\Big)\\
&\quad + 2g(\boldsymbol{k},i\omega_n+iv)\Big(\frac{\partial d^l(\boldsymbol{k})}{\partial k_i}d^a\frac{\partial d^a(\boldsymbol{k})}{\partial k_j} + d^l(\boldsymbol{k})\frac{\partial\varepsilon(\boldsymbol{k})}{\partial k_i}\frac{\partial\varepsilon(\boldsymbol{k})}{\partial k_j}\Big)
\end{aligned}$$

$$
\begin{aligned}
&+2g(\boldsymbol{k},i\omega_n)\Big(\frac{\partial d^l(\boldsymbol{k})}{\partial k_i}d^a\frac{\partial d^a(\boldsymbol{k})}{\partial k_j}+d^l\frac{\partial\varepsilon(\boldsymbol{k})}{\partial k_i}\frac{\partial\varepsilon(\boldsymbol{k})}{\partial k_j}\Big)\\
&+4d^l(\boldsymbol{k})\frac{\partial\varepsilon(\boldsymbol{k})}{\partial k_i}d^a\frac{\partial d^a(\boldsymbol{k})}{\partial k_j}-2d^bd^b\frac{\partial\varepsilon(\boldsymbol{k})}{\partial k_i}\frac{\partial d^l(\boldsymbol{k})}{\partial k_j}+2d^cd^c\frac{\partial d^l(\boldsymbol{k})}{\partial k_i}\frac{\partial\varepsilon(\boldsymbol{k})}{\partial k_j}\\
&+2i\epsilon_{lmn}\Big(g(\boldsymbol{k},i\omega_n)-g(\boldsymbol{k},i\omega_n+iv)\Big)d^m(\boldsymbol{k})\frac{\partial\varepsilon(\boldsymbol{k})}{\partial k_i}\frac{\partial d^n(\boldsymbol{k})}{\partial k_j}. \qquad (5.A.7)
\end{aligned}
$$

5.B Appendix: Matsubara summation

In Eq. 5.A.1, we need concern four terms of Matsubara summation:

$$\frac{1}{\beta}\sum_n f(\boldsymbol{k},i\omega_n)f(\boldsymbol{k},i\omega_n+iv)g(\boldsymbol{k},i\omega_n), \qquad (5.B.1a)$$

$$\frac{1}{\beta}\sum_n f(\boldsymbol{k},i\omega_n)f(\boldsymbol{k},i\omega_n+iv)g(\boldsymbol{k},i\omega_n+iv), \qquad (5.B.1b)$$

$$\frac{1}{\beta}\sum_n f(\boldsymbol{k},i\omega_n)f(\boldsymbol{k},i\omega_n+iv), \qquad (5.B.1c)$$

$$\frac{1}{\beta}\sum_n f(\boldsymbol{k},i\omega_n)f(\boldsymbol{k},i\omega_n+iv)g(\boldsymbol{k},i\omega_n)g(\boldsymbol{k},i\omega_n+iv). \qquad (5.B.1d)$$

The summation over Matsubara frequency is calculated through the residue theorem. We remind the identity of Matsubara summation:

$$\frac{1}{\beta}\sum_{n\in\mathbf{Z}}F(i\omega_n)=-\sum_{z=z_a}Res[F(z)\nu_\beta(z)], \qquad (5.B.2)$$

with $\nu_\beta(z)=\frac{1}{2}\tanh\hbar\beta z/2$ and z_a are poles of function $F(z)$ in complex plane.

All Matsubara summations consist denominator, $f(\boldsymbol{k},i\omega_n)f(\boldsymbol{k},i\omega_n+iv)$, providing four poles in the complex plane.

$$
\begin{aligned}
f^{-1}(\boldsymbol{k},i\omega_n) &= g^2(\boldsymbol{k},i\omega_n)-|d|^2=0\rightarrow g(\boldsymbol{k},i\omega_n)=\pm|d|,\\
f^{-1}(\boldsymbol{k},i\omega_n+iv) &= g^2(\boldsymbol{k},i\omega_n+iv)-|d|^2=0\rightarrow g(\boldsymbol{k},i\omega_n+iv)=\pm|d|, \qquad (5.B.3)
\end{aligned}
$$

where the four poles are defined as,

$$g(\boldsymbol{k},z_1)=|d|,\quad g(\boldsymbol{k},z_2)=-|d|,\quad g(\boldsymbol{k},z_3+iv)=|d|,\quad g(\boldsymbol{k},z_4+iv)=-|d|. \qquad (5.B.4)$$

Note that the weighting function has relation: $\nu_\beta(z_1) = \nu_\beta(z_3)$,$\nu_\beta(z_2) = \nu_\beta(z_4)$, because of the periodicity of tanh function and $v = \frac{2m\pi}{\hbar\beta}$.

Therefore, the Matsubara summation in Eq. 5.B.1 can be calculated explicitly,

$$\begin{aligned}
&\frac{1}{\beta}\sum_n f(\boldsymbol{k}, i\omega_n) f(\boldsymbol{k}, i\omega_n + iv) g(\boldsymbol{k}, i\omega_n) = \\
&-\Big\{\nu_\beta(z_1)\frac{|d|}{2|d|[(|d| + i\hbar v)^2 - |d|^2]} + \nu_\beta(z_3)\frac{|d| - i\hbar v}{[(|d| - i\hbar v)^2 - |d|^2]2|d|} \\
&+\nu_\beta(z_2)\frac{-|d|}{-2|d|[(-|d| + i\hbar v)^2 - |d|^2]} + \nu_\beta(z_4)\frac{-|d| - i\hbar v}{[(-|d| - i\hbar v)^2 - |d|^2]2|d|}\Big\} \\
= \;& (\nu_\beta(z_1) - \nu_\beta(z_3))\frac{i\hbar v}{2|d|[(i\hbar v)^2 - |d|^2]} \\
= \;& -\frac{i\hbar v\Big(n_F(\varepsilon^-(\boldsymbol{k})) - n_F(\varepsilon^+(\boldsymbol{k}))\Big)}{2|d|\Big[(i\hbar v)^2 - 4|d|^2\Big]}.
\end{aligned} \tag{5.B.5}$$

$$\begin{aligned}
&\frac{1}{\beta}\sum_n f(\boldsymbol{k}, i\omega_n) f(\boldsymbol{k}, i\omega_n + iv) g(k, i\omega_n + iv) = \\
&-\Big\{\nu_\beta(z_1)\frac{|d| + i\hbar v}{2|d|[(|d| + i\hbar v)^2 - |d|^2]} + \nu_\beta(z_3)\frac{|d|}{[(|d| - i\hbar v)^2 - |d|^2]2|d|} \\
&+\nu_\beta(z_2)\frac{-|d| + i\hbar v}{-2|d|[(-|d| + i\hbar v)^2 - |d|^2]} + \nu_\beta(z_4)\frac{-|d|}{[(-|d| - i\hbar v)^2 - |d|^2]2|d|}\Big\} \\
&= -(\nu_\beta(z_1) - \nu_\beta(z_3))\frac{i\hbar v}{2|d|[(i\hbar v)^2 - |d|^2]} \\
&= \frac{i\hbar v\Big(n_F(\varepsilon^-(\boldsymbol{k})) - n_F(\varepsilon^+(\boldsymbol{k}))\Big)}{2|d|\Big[(i\hbar v)^2 - 4|d|^2\Big]}.
\end{aligned} \tag{5.B.6}$$

$$\begin{aligned}
&\frac{1}{\beta}\sum_n f(\boldsymbol{k}, i\omega_n) f(\boldsymbol{k}, i\omega_n + iv) = \\
&-\Big\{\nu_\beta(z_1)\frac{1}{2|d|[(|d| + i\hbar v)^2 - |d|^2]} + \nu_\beta(z_3)\frac{1}{[(|d| - i\hbar v)^2 - |d|^2]2|d|} \\
&+\nu_\beta(z_2)\frac{1}{-2|d|[(-|d| + i\hbar v)^2 - |d|^2]} + \nu_\beta(z_4)\frac{1}{[(-|d| - i\hbar v)^2 - |d|^2]2|d|}\Big\} \\
&= -(\nu_\beta(z_1) - \nu_\beta(z_3))\frac{1}{|d|[(i\hbar v)^2 - |d|^2]} \\
&= \frac{\Big(n_F(\varepsilon^-(\boldsymbol{k})) - n_F(\varepsilon^+(\boldsymbol{k}))\Big)}{|d|\Big[(i\hbar v)^2 - 4|d|^2\Big]}.
\end{aligned} \tag{5.B.7}$$

$$
\begin{aligned}
&\frac{1}{\beta}\sum_n f(\boldsymbol{k},i\omega_n)f(\boldsymbol{k},i\omega_n+iv)g(k,i\omega_n)g(k,i\omega_n+iv)=\\
&-\Big\{\nu_\beta(z_1)\frac{|d|(|d|+i\hbar v)}{2|d|[(|d|+i\hbar v)^2-|d|^2]}+\nu_\beta(z_3)\frac{|d|(|d|-i\hbar v)}{[(|d|-i\hbar v)^2-|d|^2]2|d|}\\
&+\nu_\beta(z_2)\frac{-|d|(-|d|+i\hbar v)}{-2|d|[(-|d|+i\hbar v)^2-|d|^2]}+\nu_\beta(z_4)\frac{-|d|(-|d|-i\hbar v)}{[(-|d|-i\hbar v)^2-|d|^2]2|d|}\Big\}\\
&=-(\nu_\beta(z_1)-\nu_\beta(z_3))\frac{-|d|}{|d|[(i\hbar v)^2-|d|^2]}\\
&=\frac{-|d|\Big(n_F(\varepsilon^-(\boldsymbol{k}))-n_F(\varepsilon^+(\boldsymbol{k}))\Big)}{|d|\Big[(i\hbar v)^2-4|d|^2\Big]}. \qquad (5.B.8)
\end{aligned}
$$

Note that $\nu_\beta(z_1)-\nu_\beta(z_3)=-n_F(\varepsilon^-(\boldsymbol{k}))+n_F(\varepsilon^+(\boldsymbol{k})))$ in the last line of Eq. 5.B.5, as $1/2\tanh\frac{\beta z}{2}=1/2-n_F(z)$. Finally, replacing the Matsubara summation in the trace calculation, we deduce velocity-spin velocity correlation function as shown in Eq. 5.10, 5.10,

$$
\begin{aligned}
\mathrm{Re}Q^{l0}_{ij}(iv) &= \frac{4}{V\hbar^2}\sum_k\frac{|\boldsymbol{d}|\Big(n_F(\varepsilon^-(\boldsymbol{k}))-n_F(\varepsilon^+(\boldsymbol{k}))\Big)}{\Big[(\hbar iv)^2-4|\boldsymbol{d}|^2\Big]}\Big\{\frac{d^l}{|\boldsymbol{d}|}\frac{\partial\varepsilon}{\partial k_i}\frac{d^n}{|\boldsymbol{d}|}\frac{\partial d^n}{\partial k_j}-\frac{\partial\varepsilon}{\partial k_i}\frac{\partial d^a}{\partial k_j}\Big\},\\
\mathrm{Im}Q^{l0}_{ij}(iv) &= -\frac{4}{V\hbar^2}\sum_k\frac{\hbar\omega\Big(n_F(\varepsilon^-(\boldsymbol{k}))-n_F(\varepsilon^+(\boldsymbol{k}))\Big)}{2|\boldsymbol{d}|\Big[(\hbar iv)^2-4|\boldsymbol{d}|^2\Big]}\epsilon_{lnm}d^n\frac{\partial\varepsilon}{\partial k_i}\frac{\partial d^m}{\partial k_j}. \qquad (5.B.9)
\end{aligned}
$$

5.C Appendix: Calculation of integrals of SHC

Here, we present the detailed calculations of the integrals of the intrinsic SHC in the three cases: a) M_z case, $\boldsymbol{A}_0=(0,0,M)$; b) M_y case, $\boldsymbol{A}_0=(0,M,0)$; and c) M_x case, $\boldsymbol{A}_0=(M,0,0)$.

a. Exchange splitting along z direction, $\boldsymbol{A}_0=(0,0,M)$

In the M_z case, only integral I_0 in Eq. 5.26 is finite. The integration area is categorized into two types: i) circle of the bottom band ; ii) a ring between the two bands.

a.i) The integration over $\boldsymbol{k}$ is confined within area of the bottom band Ω_-. The I_0

reads

$$I_0(M_3) = e\frac{\alpha^2-\beta^2}{16\pi^2 m|\boldsymbol{M}|^3}\int\limits_{\Omega_-} k_y^2 dk = e\frac{\alpha^2-\beta^2}{16\pi m|\boldsymbol{M}|^3}\frac{1}{4}k_-^4. \tag{5.C.1}$$

a.ii) The integration over $\boldsymbol{k}$ is confined within area of a ring, $\Omega_- - \Omega_+$. The I_0 reads

$$I_0(M_3) = e\frac{\alpha^2-\beta^2}{16\pi m|\boldsymbol{M}|^3}\int\limits_{\Omega_- - \Omega_+} k_y^2 dk = e\frac{\alpha^2-\beta^2}{16\pi m|\boldsymbol{M}|^3}\frac{1}{4}(k_-^4 - k_+^4). \tag{5.C.2}$$

Eq. 5.27 is obtained by replacing the Fermi momentum with $k_\pm = \sqrt{2m\left(\mu \mp |\boldsymbol{M}|\right)}$.

b. Exchange splitting along y direction, $\boldsymbol{A}_0 = (0, M, 0)$

ii.a) The integration area is over a circle of the bottom band, Ω_-. After shifting the Fermi contour of the bottom band back to the origin, the integrals in Eq. 5.28 read

$$\begin{aligned}
I_0(M_2) &= e\frac{\alpha^2-\beta^2}{16\pi^2 m|\boldsymbol{M}|^3}\int\limits_{\Omega'_-} k_y'^2 + m^2\beta^2 d^2k' = e\frac{\alpha^2-\beta^2}{16\pi m|\boldsymbol{M}|^3}\left(\frac{1}{4}k_-'^4 + \frac{m^2\beta^2}{2}k_-'^2\right),\\
I_1(M_2) &= e\frac{M\mathrm{sgn}(M)\beta}{16\pi^2 m|\boldsymbol{M}|^3}\int\limits_{\Omega'_-} -m\beta d^2k' = \frac{\beta^2}{8\pi|\boldsymbol{M}|^2}\frac{1}{2}k_-'^2,\\
I_2(M_2) &= -e\frac{3M\mathrm{sgn}(M)}{16\pi^2 m|\boldsymbol{M}|^5}(\alpha^2-\beta^2)\\
&\quad \left[\beta\int\limits_{\Omega'_-} -\left(3k_y'^2 m\beta + m^3\beta^3\right)d^2k' + \alpha\int\limits_{\Omega'_-} -m\alpha\left(k_y'^2 + m^2\beta^2\right)d^2k'\right]\\
&= e\frac{3(\alpha^2-\beta^2)}{16\pi^2|\boldsymbol{M}|^4}\left[(3\beta^2+\alpha^2)\int\limits_{\Omega'_-} k_y'^2 d^2k' + m^2\beta^2(\beta^2+\alpha^2)\int\limits_{\Omega'_-} d^2k'\right]\\
&= e\frac{3(\alpha^2-\beta^2)}{16\pi|\boldsymbol{M}|^4}\left[(3\beta^2+\alpha^2)\frac{1}{4}k_-'^4 + m^2\beta^2(\beta^2+\alpha^2)\frac{1}{2}k_-'^2\right],\\
I_3(M_2) &= -e\frac{3}{16\pi^2 m|\boldsymbol{M}|^3}\int\limits_{\Omega'_-} d^2k'\left[-\beta^2(k_y'^2 + m^2\beta^2) - \beta\alpha(m^2\alpha\beta)\right]\\
&= e\frac{3}{16\pi m|\boldsymbol{M}|^3}\left[\beta^2\frac{1}{4}k_-'^4 + m^2\beta^2(\alpha^2+\beta^2)\frac{1}{2}k_-'^2\right].
\end{aligned} \tag{5.C.3}$$

Replacing the shifted Fermi momentum ($k'_\pm$) in the above equations, we deduce the

$\sigma^3_{yx}(\mu)$,

$$\begin{aligned}
\sigma^3_{yx}(\mu) \;&=\; \frac{em}{32\pi M^4}\left[\mu + |\boldsymbol{M}| + \frac{m}{2}\left(\alpha^2+\beta^2\right)\right] \\
&\quad \Big\{ 2|\boldsymbol{M}|\mu\left(\alpha^2+2\beta^2\right) + 2|\boldsymbol{M}|^2\left(\alpha^2+\beta^2\right) + m|\boldsymbol{M}|\left(7\alpha^4+22\alpha^2\beta^2-11\beta^4\right) \\
&\quad +3m(\alpha^2-\beta^2)\left(2\mu\left(\alpha^2+3\beta^2\right)+m\left(\alpha^2+\beta^2\right)\left(\alpha^2+5\beta^2\right)\right)\Big\}, \qquad (5.C.4)
\end{aligned}$$

where the last three terms can be neglected under strong exchange interaction approximation ($|\boldsymbol{M}| \gg |\alpha|, |\beta|$).

Thus, the SHC when Fermi level is below the top band ($-|\boldsymbol{M}| < \mu < |\boldsymbol{M}|$) is,

$$\sigma^3_{yx}(\mu) \;\approx\; \frac{em}{16\pi|\boldsymbol{M}|^3}(\mu+|\boldsymbol{M}|)\left[|\boldsymbol{M}|\left(\alpha^2+\beta^2\right)+\mu\left(\alpha^2+2\beta^2\right)\right]. \qquad (5.C.5)$$

ii.b) The integration area is over a ring between the bottom and the top band, $\Omega_- - \Omega_+$. After shifting the Fermi contours of both bands, the integrals in Eq. 5.28 are

$$\begin{aligned}
I_0(M_2) \;&=\; e\frac{\alpha^2-\beta^2}{16\pi^2 m|\boldsymbol{M}|^3}\int\limits_{\Omega'_- - \Omega'_+} k'^2_y + m^2\beta^2 d^2k' \\
&=\; e\frac{\alpha^2-\beta^2}{16\pi m|\boldsymbol{M}|^3}\left[\frac{1}{4}(k'^4_- - k'^4_+) + \frac{m^2\beta^2}{2}(k'^2_- - k'^2_+)\right], \\
I_1(M_2) \;&=\; e\frac{M\mathrm{sgn}(M)\beta}{16\pi^2 m|\boldsymbol{M}|^3}\int\limits_{\Omega'_- + \Omega'_+} -m\beta d^2k' = \frac{\beta^2}{8\pi|\boldsymbol{M}|^2}\frac{1}{2}(k'^2_- + k'^2_+), \\
I_2(M_2) \;&=\; -e\frac{3M\mathrm{sgn}(M)}{16\pi^2 m|\boldsymbol{M}|^5}(\alpha^2-\beta^2) \\
&\quad \left[\beta\int\limits_{\Omega'_- + \Omega'_+} -\left(3k'^2_y m\beta + m^3\beta^3\right)d^2k' + \alpha\int\limits_{\Omega'_- + \Omega'_+} -m\alpha\left(k'^2_y + m^2\beta^2\right)d^2k'\right] \\
&=\; e\frac{3(\alpha^2-\beta^2)}{16\pi^2|\boldsymbol{M}|^4}\left[(3\beta^2+\alpha^2)\int\limits_{\Omega'_- + \Omega'_+} k'^2_y d^2k' + m^2\beta^2(\beta^2+\alpha^2)\int\limits_{\Omega'_- + \Omega'_+} d^2k'\right] \\
&=\; e\frac{3(\alpha^2-\beta^2)}{16\pi|\boldsymbol{M}|^4}\left[(3\beta^2+\alpha^2)\frac{1}{4}(k'^4_- + k'^4_+) + m^2\beta^2(\beta^2+\alpha^2)\frac{1}{2}(k'^2_- + k'^2_+)\right], \\
I_3(M_2) \;&=\; -e\frac{3}{16\pi^2 m|\boldsymbol{M}|^3}\int\limits_{\Omega'_- - \Omega'_+} d^2k'\left[-\beta^2(k'^2_y + m^2\beta^2) - \beta\alpha(m^2\alpha\beta)\right] \\
&=\; e\frac{3}{16\pi m|\boldsymbol{M}|^3}\left[\beta^2\frac{1}{4}(k'^4_- - k'^4_+) + m^2\beta^2(\alpha^2+\beta^2)\frac{1}{2}(k'^2_- - k'^2_+)\right]. \qquad (5.C.6)
\end{aligned}$$

Replacing the shifted Fermi momentum ($k'_{\pm}$) in the above equations, we deduce the $\sigma^3_{yx}(\mu)$,

$$\begin{aligned}
\sigma^3_{yx}(\mu) &= \frac{em}{32\pi|\boldsymbol{M}|^4}\Big\{4\mu|\boldsymbol{M}|^2\left(2\alpha^2+3\beta^2\right)+12m\mu^2\left(\alpha^4+2\alpha^2\beta^2-3\beta^4\right) \\
&\quad +4m|\boldsymbol{M}|^2\left(4\alpha^4+12\alpha^2\beta^2-5\beta^4\right)+3m^3\left(\alpha^2+\beta^2\right)^2\left(\alpha^4+4\alpha^2\beta^2-5\beta^4\right) \\
&\quad +12\mu m^2(\alpha^2-\beta^2)\left(\alpha^2+\beta^2\right)\left(\alpha^2+4\beta^2\right)\Big\}, \qquad (5.C.7)
\end{aligned}$$

where the last three terms can be neglected under strong exchange interaction approximation. The SHC when Fermi level is below the top band ($\mu > |\boldsymbol{M}|$) is

$$\sigma^3_{yx}(\mu) \approx \frac{em}{8\pi|\boldsymbol{M}|^4}\left[\mu|\boldsymbol{M}|^2\left(2\alpha^2+3\beta^2\right)+3m\mu^2\left(\alpha^2-\beta^2\right)\left(\alpha^2+3\beta^3\right)\right]. \quad (5.C.8)$$

c. Exchange splitting along x direction, $\boldsymbol{A}_0 = (M, 0, 0)$

iii.a) The integration area is over a circle of the bottom band, Ω_-. After shifting the Fermi contour of the bottom band, the integrals in Eq. 5.28 read

$$\begin{aligned}
I_0(M_2) &= -\frac{\alpha^2-\beta^2}{8\pi^2 m|\boldsymbol{M}|^3}\int\limits_{\Omega'_-} k'^2_y + m^2\alpha^2 d^2k' = -\frac{\alpha^2-\beta^2}{8\pi m|\boldsymbol{M}|^3}\left(\frac{1}{4}k'^4_- + \frac{m^2\alpha^2}{2}k'^2_-\right), \\
I_1(M_2) &= -\frac{M\mathrm{sgn}(M)\alpha}{8\pi^2 m|\boldsymbol{M}|^3}\int\limits_{\Omega'_-} m\alpha d^2k' = -\frac{\alpha^2}{8\pi|\boldsymbol{M}|^2}\frac{1}{2}k'^2_-, \\
I_2(M_2) &= \frac{3M\mathrm{sgn}(M)}{8\pi^2 m|\boldsymbol{M}|^5}(\alpha^2-\beta^2) \\
&\quad \left[\alpha\int\limits_{\Omega'_-}\left(3k'^2_y m\alpha + m^3\alpha^3\right)d^2k' + \beta\int\limits_{\Omega'_-} m\beta\left(k'^2_y + m^2\alpha^2\right)d^2k'\right] \\
&= \frac{3(\alpha^2-\beta^2)}{8\pi^2|\boldsymbol{M}|^4}\left[(\beta^2+3\alpha^2)\int\limits_{\Omega'_-} k'^2_y d^2k' + m^2\alpha^2(\beta^2+\alpha^2)\int\limits_{\Omega'_-} d^2k'\right] \\
&= \frac{3(\alpha^2-\beta^2)}{8\pi|\boldsymbol{M}|^4}\left[(\beta^2+3\alpha^2)\frac{1}{4}k'^4_- + m^2\alpha^2(\beta^2+\alpha^2)\frac{1}{2}k'^2_-\right], \\
I_3(M_2) &= \frac{3}{8\pi^2 m|\boldsymbol{M}|^3}\int\limits_{\Omega'_-} d^2k'\left[\alpha^2(k'^2_y + m^2\alpha^2) + \beta\alpha(m^2\alpha\beta)\right] \\
&= \frac{3}{8\pi m|\boldsymbol{M}|^3}\left[\alpha^2\frac{1}{4}k'^4_- + m^2\alpha^2(\alpha^2+\beta^2)\frac{1}{2}k'^2_-\right]. \qquad (5.C.9)
\end{aligned}$$

Replacing the shifted Fermi momentum ($k'_\pm$), the $\sigma^3_{yx}(\mu)$ is

$$\begin{aligned}
\sigma^3_{yx}(\mu) \;=\; & -\frac{em}{32\pi M^4}\left[\mu + |\boldsymbol{M}| + \frac{m}{2}\left(\alpha^2+\beta^2\right)\right] \\
& \Big\{2|\boldsymbol{M}|\mu\left(2\alpha^2+\beta^2\right) + 2|\boldsymbol{M}|^2\left(\alpha^2+\beta^2\right) + m|\boldsymbol{M}|\left(25\alpha^4 - 2\alpha^2\beta^2 - 5\beta^4\right) \\
& +3m(\alpha^2-\beta^2)\left(2\mu\left(3\alpha^2+\beta^2\right) + m\left(\alpha^2+\beta^2\right)\left(5\alpha^2+\beta^2\right)\right)\Big\}. \qquad (5.C.10)
\end{aligned}$$

where the last three terms with high order of SOC strength is neglected, the SHC when Fermi level is below the top band ($-|\boldsymbol{M}| < \mu < |\boldsymbol{M}|$) is

$$\sigma^3_{yx}(\mu) \;\approx\; -\frac{em}{16\pi|\boldsymbol{M}|^3}(\mu + |\boldsymbol{M}|)\left[|\boldsymbol{M}|\left(\alpha^2+\beta^2\right) + \mu\left(2\alpha^2+\beta^2\right)\right]. \qquad (5.C.11)$$

iii.b) The integration area is over a ring between the bottom and the top band, $\Omega_- - \Omega_+$. After shifting the Fermi contours of both bands, the integrals in Eq. 5.28 are

$$\begin{aligned}
I_0(M_2) &= -\frac{\alpha^2-\beta^2}{8\pi^2 m|\boldsymbol{M}|^3}\int_{\Omega'_-} k'^2_y + m^2\alpha^2 d^2k' = -\frac{\alpha^2-\beta^2}{8\pi m|\boldsymbol{M}|^3}\left(\frac{1}{4}k'^4_- + \frac{m^2\alpha^2}{2}k'^2_-\right), \\
I_1(M_2) &= -\frac{M\mathrm{sgn}(M)\alpha}{8\pi^2 m|\boldsymbol{M}|^3}\int_{\Omega'_-} m\alpha d^2k' = -\frac{\alpha^2}{8\pi|\boldsymbol{M}|^2}\frac{1}{2}k'^2_-, \\
I_2(M_2) &= \frac{3M\mathrm{sgn}(M)}{8\pi^2 m|\boldsymbol{M}|^5}(\alpha^2-\beta^2) \\
& \left[\alpha\int_{\Omega'_-}\left(3k'^2_y m\alpha + m^3\alpha^3\right)d^2k' + \beta\int_{\Omega'_-} m\beta\left(k'^2_y + m^2\alpha^2\right)d^2k'\right] \\
&= \frac{3(\alpha^2-\beta^2)}{8\pi^2|\boldsymbol{M}|^4}\left[(\beta^2+3\alpha^2)\int_{\Omega'_-} k'^2_y d^2k' + m^2\alpha^2(\beta^2+\alpha^2)\int_{\Omega'_-} d^2k'\right] \\
&= \frac{3(\alpha^2-\beta^2)}{8\pi|\boldsymbol{M}|^4}\left[(\beta^2+3\alpha^2)\frac{1}{4}k'^4_- + m^2\alpha^2(\beta^2+\alpha^2)\frac{1}{2}k'^2_-\right], \\
I_3(M_2) &= \frac{3}{8\pi^2 m|\boldsymbol{M}|^3}\int_{\Omega'_-} d^2k'\left[\alpha^2(k'^2_y + m^2\alpha^2) + \beta\alpha(m^2\alpha\beta)\right] \\
&= \frac{3}{8\pi m|\boldsymbol{M}|^3}\left[\alpha^2\frac{1}{4}k'^4_- + m^2\alpha^2(\alpha^2+\beta^2)\frac{1}{2}k'^2_-\right]. \qquad (5.C.12)
\end{aligned}$$

Replacing the shifted Fermi momentum ($k'_{\pm}$) in above equations, we deduce the $\sigma^3_{yx}(\mu)$,

$$\begin{aligned}\sigma^3_{yx}(\mu) &= -\frac{em}{32\pi|\boldsymbol{M}|^4}\Big\{4\mu|\boldsymbol{M}|^2\left(3\alpha^2+2\beta^2\right)+12m\mu^2\left(3\alpha^4-2\alpha^2\beta^2-\beta^4\right)\\ &\quad +m|\boldsymbol{M}|^2\left(52\alpha^4-8\beta^4\right)+9m^3\left(\alpha^2+\beta^2\right)^3\left(\alpha^2-\beta^2\right)\\ &\quad +12\mu m^2(\alpha^2-\beta^2)\left(\alpha^2+\beta^2\right)\left(3\alpha^2+2\beta^2\right)\Big\},\end{aligned} \tag{5.C.13}$$

where the last three terms can be neglected under strong exchange interaction approximation. The SHC when Fermi level is below the top band ($\mu > |\boldsymbol{M}|$) is

$$\sigma^3_{yx}(\mu) \approx -e\frac{em}{8\pi|\boldsymbol{M}|^4}\left[\mu|\boldsymbol{M}|^2\left(3\alpha^2+2\beta^2\right)+3m\mu^2\left(\alpha^2-\beta^2\right)\left(3\alpha^2+\beta^3\right)\right] \tag{5.C.14}$$

In Fig. 5.7, we present the comparison of the numerical results between $\sigma^3_{yx}(\mu)$ with (Eq. 5.C.8, 5.C.14) and without (Eq. 5.C.7, 5.C.13) neglecting the high oder of $|\alpha|, |\beta|$.

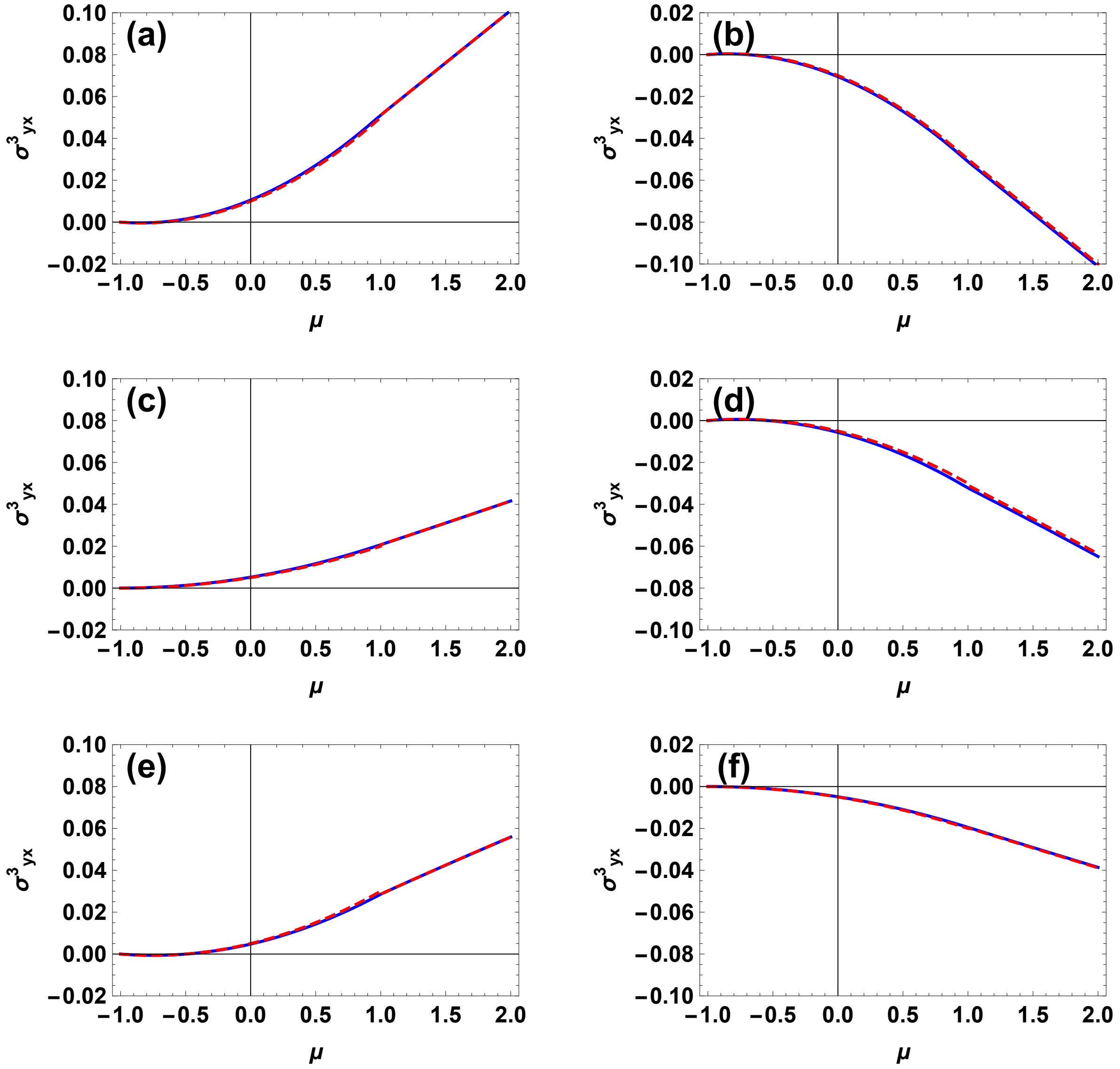

Figure 5.7: Spin Hall conductivity in strong exchange interaction approximation.

Numerical calculation results of σ^3_{yx} with (red) and without (blue) neglecting the high order of $|\alpha|, |\beta|$ terms. (a,c,e) are M_y case with the parameters: (a) $|\alpha| = |\beta| = 0.1$; (c) $|\alpha| = 0.1, |\beta| = 0$; (e) $|\alpha| = 0, |\beta| = 0.1$. (b,d,f) are M_x case with the parameters: (b) $|\alpha| = |\beta| = 0.1$; (d) $|\alpha| = 0.1, |\beta| = 0$; (f) $|\alpha| = 0, |\beta| = 0.1$. The σ^3_{yx} is in unit of $\frac{e}{8\pi}$.

Chapter 6

Spin Hall effect in Dirac ferromagnet

Contents

6.1 Introduction

One of the simplest model combining ferromagnetism and spin orbit coupling (SOC) is the Dirac ferromagnet [135]. The SOC which is a relativistic effect naturally exists in the Dirac Hamiltonian [136] and the ferromagnetic ordering can be incorporated into the Dirac Hamiltonian through a Stoner-type mean field with two historical proposals: one, introduced by MacDonald and Vosko [137], is characterized by a ferromagnetic order parameter having opposite signs between the positive/negative energy states; the other, proposed by Ramana and Rajagopal [138], is described by an order parameter having the same sign in both states. The Dirac system, originally a full relativistic model, can be extended as a low energy effective model in condensed matter physics, *e.g.*, bismuth [139] and bulk states of 3D topological insulators [140]. Hence, various transport and magneto transport properties have been examined in the (effective) Dirac model [135,135,141,142].

In this chapter, we study the intrinsic SHE in the Dirac ferromagnet, with specific emphasis on the magnetization dependence of the SHC. The key feature in the Dirac ferromagnet model is its axial anisotropy induced by the ferromagnetic ordering, for which we adapt an energy cut-off scheme with the same symmetry to deal with the ultraviolet(UV)-divergence. We find the intrinsic SHC is highly anisotropic with respect to the direction of magnetization. In addition, the anisotropy does not disappear when magnetization is asymptotically approaching zero.

6.2 Dirac ferromagnet

a. Model Hamiltonian

The model Hamiltonian of a Dirac ferromagnet is described by a 4 × 4 Dirac Hamiltonian with exchange field $\boldsymbol{M} = (M_1, M_2, M_3)$ representing the ferromagnetic ordering,

$$\mathcal{H}_0 = \hbar c k_i \rho_1 \otimes \sigma^i + mc^2 \rho_3 \otimes I_2 + M_i \rho_3 \otimes \sigma^i, \tag{6.1}$$

where the $\hbar, c, m$ are the reduced Planck constant, speed of light, and electron mass, respectively. The ρ_i $(i = 1, 2, 3)$ are the Pauli matrices representing the electron-hole space and σ^i $(i = 1, 2, 3)$ are the Pauli matrices representing the spin space. In the following calculation, we choose Planck unit, *i.e.*, $\hbar = c = 1$.

Note that we consider the exchange field $\boldsymbol{M}$ through generators $\rho_3 \otimes \sigma^i$, in which $\boldsymbol{M}$ acts oppositely on the electron (positive energy) and hole (negative energy) states. $M_i \rho_3 \otimes \sigma^i$ is the physical description of spontaneous magnetization, since generators, $\rho_3 \otimes \sigma_i$, also couple with external magnetic field $\boldsymbol{B}$ [20]. We do not consider the kind of ferromagnetic order proposed in Ref. [138], $S_i I_2 \otimes \sigma^i$, in which the field, $\boldsymbol{S}$, acts on the electron and hole states in the same way.

The band dispersions of the four states are,

$$E_{\zeta,\eta} = \zeta \sqrt{m^2 + \boldsymbol{k}^2 + M^2 + 2\eta \sqrt{(m^2 + \boldsymbol{k}^2) M^2 - (k_i M_i)^2}}, \tag{6.2}$$

where $\zeta, \eta = \pm 1$, representing the positive/negative energy (energy branch) and spin-up/spin-down (spin branch).

b. Rotation matrix

Considering the direction of spontaneous magnetization, the wave vector $\boldsymbol{k}$ can be separated into two parts: i. $k_\parallel$ is parallel with the unit direction of magnetization $\hat{m}$; ii. $k_\perp$ is perpendicular to $\hat{m}$,

$$\boldsymbol{k} = (\boldsymbol{k} \cdot \hat{m})\hat{m} - (\boldsymbol{k} \times \hat{m}) \times \hat{m} \equiv k_\parallel \hat{m} + \boldsymbol{k}_\perp. \tag{6.3}$$

Note that $k_\parallel^2 = k^2 - (\boldsymbol{k} \cdot \hat{m})^2$

The unit direction of magnetization can be rewritten in spherical coordinate, $\hat{m} = (\sin\theta\cos\varphi, \sin\theta\sin\varphi, \cos\theta)$. For simplicity, we define a rotation matrix $\mathcal{R}$ which rotates $\hat{m}$ to $\hat{z}$,

$$\mathcal{R}\hat{m} = \hat{z}. \tag{6.4}$$

The explicit form of the rotation matrix, $\mathcal{R}$, is,

$$\mathcal{R} = \begin{pmatrix} (1-\cos\theta)\cos^2\varphi - 1 & (1-\cos\theta)\sin\varphi\cos\varphi & \sin\theta\cos\varphi \\ (1-\cos\theta)\sin\varphi\cos\varphi & (1-\cos\theta)\sin^2\varphi - 1 & \sin\theta\sin\varphi \\ \sin\theta\cos\varphi & \sin\theta\sin\varphi & \cos\theta \end{pmatrix}. \tag{6.5}$$

Note that the inner product of $\boldsymbol{k}$ and $\boldsymbol{M}$ is $k_i M_i = \boldsymbol{k} \cdot \boldsymbol{M} = M\boldsymbol{k} \cdot \hat{m} = M k_\parallel$. Thus, the band dispersions of the four states can be written as,

$$\begin{aligned} E_{\zeta,\eta} &= \zeta\sqrt{\epsilon_{\boldsymbol{k}} + 2M^2 + 2\eta M\sqrt{m^2 + k_\perp^2}} \\ &= \zeta\sqrt{k_\parallel^2 + (\sqrt{m^2 + k_\perp^2} + \eta M)^2}, \end{aligned} \tag{6.6}$$

where we define $\epsilon_{\boldsymbol{k}} = \sqrt{m^2 + \boldsymbol{k}^2 - M^2}$.

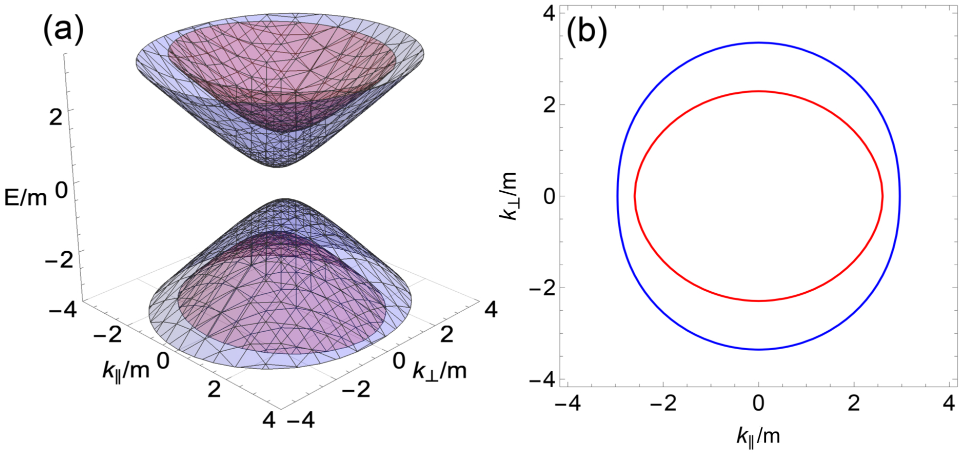

Figure 6.1: Band dispersions and Fermi contours of Dirac ferromagnet.

(a) Band dispersions and (b) Fermi contours ($\mu/m = 3$, positive energy branch) of the Dirac ferromagnet. The red colored bands correspond to $\eta = +1$ and blue colored bands correspond to $\eta = -1$.The magnetization is $M = 0.4$.

The band dispersions of a pure Dirac system is spherically symmetric and the spin branch is degenerate (setting $M \to 0$ in Eq. 6.6). In the presence of magnetization, the spin degeneracy is broken (Fig. 6.1 (a)) with spin-up and spin-down bands. Note that the spin of each band in the spin branch ($\eta = \pm 1$) is not necessarily quantized along the direction of $\boldsymbol{M}$. In addition, the Fermi sphere becomes axial anisotropic along the direction $\boldsymbol{M} \parallel \boldsymbol{k}$, which is easily checked by the Fermi contours in the $k_\parallel - k_\perp$ plane (Fig. 6.1 (b)).

c. Green's function

The electron Green's function $G^{(0)}(\varepsilon) = (\varepsilon - H_0)^{-1}$, is rewritten using the generators of $\rho_\mu \otimes \sigma^\nu$,

$$G^{(0)}(\varepsilon) = \frac{1}{D(\varepsilon)} g^{(0)}_{\mu\nu} \rho_\mu \otimes \sigma^\nu, \tag{6.7}$$

with $\mu, \nu = 0, 1, 2, 3$ and the denominator $D(\varepsilon)$ is,

$$D(\varepsilon) = \left(\varepsilon^2 - \varepsilon_{\boldsymbol{k}}^2\right)^2 + 4M^2 k_\parallel^2 - 4\varepsilon^2 M^2 = \prod_{\eta,\zeta=\pm 1} (\varepsilon - \zeta E_\eta), \tag{6.8}$$

where we redefine the energy of states $E_{\zeta,\eta} \equiv \zeta E_\eta$.

The 16 components of numerator, $g_{\mu\nu}^{(0)}$, are shown in Table. 6.1. The detailed calculation of $g_{\mu\nu}^{(0)}$ is presented in Appendix. 6.A.

Table 6.1: Table of $g_{\mu\nu}^{(0)}$ in Green's function of Dirac ferromagnet

(μ, ν)	0	1	2	3
0	$\varepsilon(\varepsilon^2 - \varepsilon_{\boldsymbol{k}}^2) - 2\varepsilon M^2$	$-2m\varepsilon M_1$	$-2m\varepsilon M_2$	$-2m\varepsilon M_3$
1	$-2mMk_\parallel$	$k_1(\varepsilon^2 - \varepsilon_{\boldsymbol{k}}^2) - 2M_1 M k_\parallel$	$k_2(\varepsilon^2 - \varepsilon_{\boldsymbol{k}}^2) - 2M_2 M k_\parallel$	$k_3(\varepsilon^2 - \varepsilon_{\boldsymbol{k}}^2) - 2M_3 M k_\parallel$
2	0	$-2\varepsilon(k_2 M_3 - k_3 M_2)$	$-2\varepsilon(k_3 M_1 - k_1 M_3)$	$-2\varepsilon(k_1 M_2 - k_2 M_1)$
3	$m(\varepsilon^2 - \varepsilon_{\boldsymbol{k}}^2)$	$-M_1(\varepsilon^2 + \varepsilon_{\boldsymbol{k}}^2) + 2Mk_\parallel$	$-M_2(\varepsilon^2 + \varepsilon_{\boldsymbol{k}}^2) + 2Mk_\parallel$	$-M_3(\varepsilon^2 + \varepsilon_{\boldsymbol{k}}^2) + 2Mk_\parallel$

d. General velocity operator

The velocity operator is obtained directly from the Hamiltonian (Eq. 6.1),

$$v_i = \frac{\partial \mathcal{H}_0}{\partial k_i} = \rho_1 \otimes \sigma^i, \tag{6.9}$$

with the charge current operator is defined as $j_i = -ev_i$.

The spin velocity operator is the anti-commutator of the velocity operator and the spin operator $\rho_3 \otimes \sigma^\alpha$,

$$v_i^\alpha = \frac{1}{2}\{v_i, \rho_3 \otimes \sigma^l\} = \epsilon_{i\alpha\beta} \rho_2 \otimes \sigma^\beta, \tag{6.10}$$

where $\alpha = 1, 2, 3$ and spin current operator is defined: $j_i^\alpha = 1/2 v_i^\alpha$.

6.3 Intrinsic spin Hall conductivity

The intrinsic spin Hall conductivity is calculated through the Kubo formula. The velocity-spin velocity correlation function reads,

$$\begin{aligned} Q_{ij}^{\alpha}(iv) &= -\frac{1}{V}\int_0^{\beta} du\; e^{ivu}\,\langle \hat{T} v_i^{\alpha}(u) v_j(0)\rangle\,, \\ &= \frac{1}{V\beta}\sum_{k,n} tr\Big\{\tilde{G}^{(0)}(i\omega_n) v_i^{\alpha}\tilde{G}^{(0)}(i\omega_n+iv)\; v_j\Big\}, \end{aligned} \tag{6.11}$$

where $iv \to \omega + i0$ is the analytic continuation on the response frequency with Matsubara frequency $v = 2m\pi/\beta$. $\tilde{G}^{(0)}(i\omega_n)$ is electron's Green's function with Matsubara frequency $w_n = (2n+1)\pi/\beta$,

$$\tilde{G}^{(0)}(i\omega_n) = G^{(0)}(i\omega_n+\mu) = \frac{1}{D(i\omega_n+\mu)} g_{\mu\nu}^{(0)}(i\omega_n+\mu)\rho_\mu \otimes \sigma^{\nu}, \tag{6.12}$$

where μ is the chemical potential.

The intrinsic SHC is obtained by taking the static limit of the correlation function,

$$\sigma_{ij}^{\alpha} = \frac{-e}{2}\lim_{v\to 0}\frac{Q_{ij}^{\alpha}(iv) - Q_{ij}^{\alpha}(0)}{-v}. \tag{6.13}$$

Assuming zero temperature, $T = 0$, and evaluating the Matsubara summation, the intrinsic SHC can be separated into two parts $\sigma_{ij}^{\alpha} = \sigma_{ij}^{\alpha,(1)} + \sigma_{ij}^{\alpha,(2)}$,

$$\begin{aligned} \sigma_{ij}^{\alpha,(1)} &= \frac{e}{8\pi V}\sum_k \\ & tr\Big\{-2G^A(\varepsilon)v_i^{\alpha}G^R(\varepsilon)v_j + G^R(\varepsilon)v_i^{\alpha}G^R(\varepsilon)v_j + G^A(\varepsilon)v_i^{\alpha}G^A(\varepsilon)v_j\Big\}\Big|_{\varepsilon=\mu}, \quad (6.14) \\ \sigma_{ij}^{\alpha,(2)} &= \frac{e}{8\pi V}\sum_k\int_{-\infty}^{\mu} d\varepsilon \\ & tr\Big\{G^R(\varepsilon)v_i^{\alpha}\partial_z G^R(\varepsilon)v_j - \partial_z G^R(\varepsilon)v_i^{\alpha}G^R(\varepsilon)v_j - \Big(R\leftrightarrow A\Big)\Big\}, \quad (6.15) \end{aligned}$$

where $f(z)$ is the Fermi distribution function, $G^{R,A}(\varepsilon) = G^{(0)}(\varepsilon \pm i\gamma)$ are the retarded and advanced Green's function with damping coefficient, γ. The calculation details are presented in Appendix. 6.B. The integral $\sigma_{ij}^{\alpha,(1)}$ contains derivative of Fermi distribution function ($\partial_\varepsilon f(\varepsilon)$), which reduces the integral to the surface term $\varepsilon = \mu$ when the temperature is assumed to be zero. $\sigma_{ij}^{\alpha,(1)}$ is often inferred to the "Fermi surface" term and $\sigma_{ij}^{\alpha,(2)}$ is called the "Fermi sea" term [143].

6.3.1 Fermi surface term, $\sigma_{ij}^{\alpha,(1)}$

The intrinsic SHC is obtained by calculating the Fermi surface and Fermi sea terms with zeroth order of damping constant, $\mathcal{O}(\gamma^0)$. We first consider the Fermi surface term,

$$\begin{aligned}\sigma_{ij}^{\alpha,(1)} &= \frac{e}{8\pi V}\sum_k \Big\{\frac{g_{\mu\nu}^R(\varepsilon)g_{\lambda\tau}^R(\varepsilon)}{D^R(\varepsilon)D^R(\varepsilon)} - 2\frac{g_{\mu\nu}^A(\varepsilon)g_{\lambda\tau}^R(\varepsilon)}{D^A(\varepsilon)D^R(\varepsilon)} + \frac{g_{\mu\nu}^A(\varepsilon)g_{\lambda\tau}^A(\varepsilon)}{D^A(\varepsilon)D^A(\varepsilon)}\Big\} \\ &\quad \epsilon_{i\alpha\beta} tr\Big\{\rho_\mu\rho_2\rho_\lambda\rho_1\Big\} tr\Big\{\sigma^\nu\sigma^\beta\sigma^\tau\sigma^j\Big\}\Big|_{\varepsilon=\mu}. \qquad (6.16)\end{aligned}$$

Considering the symmetry of the SHC tensor, we calculate the non-zero component of the SHC tensor. Using the σ_{21}^3 as an example, the trace in Eq. 6.16 can be evaluated using the following identity (See Appendix. 6.C),

$$\begin{aligned}& tr\Big\{\rho_\mu\rho_2\rho_\lambda\rho_1\Big\} tr\Big\{\sigma^\nu\sigma^1\sigma^\tau\sigma^1\Big\} = \\ & 4(\delta_{\mu1}\delta_{\lambda2}+\delta_{\mu2}\delta_{\lambda1})\sum_\alpha s_\alpha\delta_{\nu\alpha}\delta_{\tau\alpha} + 4i(\delta_{\mu0}\delta_{\lambda3}-\delta_{\mu3}\delta_{\lambda0})\sum_\alpha s_\alpha\delta_{\nu\alpha}\delta_{\tau\alpha}., \qquad (6.17)\end{aligned}$$

where we defined $s_{0,1}=1, s_{2,3}=-1$,

Thus, the integrand in Eq. 6.16 reduces to ,

$$\begin{aligned}& \Big\{\frac{g_{\mu\nu}^R(\varepsilon)g_{\lambda\tau}^R(\varepsilon)}{D^R(\varepsilon)D^R(\varepsilon)} - 2\frac{g_{\mu\nu}^A(\varepsilon)g_{\lambda\tau}^R(\varepsilon)}{D^A(\varepsilon)D^R(\varepsilon)} + \frac{g_{\mu\nu}^A(\varepsilon)g_{\lambda\tau}^A(\varepsilon)}{D^A(\varepsilon)D^A(\varepsilon)}\Big\}\epsilon_{i\alpha\beta} tr\Big\{\rho_\mu\rho_2\rho_\lambda\rho_1\Big\} tr\Big\{\sigma^\nu\sigma^\beta\sigma^\tau\sigma^j\Big\}\Big|_{\varepsilon=\mu} \\ =\ & 16\sum_\alpha s_\alpha \mathrm{Re}\Big\{\frac{g_{1\alpha}^R(\varepsilon)g_{2\alpha}^R(\varepsilon)}{D^R(\varepsilon)D^R(\varepsilon)} - \frac{g_{1\alpha}^A(\varepsilon)g_{2\alpha}^R(\varepsilon)}{D^A(\varepsilon)D^R(\varepsilon)}\Big\} + 16\sum_\alpha s_\alpha \mathrm{Im}\Big\{\frac{g_{0\alpha}^A(\varepsilon)g_{3\alpha}^R(\varepsilon)}{D^A(\varepsilon)D^R(\varepsilon)}\Big\}\Big|_{\varepsilon=\mu}. \qquad (6.18)\end{aligned}$$

To obtain the leading order contribution of γ, we expand the numerator and denominator of the retarded/advanced Green's function in order of damping constant γ,

$$\begin{aligned} g^{R,A}(\varepsilon) &= g(\varepsilon) \pm i\gamma g'(\varepsilon) + \mathcal{O}(\gamma^2), \\ D^{R,A}(\varepsilon) &= D(\varepsilon) \pm i\gamma D'(\varepsilon) + \mathcal{O}(\gamma^2). \qquad (6.19)\end{aligned}$$

The first term in Eq. 6.18 is,

$$\begin{aligned}
&\mathrm{Re}\Big\{\frac{g^R_{1\alpha}(\varepsilon)g^R_{2\alpha}(\varepsilon)}{D^R(\varepsilon)D^R(\varepsilon)}-\frac{g^A_{1\alpha}(\varepsilon)g^R_{2\alpha}(\varepsilon)}{D^A(\varepsilon)D^R(\varepsilon)}\Big\}\\
=&\ \frac{\gamma^2[D'(\varepsilon)(g'_{1\alpha}(\varepsilon)g_{2\alpha}(\varepsilon)-g_{1\alpha}(\varepsilon)g'_{2\alpha}(\varepsilon))-D(\varepsilon)g'_{1\alpha}(\varepsilon)g'_{2\alpha}(\varepsilon)]+\mathcal{O}(\gamma^2)}{(D^2(\varepsilon)+\gamma^2D'^2(\varepsilon))^2}. \qquad (6.20)
\end{aligned}$$

The leading order is γ^2 in the numerator.

The second term in Eq. 6.18 is,

$$\mathrm{Im}\Big\{\frac{g^A_{0\alpha}(\varepsilon)g^R_{3\alpha}(\varepsilon)}{D^A(\varepsilon)D^R(\varepsilon)}\Big\} = \frac{\gamma(g'_{3\alpha}(\varepsilon)g_{0\alpha}(\varepsilon)-g_{3\alpha}(\varepsilon)g'_{0\alpha}(\varepsilon))}{D^2(\varepsilon)+\gamma^2(D'(\varepsilon))^2}. \qquad (6.21)$$

The leading order is γ^1 in the numerator.

Note that for the denominators, we have identities,

$$\frac{1}{D^2(\varepsilon)+\gamma^2(D'(\varepsilon))^2}=\frac{\pi}{|D'(\varepsilon)|\gamma}\delta(D(\varepsilon)). \qquad (6.22)$$

The denominators of Eq. 6.22 has the leading order of γ^{-1}. Thus, the second part (Eq. 6.18) is the leading order contribution (γ^0) to the Fermi surface term in the clean limit. The intrinsic Fermi surface term is

$$\sigma^{3,(1)}_{21} = \frac{2e}{V}\sum_k\frac{\delta(D(\varepsilon))}{|D'(\varepsilon)|}\sum_\alpha s_\alpha X_\alpha(\varepsilon)\Big|_{\varepsilon=\mu}, \qquad (6.23)$$

with

$$X^{(0)}_\alpha(\varepsilon)\equiv g^{(0)}_{0\alpha}(\varepsilon)\partial_\varepsilon g^{(0)}_{3\alpha}(\varepsilon)-\partial_\varepsilon g^{(0)}_{0\alpha}(\varepsilon)g^{(0)}_{3\alpha}(\varepsilon). \qquad (6.24)$$

6.3.2 Fermi sea term, $\sigma^{\alpha,(2)}_{ij}$

Now, we check the the Fermi Sea term,

$$\begin{aligned}
\sigma^{\alpha,(2)}_{ij} =&\ \frac{e}{8\pi V}\sum_k\int_{-\infty}^{\mu}d\varepsilon\Big\{\frac{g^R_{\mu\nu}(\varepsilon)\partial_z g^R_{\lambda\tau}(\varepsilon)-\partial_\varepsilon g^R_{\mu\nu}(\varepsilon)g^R_{\lambda\tau}(\varepsilon)}{(D^R(\varepsilon))^2}-\Big(R\leftrightarrow A\Big)\Big\}\\
&\epsilon_{i\alpha\beta}tr\Big\{\rho_\mu\rho_2\rho_\lambda\rho_1\Big\}tr\Big\{\sigma^\nu\sigma^\beta\sigma^\tau\sigma^j\Big\}. \qquad (6.25)
\end{aligned}$$

Evaluating the trace using Eq. 6.18, we have (see Appendix. 6.C),

$$\begin{aligned}&\Big\{\frac{g^R_{\mu\nu}(\varepsilon)\partial_z g^R_{\lambda\tau}(\varepsilon)-\partial_\varepsilon g^R_{\mu\nu}(\varepsilon)g^R_{\lambda\tau}(\varepsilon)}{(D^R(\varepsilon))^2}-\Big(R\leftrightarrow A\Big)\Big\}\epsilon_{i\alpha\beta}tr\Big\{\rho_\mu\rho_2\rho_\lambda\rho_1\Big\}tr\Big\{\sigma^\nu\sigma^\beta\sigma^\tau\sigma^j\Big\},\\ =\;&-16\sum_\gamma s_\gamma \mathrm{Im}\Big[\frac{g^R_{0\gamma}(\varepsilon)\partial_\varepsilon g^R_{3\gamma}(\varepsilon)-\partial_\varepsilon g^R_{0\gamma}(\varepsilon)g^R_{3\gamma}(\varepsilon)}{D^R(\varepsilon)^2}\Big]. \qquad (6.26)\end{aligned}$$

To obtain the leading order contribution, we expand $X^{R,A}(\varepsilon)$ in order of γ,

$$X^{R,A}(\varepsilon)\equiv X^{(0)}(z\pm i\gamma)=X^{(0)}(\varepsilon)+i\gamma X'^{(0)}(\varepsilon)+\mathcal{O}(\gamma^2). \qquad (6.27)$$

Thus, Eq. 6.26 reads

$$\mathrm{Im}\Big[\frac{g^R_{0\alpha}(\varepsilon)\partial_\varepsilon g^R_{3\alpha}(\varepsilon)-\partial_\varepsilon g^R_{0\alpha}(\varepsilon)g^R_{3\alpha}(\varepsilon)}{D^R(\varepsilon)^2}\Big] \;\approx\; \pi\mathrm{sgn}D'(\zeta E_\eta)\partial_\varepsilon\delta(D(\varepsilon))\frac{X^{(0)}(\varepsilon)}{D'(\varepsilon)}, \qquad (6.28)$$

where we kept only the leading order term of γ^0 (see Appendix. 6.C). The intrinsic Fermi sea term reads

$$\begin{aligned}\sigma^{3,(2)}_{21}&=-\frac{2e}{V}\sum_k\int_{-\infty}^{\mu}d\varepsilon\mathrm{sgn}D'(\zeta E_\eta)\partial_\varepsilon\delta(D(\varepsilon))\frac{X^{(0)}(\varepsilon)}{D'(\varepsilon)}\\ &=-\frac{2e}{V}\Big\{\sum_k\mathrm{sgn}D'(\zeta E_\eta)\frac{\delta(D(\varepsilon))}{D'(\varepsilon)}X^{(0)}(\varepsilon)\Big|_{-\infty}^{\mu}-\int_{-\infty}^{\mu}d\varepsilon\mathrm{sgn}D'(\zeta E_\eta)\delta(D(\varepsilon))\partial_\varepsilon\Big(\frac{X^{(0)}(\varepsilon)}{D'(\varepsilon)}\Big)\Big\},\end{aligned} \qquad (6.29)$$

where we apply integration by part in the last equation.

Note that boundary term vanishes at $\varepsilon\to-\infty$, wherefore the first term in Eq. 6.29 exactly cancels the Fermi surface term (Eq. 6.23). The total intrinsic SHC is,

$$\sigma^3_{21}=\sigma^{3,(1)}_{21}+\sigma^{3,(2)}_{21}=\frac{2e}{V}\sum_k\int_{-\infty}^{\mu}d\varepsilon\;\mathrm{sgn}D'(\zeta E_\eta)\delta(D(\varepsilon))\partial_\varepsilon\Big(\frac{X^{(0)}(\varepsilon)}{D'(\varepsilon)}\Big). \qquad (6.30)$$

The cancellation between Fermi surface and Fermi sea is straightforward in clean limit and without vertex correction, in which the Fermi surface term does not contribute to the intrinsic SHE [21]. The intrinsic AHE, as a reference, is the summation over the Berry curvature of all bands below the Fermi surface [29]. Despite the problematic definition of spin Berry curvature, it is not surprise that the intrinsic SHE originates from the electrons below the Fermi surface (Fermi sea).

6.4 Calculation of intrinsic SHC

To calculate Eq. 6.30, we first resolve the δ-function, $\delta(D(\varepsilon))$,

$$\delta(D(\varepsilon)) \;=\; \sum_{\eta,\zeta\pm 1} \frac{\delta(\varepsilon-\zeta E_\eta)}{8ME_\eta \tilde{k}_\perp}, \tag{6.31}$$

where we define $\tilde{k}_\perp = \sqrt{m^2+k_\perp^2}$.

Eq. 6.30 is rewritten as,

$$\begin{aligned}\sigma^3_{21} &= \frac{2e}{V}\sum_k \int_{-\infty}^{\mu} d\varepsilon \sum_{\eta,\zeta=\pm 1} \frac{\delta(\varepsilon-\zeta E_\eta)}{8M\zeta E_\eta \eta \tilde{k}_\perp}\Big(\frac{\partial_\varepsilon X^{(0)}(\varepsilon)}{D'(\varepsilon)} - \frac{X^{(0)}(\varepsilon)D''(\varepsilon)}{D'(\varepsilon)^2}\Big) \\ &= \frac{2e}{V}\sum_k \int_{-\infty}^{\mu} d\varepsilon \sum_{\eta,\zeta=\pm 1} \frac{\delta(\varepsilon-\zeta E_\eta)}{64M^2E_\eta^2\tilde{k}_\perp^2}\Big[\partial_\varepsilon X^{(0)}(\varepsilon) - \zeta X^{(0)}(\varepsilon)\big(\frac{1}{E_\eta} + \frac{\eta}{M}\frac{E_\eta}{\tilde{k}_\perp}\big)\Big]\end{aligned} \tag{6.32}$$

In the presence of $\delta(\varepsilon-\zeta E_\eta)$, $X^{(0)}(\varepsilon)$ and $X'^{(0)}(\varepsilon)$ are confined to $\varepsilon = \zeta E_\eta$ (Appendix. 6.D),

$$X^{(0)}(\zeta E_\eta) = -8mM^2\Big\{(1-m_1^2){E_\eta}^2 + m_1^2\eta M\tilde{k}_\perp + m_1^2\tilde{k}_\perp^2\Big\}, \tag{6.33}$$

$$X'^{(0)}(\zeta E_\eta) = -8m\zeta E_\eta\Big\{2M^2 + \eta M\tilde{k}_\perp - M_1^2\Big\}, \tag{6.34}$$

where $\boldsymbol{m} = (m_1, m_2, m_3)$ is the unit vector of magnetization $\boldsymbol{M}$.

Replacing $X^{(0)}(\delta(z-\zeta E_\eta))$ and $X'^{(0)}(\delta(z-\zeta E_\eta))$ in Eq. 6.32, the intrinsic SHC, σ^3_{21}, is

$$\begin{aligned}\sigma^3_{21} = &-\frac{em}{4V}\sum_k \int_{-\infty}^{\mu} d\epsilon\delta(z-\zeta E_\eta) \sum_{\eta,\zeta=\pm 1} \zeta\delta(\varepsilon-\zeta E_\eta) \\ &\Big\{\frac{1}{E_\eta\tilde{k}_\perp^2} + \frac{\eta}{M}\frac{1}{E_\eta\tilde{k}_\perp} - \frac{\eta}{M}\frac{E_\eta}{\tilde{k}_\perp^3} + m_1^2\Big(- \frac{\eta M}{{E_\eta}^3\tilde{k}_\perp} - \frac{1}{{E_\eta}^3} - \frac{1}{E_\eta\tilde{k}_\perp^2} + \frac{\eta}{M}\frac{E_\eta}{\tilde{k}_\perp^3} - \frac{\eta}{M}\frac{1}{E_\eta\tilde{k}_\perp}\Big)\Big\}, \\ &\equiv \sigma^{3,iso.}_{21} + m_1^2(\sigma^{3,\boldsymbol{m}}_{21} - \sigma^{3,iso.}_{21}),\end{aligned} \tag{6.35}$$

where we define $\sigma_{21}^{3,iso.}$ and $\sigma_{21}^{3,\boldsymbol{m}}$ as,

$$\sigma_{21}^{3,iso.} \equiv -\frac{em}{4V}\sum_{k}\int_{-\infty}^{\mu} d\varepsilon \sum_{\eta,\zeta=\pm1}\zeta\delta(\varepsilon-\zeta E_{\eta})\Big\{\frac{1}{E_{\eta}\tilde{k}_{\perp}^{2}}+\frac{\eta}{M}\frac{1}{E_{\eta}\tilde{k}_{\perp}}-\frac{\eta}{M}\frac{E_{\eta}}{\tilde{k}_{\perp}^{3}}\Big\}, \tag{6.36}$$

$$\sigma_{21}^{3,\boldsymbol{m}} \equiv -\frac{em}{4V}\sum_{k}\int_{-\infty}^{\mu} d\varepsilon \sum_{\eta,\zeta=\pm1}\zeta\delta(\varepsilon-\zeta E_{\eta})\Big\{-\frac{\eta M}{{E_{\eta}}^{3}\tilde{k}_{\perp}}-\frac{1}{{E_{\eta}}^{3}}\Big\}. \tag{6.37}$$

Apparently, the $\sigma_{21}^{3,iso.}$ term depends on the strength of magnetization (M) only, for which is the isotropic contribution to the intrinsic SHC. The $\sigma_{21}^{3,\boldsymbol{m}} - \sigma_{21}^{3,iso.}$ term depends on both the strength of the magnetization and the direction of unit magnetization (*i.e.*, m_1), which is the anisotropic contribution to the intrinsic SHC.

The $\sigma_{21}^{3,iso.}$ and $\sigma_{21}^{3,\boldsymbol{m}}$ terms contain integrals with energy to minus infinity, which diverges when Fermi sphere is infinitely large (UV-divergence). Hence, we separate the integration of $\sigma_{21}^{3,iso.}$ and $\sigma_{21}^{3,\boldsymbol{m}}$ terms into a divergent part ($\varepsilon \in (-\infty, 0)$) and a convergent part ($\varepsilon \in (0,\mu)$),

$$\sigma_{21}^{3,iso.} = D^{iso.} + C^{iso.}, \tag{6.38}$$

$$\sigma_{21}^{3,\boldsymbol{m}} = D^{\boldsymbol{m}} + C^{\boldsymbol{m}}, \tag{6.39}$$

where $C^{iso.}/C^{\boldsymbol{m}}$ and $D^{iso.}/D^{\boldsymbol{m}}$ are the convergent and divergent part of isotropic/anisotropic contribution to the intrinsic SHC, respectively.

6.4.1 Divergent part of $\sigma_{21}^{3,iso.}$ and $\sigma_{21}^{3,m}$ terms

The divergent part represents the chemical potential placed at the center of the band gap between positive and negative energy branch ($\mu = 0$). Thus, it contains contributions from the whole negative energy branch ($\zeta = -1, \eta = \pm1$),

$$D^{iso.} = \frac{em}{4V}\sum_{k,\eta}\frac{1}{E_{\eta}\tilde{k}_{\perp}^{2}}+\frac{\eta}{M}\frac{1}{E_{\eta}\tilde{k}_{\perp}}-\frac{\eta}{M}\frac{E_{\eta}}{\tilde{k}_{\perp}^{3}}. \tag{6.40}$$

$$D^{\boldsymbol{m}} = -\frac{em}{4V}\sum_{k,\eta}\left(\frac{\eta M}{\tilde{k}_{\perp}}+1\right)\frac{1}{{E_{\eta}}^{3}}. \tag{6.41}$$

To deal with the divergence of integration over $\boldsymbol{k}$ in Eq. 6.40, 6.41, we introduce two $\boldsymbol{k}$ cut-off schemes: a. momentum cut-off Λ; b. energy cut-off Λ_{ε}.

a. Momentum cut-off Λ in the divergent part

In the momentum cut-off scheme, $\boldsymbol{k}$ is truncated at the cut-off momentum Λ,

$$k_{\parallel}^2 + k_{\perp}^2 \leqslant \Lambda^2. \tag{6.42}$$

Thus, $\boldsymbol{k}$ is truncated with a sphere of radius Λ in the momentum space. In the negative energy branch, the Fermi spheres of spin-up and spin-down bands ($\eta = \pm 1$) are ellipsoid with axial anisotropy along $k_{\parallel}$. However, the ellipticity of Fermi spheres asymptotically vanishes when $|\boldsymbol{k}| \gg |\boldsymbol{M}|$ and Fermi spheres of the spin-up and spin-down bands tend to coincide, in accordance with the momentum cut-off scheme.

$D_{\Lambda}^{iso.}$ and $D_{\Lambda}^{\boldsymbol{m}}$ in the momentum cut-off are (Appendix. 6.E)

$$D_{\Lambda}^{iso.} \approx -\frac{em}{4\pi^2}\left(\log\frac{2\Lambda}{m} - 1 - \frac{M^2}{6m^2}\right), \tag{6.43}$$

$$D_{\Lambda}^{\boldsymbol{m}} \approx -\frac{em}{4\pi^2}\left(\log\frac{2\Lambda}{m} - 1 + \frac{M^2}{2m^2}\right), \tag{6.44}$$

where we neglect the terms with higher order of strength of magnetization $\mathcal{O}(M^4)$.

The divergent part of intrinsic SHC through the momentum cut-off is

$$\sigma_{21}^3(\mu = 0) = -\frac{em}{4\pi^2}\left[(\log\frac{2\Lambda}{m} - 1) - \frac{M^2}{6m^2}(1 - 4m_x^2)\right]. \tag{6.45}$$

In the momentum cut-off scheme, when magnetization asymptotically goes to zero ($M \to 0$), the σ_{21}^3 reduces to the result of intrinsic SHC in a pure Dirac electron system [141,142].

b. Energy cut-off Λ_ε in the divergent part

In the energy cut-off scheme, $\boldsymbol{k}$ is truncated at the momentum confined by a specific energy, Λ_ε,

$$E_\eta^2 = k_{\parallel}^2 + (\tilde{k}_{\perp} + \eta M)^2 \leqslant \Lambda_\epsilon^2. \tag{6.46}$$

Thus, the spin-up and spin-down bands in the negative energy branch are truncated by two different ellipsoids. Apparently, the energy cut-off scheme retains the symmetry of the Dirac ferromagnet Hamiltonian.

Neglecting the high order term $\mathcal{O}(M^4)$, $D^{iso.}$ and $D^{\boldsymbol{m}}$ in the energy cut-off scheme read (Appendix. 6.E)

$$D^{iso.}_{\Lambda_\varepsilon} \approx \frac{em}{4\pi^2}\frac{M^2}{6m^2}, \tag{6.47}$$

$$D^{\boldsymbol{m}}_{\Lambda_\varepsilon} \approx -\frac{em}{4\pi^2}\left(\log\frac{2\Lambda_\varepsilon}{m} - 1 + \frac{M^2}{2m^2}\right). \tag{6.48}$$

$D^{\boldsymbol{m}}$ show exactly the same the result in the two cut-off schemes, while $D^{iso.}$ diverges in the two cut-off schemes. The difference between the two cut-off schemes is the ellipticity of the Fermi sphere, which is of the order of M/Λ. $D^{iso.}$ (Eq. 6.39) contains terms with order of M^{-1}, which gives a non-vanishing contribution in the energy cut-off scheme.

The divergent part of intrinsic SHC through the energy cut-off is,

$$\sigma^3_{21}(\mu = 0) = -\frac{em}{4\pi^2}\left[m_x^2(\log\frac{2\Lambda_\varepsilon}{m} - 1) - \frac{M^2}{6m^2}(1 - 4m_x^2)\right]. \tag{6.49}$$

To the second order of M, the magnetization induced term in the two cut-off schemes are identical but the M-independent part diverges. Specifically, in energy cut-off schemes, the M-independent part of intrinsic SHC depends on the direction of magnetization when it goes to zero. If M goes to zero along the x-axis ($m_x = 1$), the two cut-off schemes are the same. If M goes to zero along the direction perpendicular to the x-axis ($m_x = 0$), the intrinsic SHC at $\mu = 0$ nearly vanishes.

6.4.2 Convergent part of $\sigma^{3,iso.}_{21}$ and $\sigma^{3,m}_{21}$ terms

In the convergent part of integral, the $\boldsymbol{k}$ integration is confined to the area with $E_\eta \in (0, \mu)$,

$$E^2_\eta = k^2_\parallel + (\tilde{k}_\perp + \eta M)^2 \leqslant \mu^2. \tag{6.50}$$

The integration area is similar with the energy cut-off scheme, in which two ellipsoids are associated with spin-up and spin-down bands ($\eta = \pm 1$) in either positive or negative energy branch ($\zeta = \pm 1$).

The $C^{iso.}$ and $C^{\boldsymbol{m}}$ are,

$$
\begin{aligned}
C^{iso.} &= -\frac{em}{8\pi^2}\sum_{\eta=\pm1}\frac{\eta|\mu|}{2M}\Theta(\mu) \\
&\int_{\theta_\alpha}^{\theta_\beta} d\theta\Big(1-\frac{M^2}{|\mu|^2(\sin\theta-\eta\frac{M}{|\mu|})^2}\Big)\cos\theta\,\mathrm{arctanh}\cos\theta-\frac{\cos^2\theta}{(\sin\theta-\eta\frac{M}{|\mu|})^2} \qquad (6.51)\\
C^{\boldsymbol{m}} &= -\frac{em}{8\pi^2}\sum_{\eta=\pm1}\Theta(\mu)(\cos\theta_\alpha+\log\tan\theta_\alpha/2) \qquad (6.52)
\end{aligned}
$$

where the $\Theta(\mu)$ is defined as,

$$
\Theta_\eta(\mu)=\begin{cases}1, & |\mu|>m-\eta M\\ 0, & \text{(otherwise)}\end{cases} \tag{6.53}
$$

6.4.3 Consistency between the convergent part and divergent part

The intrinsic SHC contains both contributions from the convergent part and the divergent part. Thus, the convergent past is expected to exactly cancel the divergent part when the chemical potential approaches $-\infty$. In Fig. 6.2, we present the convergent part (C-term) and divergent part (D-term) with both cut-off schemes to check their consistency.

In the momentum cut-off scheme, the convergent part ($C^{iso.}$) and the divergent part ($D_\Lambda^{iso.}$) do not show consistency in isotropic contribution (Fig. 6.2 (a)) but are consistent in anisotropic contribution (Fig. 6.2 (b)), since the C^m term cancels the D_Λ^m term in the limit $\mu\to\Lambda$. In contrast, for the energy cur-off scheme, the convergent part and the divergent part are consistent in either isotropic contribution (Fig. 6.2 (c)) or anisotropic contribution (Fig. 6.2 (d)). It indicates the energy cut-off should be the appropriate cut-off scheme, for it follows the the symmetry of system which is axial anisotropic along $\hat{M}$. Note that when M is large, there is a non-negligible deviation between the convergent part and the divergent part, indicating the contributions from high order terms of $\mathcal{O}(M^4)$ in the divergent terms.

In Fig. 6.3, we present the chemical potential dependence of the isotropic contribution $\sigma_{21}^{3,iso.}$ and the anisotropic contribution $\sigma_{21}^{3,\boldsymbol{m}}$ in the energy cut-off scheme. Apparently, the intrinsic SHC is even with respect to μ, while the intrinsics AHC is odd with μ in comparison [135]. Both $\sigma_{21}^{3,iso.}$ and $\sigma_{21}^{3,\boldsymbol{m}}$ have plateaus at the band gap between positive

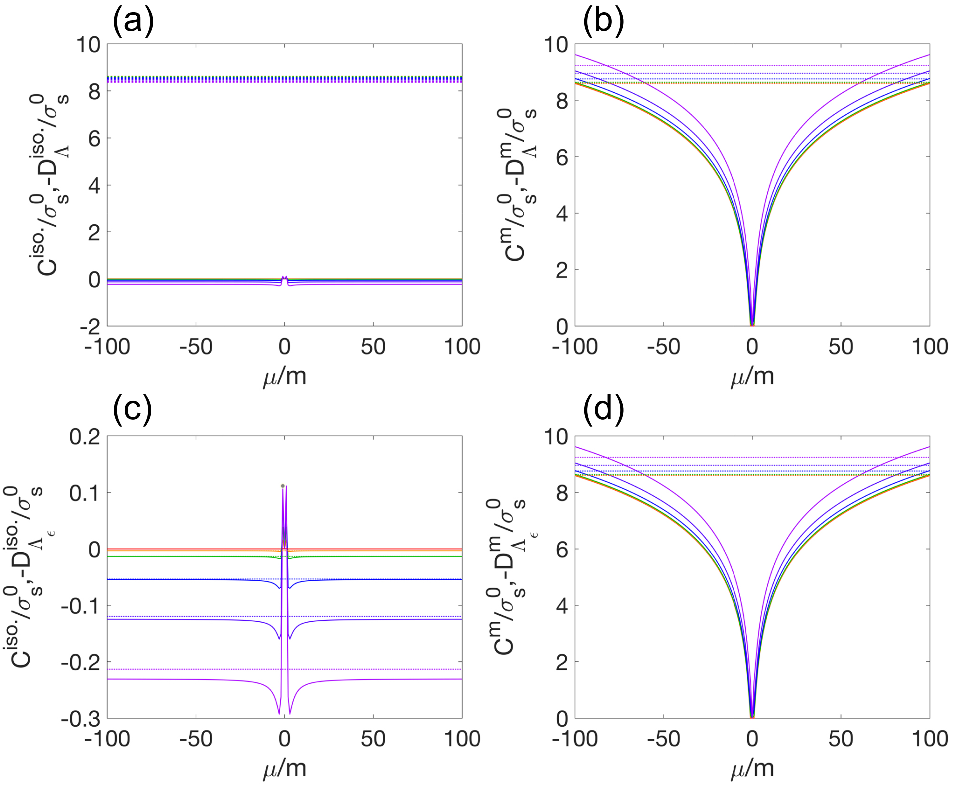

Figure 6.2: Consistency between convergent part and divergent part.

Comparison between (a) $C^{iso.}$ and $-D_{\Lambda}^{iso.}$ (dashed) ; (b) C^{m} and $-D_{\Lambda}^{m}$ (dashed); (c) $C^{iso.}$ and $-D_{\Lambda_\varepsilon}^{iso.}$ (dashed);(c) C^{m} and $-D_{\Lambda_\varepsilon}^{m}$ (dashed). The M is set to be $0.01, 0.1, 0.2, 0.4, 0.6, 0.8$, corresponding to color sequence from red to purple. The cut-off momentum/energy is set to be $\Lambda = \Lambda_\varepsilon = 100$, according to the limit of chemical potential $\mu_{min} = -100$. The divergent parts are taken in opposite sign for comparison. The conductivity is in the unit of $\sigma_s^0 = em/8\pi^2$.

and negative energy branch whose width linearly reduce with the strength of M. The magnitude of plateaus in $\sigma_{21}^{3,iso.}$ and $\sigma_{21}^{3,\boldsymbol{m}}$ are enhanced by the strength of magnetization but the signs are opposite. When the chemical potential touches the positive/negative energy branch, $\sigma_{21}^{3,iso.}$ is further enhanced with a maximum at $\mu = m$ for all strength of M and then drastically decays to a negative sign. The $\mu = m$ condition corresponds to the chemical potential at the center of spin-up and spin-down bands. In contrast, $\sigma_{21}^{3,\boldsymbol{m}}$ monotonically decreases with increasing chemical potential.

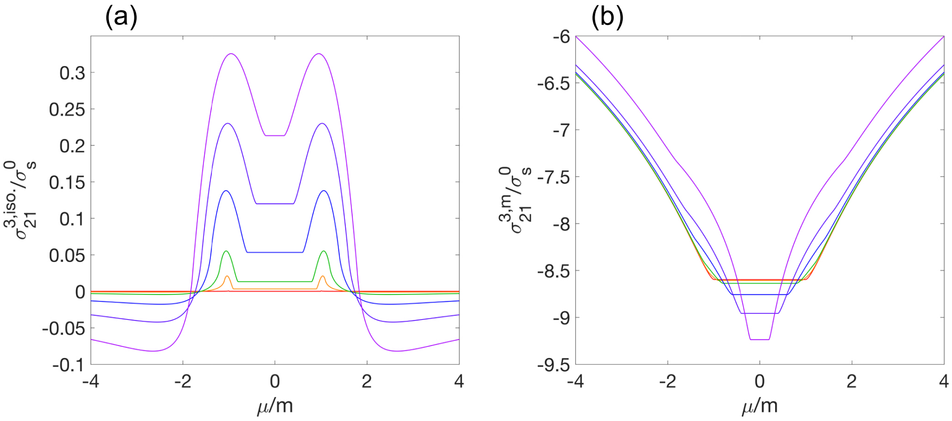

Figure 6.3: Chemical potential dependence of $\sigma_{21}^{3,iso.}$ and $\sigma_{21}^{3,\boldsymbol{m}}$.

Chemical potential dependence of intrinsic SHC contributions: (a) $\sigma_{21}^{3,iso.}$ and (b) $\sigma_{21}^{3,\boldsymbol{m}}$. The $\boldsymbol{M}$ is set to be $0.01, 0.1, 0.2, 0.4, 0.6, 0.8$, corresponding to color sequence from red to purple. The cut-off energy is set to be $\Lambda_\varepsilon = 100$. The conductivity is in the unit of $\sigma_s^0 = em/8\pi^2$.

6.5 The anisotropy of intrinsic SHC

The anisotropy of intrinsic SHC in Dirac ferromagnet is presented through the angular dependence of σ_{21}^3 (Fig. 6.4). θ corresponds to the angle between the unit magnetization and x-axis. The intrinsic SHC is highly anisotropic, despite the chemical potential and strength of magnetization. Specifically, σ_{21}^3 takes a maximum in magnitude when $\boldsymbol{M} \parallel x$ $(\theta = 0, \pi)$ and is nearly zero when $\boldsymbol{M} \perp x$ $(\theta = \pi/2)$. Strikingly, the anisotropy of the intrinsic SHC do not vanish when the magnetization is asymptotically zero. It indicates that when M asymptotically goes to zero along the x-axis, σ_{21}^3 reaches a non-vanishing value, which is the exact value of intrinsic SHC in the pure Dirac system [141]. However, if M asymptotically goes to zero along the direction orthogonal to the x-axis (*e.g.*, y or z axes), σ_{21}^3 vanishes.

The massive Dirac electron system is spherically symmetric, while the Dirac ferromagnet is axial anisotropic due to the existence of ferromagnetic ordering (exchange interaction). The diverged asymptotical behavior of the intrinsic SHC implies a non-trivial transition between the ferromagnetic state and paramagnetic state in massive Dirac system. It has been argued the the intrinsic skew scattering which is also independent of the life-time of quasiparticles (order of γ^0) can cancel the contribution of intrinsic SHC [43]. Thus, it is of interest to investigate this diverged asymptotical behavior by taking the

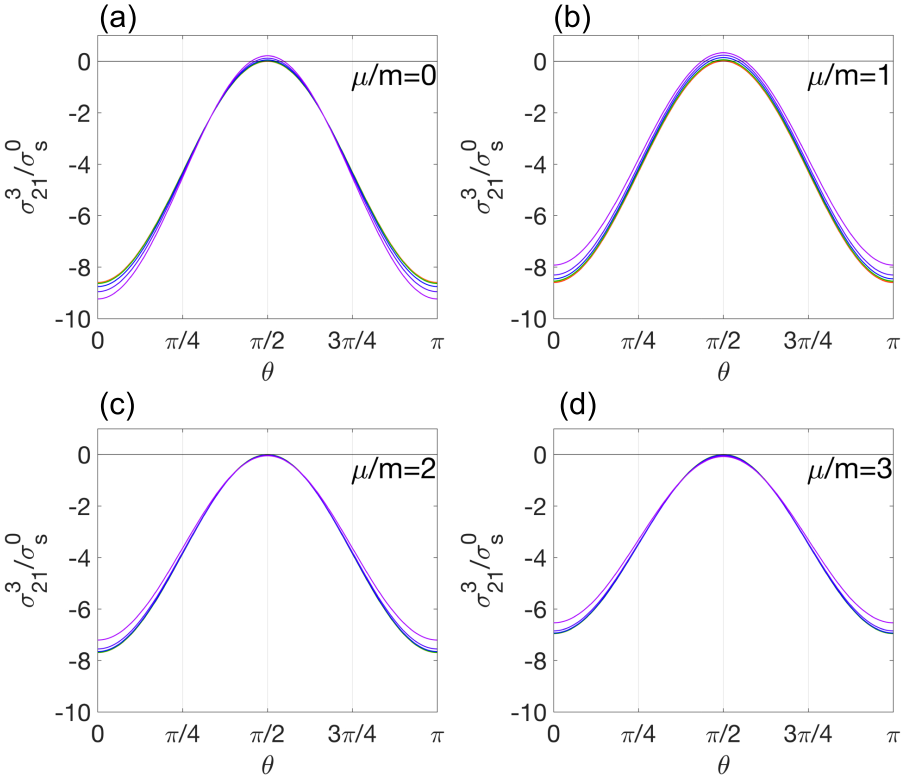

Figure 6.4: Magneto angular dependence of σ^3_{21}.

The angular dependence ($\cos\theta = m_x$) of intrinsic SHC σ^3_{21} for various chemical potential: (a) $\mu/m = 0$, (b) $\mu/m = 1$, (c) $\mu/m = 2$, (d) $\mu/m = 3$. The $|\boldsymbol{M}|$ is set to be $0.01, 0.1, 0.2, 0.4, 0.6, 0.8$, corresponding to color sequence from red to purple. The cut-off energy is set to be $\Lambda_\varepsilon = 100$. The conductivity is in the unit of $\sigma^0_s = em/8\pi^2$.

extrinsic effects into account.

6.6 Brief summary

In this chapter, we study the intrinsic SHC on massive Dirac electron system with ferromagnetic ordering in the intrinsic regime. Considering the symmetry of the Dirac system in the presence of magnetization, we employ two cut-off schemes to deal with the UV-divergence, where the intrinsic SHC diverges in the energy and momentum cut-off schemes. We adapt the energy cut-off scheme in accordance with the axial anisotropy of the Dirac ferromagnet. We find the intrinsic SHC σ^3_{21} is highly anisotropic, where it reaches the maximum when magnetization is along the x-axis and nearly vanishes when the magnetization is orthogonal to the x-axis. Further, we find a diverged asymptotical behavior of M as it approaches zero. Only when M approaches zero along the x-axis, the intrinsic SHC reduces to the result of massive Dirac electron in the zero-M limit. This divergence indicates a non-trivial transition between the ferromagnetic state and the paramagnetic state in massive Dirac system. Additionally, it is reported that the intrinsic SHC was correlated with the magnetic susceptibility within the Dirac band gap [141]. It is also of interest to investigate the correlation between magnetic susceptibility and intrinsics SHC in the Dirac ferromagnet, since the magnetic susceptibility is strongly affected by the magnetic ordering.

6.A Appendix: Calculation details of $g^{(0)}_{\mu\nu}$

Here, we present the calculation details of $g^{(0)}_{\mu\nu}$ in Table. 6.1. The explicit form of model Hamiltonian (Eq. 6.1) is

$$\mathcal{H}_0 = \begin{pmatrix} m - M_3 & -M_1 + iM_2 & k_3 & k_1 - ik_2 \\ -M_1 - iM_2 & m + M_3 & k_1 + ik_2 & -k_3 \\ k_3 & k_1 - ik_2 & M_3 - m & M_1 - iM_2 \\ k_1 + ik_2 & -k_3 & M_1 + iM_2 & -m - M_3 \end{pmatrix}. \tag{6.A.1}$$

The electron's Green's function is obtained by inverting the matrix $\epsilon - \mathcal{H}_0$,

$$(\epsilon - \mathcal{H}_0)^{-1} \equiv \frac{1}{D(\epsilon)} N_{\alpha\beta} s_\alpha \otimes s^\beta, \tag{6.A.2}$$

where the matrix inversion is calculated directly by *Mathematica*. The $N_{\alpha\beta}$ is the matrix elements and the $s_\alpha(\alpha = 1, 2, 3, 4)$ is single-entry matrix generators,

$$s_1 = \begin{pmatrix} 1 & 0 \\ 0 & 0 \end{pmatrix}, s_2 = \begin{pmatrix} 0 & 1 \\ 0 & 0 \end{pmatrix}, s_3 = \begin{pmatrix} 0 & 0 \\ 1 & 0 \end{pmatrix}, s_4 = \begin{pmatrix} 0 & 0 \\ 0 & 1 \end{pmatrix}. \tag{6.A.3}$$

Thus, the Green's function in matrix form is written,

$$D(\epsilon)(\epsilon - \mathcal{H}_0)^{-1} = \begin{pmatrix} N_{11} & N_{12} & N_{21} & N_{22} \\ N_{13} & N_{14} & N_{23} & N_{24} \\ N_{31} & N_{32} & N_{41} & N_{42} \\ N_{33} & N_{34} & N_{43} & N_{44} \end{pmatrix} \tag{6.A.4}$$

We would like to rewrite the matrix in generators of $\rho_\mu \otimes \sigma^\nu$,

$$N_{\alpha\beta} s_\alpha \otimes s^\beta = g_{\mu\nu} \rho^\mu \otimes \sigma^\nu. \tag{6.A.5}$$

The relation between Pauli matrices and s-matrices are

$$s_1 = \frac{1}{2}(\sigma_0 + \sigma_3), s_2 = \frac{1}{2}(\sigma_1 + i\sigma_2), s_3 = \frac{1}{2}(\sigma_1 - i\sigma_2), s_4 = \frac{1}{2}(\sigma_0 - \sigma_3). \tag{6.A.6}$$

In general, we obtain a 4 × 4 transformation matrix between σ^μ and s_α,

$$s_\alpha = \Gamma^\alpha_\mu \sigma^\mu. \tag{6.A.7}$$

The transformation between generators $s_\alpha \otimes s^\beta$ and $\rho_\mu \otimes \sigma^\nu$ is

$$\begin{aligned} s_\alpha \otimes s^\beta &= \Gamma^\mu_\alpha \rho_\mu \otimes \Gamma^\beta_\nu \sigma^\nu \\ &= \Gamma^\mu_\alpha \otimes \Gamma^\beta_\nu \rho_\mu \otimes \sigma^\nu, \end{aligned} \tag{6.A.8}$$

where we introduce a basis transformation matrix $\Gamma^\mu_\alpha \otimes \Gamma^\beta_\nu$.

The matrix elements $g_{\mu\nu}$ and $N_{\alpha\beta}$ have relation,

$$g_{\mu\nu} = \Gamma^\mu_\alpha \otimes \Gamma^\beta_\nu N_{\alpha\beta}. \tag{6.A.9}$$

The $g_{\mu\nu}$ can be explicitly calculated,

$$\begin{aligned}
g^{(0)}_{00} &= \frac{1}{4}(N_{11} + N_{14} + N_{41} + N_{44}), \quad g^{(0)}_{01} = \frac{1}{4}(N_{12} + N_{13} + N_{43} + N_{42}) \\
g^{(0)}_{02} &= \frac{1}{4}(iN_{12} - iN_{13} - iN_{43} + iN_{42}), \quad g^{(0)}_{03} = \frac{1}{4}(N_{11} - N_{14} + N_{41} - N_{44}) \\
g^{(0)}_{10} &= \frac{1}{4}(N_{21} + N_{24} + N_{31} + N_{34}), \quad g^{(0)}_{11} = \frac{1}{4}(N_{22} + N_{23} + N_{32} + N_{41}) \\
g^{(0)}_{12} &= \frac{1}{4}(N_{22} - iN_{23} + iN_{32} - iN_{41}), \quad g^{(0)}_{13} = \frac{1}{4}(N_{21} - N_{24} + N_{31} - N_{34}) \\
g^{(0)}_{20} &= \frac{1}{4}(N_{21} + N_{24} - iN_{31} - N_{34}), \quad g^{(0)}_{21} = \frac{1}{4}(N_{22} + iN_{23} - iN_{32} - iN_{33}) \\
g^{(0)}_{22} &= \frac{1}{4}(-N_{22} + N_{23} + N_{32} - N_{33}), \quad g^{(0)}_{23} = \frac{1}{4}(iN_{21} - iN_{24} - iN_{31} + iN_{34}) \\
g^{(0)}_{30} &= \frac{1}{4}(N_{11} + N_{14} - N_{41} - N_{44}), \quad g^{(0)}_{31} = \frac{1}{4}(N_{12} + N_{13} - N_{43} - N_{42}) \\
g^{(0)}_{32} &= \frac{1}{4}(N_{12} - iN_{13} + iN_{43} - iN_{42}), \quad g^{(0)}_{33} = \frac{1}{4}(N_{11} - N_{14} - N_{41} + N_{44}).
\end{aligned} \tag{6.A.10}$$

The results is shown in Table. 6.1.

6.B Appendix: Matsubara summation

To evaluate the Matsubara summation in Eq. 6.11, we remind the identity,

$$\frac{1}{\beta}\sum_{n\in \boldsymbol{Z}} F(i\omega_n) = -\frac{1}{2\pi i}\int_{C'} d\varepsilon F(z)\nu_\beta(z), \tag{6.B.1}$$

where $\nu_\beta(z) = 1/2\tanh(\beta z/2)$ is the weighting function for fermion and C' contains all poles of $F(z)$ in complex plane (Fig. 6.5 (a)).

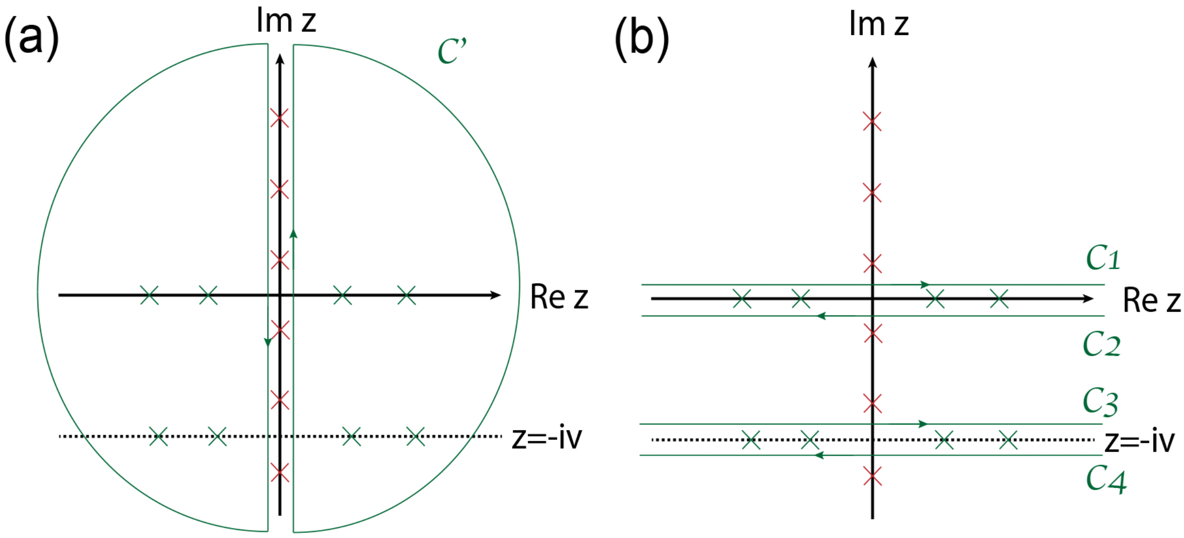

Figure 6.5: Integration paths of Matsubara summation.
(a) Integration path C', (b) Integration path C_1, C_2, C_3, C_4 in the Matsubara summation.

The integration path C' is equivalent with sum over path $C_1 + C_2 + C_3 + C_4$, which both contain only poles of $F(z)$ in complex plane. Thus, velocity-spin velocity correlation function is rewritten as,

$$\begin{aligned} Q^\alpha_{ij}(iv) &= \frac{1}{V\beta}\sum_{k,n} tr\Big\{G^{(0)}(i\omega_n)v^\alpha_i G^{(0)}(i\omega_n + iv)v_j\Big\} \\ &= -\frac{1}{4i\pi V}\sum_k \int_{C_1+C_2+C_3+C_4} d\varepsilon \tanh\frac{\beta z}{2} tr\Big\{G^{(0)}(z)v^\alpha_i G^{(0)}(z+iv)v_j\Big\} \end{aligned}$$

$$
\begin{aligned}
&= -\frac{1}{4i\pi V}\sum_k \Big\{ \int_{-\infty+i0}^{+\infty+i0} d\varepsilon \tanh\frac{\beta z}{2} tr\Big(G^{(0)}(z)v_i^\alpha G^{(0)}(z+iv)v_j\Big) \\
&\int_{+\infty-i0}^{-\infty-i0} d\varepsilon \tanh\frac{\beta z}{2} tr\Big(G^{(0)}(z)v_i^\alpha G^{(0)}(z+iv)v_j\Big) \\
&\int_{-\infty-iv+i0}^{+\infty-iv+i0} d\varepsilon \tanh\frac{\beta z}{2} tr\Big(G^{(0)}(z)v_i^\alpha G^{(0)}(z+iv)v_j\Big) \\
&\int_{+\infty-iv-i0}^{-\infty-iv-i0} d\varepsilon \tanh\frac{\beta z}{2} tr\Big(G^{(0)}(z)v_i^\alpha G^{(0)}(z+iv)v_j\Big)\Big\}. \qquad (6.B.2)
\end{aligned}
$$

Folding the paths, C_3 and C_4, back to the real axis, we have

$$
\begin{aligned}
Q_{ij}^\alpha(iv) &= -\frac{1}{4i\pi V}\sum_k \Big\{ \int_{-\infty}^{+\infty} d\varepsilon \tanh\frac{\beta z}{2} tr\Big(G^{(0)}(z+i0)v_i^\alpha G^{(0)}(z+iv)v_j\Big) \\
&- \int_{-\infty}^{+\infty} d\varepsilon \tanh\frac{\beta z}{2} tr\Big(G^{(0)}(z-i0)v_i^\alpha G^{(0)}(z+iv)v_j\Big) \\
&\int_{-\infty}^{+\infty} d\varepsilon \tanh\frac{\beta(z-iv)}{2} tr\Big(G^{(0)}(z-iv)v_i^\alpha G^{(0)}(z+i0)v_j\Big) \\
&- \int_{-\infty}^{+\infty} d\varepsilon \tanh\frac{\beta(z-iv)}{2} tr\Big(G^{(0)}(z-iv)v_i^\alpha G^{(0)}(z-i0)v_j\Big)\Big\} \\
&= -\frac{1}{4i\pi V}\sum_k \int_{-\infty}^{+\infty} d\varepsilon \tanh\frac{\beta z}{2} \\
&tr\Big\{[G^R(z)-G^A(z)]v_i^\alpha G^{(0)}(z+iv)v_j + G^{(0)}(z-iv)v_i^\alpha [G^R(z)-G^A(z)]v_j\Big\}. \\
&\qquad (6.B.3)
\end{aligned}
$$

Note that, $\tanh\frac{\beta(z\pm iv)}{2} = \tanh\frac{\beta z}{2}$ with $\nu = 2m\pi/\beta$.

Replacing tanh function with Fermi distribution function, $\tanh\frac{\beta z}{2} = 1 - 2f(z)$, we have

$$
\begin{aligned}
Q_{ij}^\alpha(iv) &= \frac{1}{2\pi i V}\sum_k \int_{-\infty}^{+\infty} d\varepsilon f(z) tr\Big\{[G^R(z)-G^A(z)]v_i^\alpha G^{(0)}(z+iv)v_j \\
&+G^{(0)}(z-iv)v_i^\alpha[G^R(z)-G^A(z)]v_j\Big\}. \qquad (6.B.4)
\end{aligned}
$$

The spin Hall conductivity is obtained by taking the static limit of correlation function,

$$
\sigma_{ij}^\alpha = \frac{-e}{2}\lim_{v\to 0}\frac{Q_{ij}^\alpha(iv)-Q_{ij}^\alpha(0)}{i(iv)}. \qquad (6.B.5)
$$

Expand the retarded and advanced Green's function in order of v,

$$G^{R,A}(z) = G^{(0)}(z \pm iv) = G^{R,A}(z) \pm iv\partial_z G^{R,A}(z) + \mathcal{O}(v^2). \tag{6.B.6}$$

Note that the retarded and advanced, $G^{R,A}(z)$, are applied to keep the analytic continuation with $G^{(0)}(z \pm iv)$.

The spin Hall conductivity,σ_{ij}^{α}, is

$$\begin{aligned}
\sigma_{ij}^{\alpha} \quad &= \frac{e}{4\pi V}\sum_k \int_{-\infty}^{+\infty} d\varepsilon f(z) tr\Big\{ \\
&[G^R(z) - G^A(z)]v_i^{\alpha}\frac{\partial G^R(z)}{\partial z}v_j - \frac{\partial G^A(z)}{\partial z}v_i^{\alpha}[G^R(z) - G^A(z)]v_j\Big\} \\
&= \frac{e}{4\pi V}\sum_k \int_{-\infty}^{+\infty} d\varepsilon f(z) tr\Big\{ \\
&G^R(z)v_i^{\alpha}\frac{\partial G^R(z)}{\partial z}v_j - G^A(z)v_i^{\alpha}\frac{\partial G^R(z)}{\partial z}v_j - \frac{\partial G^A(z)}{\partial z}v_i^{\alpha}G^R(z)v_j + \frac{\partial G^A(z)}{\partial z}v_i^{\alpha}G^A(z)v_j\Big\} \\
&= -\frac{e}{4\pi V}\sum_k \int_{-\infty}^{+\infty} d\varepsilon \frac{\partial f(z)}{\partial z} tr\Big\{G^A(z)v_i^{\alpha}G^R(z)v_j\Big\} \\
&+\frac{e}{4\pi V}\sum_k \int_{-\infty}^{+\infty} d\varepsilon f(z) tr\Big\{G^R(z)v_i^{\alpha}\frac{\partial G^R(z)}{\partial z}v_j + \frac{\partial G^A(z)}{\partial z}v_i^{\alpha}G^A(z)v_j\Big\} \\
&= -\frac{e}{4\pi V}\sum_k \int_{-\infty}^{+\infty} d\varepsilon \frac{\partial f(z)}{\partial z} tr\Big\{G^A(z)v_i^{\alpha}G^R(z)v_j\Big\} \\
&+\frac{e}{8\pi V}\sum_k \int_{-\infty}^{+\infty} d\varepsilon \frac{\partial f(z)}{\partial z} tr\Big\{G^R(z)v_i^{\alpha}G^R(z)v_j + G^A(z)v_i^{\alpha}G^A(z)v_j\Big\} \\
&+\frac{e}{8\pi V}\sum_k \int_{-\infty}^{+\infty} d\varepsilon f(z) tr\Big\{G^R(z)v_i^{\alpha}\frac{\partial G^R(z)}{\partial z}v_j - \frac{\partial G^R(z)}{\partial z}v_i^{\alpha}G^R(z)v_j \\
&+\frac{\partial G^A(z)}{\partial z}v_i^{\alpha}G^A(z)v_j - G^A(z)v_i^{\alpha}\frac{\partial G^A(z)}{\partial z}v_j\Big\},
\end{aligned} \tag{6.B.7}$$

where the first two integrals are Fermi surface term in Eq. 6.14 and the last integral is Fermi sea term in Eq. 6.15.

6.C Appendix: Trace of Pauli matrices

Here, we present the trace calculation in Eq. 6.16, 6.26. We first consider the trace over the Pauli matrices ρ_μ,

$$\begin{aligned}
tr\Big\{\rho_\mu\rho_2\rho_\lambda\rho_1\Big\} &= tr\Big\{\rho_0\rho_2\rho_0\rho_1\Big\} + \sum_{\lambda=1,2,3} tr\Big\{\rho_0\rho_2\rho_\lambda\rho_1\Big\} \sum_{\mu=1,2,3} tr\Big\{\rho_\mu\rho_2\rho_0\rho_1\Big\} + \sum_{\mu,\lambda=1,2,3} tr\Big\{\rho_\mu\rho_2\rho_\lambda\rho_1\Big\} \\
&= \sum_{\mu,\lambda=1,2,3} tr\Big\{\rho_\mu\rho_2\rho_\lambda\rho_1\Big\} + 2i\delta_{\mu0}\delta_{\lambda3} - 2i\delta_{\mu3}\delta_{\lambda0} \\
&= \sum_{\mu,\lambda=1,2,3} tr\Big\{\rho_\mu\{\rho_2,\rho_\lambda\}\rho_1 - \rho_\mu\rho_\lambda\rho_2\rho_1\Big\} + 2i\delta_{\mu0}\delta_{\lambda3} - 2i\delta_{\mu3}\delta_{\lambda0} \\
&= \sum_{\mu,\lambda=1,2,3} 2\delta_{2\lambda} tr\Big\{\rho_\mu\rho_1\Big\} + i\; tr\Big\{\rho_\mu\rho_\lambda\rho_3\Big\} + 2i\delta_{\mu0}\delta_{\lambda3} - 2i\delta_{\mu3}\delta_{\lambda0} \\
&= \sum_{\mu,\lambda=1,2,3} 4\delta_{2\lambda}\delta_{\mu1} - 2\epsilon_{\mu\lambda3} + 2i\delta_{\mu0}\delta_{\lambda3} - 2i\delta_{\mu3}\delta_{\lambda0}. \qquad (6.C.1)
\end{aligned}$$

Nota that the sum over fist two terms is,

$$\sum_{\mu,\lambda=1,2,3} 4\delta_{2\lambda}\delta_{\mu1} - 2\epsilon_{\mu\lambda3} = \begin{cases} 2 & \mu=1,\lambda=2 \\ 2 & \mu=2,\lambda=1 \end{cases} \qquad (6.C.2)$$

In summary, the trace over ρ_μ is

$$tr\Big\{\rho_\mu\rho_2\rho_\lambda\rho_1\Big\} = 2\delta_{\mu1}\delta_{\lambda2} + 2\delta_{\mu2}\delta_{\lambda1} + 2i\delta_{\mu0}\delta_{\lambda3} - 2i\delta_{\mu3}\delta_{\lambda0}. \qquad (6.C.3)$$

The trace over σ^ν is,

$$\begin{aligned}
tr\Big\{\sigma^\nu\sigma^\beta\sigma^\tau\sigma^j\Big\} &= tr\Big\{\sigma^0\sigma^\beta\sigma^0\sigma^j\Big\} + \sum_{\tau=1,2,3} tr\Big\{\sigma^0\sigma^\beta\sigma^\tau\sigma^j\Big\} \\
&\quad + \sum_{\nu=1,2,3} tr\Big\{\sigma^\nu\sigma^\beta\sigma^0\sigma^j\Big\} + \sum_{\nu,\tau=1,2,3} tr\Big\{\sigma^\nu\sigma^\beta\sigma^\tau\sigma^j\Big\} \\
&= 2\delta_{\beta j}\delta_{\nu0}\delta_{\tau0} + \sum_{\tau=1,2,3} tr\Big\{\sigma^\tau\sigma^j\sigma^\beta\Big\} + \sum_{\nu=1,2,3} tr\Big\{\sigma^\nu\sigma^\beta\sigma^j\Big\} + \sum_{\nu,\tau=1,2,3} tr\Big\{\sigma^\nu\sigma^\beta\sigma^\tau\sigma^j\Big\} \\
&= 2\delta_{\beta j}\delta_{\nu0}\delta_{\tau0} + 2i\epsilon_{\tau j\beta}\delta_{\nu0} + 2i\epsilon_{\nu\beta j}\delta_{\tau0} + \sum_{\nu,\tau=1,2,3} tr\Big\{\sigma^\nu\sigma^\beta\sigma^\tau\sigma^j\Big\}
\end{aligned}$$

$$= 2\delta_{\beta j}\delta_{\nu 0}\delta_{\tau 0} + 2i\epsilon_{\tau j\beta}\delta_{\nu 0} + 2i\epsilon_{\nu\beta j}\delta_{\tau 0} + \sum_{\nu,\tau=1,2,3} 2\delta_{\nu\beta}\delta_{\tau j} - 2\delta_{\nu\tau}\delta_{\beta j} + 2\delta_{\nu j}\delta_{\tau\beta}. \tag{6.C.4}$$

Consider the symmetry of spin Hall conductivity tensor, we calculate the σ^3_{21} as an example,

$$\epsilon_{i\alpha\beta} tr\Big\{\rho_\mu\rho_2\rho_\lambda\rho_1\Big\} tr\Big\{\sigma^\nu\sigma^\beta\sigma^\tau\sigma^j\Big\} = tr\Big\{\rho_\mu\rho_2\rho_\lambda\rho_1\Big\} tr\Big\{\sigma^\nu\sigma^1\sigma^\tau\sigma^1\Big\}. \tag{6.C.5}$$

The trace over σ reduces to,

$$\begin{aligned} tr\Big\{\sigma^\nu\sigma^1\sigma^\tau\sigma^1\Big\} &= 2\delta_{\nu 0}\delta_{\tau 0} + \sum_{\nu,\tau=1,2,3} 2\delta_{\nu 1}\delta_{\tau 1} - 2\delta_{\nu\tau} + 2\delta_{\nu 1}\delta_{\tau 1} \\ &= 2\delta_{\nu 0}\delta_{\tau 0} + 2\delta_{\nu 1}\delta_{\tau 1} - 2\delta_{\nu 2}\delta_{\tau 2} - 2\delta_{\nu 3}\delta_{\tau 3}. \end{aligned} \tag{6.C.6}$$

The product of trace parts is

$$\begin{aligned} & tr\Big\{\rho_\mu\rho_2\rho_\lambda\rho_1\Big\} tr\Big\{\sigma^\nu\sigma^1\sigma^\tau\sigma^1\Big\} = \\ & 4\Big(\delta_{\mu 1}\delta_{\lambda 2} + \delta_{\mu 2}\delta_{\lambda 1} + i\delta_{\mu 0}\delta_{\lambda 3} - i\delta_{\mu 3}\delta_{\lambda 0}\Big)\Big(\delta_{\nu 0}\delta_{\tau 0} + \delta_{\nu 1}\delta_{\tau 1} - \delta_{\nu 2}\delta_{\tau 2} - \delta_{\nu 3}\delta_{\tau 3}\Big) \\ = \; & 4\Big(\delta_{\mu 1}\delta_{\nu 0}\delta_{\lambda 2}\delta_{\tau 0} + \delta_{\mu 1}\delta_{\nu 1}\delta_{\lambda 2}\delta_{\tau 1} - \delta_{\mu 1}\delta_{\nu 2}\delta_{\lambda 2}\delta_{\tau 2} - \delta_{\mu 1}\delta_{\nu 3}\delta_{\lambda 2}\delta_{\tau 3}, \\ & +\delta_{\mu 2}\delta_{\nu 0}\delta_{\lambda 1}\delta_{\tau 0} + \delta_{\mu 2}\delta_{\nu 1}\delta_{\lambda 1}\delta_{\tau 1} - \delta_{\mu 2}\delta_{\nu 2}\delta_{\lambda 1}\delta_{\tau 2} - \delta_{\mu 2}\delta_{\nu 3}\delta_{\lambda 1}\delta_{\tau 3}\Big) \\ & +4i\Big(\delta_{\mu 0}\delta_{\nu 0}\delta_{\lambda 3}\delta_{\tau 0} + \delta_{\mu 0}\delta_{\nu 1}\delta_{\lambda 3}\delta_{\tau 1} - \delta_{\mu 0}\delta_{\nu 2}\delta_{\lambda 3}\delta_{\tau 2} - \delta_{\mu 0}\delta_{\nu 3}\delta_{\lambda 3}\delta_{\tau 3} \\ & -\delta_{\mu 3}\delta_{\nu 0}\delta_{\lambda 0}\delta_{\tau 0} - \delta_{\mu 3}\delta_{\nu 1}\delta_{\lambda 0}\delta_{\tau 1} + \delta_{\mu 3}\delta_{\nu 2}\delta_{\lambda 0}\delta_{\tau 2} + \delta_{\mu 3}\delta_{\nu 3}\delta_{\lambda 0}\delta_{\tau 3}\Big) \\ = \; & 4(\delta_{\mu 1}\delta_{\lambda 2} + \delta_{\mu 2}\delta_{\lambda 1})\sum_\gamma s_\gamma\delta_{\nu\gamma}\delta_{\tau\gamma} + 4i(\delta_{\mu 0}\delta_{\lambda 3} - \delta_{\mu 3}\delta_{\lambda 0})\sum_\gamma s_\gamma\delta_{\nu\gamma}\delta_{\tau\gamma}, \end{aligned} \tag{6.C.7}$$

where we define $s_{0,1} = 1, s_{2,3} = -1$.

In Fermi surface term (Eq. 6.16), the product of $g_{\mu\nu}g_{\lambda\tau}$ are contracted by the trace term. We have,

$$\begin{aligned} & \Big\{\frac{g^R_{\mu\nu}(\varepsilon)g^R_{\lambda\tau}(\varepsilon)}{D^R(\varepsilon)D^R(\varepsilon)} - 2\frac{g^A_{\mu\nu}(\varepsilon)g^R_{\lambda\tau}(\varepsilon)}{D^A(\varepsilon)D^R(\varepsilon)} + \frac{g^A_{\mu\nu}(\varepsilon)g^A_{\lambda\tau}(\varepsilon)}{D^A(\varepsilon)D^A(\varepsilon)}\Big\} tr\Big\{\rho_\mu\rho_2\rho_\lambda\rho_1\Big\} tr\Big\{\sigma^\nu\sigma^1\sigma^\tau\sigma^1\Big\} \\ = \; & 4\sum_\gamma s_\gamma \Big\{\frac{g^R_{1\gamma}(\varepsilon)g^R_{2\gamma}(\varepsilon)}{D^R(\varepsilon)D^R(\varepsilon)} - 2\frac{g^A_{1\gamma}(\varepsilon)g^R_{2\gamma}(\varepsilon)}{D^A(\varepsilon)D^R(\varepsilon)} + \frac{g^A_{1\gamma}(\varepsilon)g^A_{2\gamma}(\varepsilon)}{D^A(\varepsilon)D^A(\varepsilon)} + \Big(2 \leftrightarrow 1\Big)\Big\} \end{aligned}$$

$$
\begin{aligned}
& +4i\sum_{\gamma} s_{\gamma}\Big\{\frac{g^R_{0\gamma}(\varepsilon)g^R_{3\gamma}(\varepsilon)}{D^R(\varepsilon)D^R(\varepsilon)} - 2\frac{g^A_{0\gamma}(\varepsilon)g^R_{3\gamma}(\varepsilon)}{D^A(\varepsilon)D^R(\varepsilon)} + \frac{g^A_{0\gamma}(\varepsilon)g^A_{3\gamma}(\varepsilon)}{D^A(\varepsilon)D^A(\varepsilon)} - \Big(0 \leftrightarrow 3\Big)\Big\} \\
= \;& 8\sum_{\gamma} s_{\gamma}\Big\{\frac{g^R_{1\gamma}(\varepsilon)g^R_{2\gamma}(\varepsilon)}{D^R(\varepsilon)D^R(\varepsilon)} - \frac{g^A_{1\gamma}(\varepsilon)g^R_{2\gamma}(\varepsilon) + g^R_{1\gamma}(\varepsilon)g^A_{2\gamma}(\varepsilon)}{D^A(\varepsilon)D^R(\varepsilon)} + \frac{g^A_{1\gamma}(\varepsilon)g^A_{2\gamma}(\varepsilon)}{D^A(\varepsilon)D^A(\varepsilon)}\Big\} \\
& -8i\sum_{\gamma} s_{\gamma}\Big\{\frac{g^A_{0\gamma}(\varepsilon)g^R_{3\gamma}(\varepsilon) - g^R_{0\gamma}(\varepsilon)g^A_{3\gamma}(\varepsilon)}{D^A(\varepsilon)D^R(\varepsilon)}\Big\} \\
= \;& 16\sum_{\gamma} s_{\gamma}\mathrm{Re}\Big\{\frac{g^R_{1\gamma}(\varepsilon)g^R_{2\gamma}(\varepsilon)}{D^R(\varepsilon)D^R(\varepsilon)} - \frac{g^A_{1\gamma}(\varepsilon)g^R_{2\gamma}(\varepsilon)}{D^A(\varepsilon)D^R(\varepsilon)}\Big\} + 16\sum_{\gamma} s_{\gamma}\mathrm{Im}\Big\{\frac{g^A_{0\gamma}(\varepsilon)g^R_{3\gamma}(\varepsilon)}{D^A(\varepsilon)D^R(\varepsilon)}\Big\}.
\end{aligned}
\tag{6.C.8}
$$

Similarly, the Fermi sea term (Eq. 6.25) is,

$$
\begin{aligned}
& \Big\{\frac{g^R_{\mu\nu}(\varepsilon)\partial_z g^R_{\lambda\tau}(\varepsilon) - \partial_z g^R_{\mu\nu}(\varepsilon)g^R_{\lambda\tau}(\varepsilon)}{D^R(\varepsilon)^2} - \Big(R \leftrightarrow A\Big)\Big\} tr\Big\{\rho_\mu\rho_2\rho_\lambda\rho_1\Big\} tr\Big\{\sigma^\nu\sigma^1\sigma^\tau\sigma^1\Big\} \\
= \;& 8i\sum_{\gamma} s_{\gamma}\mathrm{Im}\Big[\frac{g^R_{1\gamma}(\varepsilon)\partial_z g^R_{2\gamma}(\varepsilon) - \partial_z g^R_{1\gamma}(\varepsilon)g^R_{2\gamma}(\varepsilon) + g^R_{2\gamma}(\varepsilon)\partial_z g^R_{1\gamma}(\varepsilon) - \partial_z g^R_{2\gamma}(\varepsilon)g^R_{1\gamma}(\varepsilon)}{D^R(\varepsilon)^2}\Big] \\
& -8\sum_{\gamma} s_{\gamma}\mathrm{Im}\Big[\frac{g^R_{0\gamma}(\varepsilon)\partial_z g^R_{3\gamma}(\varepsilon) - \partial_z g^R_{0\gamma}(\varepsilon)g^R_{3\gamma}(\varepsilon) - g^R_{3\gamma}(\varepsilon)\partial_z g^R_{0\gamma}(\varepsilon) + \partial_z g^R_{3\gamma}(\varepsilon)g^R_{0\gamma}(\varepsilon)}{D^R(\varepsilon)^2}\Big] \\
= \;& -16\sum_{\gamma} s_{\gamma}\mathrm{Im}\Big[\frac{g^R_{0\gamma}(\varepsilon)\partial_z g^R_{3\gamma}(\varepsilon) - \partial_z g^R_{0\gamma}(\varepsilon)g^R_{3\gamma}(\varepsilon)}{D^R(\varepsilon)^2}\Big].
\end{aligned}
\tag{6.C.9}
$$

The retarded denominator is

$$
\frac{1}{D^R(\varepsilon)} = \prod_{\eta,\zeta}\frac{1}{\varepsilon - \zeta E_\eta + i\gamma} = \frac{1}{8M\tilde{k}_\perp}\sum_{\eta,\zeta}\frac{\eta\zeta}{E_\eta}\frac{1}{\varepsilon - \zeta E_\eta + i\gamma} \tag{6.C.10}
$$

$$
\begin{aligned}
\frac{1}{(D^R(\varepsilon))^2} &= \frac{1}{64M^2\tilde{k}_\perp^2}\Big(\sum_{\eta,\zeta}\frac{\eta\zeta}{E_\eta}\frac{1}{\varepsilon - \zeta E_\eta + i\gamma}\Big)\Big(\sum_{\eta',\zeta'}\frac{\eta'\zeta'}{E_{\eta'}}\frac{1}{\varepsilon - \zeta' E_{\eta'} + i\gamma}\Big) \\
&= \frac{1}{64M^2\tilde{k}_\perp^2}\Big\{\sum_{\eta,\zeta}\frac{1}{E_\eta^2}\frac{1}{(\varepsilon - \zeta E_\eta + i\gamma)^2} + \sum_{\eta,\zeta}\sum_{\eta',\zeta'}\frac{\eta\zeta}{E_\eta}\frac{\eta'\zeta'}{E_{\eta'}}\frac{(1-\delta_{\eta,\eta'}\delta_{\zeta,\zeta'})}{(\varepsilon - \zeta E_\eta + i\gamma)(\varepsilon - \zeta' E_{\eta'} + i\gamma)}\Big\} \\
&= \frac{1}{64M^2\tilde{k}_\perp^2}\Big\{\sum_{\eta,\zeta}\frac{1}{E_\eta^2}\frac{1}{(\varepsilon - \zeta E_\eta + i\gamma)^2} \\
&\quad + \sum_{\eta,\zeta}\sum_{\eta',\zeta'}\frac{\eta\zeta}{E_\eta}\frac{\eta'\zeta'}{E_{\eta'}}\frac{(1-\delta_{\eta,\eta'}\delta_{\zeta,\zeta'})}{\zeta E_\eta - \zeta' E_{\eta'}}\Big(\frac{1}{(\varepsilon - \zeta E_\eta + i\gamma)} - \frac{1}{(\varepsilon - \zeta' E_{\eta'} + i\gamma)}\Big)\Big\}
\end{aligned}
\tag{6.C.11}
$$

The first term in Eq. 6.C.11 is

$$\begin{aligned}\mathrm{Im}\frac{X(\varepsilon)+i\gamma X'(\varepsilon)}{(\varepsilon-\zeta E_\eta+i\gamma)^2} &= \mathrm{Im}\frac{(X+i\gamma X')[(\varepsilon-\zeta E_\eta)^2-\gamma^2-i2\gamma(\varepsilon-\zeta E_\eta)]}{[(\varepsilon-\zeta E_\eta)^2+\gamma^2]^2}\\ &= \frac{-2\gamma(\varepsilon-\zeta E_\eta)X+\gamma X'(\varepsilon-\zeta E_\eta)^2}{[(\varepsilon-\zeta E_\eta)^2+\gamma^2]^2}\\ &\approx -\pi X\partial_\varepsilon\delta(\varepsilon-\zeta E_\eta) \qquad (6.C.12)\end{aligned}$$

The second term in Eq. 6.C.11 is

$$\begin{aligned}\mathrm{Im}\frac{X(\varepsilon)+i\gamma X'(\varepsilon)}{(\varepsilon-\zeta E_\eta+i\gamma)} &= \mathrm{Im}\frac{X(\varepsilon)+i\gamma X'(\varepsilon)(\varepsilon-\zeta E_\eta+i\gamma)}{(\varepsilon-\zeta E_\eta)^2+\gamma^2}\\ &= \frac{\gamma X+\gamma X'(\varepsilon-\zeta E_\eta)}{(\varepsilon-\zeta E_\eta)^2+\gamma^2}\\ &\approx \pi X\delta(\varepsilon-\zeta E_\eta) \qquad (6.C.13)\end{aligned}$$

Therefore, the leading order of Eq. 6.C.9 is

$$\begin{aligned}&\mathrm{Im}\frac{X^R(\varepsilon)}{(D^R(\varepsilon))^2} = \frac{\pi}{64M^2\tilde{k}_\perp^2}\Big\{-\sum_{\eta,\zeta}\frac{1}{E_\eta^2}X(\varepsilon)\partial_\varepsilon\delta(\varepsilon-\zeta E_\eta)\\ &+\sum_{\eta,\zeta}\sum_{\eta',\zeta'}X(\varepsilon)\frac{\eta\zeta}{E_\eta}\frac{\eta'\zeta'}{E_{\eta'}}\frac{(1-\delta_{\eta,\eta'}\delta_{\zeta,\zeta'})}{\zeta E_\eta-\zeta' E_{\eta'}}\Big(\delta(\varepsilon-\zeta E_\eta)-\delta(\varepsilon-\zeta' E_{\eta'})\Big)\Big\} \qquad (6.C.14)\end{aligned}$$

Note that the second term in Eq. 6.C.14 is

$$\begin{aligned}&\sum_{\eta,\zeta}\sum_{\eta',\zeta'}\frac{\eta\zeta}{E_\eta}\frac{\eta'\zeta'}{E_{\eta'}}\frac{(1-\delta_{\eta,\eta'}\delta_{\zeta,\zeta'})}{\zeta E_\eta-\zeta' E_{\eta'}}\Big(\delta(\varepsilon-\zeta E_\eta)-\delta(\varepsilon-\zeta' E_{\eta'})\Big)\\ &=\sum_{\eta,\zeta}\frac{\eta\zeta}{E_\eta}\frac{-\eta(-\zeta)}{E_{-\eta}}\frac{1}{\zeta E_\eta+\zeta E_{-\eta}}\Big(\delta(\varepsilon-\zeta E_\eta)-\delta(\varepsilon+\zeta E_{-\eta})\Big)\\ &+\sum_{\eta,\zeta}\frac{\eta\zeta}{E_\eta}\frac{\eta(-\zeta)}{E_\eta}\frac{1}{\zeta E_\eta+\zeta E_\eta}\Big(\delta(\varepsilon-\zeta E_\eta)-\delta(\varepsilon+\zeta E_\eta)\Big)\\ &+\sum_{\eta,\zeta}\frac{\eta\zeta}{E_\eta}\frac{(-\eta)\zeta}{E_{-\eta}}\frac{1}{\zeta E_\eta-\zeta E_{-\eta}}\Big(\delta(\varepsilon-\zeta E_\eta)-\delta(\varepsilon-\zeta E_{-\eta})\Big)\\ &=\sum_{\eta,\zeta}\frac{2}{\zeta E_\eta E_{-\eta}}\frac{1}{E_\eta+E_{-\eta}}\delta(\varepsilon-\zeta E_\eta)+\sum_{\eta,\zeta}\frac{-1}{\zeta E_\eta^3}\delta(\varepsilon-\zeta E_\eta)+\sum_{\eta,\zeta}\frac{-2}{\zeta E_\eta E_{-\eta}}\frac{1}{E_\eta-E_{-\eta}}\delta(\varepsilon-\zeta E_\eta)\\ &=\sum_{\eta,\zeta}\delta(\varepsilon-\zeta E_\eta)\Big\{\frac{-1}{\zeta E_\eta^3}+\frac{-1}{\zeta\eta E_\eta M\tilde{k}_\perp}\Big\} \qquad (6.C.15)\end{aligned}$$

The leading order of Eq. 6.C.9 is

$$\begin{aligned}
&\mathrm{Im}\frac{X^R(\varepsilon)}{(D^R(\varepsilon))^2} = \frac{\pi}{64M^2\tilde{k}_\perp^2}\Big\{-\sum_{\eta,\zeta}\frac{1}{E_\eta^2}X(\varepsilon)\partial_\varepsilon\delta(\varepsilon-\zeta E_\eta) - \sum_{\eta,\zeta}\frac{X(\varepsilon)\zeta}{E_\eta}\big(\frac{1}{E_\eta^2}+\frac{1}{\eta M\tilde{k}_\perp}\big)\delta(\varepsilon-\zeta E_\eta)\Big\} \\
&= -\pi\sum_{\eta,\zeta}\Big\{\frac{X(\varepsilon)\partial_\varepsilon\delta(\varepsilon-\zeta E_\eta)}{(D'(\zeta E_\eta))^2}+\frac{X(\varepsilon)D''(\zeta E_\eta)}{(D'(\zeta E_\eta))^3}\delta(\varepsilon-\zeta E_\eta)\Big\} \\
&= -\pi\sum_{\eta,\zeta}\Big\{\frac{\partial_\varepsilon(X(\varepsilon)\delta(\varepsilon-\zeta E_\eta))-\partial_\varepsilon X(\varepsilon)\delta(\varepsilon-\zeta E_\eta)}{(D'(\zeta E_\eta))^2}+\frac{X(\varepsilon)D''(\zeta E_\eta)}{(D'(\zeta E_\eta))^3}\delta(\varepsilon-\zeta E_\eta)\Big\} \\
&= -\pi\sum_{\eta,\zeta}\Big\{\frac{\partial_\varepsilon(X(\varepsilon)\delta(\varepsilon-\zeta E_\eta))}{(D'(\zeta E_\eta))^2}+\frac{-\partial_\varepsilon X(\varepsilon)\delta(\varepsilon-\zeta E_\eta)}{(D'(\zeta E_\eta))^2}+\frac{X(\varepsilon)D''(\zeta E_\eta)}{(D'(\zeta E_\eta))^3}\delta(\varepsilon-\zeta E_\eta)\Big\} \\
&= -\pi\partial_\varepsilon\Big(\sum_{\eta,\zeta}\frac{X(\varepsilon)\delta(\varepsilon-\zeta E_\eta)}{(D'(\zeta E_\eta))^2}\Big)+\sum_{\eta,\zeta}\frac{\delta(\varepsilon-\zeta E_\eta)}{|D'(\zeta E_\eta)|}\eta\zeta\Big\{\frac{\partial_\varepsilon X(\varepsilon)}{(D'(\zeta E_\eta))}-\frac{X(\varepsilon)D''(\zeta E_\eta)}{(D'(\zeta E_\eta))^2}\Big\} \\
&= -\pi\partial_\varepsilon\Big(\eta\zeta\delta(D(\varepsilon))\frac{X(\varepsilon)}{(D'(\zeta E_\eta))}\Big)+\pi\eta\zeta\delta(D(\varepsilon))\Big\{\frac{\partial_\varepsilon X(\varepsilon)}{(D'(\zeta E_\eta))}-\frac{X(\varepsilon)D''(\zeta E_\eta)}{(D'(\zeta E_\eta))^2}\Big\} \\
&= -\pi\partial_\varepsilon\Big(\eta\zeta\delta(D(\varepsilon))\frac{X(\varepsilon)}{(D'(\varepsilon))}\Big)+\pi\eta\zeta\delta(D(\varepsilon))\Big\{\frac{\partial_\varepsilon X(\varepsilon)}{(D'(\varepsilon))}-\frac{X(\varepsilon)D''(\varepsilon)}{(D'(\varepsilon))^2}\Big\} \\
&= -\pi\eta\zeta\partial_\varepsilon\Big(\delta(D(\varepsilon))\frac{X(\varepsilon)}{(D'(\varepsilon))}\Big)+\pi\eta\zeta\delta(D(\varepsilon))\partial_\varepsilon\Big(\frac{X(\varepsilon)}{(D'(\varepsilon))}\Big) \\
&= -\pi\eta\zeta\partial_\varepsilon\delta(D(\varepsilon))\frac{X(\varepsilon)}{(D'(\varepsilon))} \qquad (6.C.16)
\end{aligned}$$

where we derive the Eq. 6.28. Note that $\mathrm{sgn}D'(\zeta E_\eta)=\eta\zeta$.

6.D Appendix: Calculation of $X(\varepsilon)$ and $X'(\varepsilon)$

$X_\alpha^{(0)}$ is calculated from the Table 6.1,

$$\begin{aligned}
X_0^{(0)}(\varepsilon) &= \varepsilon(\varepsilon^2-\varepsilon_{\boldsymbol{k}}^2-2M^2)2m\varepsilon-(3\varepsilon^2-\varepsilon_{\boldsymbol{k}}^2-2M^2)m(\varepsilon^2-\varepsilon_{\boldsymbol{k}}^2) \\
&= -m(\varepsilon^2-\varepsilon_{\boldsymbol{k}}^2)^2-2mM^2(\varepsilon^2+\varepsilon_{\boldsymbol{k}}^2), \qquad (6.D.1) \\
X_i^{(0)}(\varepsilon) &= (-2m\varepsilon M_i)(-M_i2\varepsilon)-(-2mM_i)(-M_i(\varepsilon^2+\varepsilon_{\boldsymbol{k}}^2)+2k_iMk_\parallel) \\
&= 2mM_i^2(\varepsilon^2-\varepsilon_{\boldsymbol{k}}^2)+4mM_ik_iMk_\parallel, \qquad (6.D.2)
\end{aligned}$$

where $i=1,2,3$.

$X^{(0)}(\varepsilon)$ and $X'^{(0)}(\varepsilon)$ are,

$$\begin{aligned} X^{(0)}(\varepsilon) &= \sum_\alpha X^{(0)}_\alpha = m\Big\{ -(\varepsilon^2-\varepsilon_{\boldsymbol{k}}^2)^2 - 4M^2\varepsilon^2 + 4M_1^2(\varepsilon^2-\varepsilon_{\boldsymbol{k}}^2) \\ &+ 8Mk_\parallel M_1 k_1 - 4M^2 k_\parallel^2\Big\}, \qquad (6.D.3) \\ X'^{(0)}(\varepsilon) &= m\Big\{ -4\varepsilon(\varepsilon^2-\varepsilon_{\boldsymbol{k}}^2) - 8M^2\varepsilon + 8M_1^2\varepsilon\Big\}. \qquad (6.D.4) \end{aligned}$$

In the presence of delta function, $\delta(\varepsilon-\zeta E_\eta)$, $X^{(0)}(\varepsilon)$ and $X'^{(0)}(\varepsilon)$ are confined to $\varepsilon = \zeta E_\eta$. The $X^{(0)}(\zeta E_\eta)$ is,

$$\begin{aligned} X^{(0)}(\zeta E_\eta) &= m\Big\{ -(2M^2+\eta\Gamma_{\boldsymbol{k}})^2 - 4M^2{E_\eta}^2 + 4M_1^2(2M^2+\eta\Gamma_{\boldsymbol{k}}) + 8Mk_\parallel M_1 k_1 - 4M^2k_\parallel^2\Big\} \\ &= m\Big\{ -(2M^2+\eta 2M\tilde{k}_\perp)^2 - 4M^2{E_\eta}^2 + 4M_1^2(2M^2+\eta 2M\tilde{k}_\perp) + 8Mk_\parallel M_1k_1 - 4M^2k_\parallel^2\Big\} \\ &= -4mM^2\Big\{(M+\eta\tilde{k}_\perp)^2 + {E_\eta}^2 - m_1^2(2M^2+\eta 2M\tilde{k}_\perp) - 2m_1k_\parallel k_1 + k_\parallel^2\Big\} \\ &= -4mM^2\Big\{M^2 + \tilde{k}_\perp^2 + 2\eta M\tilde{k}_\perp + {E_\eta}^2 - m_1^2(2M^2+\eta 2M\tilde{k}_\perp) - 2m_1k_\parallel k_1 + k_\parallel^2\Big\} \\ &= -8mM^2\Big\{{E_\eta}^2 - m_1^2(M^2+\eta M\tilde{k}_\perp) - m_1k_\parallel k_1\Big\}. \qquad (6.D.5) \end{aligned}$$

In the last term of Eq. 6.D.5, we separate k_1 into parallel and perpendicular components,

$$\begin{aligned} k_1 = \boldsymbol{k}\cdot\hat{x} &= (\mathcal{R}\boldsymbol{k})\cdot(\mathcal{R}\hat{x}) \\ &= k_1'[(1-\cos\theta)\cos^2\varphi - 1] + k_2'(1-\cos\theta)\sin\varphi\cos\varphi + k_3'\sin\theta\cos\varphi, \end{aligned} \qquad (6.D.6)$$

where $k_3' \equiv k_\perp$ and k_1', k_2' are in the plane perpendicular to $k_\perp$. Thus, $k_\parallel k_1$ reads,

$$k_\parallel k_1 = k_3'k_1'[(1-\cos\theta)\cos^2\varphi - 1] + k_3'k_2'(1-\cos\theta)\sin\varphi\cos\varphi + {k_3'}^2\sin\theta\cos\varphi. \qquad (6.D.7)$$

Note that integrand consisting $k_3'k_1'$ and $k_3'k_2'$ would eventually vanish in $\boldsymbol{k}$ integration, as $I(k_{1,2}') = -I(-k_{1,2}')$.

The non-vanishing $X^{(0)}$ is

$$\begin{aligned} X^{(0)}(\zeta E_\eta) &= -8mM^2\Big\{{E_\eta}^2 - m_1^2(M^2+\eta M\tilde{k}_\perp) - m_1^2 k_\parallel^2\Big\} \\ &= -8mM^2\Big\{(1-m_1^2){E_\eta}^2 + m_1^2\eta M\tilde{k}_\perp + m_1^2\tilde{k}_\perp^2\Big\}. \end{aligned} \tag{6.D.8}$$

Similarly, we have $X'^{(0)}(\zeta E_\eta)$,

$$\begin{aligned} X'^{(0)}(\zeta E_\eta) &= m\zeta\Big\{-4E_\eta(2M^2+\eta\Gamma_{\boldsymbol{k}}) - 8M^2E_\eta + 8M_1^2E_\eta\Big\} \\ &= -8m\zeta E_\eta\Big\{2M^2+\eta M\tilde{k}_\perp - M_1^2\Big\}. \end{aligned} \tag{6.D.9}$$

6.E Appendix: Calculation of $\sigma_{21}^{3,iso.}$ and $\sigma_{21}^{3,m}$ terms

a. Momentum cut-off scheme

To calculate the divergent part of $\sigma_{21}^{3,iso.}$ term, we expand it in the order of M and calculate it to the second order. We first expand the E_η and E_η^{-1} to the third order of M,

$$E_\eta \approx \tilde{k} + \eta M\frac{\tilde{k}_\perp}{\tilde{k}} + \frac{\tilde{k}^2-\tilde{k}_\perp^2}{2\tilde{k}^3}M^2 - \eta M^3\frac{(\tilde{k}_\perp\tilde{k}^2-\tilde{k}_\perp^3)}{2\tilde{k}^5}, \tag{6.E.1}$$

$${E_\eta}^{-1} \approx \frac{1}{\tilde{k}} - \frac{\eta M\tilde{k}_\perp}{\tilde{k}^3} + M^2\frac{3\tilde{k}_\perp^2-\tilde{k}^2}{2\tilde{k}^5} + \eta M^3\frac{3\tilde{k}_\perp\tilde{k}^2-5\tilde{k}_\perp^3}{2\tilde{k}^7}, \tag{6.E.2}$$

where we define $\tilde{k} \equiv \sqrt{k^2+m^2}$, similar with $\tilde{k}_\perp$.

The divergent part of $\sigma_{21}^{3,iso.}$ term to the second order of M is

$$\begin{aligned} D^{iso.} &= \frac{em}{4V}\sum_k\sum_{\eta=\pm1} \\ &\quad \frac{1}{\tilde{k}_\perp^2}\Big(\frac{1}{\tilde{k}} + M^2\frac{3\tilde{k}_\perp^2-\tilde{k}^2}{2\tilde{k}^5}\Big) + \Big(-\frac{1}{\tilde{k}^3} + M^2\frac{3\tilde{k}^2-5\tilde{k}_\perp^2}{2\tilde{k}^7}\Big) - \frac{1}{\tilde{k}_\perp^3}\Big(\frac{\tilde{k}_\perp}{\tilde{k}} - M^2\frac{(\tilde{k}_\perp\tilde{k}^2-\tilde{k}_\perp^3)}{2\tilde{k}^5}\Big) \\ &= \frac{em}{4V}\sum_k\sum_{\eta=\pm1} -\frac{1}{\tilde{k}^3} + \frac{1}{\tilde{k}_\perp^2}\Big(M^2\frac{3\tilde{k}_\perp^2-\tilde{k}^2}{2\tilde{k}^5}\Big) + \Big(M^2\frac{3\tilde{k}^2-5\tilde{k}_\perp^2}{2\tilde{k}^7}\Big) - \frac{1}{\tilde{k}_\perp^3}\Big(-M^2\frac{(\tilde{k}_\perp\tilde{k}^2-\tilde{k}_\perp^3)}{2\tilde{k}^5}\Big) \\ &= \frac{em}{V}\sum_k\sum_{\eta=\pm1} -\frac{1}{\tilde{k}^3} + M^2\Big(\frac{3\tilde{k}_\perp^2-\tilde{k}^2}{2\tilde{k}_\perp^2\tilde{k}^5} + \frac{3\tilde{k}^2-5\tilde{k}_\perp^2}{2\tilde{k}^7} + \frac{(\tilde{k}^2-\tilde{k}_\perp^2)}{2\tilde{k}_\perp^2\tilde{k}^5}\Big) \\ &= -\frac{em}{2V}\sum_k\frac{1}{\tilde{k}^3} - \frac{5M^2}{2}\frac{k_\parallel^2}{\tilde{k}^7}. \end{aligned} \tag{6.E.3}$$

Using identities of integrals (Eqs. 6.E.21, 6.E.23), Eq. 6.E.3 is calculated explicitly,

$$D^{iso.} \approx -\frac{em}{8\pi^2}(2\log(2\Lambda/m) - 2 - \frac{M^2}{3m^2}). \tag{6.E.4}$$

To calculate the divergent part of $\sigma_{21}^{3,\boldsymbol{m}}$ term, we expand E_η^{-3} to second order of M,

$$E_\eta^{-3} \approx \frac{1}{\tilde{k}^3} - \eta M\frac{3\tilde{k}_\perp}{\tilde{k}^5} - M^2\frac{3(\tilde{k}^2 - 5\tilde{k}_\perp^2)}{2\tilde{k}^7}. \tag{6.E.5}$$

The divergent part of $\sigma_{21}^{3,\boldsymbol{m}}$ term to the second order of M,

$$\begin{aligned} D^{\boldsymbol{m}} &\approx -\frac{em}{2V}\sum_{k}\frac{1}{\tilde{k}^3} - M^2\frac{3}{\tilde{k}^5} - M^2\frac{3(\tilde{k}^2 - 5\tilde{k}_\perp^2)}{2\tilde{k}^7} \\ &= -\frac{em}{2V}\sum_{k}\frac{1}{\tilde{k}^3} + M^2\frac{3}{\tilde{k}^5} - M^2\frac{15k_\parallel^2}{2\tilde{k}^7}. \end{aligned} \tag{6.E.6}$$

Use identities (Eqs. 6.E.21,6.E.22,6.E.23), the $D^{\boldsymbol{m}}$ is

$$D^{\boldsymbol{m}} \approx -\frac{em}{8\pi^2}\Big(2\log(2\Lambda/m) - 2 + \frac{M^2}{m^2}\Big). \tag{6.E.7}$$

b. Energy cut-off scheme

We can also employ an energy cut-off $E_\eta \leqslant \Lambda_\epsilon$ to calculate the divergent part of $D^{iso.}$ and $D^{\boldsymbol{m}}$ terms. The integration area is,

$$k_\parallel^2 + (\tilde{k}_\perp + \eta M)^2 \leqslant \Lambda_\epsilon^2. \tag{6.E.8}$$

The integration area in energy cut-off scheme is replaced by

$$\frac{1}{V}\sum_{\boldsymbol{k}<\Omega_{E-cut}} \rightarrow \frac{1}{2\pi^2}\int_m^{\Lambda_\epsilon - \eta M} d\tilde{k}_\perp \int_0^{\sqrt{\Lambda_\epsilon^2 - (\tilde{k}_\perp + \eta M)^2}} dk_\parallel \tag{6.E.9}$$

For $D^{iso.}$ term, we have

$$\begin{aligned}
&\frac{em}{8\pi^2}\sum_\eta \int_m^{\Lambda_\epsilon-\eta M} d\tilde{k}_\perp \int_0^{\sqrt{\Lambda_\epsilon^2-(\tilde{k}_\perp+\eta M)^2}} dk_\parallel \Big(\frac{1}{\tilde{k}_\perp}+\frac{\eta}{M}\Big)\frac{1}{\sqrt{k_\parallel^2+(\tilde{k}_\perp+\eta M)^2}} - \frac{\eta}{M\tilde{k}_\perp^2}\sqrt{k_\parallel^2+(\tilde{k}_\perp+\eta M)^2} \\
&= \frac{em}{8\pi^2}\sum_\eta \int_m^{\Lambda_\epsilon-\eta M} d\tilde{k}_\perp \frac{\eta}{2\tilde{k}_\perp^2 M}\Big\{-\sqrt{\Lambda_\epsilon^2-(\tilde{k}_\perp+\eta M)^2}\Lambda_\epsilon + (\tilde{k}_\perp^2-M^2)\,\mathrm{arctanh}\,\frac{\sqrt{\Lambda_\epsilon^2-(\tilde{k}_\perp+\eta M)^2}}{\Lambda_\epsilon}\Big\}
\end{aligned} \tag{6.E.10}$$

Change the variable:

$$y = \tilde{k}_\perp + \eta M \tag{6.E.11}$$

Thus, the $D^{iso.}$ term is

$$\begin{aligned}
&\frac{em}{8\pi^2}\sum_\eta \int_{m+\eta M}^{\Lambda_\epsilon} dy \frac{\eta}{2M(y-\eta M)^2}\Big\{-\sqrt{\Lambda_\epsilon^2-y^2}\Lambda_\epsilon + (y^2-2\eta M y)\,\mathrm{arctanh}\,\frac{\sqrt{\Lambda_\epsilon^2-y^2}}{\Lambda_\epsilon}\Big\} \\
&= \frac{em}{8\pi^2}\sum_\eta \int_m^{\Lambda_\epsilon} dy \Big\{-\Big(\frac{\eta}{2My^2}+\frac{1}{y^3}+\frac{3\eta M}{2y^4}+\frac{2M^2}{y^5}\Big)\sqrt{\Lambda_\epsilon^2-y^2}\Lambda_\epsilon \\
&+ \Big(\frac{\eta}{2M}-\frac{\eta M}{2y^2}-\frac{M^2}{y^3}\Big)\,\mathrm{arctanh}\,\frac{\sqrt{\Lambda_\epsilon^2-y^2}}{\Lambda_\epsilon}\Big\} + \mathcal{O}(M^2) \\
&- \frac{em}{8\pi^2}\int_m^{m+\eta M} \frac{\eta}{2M(y-\eta M)^2}\Big\{-\sqrt{\Lambda_\epsilon^2-y^2}\Lambda_\epsilon + (y^2-2\eta M y)\,\mathrm{arctanh}\,\frac{\sqrt{\Lambda_\epsilon^2-y^2}}{\Lambda_\epsilon}\Big\}
\end{aligned} \tag{6.E.12}$$

We employ the follow relation:

$$\sum_\eta \int_m^{\Lambda_\epsilon} dy\ \eta A + B = 2\int_m^{\Lambda_\epsilon} dy\ B \tag{6.E.13}$$

where A, B do not contain η.

Thus, the $D^{iso.}$ term is reduced to

$$D^{iso.} = -\frac{em}{4\pi^2}\int_m^{\Lambda_\epsilon} dy(\frac{1}{y^3}+\frac{2M^2}{y^5})\sqrt{\Lambda_\epsilon^2-y^2}\Lambda_\epsilon + \frac{M^2}{y^3}\operatorname{arctanh}\frac{\sqrt{\Lambda_\epsilon^2-y^2}}{\Lambda_\epsilon}$$
$$-\frac{em}{8\pi^2}\sum_\eta\int_m^{m+\eta M} dy - \frac{\sqrt{\Lambda_\epsilon^2-y^2}\Lambda_\epsilon}{y^2}(\frac{\eta}{2M}+\frac{3\eta M}{2y^2}) + (\frac{\eta}{2M}-\frac{\eta M}{2y^2})\operatorname{arctanh}\frac{\sqrt{\Lambda_\epsilon^2-y^2}}{\Lambda_\epsilon}\Big\} + \mathcal{O}(M^3)$$
$$(6.E.14)$$

The first integral in Eq. 6.E.14 is

$$\approx -\frac{em}{4\pi^2}\Big\{\frac{\sqrt{\Lambda_\epsilon^2-m^2}\Lambda_\epsilon}{2m^2} - \frac{1}{2}\operatorname{arctanh}\frac{\sqrt{\Lambda_\epsilon^2-m^2}}{\Lambda_\epsilon}$$
$$+\frac{M^2}{2m^2}(\operatorname{arctanh}\frac{\sqrt{\Lambda_\epsilon^2-m^2}}{\Lambda_\epsilon} + \frac{(\Lambda_\epsilon^2-m^2)^{3/2}}{m^2\Lambda_\epsilon})\Big\} + \mathcal{O}(M^4) \qquad (6.E.15)$$

The second integral Eq. 6.E.14 is

$$= -\frac{em}{4\pi^2}\Big\{-\frac{\sqrt{\Lambda_\epsilon^2-m^2}\Lambda_\epsilon}{2m^2} + \frac{1}{2}\operatorname{arctanh}\frac{\sqrt{\Lambda_\epsilon^2-m^2}}{\Lambda_\epsilon}$$
$$+\frac{M^2}{2m^2}(-\operatorname{arctanh}\frac{\sqrt{\Lambda_\epsilon^2-m^2}}{\Lambda_\epsilon} - \frac{\sqrt{\Lambda_\epsilon^2-m^2}\Lambda_\epsilon(3\Lambda_\epsilon^2-5m^2)}{3m^2(\Lambda_\epsilon^2-m^2)}) + \mathcal{O}(M^4)\Big\} \qquad (6.E.16)$$

Sum over two integrals, we have

$$D^{iso.} = -\frac{em}{4\pi^2}\frac{M^2}{2m^2}\Big\{\frac{(\Lambda_\epsilon^2-m^2)^{3/2}}{m^2\Lambda_\epsilon} - \frac{\sqrt{\Lambda_\epsilon^2-m^2}\Lambda_\epsilon(3\Lambda_\epsilon^2-5m^2)}{3m^2(\Lambda_\epsilon^2-m^2)}\Big\}$$
$$= -\frac{em}{8\pi^2}\Big\{-\frac{M^2}{3m^2}\Big\} + \mathcal{O}(M^4) \qquad (6.E.17)$$

which is the result of Eq. 6.47 in the dissertation.

For $D^{\boldsymbol{m}}$ term, we have

$$D^{\boldsymbol{m}} = -\frac{em}{8\pi^2}\sum_\eta\int_m^{\Lambda_\epsilon-\eta M} d\tilde{k}_\perp \int_0^{\sqrt{\Lambda_\epsilon^2-(\tilde{k}_\perp+\eta M)^2}} dk_\parallel(\eta M+\tilde{k}_\perp)\frac{1}{(k_\parallel^2+(\tilde{k}_\perp+\eta M)^2)^{3/2}}$$
$$= -\frac{em}{8\pi^2}\sum_\eta\int_m^{\Lambda_\epsilon-\eta M} d\tilde{k}_\perp(\eta M+\tilde{k}_\perp)^{-1}\frac{\sqrt{\Lambda_\epsilon^2-(\tilde{k}_\perp+\eta M)^2}}{\Lambda_\epsilon} \qquad (6.E.18)$$

Change the variable:

$$y = \tilde{k}_\perp + \eta M \tag{6.E.19}$$

$$\begin{aligned}
D^{\boldsymbol{m}} &= -\frac{em}{8\pi^2}\sum_\eta \int_{m+\eta M}^{\Lambda_\epsilon} dy \frac{\sqrt{\Lambda_\epsilon^2 - y^2}}{\Lambda_\epsilon y} \\
&= -\frac{em}{8\pi^2}\sum_\eta \operatorname{arctanh}\frac{\sqrt{\Lambda_\epsilon^2 - (m+\eta M)^2}}{\Lambda_\epsilon} - \frac{\sqrt{\Lambda_\epsilon^2 - (m+\eta M)^2}}{\Lambda_\epsilon} \\
&= -\frac{em}{8\pi^2}\Big\{2\operatorname{arctanh}\frac{\sqrt{\Lambda_\epsilon^2 - m^2}}{\Lambda_\epsilon} - 2\frac{\sqrt{\Lambda_\epsilon^2 - m^2}}{\Lambda_\epsilon} + \frac{M^2}{m^2}\frac{\Lambda_\epsilon}{\sqrt{\Lambda_\epsilon^2 - m^2}} + \frac{M^4}{2m^4} + \mathcal{O}(M^4)\Big\} \\
&\approx -\frac{em}{8\pi^2}\Big\{2\log\frac{\Lambda_\epsilon}{m} - 2 + \frac{M^2}{m^2} + \frac{M^4}{2m^4}\Big\} + \mathcal{O}(M^6)
\end{aligned} \tag{6.E.20}$$

which is the result of Eq. 6.48.

c. Convergent part of $C^{iso.}$ and C^m terms

The convergent part is the integration near the zero energy. The $C^{iso.}$ term is

$$C^{iso.} = -\frac{em}{4V}\sum_k \sum_{\eta=\pm1}\Big\{\frac{1}{E_\eta \tilde{k}_\perp^2} + \frac{\eta}{M}\frac{1}{E_\eta \tilde{k}_\perp} - \frac{\eta}{M}\frac{E_\eta}{\tilde{k}_\perp^3}\Big\}\int_0^\mu d\varepsilon \sum_{\zeta=\pm1}\zeta\delta(\varepsilon - \zeta E_\eta). \tag{6.E.21}$$

The first and second integrands in Eq. 6.45 are

$$\begin{aligned}
C^{iso.}_{(1,2)} &= -\frac{em}{4(2\pi)^2}\sum_{\eta=\pm1}\Theta(\mu)\int_0^{\xi_\eta} dk_\perp 2k_\perp \Big\{\frac{1}{\tilde{k}_\perp^2} + \frac{\eta}{M}\frac{1}{\tilde{k}_\perp}\Big\}\int_0^{\alpha_\eta} dk_\parallel \frac{1}{(k_\parallel^2 + (\tilde{k}_\perp + \eta M)^2)^{1/2}} \\
&= -\frac{em}{4(2\pi)^2}\sum_{\eta=\pm1}\Theta(\mu)\int_0^{\xi_\eta} dk_\perp 2k_\perp \Big\{\frac{1}{\tilde{k}_\perp^2} + \frac{\eta}{M}\frac{1}{\tilde{k}_\perp}\Big\}\operatorname{arctanh}\frac{\sqrt{\mu^2 - (\tilde{k}_\perp + \eta M)^2}}{|\mu|},
\end{aligned} \tag{6.E.22}$$

where $\xi_\eta = \sqrt{(\mu - \eta M)^2 - m^2}, \alpha_\eta = \sqrt{\mu^2 - (\tilde{k}_\perp + \eta M)^2}$.

The third integrand is

$$
\begin{aligned}
C^{iso.}_{(3)} &= -\frac{em}{4(2\pi)^2}\sum_{\eta=\pm1}\Theta(\mu)\int_0^{\xi_\eta} dk_\perp 2k_\perp \Big\{-\frac{\eta}{M}\frac{1}{\tilde{k}_\perp^3}\Big\}\int_0^{\alpha_\eta} dk_\parallel (k_\parallel^2+(\tilde{k}_\perp+\eta M)^2)^{1/2} \\
&= \frac{em}{4(2\pi)^2}\sum_{\eta=\pm1}\Theta(\mu)\int_0^{\xi_\eta} dk_\perp 2k_\perp \frac{\eta}{M}\frac{1}{\tilde{k}_\perp^3}\frac{1}{2}\Big\{|\mu|\sqrt{\mu^2-(\tilde{k}_\perp+\eta M)^2} \\
&\quad +(\tilde{k}_\perp+\eta M)^2\,\mathrm{arctanh}\,\frac{\sqrt{\mu^2-(\tilde{k}_\perp+\eta M)^2}}{|\mu|}\Big\}. \qquad (6.E.23)
\end{aligned}
$$

Change variable: $|\mu|\sin\theta=\tilde{k}_\perp+\eta M$ with

$$
\theta_\alpha=\sin^{-1}\frac{m+\eta M}{|\mu|},\quad \theta_\beta=\pi/2. \qquad (6.E.24)
$$

The $C^{iso.}$ term is

$$
\begin{aligned}
C^{iso.} &= C^{iso.}_{(1,2)}+C^{iso.}_{(3)} \\
&= -\frac{em}{8\pi^2}\sum_{\eta=\pm1}\frac{\eta|\mu|}{2M}\Theta(\mu)\int_{\theta_\alpha}^{\theta_\beta} d\theta\Big(1-\frac{M^2}{|\mu|^2(\sin\theta-\eta\frac{M}{|\mu|})^2}\Big)\cos\theta\,\mathrm{arctanh}\cos\theta-\frac{\cos^2\theta}{(\sin\theta-\eta\frac{M}{|\mu|})^2}.
\end{aligned}
$$
$$(6.E.25)$$

The $C^{\boldsymbol{m}}$ term is

$$
\begin{aligned}
C^{\boldsymbol{m}} &= -\frac{em}{4V}\sum_{k}\sum_{\eta=\pm1}\Big\{-\frac{\eta M}{E_\eta{}^3\tilde{k}_\perp}-\frac{1}{E_\eta{}^3}\Big\}\int_0^{\mu} d\varepsilon \sum_{\zeta=\pm1}\zeta\delta(\varepsilon-\zeta E_\eta) \\
&= \frac{em}{4(2\pi)^2}\sum_{\eta=\pm1}\Theta(\mu)\int_0^{\xi_\eta} dk_\perp 2k_\perp\Big\{\frac{\eta M}{\tilde{k}_\perp}+1\Big\}\int_0^{\alpha_\eta} dk_\parallel \frac{1}{(k_\parallel^2+(\tilde{k}_\perp+\eta M)^2)^{3/2}} \\
&= \frac{em}{4(2\pi)^2}\sum_{\eta=\pm1}\Theta(\mu)\int_0^{\xi_\eta} dk_\perp 2k_\perp\Big\{\frac{\eta M}{\tilde{k}_\perp}+1\Big\}\frac{\sqrt{\mu^2-(\tilde{k}_\perp+\eta M)^2}}{(\tilde{k}_\perp+\eta M)^2|\mu|} \\
&= \frac{em}{2(2\pi)^2}\sum_{\eta=\pm1}\Theta(\mu)\int_{\theta_\alpha}^{\theta_\beta} d\theta|\mu|\cos\theta\Big\{|\mu|\sin\theta\Big\}\frac{|\mu|\cos\theta}{|\mu|^3\sin^2\theta} \\
&= \frac{em}{2(2\pi)^2}\sum_{\eta=\pm1}\Theta(\mu)\int_{\theta_\alpha}^{\theta_\beta} d\theta\frac{\cos^2\theta}{\sin\theta} \\
&= -\frac{em}{2(2\pi)^2}\sum_{\eta=\pm1}\Theta(\mu)(\cos\theta_\alpha+\log\tan\theta_\alpha/2). \qquad (6.E.26)
\end{aligned}
$$

d. Appendix: Tables of integrals

i) Integral: $\sum_k \frac{1}{\tilde{k}^3}$,

$$\begin{aligned}
\frac{1}{V}\sum_k \frac{1}{\tilde{k}^3} &= \frac{2}{(2\pi)^2}\int_0^{\Lambda} dk \frac{k^2}{(k^2+m^2)^{3/2}} \\
&= \frac{2}{4\pi^2}(\operatorname{arcsinh}\frac{\Lambda}{m} - \frac{\Lambda}{\sqrt{\Lambda^2+m^2}}) \\
&\approx \frac{1}{4\pi^2}(2\log(2\Lambda/m)-2), \qquad (6.E.27)
\end{aligned}$$

with $\Lambda \gg m$.

ii) Integral: $\sum_k \frac{1}{\tilde{k}^5}$,

$$\begin{aligned}
\frac{1}{V}\sum_k \frac{1}{\tilde{k}^5} &= \frac{2}{(2\pi)^2}\int_0^{\Lambda} dk \frac{k^2}{(k^2+m^2)^{5/2}} \\
&= \frac{2}{4\pi^2}\frac{\Lambda^3}{3m^2(\Lambda^2+m^2)^{3/2}} \\
&\approx \frac{1}{4\pi^2}\frac{2}{3m^2}. \qquad (6.E.28)
\end{aligned}$$

iii) Integral: $\sum_k \frac{k_\parallel^2}{\tilde{k}^7}$,

$$\begin{aligned}
\frac{1}{V}\sum_k \frac{k_\parallel^2}{\tilde{k}^7} &= -\frac{1}{(2\pi)^2}\int_0^{\Lambda} dk_\perp 2k_\perp \int_0^{\sqrt{\Lambda^2-k_\perp^2}} dk_\parallel \frac{k_\parallel^2}{(k_\parallel^2+\tilde{k}_\perp^2)^{7/2}} \\
&= \frac{1}{(2\pi)^2}\int_0^{\Lambda} dk_\perp 2k_\perp \frac{(\Lambda^2-k_\perp^2)^{3/2}(5\tilde{k}_\perp^2+2\Lambda^2-2k_\perp^2)}{15\tilde{k}_\perp^4(\Lambda^2+m^2)^{5/2}} \\
&= \frac{2}{4\pi^2}\int_m^{\tilde{\Lambda}} d\tilde{k}_\perp \frac{(\tilde{\Lambda}^2-\tilde{k}_\perp^2)^{3/2}(3\tilde{k}_\perp^2+2\tilde{\Lambda}^2)}{15\tilde{k}_\perp^3\tilde{\Lambda}^5} \\
&= \frac{2}{4\pi^2}\int_m^{\tilde{\Lambda}} d\tilde{k}_\perp \frac{(\tilde{\Lambda}^2-\tilde{k}_\perp^2)^{3/2}}{5\tilde{k}_\perp\tilde{\Lambda}^5} + \frac{2(\tilde{\Lambda}^2-\tilde{k}_\perp^2)^{3/2}}{15\tilde{k}_\perp^3\tilde{\Lambda}^3} \\
&= \frac{2}{4\pi^2}\int_m^{\tilde{\Lambda}} d\tilde{k}_\perp(\tilde{\Lambda}^2-\tilde{k}_\perp^2)^{1/2}\Big\{\frac{1}{5\tilde{k}_\perp\tilde{\Lambda}^3} - \frac{\tilde{k}_\perp}{5\tilde{\Lambda}^5} + \frac{2}{15\tilde{k}_\perp^3\tilde{\Lambda}} - \frac{2}{15\tilde{k}_\perp\tilde{\Lambda}^3}\Big\} \\
&= \frac{2}{4\pi^2}\int_m^{\tilde{\Lambda}} d\tilde{k}_\perp(\tilde{\Lambda}^2-\tilde{k}_\perp^2)^{1/2}\Big\{\frac{1}{15\tilde{k}_\perp\tilde{\Lambda}^3} - \frac{\tilde{k}_\perp}{5\tilde{\Lambda}^5} + \frac{2}{15\tilde{k}_\perp^3\tilde{\Lambda}}\Big\} \\
&\approx \frac{1}{4\pi^2}\frac{2}{15m^2}, \qquad (6.E.29)
\end{aligned}$$

where we define $\tilde{\Lambda} \equiv \sqrt{\Lambda^2 + m^2}$. Note that we have $\tilde{A} = \sqrt{A^2 + m^2}$ for $A = k, k_\perp$ and Λ.

iv) Integral: $\sqrt{\tilde{\Lambda}^2 - \tilde{k}_\perp^2}\tilde{k}_\perp^1$,

$$\int_m^{\tilde{\Lambda}} d\tilde{k}_\perp \sqrt{\tilde{\Lambda}^2 - \tilde{k}_\perp^2}\tilde{k}_\perp = \frac{(\tilde{\Lambda}^2 - m^2)^{3/2}}{3}. \tag{6.E.30}$$

v) Integral: $\sqrt{\tilde{\Lambda}^2 - \tilde{k}_\perp^2}\tilde{k}_\perp^{-1}$,

$$\int_m^{\tilde{\Lambda}} d\tilde{k}_\perp \sqrt{\tilde{\Lambda}^2 - \tilde{k}_\perp^2}\frac{1}{\tilde{k}_\perp} = \tilde{\Lambda}\,\mathrm{arctanh}\sqrt{1 - \frac{m^2}{\tilde{\Lambda}^2}} - \sqrt{\tilde{\Lambda}^2 - m^2}. \tag{6.E.31}$$

vi) Integral: $\sqrt{\tilde{\Lambda}^2 - \tilde{k}_\perp^2}\tilde{k}_\perp^{-3}$,

$$\int_m^{\tilde{\Lambda}} d\tilde{k}_\perp \sqrt{\tilde{\Lambda}^2 - \tilde{k}_\perp^2}\frac{1}{\tilde{k}_\perp^3} = \frac{1}{2m^2}\Big(\sqrt{\tilde{\Lambda}^2 - m^2} - \frac{m^2}{\tilde{\Lambda}}\,\mathrm{arctanh}\sqrt{1 - \frac{m^2}{\tilde{\Lambda}^2}}\Big). \tag{6.E.32}$$

Chapter 7

Summary

In this dissertation, I employ numerical and analytical *ab initio* techniques to study the intrinsic spin Hall effect in various type of ferromagnets, primarily focusing on two key issues: i, the relationship between the AHE and SHE in ferromagnets; ii, the anisotropy of SHC with respect to magnetization.

In chapter III, I first study the relationship between SHC and AHC in the ferromagnetic CoPt. Despite the fact that the symmetry of the Berry curvature follows the band structure, the spin Berry curvature has a reduced symmetry, only reflecting the spatial inversion symmetry. Such symmetry reduction is clearly observed at the anti-crossing points of Bloch bands with opposite spin (*Class II*). I find the interband matrix elements of velocity and spin velocity operator are significantly different at the *Class II* anti-crossings, which causes the symmetry reduction of spin Berry curvature. The diverged behaviors of Berry curvature and spin Berry curvature at the *Class II* anti-crossings can explain previous experimental results that the intrinsic AHC and SHC are not correlated by the spin polarization.

In chapter IV, I investigate the magnetization dependence of the intrinsic SHC in bcc-Fe and fcc-Ni, which is inspired by the unique feature of the *Class II* anti-crossings. I find the intrinsic SHC in these cubic phase ferromagnets are highly anisotropic with respect to the direction of magnetization, *e.g.*, the change in magnitude of the intrinsic SHC for bcc-Fe is four-fold when $\hat{m}$ is rotated from the z to x axes. The magnetization dependence of the intrinsic SHC is closely related to the *Class II* anti-crossings, where the interband matrix elements are enhanced when magnetization is rotated away from the quantization axis. The Fermi level dependence further indicates that the anisotropy of the intrinsic SHC can be tuned by delicate band engineering.

Both results of first principles calculations underscore the significance of *Class II* anti-crossings where the behavior of AHE and SHE diverge. It explains the results that the intrinsic AHE and SHE are not correlated in ferromagnets, unless the spin is exact or nearly a good quantum number, *e.g.*, for *Class I* anti-crossings. To investigate the anisotropic SHE in the ferromagnets, I choose two types of model Hamiltonian for analytical *ab initio* calculation: 2DEGs with exchange interaction and Dirac ferromagnet.

In chapter V, 2DEG with the Rashba and Dresselhaus SOC and the exchange interaction is studied. An exact cancellation of the intrinsic SHC is observed when the Rashba and Dresselhaus have equal strength ($|\alpha| = |\beta|$) and the magnetization is out of plane. In contrast, I find the Fermi contours are shifted by the interplay between the SOCs and the in-plane magnetization, which leas to a finite intrinsic SHC. It shows that the interplay between SOC and exchange interaction has a significant effect on the Fermi contours and contributes to the intrinsic SHE. Consequently, the intrinsic SHC in 2DEGs system is highly anisotropic, depending on the magnitudes of Rashba and Dresselhaus SOC and exchange interaction.

In chapter VI, I introduce ferromagnetic ordering into the massive Dirac system which is spherically symmetric. This allows to avoid the ambiguity on the low symmetry of Rashba and Dresselhaus SOC. The band dispersions of Dirac ferromagnet shows axial anisotropy along the direction of magnetization, for which the energy cut-off scheme with the same symmetry is implemented to deal with the UV-divergence. I find the intrinsic SHC is highly anisotropic with respect to the direction of magnetization. Hence, the anisotropy does not disappear when the strength of magnetization asymptotically approaches zero. It suggests that for intrinsic SHC in massive Dirac electron, a non-trivial transition exists from ferromagnetic state to paramagnetic state. However, extrinsic contributions may account for the discrepancy, which requires further investigation.

In summary, I study the intrinsic SHE in various ferromagnetic materials and models through *ab initio* techniques. The ferromagnets is a natural playground to study the correlation between SHE and AHE, from which I emphasize the unique feature of anti-crossings with opposite spin. A more general theoretical framework is required to formulate these anti-crossing. In addition, I show that in various type of ferromagnets the intrinsic SHC is anisotropic with respect to direction of magnetization, possibly because the symmetry of the system is reduced by the ferromagnetic ordering. The anisotropy of the SHE either in the intrinsic or extrinsic regime would be the central issue in the SHE studies on ferromagnets.

Bibliography

[1] SA Wolf, DD Awschalom, RA Buhrman, et al. Spintronics: a spin-based electronics vision for the future. *Science*, 294(5546):1488–1495, 2001.

[2] Igor Žutić, Jaroslav Fabian, and S. Das Sarma. Spintronics: Fundamentals and applications. *Rev. Mod. Phys.*, 76:323–410, Apr 2004.

[3] Y. K. Kato, R. C. Myers, A. C. Gossard, and D. D. Awschalom. Observation of the spin hall effect in semiconductors. *Science*, 306(5703):1910–1913, 2004.

[4] J. Wunderlich, B. Kaestner, J. Sinova, and T. Jungwirth. Experimental observation of the spin-hall effect in a two-dimensional spin-orbit coupled semiconductor system. *Phys. Rev. Lett.*, 94:047204, Feb 2005.

[5] Jairo Sinova, Sergio O. Valenzuela, J. Wunderlich, et al. Spin Hall effects. *Rev. Mod. Phys.*, 87(4):1213–1260, 2015.

[6] Naoto Nagaosa, Jairo Sinova, Shigeki Onoda, et al. Anomalous hall effect. *Rev. Mod. Phys.*, 82(2):1539, 2010.

[7] Mikhail I Dyakonov and VI Perel. Current-induced spin orientation of electrons in semiconductors. *Phys. Lett. A*, 35(6):459–460, 1971.

[8] Robert Karplus and J. M. Luttinger. Hall effect in ferromagnetics. *Phys. Rev.*, 95:1154–1160, Sep 1954.

[9] Nevill Francis Mott. The scattering of fast electrons by atomic nuclei. *Proc. R. Soc. A*, 124(794):425–442, 1929.

[10] Nevill Francis Mott. The polarisation of electrons by double scattering. *Proc. R. Soc. A*, 135(827):429–458, 1932.

[11] J. E. Hirsch. Spin hall effect. *Phys. Rev. Lett.*, 83:1834–1837, Aug 1999.

[12] Shufeng Zhang. Spin hall effect in the presence of spin diffusion. *Phys. Rev. Lett.*, 85:393–396, Jul 2000.

[13] Shuichi Murakami, Naoto Nagaosa, and Shou-Cheng Zhang. Dissipationless quantum spin current at room temperature. *Science*, 301(5638):1348–1351, 2003.

[14] Jairo Sinova, Dimitrie Culcer, Q. Niu, et al. Universal intrinsic spin hall effect. *Phys. Rev. Lett.*, 92:126603, Mar 2004.

[15] Sergio O Valenzuela and M Tinkham. Direct electronic measurement of the spin hall effect. *Nature*, 442(7099):176–179, 2006.

[16] E Saitoh, M Ueda, H Miyajima, and G Tatara. Conversion of spin current into charge current at room temperature: Inverse spin-hall effect. *Appl. Phys. Lett.*, 88(18):182509, 2006.

[17] Luqiao Liu, Chi Feng Pai, Y. Li, et al. Spin-torque switching with the giant spin hall effect of tantalum. *Science*, 336(6081):555–558, 2012.

[18] Ioan Mihai Miron, Kevin Garello, Gilles Gaudin, et al. Perpendicular switching of a single ferromagnetic layer induced by in-plane current injection. *Nature*, 476(7359):189–193, 2011.

[19] Yasutomo Omori, Edurne Sagasta, Yasuhiro Niimi, et al. Relation between spin hall effect and anomalous hall effect in $3d$ ferromagnetic metals. *Phys. Rev. B*, 99:014403, Jan 2019.

[20] A. Crépieux and P. Bruno. Theory of the anomalous hall effect from the kubo formula and the dirac equation. *Phys. Rev. B*, 64:014416, Jun 2001.

[21] N. A. Sinitsyn, A. H. MacDonald, T. Jungwirth, et al. Anomalous hall effect in a two-dimensional dirac band: The link between the kubo-streda formula and the semiclassical boltzmann equation approach. *Phys. Rev. B*, 75:045315, Jan 2007.

[22] L. Berger. Side-jump mechanism for the hall effect of ferromagnets. *Phys. Rev. B*, 2:4559–4566, Dec 1970.

[23] Jan Smit. The spontaneous hall effect in ferromagnetics ii. *Physica*, 24(1-5):39–51, 1958.

[24] T. Jungwirth, Qian Niu, and A. H. MacDonald. Anomalous hall effect in ferromagnetic semiconductors. *Phys. Rev. Lett.*, 88:207208, May 2002.

[25] Masaru Onoda and Naoto Nagaosa. Topological nature of anomalous hall effect in ferromagnets. *J. Phys. Soc. Jpn.*, 71(1):19–22, 2002.

[26] Ming-Che Chang and Qian Niu. Berry phase, hyperorbits, and the hofstadter spectrum: Semiclassical dynamics in magnetic bloch bands. *Phys. Rev. B*, 53:7010–7023, Mar 1996.

[27] Ganesh Sundaram and Qian Niu. Wave-packet dynamics in slowly perturbed crystals: Gradient corrections and berry-phase effects. *Phys. Rev. B*, 59:14915–14925, Jun 1999.

[28] Yugui Yao, Leonard Kleinman, A. H. MacDonald, et al. First principles calculation of anomalous hall conductivity in ferromagnetic bcc fe. *Phys. Rev. Lett.*, 92:037204, Jan 2004.

[29] F. D. M. Haldane. Berry curvature on the fermi surface: Anomalous hall effect as a topological fermi-liquid property. *Phys. Rev. Lett.*, 93:206602, Nov 2004.

[30] Xinjie Wang, David Vanderbilt, Jonathan R. Yates, and Ivo Souza. Fermi-surface calculation of the anomalous hall conductivity. *Phys. Rev. B*, 76:195109, Nov 2007.

[31] Shuichi Murakami, Naoto Nagosa, and Shou-Cheng Zhang. SU(2) non-abelian holonomy and dissipationless spin current in semiconductors. *Phys. Rev. B*, 69:235206, Jun 2004.

[32] G. Y. Guo, S. Murakami, T.-W. Chen, and N. Nagaosa. Intrinsic spin hall effect in platinum: First-principles calculations. *Phys. Rev. Lett.*, 100:096401, Mar 2008.

[33] T. Tanaka, H. Kontani, M. Naito, et al. Intrinsic spin hall effect and orbital hall effect in 4*d* and 5*d* transition metals. *Phys. Rev. B*, 77:165117, Apr 2008.

[34] Martin Gradhand, Dmitry V. Fedorov, Peter Zahn, and Ingrid Mertig. Spin hall angle versus spin diffusion length: Tailored by impurities. *Phys. Rev. B*, 81:245109, Jun 2010.

[35] Stephan Lowitzer, Martin Gradhand, Diemo Ködderitzsch, et al. Extrinsic and intrinsic contributions to the spin hall effect of alloys. *Phys. Rev. Lett.*, 106:056601, Feb 2011.

[36] M Gradhand, DV Fedorov, Falko Pientka, et al. First-principle calculations of the berry curvature of bloch states for charge and spin transport of electrons. *J. Phys. Condens. Matter*, 24(21):213202, 2012.

[37] Nguyen H. Long, Phivos Mavropoulos, Bernd Zimmermann, et al. Spin relaxation and spin hall transport in $5d$ transition-metal ultrathin films. *Phys. Rev. B*, 90:064406, Aug 2014.

[38] Bernd Zimmermann, Kristina Chadova, Diemo Ködderitzsch, et al. Skew scattering in dilute ferromagnetic alloys. *Phys. Rev. B*, 90:220403, Dec 2014.

[39] Hans-Andreas Engel, Bertrand I. Halperin, and Emmanuel I. Rashba. Theory of spin hall conductivity in n-doped gaas. *Phys. Rev. Lett.*, 95:166605, Oct 2005.

[40] Jürgen Weischenberg, Frank Freimuth, Jairo Sinova, et al. Ab initio theory of the scattering-independent anomalous hall effect. *Phys. Rev. Lett.*, 107:106601, Sep 2011.

[41] NA Sinitsyn. Semiclassical theories of the anomalous hall effect. *J. Phys. Condens. Matter*, 20(2):023201, 2007.

[42] P Nozieres and CJJPF Lewiner. A simple theory of the anomalous hall effect in semiconductors. *J. Phys. I*, 34(10):901–915, 1973.

[43] Jun-ichiro Inoue, Gerrit E. W. Bauer, and Laurens W. Molenkamp. Suppression of the persistent spin hall current by defect scattering. *Phys. Rev. B*, 70:041303, Jul 2004.

[44] Ol'ga V. Dimitrova. Spin-hall conductivity in a two-dimensional rashba electron gas. *Phys. Rev. B*, 71:245327, Jun 2005.

[45] Jairo Sinova, Shuichi Murakami, Shun-Qing Shen, and Mahn-Soo Choi. Spin-hall effect: Back to the beginning at a higher level. *Solid State Commun.*, 138(4):214–217, 2006.

[46] Pierre Weiss and R Forrer. Magnetization and magnetocaloric phenomena of nickel. *Ann. Physique*, 5(10):171, 1926.

[47] John MD Coey. *Magnetism and magnetic materials.* Cambridge university press, 2010.

[48] Edmund Clifton Stoner. Collective electron ferronmagnetism. *Proceedings of the Royal Society of London. Series A. Mathematical and Physical Sciences*, 165(922):372–414, 1938.

[49] B. F. Miao, S. Y. Huang, D. Qu, and C. L. Chien. Inverse spin hall effect in a ferromagnetic metal. *Phys. Rev. Lett.*, 111(6):066602, 2013.

[50] Dai Tian, Yufan Li, D. Qu, et al. Manipulation of pure spin current in ferromagnetic metals independent of magnetization. *Phys. Rev. B*, 94:020403, Jul 2016.

[51] K Uchida, S Takahashi, K Harii, et al. Observation of the spin seebeck effect. *Nature*, 455(7214):778–781, 2008.

[52] K. S. Das, W. Y. Schoemaker, B. J. van Wees, and I. J. Vera-Marun. Spin injection and detection via the anomalous spin hall effect of a ferromagnetic metal. *Phys. Rev. B*, 96:220408, Dec 2017.

[53] LJ Cornelissen, J Liu, RA Duine, et al. Long-distance transport of magnon spin information in a magnetic insulator at room temperature. *Nat. Phys.*, 11(12):1022–1026, 2015.

[54] S. C. Baek, Vivek P. Amin, Young-Wan Oh, et al. Spin currents and spin orbit torques in ferromagnetic trilayers. *Nat. Mater.*, 17(6):509–513, 2018.

[55] Satoshi Iihama, Tomohiro Taniguchi, Kay Yakushiji, et al. Spin-transfer torque induced by the spin anomalous Hall effect. *Nat. Electron.*, 1(2):120–123, 2018.

[56] Luqiao Liu, O. J. Lee, T. J. Gudmundsen, et al. Current-induced switching of perpendicularly magnetized magnetic layers using spin torque from the spin hall effect. *Phys. Rev. Lett.*, 109(9), 2012.

[57] Angie Davidson, Vivek P Amin, Wafa S Aljuaid, et al. Perspectives of electrically generated spin currents in ferromagnetic materials. *Phys. Lett. A*, 384(11):126228, 2020.

[58] T. Taniguchi, J. Grollier, and M. D. Stiles. Spin-transfer torques generated by the anomalous hall effect and anisotropic magnetoresistance. *Phys. Rev. Appl.*, 3(4):044001, 2015.

[59] V. P. Amin, J. Zemen, and M. D. Stiles. Interface-generated spin currents. *Phys. Rev. Lett.*, 121:136805, Sep 2018.

[60] V. P. Amin, J. W. Li, M. D. Stiles, and P. M. Haney. Intrinsic spin currents in ferromagnets. *Phys. Rev. B*, 99(22):220405, 2019.

[61] Kyoung-Whan Kim and Kyung-Jin Lee. Generalized spin drift-diffusion formalism in the presence of spin-orbit interaction of ferromagnets. *Phys. Rev. Lett.*, 125:207205, Nov 2020.

[62] A. Fert and I. A. Campbell. Two-current conduction in nickel. *Phys. Rev. Lett.*, 21:1190–1192, Oct 1968.

[63] Chao-Xing Liu, Xiao-Liang Qi, Xi Dai, et al. Quantum anomalous hall effect in $\mathrm{hg}_{1-y}\mathrm{mn}_y\mathrm{Te}$ quantum wells. *Phys. Rev. Lett.*, 101:146802, Oct 2008.

[64] John David Jackson. *Classical electrodynamics.* John Wiley & Sons, 2007.

[65] Gerald D Mahan. *Many-particle physics.* Springer Science & Business Media, 2013.

[66] Takeo Matsubara. A new approach to quantum-statistical mechanics. *Prog. Theor. Phys.*, 14(4):351–378, 1955.

[67] Agustin Nieto. Evaluating sums over the matsubara frequencies. *Comput. Phys. Commun.*, 92(1):54–64, 1995.

[68] Robert O Jones and Olle Gunnarsson. The density functional formalism, its applications and prospects. *Rev. Mod. Phys.*, 61(3):689, 1989.

[69] P. Hohenberg and W. Kohn. Inhomogeneous electron gas. *Phys. Rev.*, 136:B864–B871, Nov 1964.

[70] W. Kohn and L. J. Sham. Self-consistent equations including exchange and correlation effects. *Phys. Rev.*, 140:A1133–A1138, Nov 1965.

[71] JK Percus. The role of model systems in the few-body reduction of the n-fermion problem. *Int. J. Quantum Chem.*, 13(1):89–124, 1978.

[72] Mel Levy. Universal variational functionals of electron densities, first-order density matrices, and natural spin-orbitals and solution of the v-representability problem. *Proc. Natl. Acad. Sci.*, 76(12):6062–6065, 1979.

[73] Axel D. Becke. Perspective: Fifty years of density-functional theory in chemical physics. *The Journal of Chemical Physics*, 140(18):18A301, 2014.

[74] John P. Perdew, J. A. Chevary, S. H. Vosko, et al. Atoms, molecules, solids, and surfaces: Applications of the generalized gradient approximation for exchange and correlation. *Phys. Rev. B*, 46:6671–6687, Sep 1992.

[75] Lars Hedin and Bengt I Lundqvist. Explicit local exchange-correlation potentials. *J. Phys. C: Solid State Phys.*, 4(14):2064, 1971.

[76] Ulf von Barth and Lars Hedin. A local exchange-correlation potential for the spin polarized case. i. *J. Phys. C: Solid State Phys.*, 5(13):1629, 1972.

[77] O Gunnarsson, BI Lundqvist, and JW Wilkins. Contribution to the cohesive energy of simple metals: Spin-dependent effect. *Phys. Rev. B*, 10(4):1319, 1974.

[78] Olle Gunnarsson and Bengt I Lundqvist. Exchange and correlation in atoms, molecules, and solids by the spin-density-functional formalism. *Phys. Rev. B*, 13(10):4274, 1976.

[79] Seymour H Vosko, Leslie Wilk, and Marwan Nusair. Accurate spin-dependent electron liquid correlation energies for local spin density calculations: a critical analysis. *Can. J. Phys.*, 58(8):1200–1211, 1980.

[80] David M Ceperley and Berni J Alder. Ground state of the electron gas by a stochastic method. *Phys. Rev. Lett.*, 45(7):566, 1980.

[81] J. P. Perdew and Alex Zunger. Self-interaction correction to density-functional approximations for many-electron systems. *Phys. Rev. B*, 23:5048–5079, May 1981.

[82] Yue Wang and John P. Perdew. Correlation hole of the spin-polarized electron gas, with exact small-wave-vector and high-density scaling. *Phys. Rev. B*, 44:13298–13307, Dec 1991.

[83] John P. Perdew, Kieron Burke, and Matthias Ernzerhof. Generalized gradient approximation made simple. *Phys. Rev. Lett.*, 77:3865–3868, Oct 1996.

[84] Chun Li, Arthur J Freeman, HJF Jansen, and CL Fu. Magnetic anisotropy in low-dimensional ferromagnetic systems: Fe monolayers on ag (001), au (001), and pd (001) substrates. *Phys. Rev. B*, 42(9):5433, 1990.

[85] HJF Jansen. Magnetic anisotropy in density-functional theory. *Phys. Rev. B*, 38(12):8022, 1988.

[86] DD Koelling and BN Harmon. A technique for relativistic spin-polarised calculations. *J. Phys. C: Solid State Phys.*, 10(16):3107, 1977.

[87] T Takeda. The scalar relativistic approximation. *Z. Phys*, 32(1):43–48, 1978.

[88] E. Wimmer, H. Krakauer, M. Weinert, and A. J. Freeman. Full-potential self-consistent linearized-augmented-plane-wave method for calculating the electronic structure of molecules and surfaces: o_2 molecule. *Phys. Rev. B*, 24:864–875, Jul 1981.

[89] M. Weinert, E. Wimmer, and A. J. Freeman. Total-energy all-electron density functional method for bulk solids and surfaces. *Phys. Rev. B*, 26:4571–4578, Oct 1982.

[90] HJF Jansen and Arthur J Freeman. Total-energy full-potential linearized augmented-plane-wave method for bulk solids: Electronic and structural properties of tungsten. *Phys. Rev. B*, 30(2):561, 1984.

[91] David J Singh and Lars Nordstrom. *Planewaves, Pseudopotentials, and the LAPW method*. Springer Science & Business Media, 2006.

[92] O Krogh Andersen. Linear methods in band theory. *Phys. Rev. B*, 12(8):3060, 1975.

[93] DD Koelling and GO Arbman. Use of energy derivative of the radial solution in an augmented plane wave method: application to copper. *J. Phys. Condens. Matter*, 5(11):2041, 1975.

[94] M Weinert. Solution of poisson's equation: Beyond ewald-type methods. *J. Math. Phys.*, 22(11):2433–2439, 1981.

[95] Ryogo Kubo. Statistical-mechanical theory of irreversible processes. i. general theory and simple applications to magnetic and conduction problems. *J. Phys. Soc. Jpn.*, 12(6):570–586, 1957.

[96] C. S. Wang and J. Callaway. Band structure of nickel: Spin-orbit coupling, the fermi surface, and the optical conductivity. *Phys. Rev. B*, 9:4897–4907, Jun 1974.

[97] P. M. Oppeneer, T. Maurer, J. Sticht, and J. Kübler. Ab initio calculated magneto-optical kerr effect of ferromagnetic metals: Fe and ni. *Phys. Rev. B*, 45:10924–10933, May 1992.

[98] Shuichi Murakami, Naoto Nagosa, and Shou-Cheng Zhang. SU(2) non-abelian holonomy and dissipationless spin current in semiconductors. *Phys. Rev. B*, 69:235206, Jun 2004.

[99] Qing-feng Sun and X. C. Xie. Definition of the spin current: The angular spin current and its physical consequences. *Phys. Rev. B*, 72:245305, Dec 2005.

[100] Junren Shi, Ping Zhang, Di Xiao, and Qian Niu. Proper definition of spin current in spin-orbit coupled systems. *Phys. Rev. Lett.*, 96:076604, Feb 2006.

[101] A. Vernes, B. L. Györffy, and P. Weinberger. Spin currents, spin-transfer torque, and spin-hall effects in relativistic quantum mechanics. *Phys. Rev. B*, 76:012408, Jul 2007.

[102] S. Lowitzer, D. Ködderitzsch, and H. Ebert. Spin projection and spin current density within relativistic electronic-transport calculations. *Phys. Rev. B*, 82:140402, Oct 2010.

[103] G. Y. Guo, Yugui Yao, and Qian Niu. Ab initio calculation of the intrinsic spin hall effect in semiconductors. *Phys. Rev. Lett.*, 94:226601, Jun 2005.

[104] Lev Davidovich Landau and Evgenii Mikhailovich Lifshitz. *Course of theoretical physics*. Elsevier, 2013.

[105] Pei-Qing Jin, You-Quan Li, and Fu-Chun Zhang. Su (2)× u (1) unified theory for charge, orbit and spin currents. *J. of Phys. A*, 39(22):7115, 2006.

[106] Michael Victor Berry. Quantal phase factors accompanying adiabatic changes. *Proc. R. Soc. Lond.*, 392(1802):45–57, 1984.

[107] D. J. Thouless, M. Kohmoto, M. P. Nightingale, and M. den Nijs. Quantized hall conductance in a two-dimensional periodic potential. *Phys. Rev. Lett.*, 49:405–408, Aug 1982.

[108] Di Xiao, Ming-Che Chang, and Qian Niu. Berry phase effects on electronic properties. *Rev. Mod. Phys.*, 82(3):1959, 2010.

[109] Ryuichi Shindou and Ken-Ichiro Imura. Noncommutative geometry and non-abelian berry phase in the wave-packet dynamics of bloch electrons. *Nucl. Phys. B*, 720(3):399–435, 2005.

[110] Yan Sun, Yang Zhang, Claudia Felser, and Binghai Yan. Strong intrinsic spin hall effect in the taas family of weyl semimetals. *Phys. Rev. Lett.*, 117(14):146403, 2016.

[111] Peng Song, Chuang-Han Hsu, Giovanni Vignale, et al. Coexistence of large conventional and planar spin hall effect with long spin diffusion length in a low-symmetry semimetal at room temperature. *Nat. Mater.*, 19(3):292–298, 2020.

[112] E Derunova, Y Sun, C Felser, et al. Giant intrinsic spin hall effect in w3ta and other a15 superconductors. *Sci. Adv.*, 5(4):eaav8575, 2019.

[113] Jorgen Rammer. *Quantum transport theory.* CRC Press, 2018.

[114] Yasutomo Omori, Edurne Sagasta, Yasuhiro Niimi, et al. Relation between spin hall effect and anomalous hall effect in $3d$ ferromagnetic metals. *Phys. Rev. B*, 99:014403, Jan 2019.

[115] Alexander B. Shick and Oleg N. Mryasov. Coulomb correlations and magnetic anisotropy in ordered $L1_0$ copt and fept alloys. *Phys. Rev. B*, 67:172407, May 2003.

[116] Naoto Nagaosa, Jairo Sinova, Shigeki Onoda, et al. Anomalous hall effect. *Rev. Mod. Phys.*, 82:1539–1592, May 2010.

[117] Kohji Nakamura, Tomonori Ito, A. J. Freeman, et al. Enhancement of magnetocrystalline anisotropy in ferromagnetic fe films by intra-atomic noncollinear magnetism. *Phys. Rev. B*, 67:014420, Jan 2003.

[118] Hongbin Zhang, Stefan Blügel, and Yuriy Mokrousov. Anisotropic intrinsic anomalous hall effect in ordered 3 d pt alloys. *Phys. Rev. B*, 84(2):024401, 2011.

[119] Huei-Ru Fuh and Guang-Yu Guo. Intrinsic anomalous hall effect in nickel: A gga+ u study. *Phys. Rev. B*, 84(14):144427, 2011.

[120] Marten Seemann, Diemo Ködderitzsch, Sebastian Wimmer, and Hubert Ebert. Symmetry-imposed shape of linear response tensors. *Phys. Rev. B*, 92(15):155138, 2015.

[121] Pei-Qing Jin Zhang, You-Quan Li, and Fu-Chun. SU (2) × U (1) unified theory for charge, orbit and spin currents. *J. Phys. A*, 39(22):7115, 2006.

[122] Pei Qing Jin and You Quan Li. Generalized Kubo formula for spin transport: A theory of linear response to non-Abelian fields. *Phys. Rev. B*, 74(8), 2006.

[123] B. W.A. Leurs, Z. Nazario, D. I. Santiago, and J. Zaanen. Non-Abelian hydrodynamics and the flow of spin in spin-orbit coupled substances. *Ann. Phys.*, 323(4):907–945, 2008.

[124] Guanxiong Qu, Kohji Nakamura, and Masamitsu Hayashi. Symmetry of berry and spin berry curvatures in ferromagnetic copt. *arXiv:1901.05651*, 2019.

[125] EP Yelsukov, EV Voronina, and VA Barinov. Mössbauer study of magnetic properties formation in disordered fe-al alloys. *J. Magn. Magn. Mater.*, 115(2-3):271–280, 1992.

[126] RP Van Ingen, RHJ Fastenau, and EJ Mittemeijer. Laser ablation deposition of cu-ni and ag-ni films: Nonconservation of alloy composition and film microstructure. *J. Appl. Phys.*, 76(3):1871–1883, 1994.

[127] NA Sinitsyn, EM Hankiewicz, Winfried Teizer, and Jairo Sinova. Spin hall and spin-diagonal conductivity in the presence of rashba and dresselhaus spin-orbit coupling. *Phys. Rev. B*, 70(8):081312, 2004.

[128] Emmanuel I Rashba. Sum rules for spin hall conductivity cancellation. *Phys. Rev. B*, 70(20):201309, 2004.

[129] AG Mal' shukov and Koung-An Chao. Spin hall conductivity of a disordered two-dimensional electron gas with dresselhaus spin-orbit interaction. *Phys. Rev. B*, 71(12):121308, 2005.

[130] Tsung-Wei Chen. Maximum intrinsic spin-hall conductivity in two-dimensional systems with k-linear spin–orbit interaction. *J. Phys. Condens. Matter*, 25(15):155801, 2013.

[131] Shuichi Murakami. Absence of vertex correction for the spin hall effect in p-type semiconductors. *Phys. Rev. B*, 69:241202, Jun 2004.

[132] John Schliemann and Daniel Loss. Anisotropic transport in a two-dimensional electron gas in the presence of spin-orbit coupling. *Phys. Rev. B*, 68:165311, Oct 2003.

[133] John Schliemann, J. Carlos Egues, and Daniel Loss. Nonballistic spin-field-effect transistor. *Phys. Rev. Lett.*, 90:146801, Apr 2003.

[134] N. A. Sinitsyn, E. M. Hankiewicz, Winfried Teizer, and Jairo Sinova. Spin hall and spin-diagonal conductivity in the presence of rashba and dresselhaus spin-orbit coupling. *Phys. Rev. B*, 70:081312, Aug 2004.

[135] Junji Fujimoto and Hiroshi Kohno. Transport properties of dirac ferromagnet. *Phys. Rev. B*, 90:214418, Dec 2014.

[136] Adeline Crépieux and Patrick Bruno. Relativistic corrections in magnetic systems. *Phys. Rev. B*, 64(9):094434, 2001.

[137] Allan Hugh MacDonald and SH Vosko. A relativistic density functional formalism. *J. Phys. C: Solid State Phys.*, 12(15):2977, 1979.

[138] MV Ramana and AK Rajagopal. Theory of spin polarised inhomogeneous relativistic electron gas. *J. Phys. C: Solid State Phys.*, 14(29):4291, 1981.

[139] PA Wolff. Matrix elements and selection rules for the two-band model of bismuth. *J. Phys. Chem. Solids*, 25(10):1057–1068, 1964.

[140] Joseph G Checkelsky, Jianting Ye, Yoshinori Onose, et al. Dirac-fermion-mediated ferromagnetism in a topological insulator. *Nat. Phys.*, 8(10):729–733, 2012.

[141] Yuki Fuseya, Masao Ogata, and Hidetoshi Fukuyama. Spin-hall effect and diamagnetism of dirac electrons. *J. Phys. Soc. Jpn.*, 81(9):093704, 2012.

[142] Takaaki Fukazawa, Hiroshi Kohno, and Junji Fujimoto. Intrinsic and extrinsic spin hall effects of dirac electrons. *J. Phys. Soc. Jpn.*, 86(9):094704, 2017.

[143] P Streda. Theory of quantised hall conductivity in two dimensions. *J. Phys. C: Solid State Phys.*, 15(22):L717–L721, aug 1982.